

The Implementation and Application of Quantitative Susceptibility Mapping in the Pre-clinical Liver

Eoin Finnerty, M.Phil, M.Sci

Submitted for the degree of Doctor of Philosophy in
Medical Physics and Biomedical Engineering

January 2018

Department of Medical Physics and Biomedical Engineering

And

Centre for Advanced Biomedical Imaging, Division of Medicine

University College London

Declaration

I, Eoin Finnerty, confirm that the work presented in this thesis is my own, except where stated otherwise in the text. This work is based on research conducted by me during the time period from October 2012 to August 2015 at University College London.

Eoin Finnerty

..... January 2018

Abstract

Quantitative Susceptibility Mapping (QSM) is a relatively new Magnetic Resonance Imaging (MRI) technique that gives information about the relative quantities of magnetically active constituents of a biological system. Using phase data, not normally utilised in standard MRI, measurements are made of local variations in the main magnetic field, B_0 . This data is then processed to calculate a map of local magnetic susceptibility within an organ of interest. This map yields relatively quantitative information, and compositional inferences can be made regarding the organ. Thus far, the body of literature on QSM has focussed almost exclusively on the brain, and has been performed on clinical data. This will be a preclinical project, and will focus primarily on the liver.

The first two chapters of this thesis will establish the context of the research, as well as the background theory of QSM, including a detailed discussion of the set of algorithms selected to calculate the susceptibility maps for this body of work. The implementation of QSM in the preclinical liver has not been performed previously, and the novelty of the technique and the experimental work performed necessitated optimising both data acquisition and processing protocols. This was done on an empirical basis, and comprises the experimental work detailed in chapter 3.

Chapters 4 – 6 describe the application of QSM to a number of hepatic conditions. It was established in chapter 4 that QSM is sensitive to changes in the oxygen saturation of blood in large branches of the major hepatic blood vessels in healthy mice. Chapter 5 discusses the application of QSM to a preclinical model of colorectal liver metastases, and also examines the ability of QSM to assess the efficacy of a Vascular Disrupting Agent (VDA), a novel chemotherapeutic drug. Finally, chapter 6 details the application of QSM to a model of liver cirrhosis.

Impact Statement

This is the first application of Quantitative Susceptibility Mapping to the preclinical liver, and, furthermore, the first application of QSM to a number of hepatic conditions. The implementation of QSM in this context required extensive experimental work, and the undertaking has resulted in a viable paradigm within which future experiments can be carried out. Furthermore, it has been established that QSM can yield relevant information regarding a number of clinically pertinent conditions. While more work is required before clinical implementation, this work has laid the groundwork for further avenues of study.

Acknowledgements

There are a vast number of people who deserve my sincerest gratitude for all of their help though-out my time in academia, but in the interests of brevity I will narrow it down to just a few.

First of all, my supervisors Dr. Simon Walker-Samuel and Dr. David Thomas. Your support and encouragement over the last 5 years was invaluable, and I would not have gotten this far without it. I truly believe that you both went above and beyond during the course of this PhD, and I really appreciate the work that you have put in. Thank-you both.

I would also like to thank Professor Mark Lythgoe everyone at CABI for taking me in in the early days. I couldn't imagine a kinder and more welcoming group of people with whom to work.

Lastly, and most importantly, I would like to thank my family, and in particular my parents, for their unwavering support through the years in everything I have done. I honestly can't thank you enough.

Eoin Michael Finnerty.

Publications & Proceedings

Conference Proceedings:

E. Finnerty, R. Ramasawmy, J. O'Callaghan, M. F. Lythgoe, K. Shmueli, D. Thomas, S. Walker-Samuel. Characterising Liver Haemodynamics with Quantitative Susceptibility Mapping. *Proc Soc Mag Reson (Brit. Chap.) Med* 2014; (20)

E. Finnerty, R. Ramasawmy, J. O'Callaghan, M. Lythgoe, K. Shmueli, D. Thomas, S. Walker-Samuel. Evaluation of Quantitative Susceptibility Mapping to Detect and Monitor Colorectal Metastases in Mouse Liver. *Proc Intl Soc Mag Reson Med*. 2015; (23) eP0193.

E. Finnerty, R. Ramasawmy, J. O'Callaghan, J. Connell, K. Shmueli, David L Thomas, S. Walker-Samuel. Quantitative Susceptibility Mapping to Characterise Hepatic Hyperoxia in Mice. *Proc Intl Soc Mag Reson Med*. 2016; (24) eP4844.

J. J. Connell, R. Ramasawmy, T. A. Roberts, M. Zaw Thin, R. Bofinger, S. Patrick, E. Finnerty, S. Walker-Samuel, T. L. Kalber, M. F. Lythgoe. Monitoring Liver Fibrosis Disease Progression and Resolution with Cell Therapy. *Europ. Soc. Mol. Img*. 2016

Publications:

E. Finnerty, R. Ramasawmy, J. O'Callaghan, J. Connell, M. F. Lythgoe, K. Shmueli, D. Thomas, S. Walker-Samuel. Measurement of Hepatic Venous Haemoglobin Oxygen Saturation (ShvO₂) with Quantitative Susceptibility Mapping. *Manuscript in Preparation*.

E. Finnerty, R. Ramasawmy, J. Connell, T. Kalber, P. Johnson, J. O'Callaghan, M. F. Lythgoe, K. Shmueli, D. L. Thomas, S. Walker-Samuel. Quantitative Susceptibility Mapping (QSM) of Colorectal Liver Metastases in the Mouse Liver: Assessment of Tissue Status and Oxygen Utilisation. *Manuscript in Preparation*.

Table of Contents

Chapter 1: Context of Research.....	2
1.1: The Liver.....	3
1.2: Liver Imaging.....	6
Chapter 2: Background Theory.....	13
2.1: Phase.....	15
2.2: Magnetic Susceptibility.....	17
2.3 Calculation of Susceptibility Map.....	18
2.3.1: Phase Unwrapping.....	18
2.3.2: Background Field Suppression.....	19
2.3.3: Susceptibility Calculation.....	20
2.3.4: Algorithms.....	21
2.3.5: SHARP Algorithm.....	22
2.3.6: Laplacian Phase Unwrapping.....	23
2.3.7: Thresholded k-space Division.....	24
2.4: Quantitative Susceptibility Mapping.....	26
2.5: QSM in the Liver.....	27
Chapter 3: Optimisation.....	38
3.1: Acquisition.....	38
3.1.1: Acquisition Parameters.....	38

3.1.1.1: Echo Time.....	39
3.1.1.2: Respiratory Gating.....	40
3.1.1.3: Repetition Time & Flip Angle.....	41
3.1.1.4: Resolution & Averages.....	41
3.1.2: Flow Compensation.....	41
3.1.2.1: Implementation.....	42
3.1.2.2: Stage I – Flow Phantom.....	45
3.1.2.2.1: Stage I – Results.....	47
3.1.2.2.2: Stage I – Conclusions.....	49
3.1.2.3: Stage II – In-vivo Acquisition.....	50
3.1.2.3.1: Stage II – Results.....	51
3.1.2.3.2: Stage II – Conclusions.....	53
3.1.3: 2D vs 3D Images.....	53
3.1.3.1: Methods.....	54
3.1.3.2: Results.....	55
3.1.3.3: Discussion.....	58
3.1.3.4: Conclusions.....	59
3.1.4: Mouse Liver Fat Fraction:.....	59
3.2: Processing.....	62
3.2.1: Heuristic vs Physical Background Field Suppression.....	63
3.2.1.1: Heuristic vs Physical Background Field Suppression.....	64
3.2.1.2 Data Acquisition.....	65
3.2.1.3 ROI	65

3.2.1.4 Results.....	68
3.2.1.5 Conclusion.....	68
3.3.1: SHARP Algorithm.....	72
3.3.11: SHARP Results.....	74
3.3.2: Thresholded k-space (TKD) algorithm.....	76
3.3.2.1: TKD Results.....	76
3.3.3: Interaction Between Algorithms.....	78
3.3.3.1: Results.....	78
3.3.3.2: Conclusions.....	82
3.3.4: TKD Systematic Underestimation.....	82
3.3.4.1: Results.....	83
3.3.4.2: Discussion & Conclusions.....	86
Chapter 4: Hyperoxia in Healthy Mice.....	90
4.1: QSM with Optimised Pipeline.....	91
4.1.1: Introduction.....	91
4.1.1.1: Susceptibility Reference.....	91
4.1.1.2: Regions of Interest.....	92
4.1.1.3: Precision & Robustness.....	93
4.1.2: Materials & Methods.....	93
4.1.2.1: Animal Preparation.....	93
4.1.2.2: Data Acquisition.....	93

4.1.2.3: QSM processing.....	94
4.1.2.4: External Reference.....	94
4.1.2.5: Regions of Interest.....	95
4.1.2.6: Precision & Robustness.....	97
4.1.2.7: QSM in Blood Vessels.....	98
4.1.2.8: Histology.....	99
4.1.3: Results.....	99
4.1.3.1: External Reference.....	99
4.1.3.2: Precision & Robustness.....	101
4.1.4: Discussion.....	105
4.1.5: Conclusions.....	108
4.2: Hyperoxic Gas Challenge.....	109
4.2.1 Introduction.....	109
4.2.2: Theory.....	110
4.2.2.1: Magnetic Susceptibility of Blood.....	110
4.2.2.2: Calculating SvO ₂	111
4.2.3 Materials & Methods.....	111
4.2.3.1: Animal Preparation.....	111
4.2.3.2: Blood Gas Measurement.....	112
4.2.3.3: Statistical Analysis.....	112
4.2.4: Results.....	112
4.2.5: Discussion.....	119

4.2.6: Conclusions.....	121
Chapter 5: Colorectal Liver Metastases.....	124
5.1: QSM and Colorectal Liver Metastases.....	125
5.1.1: Introduction.....	125
5.1.2: Materials & Methods.....	127
5.1.2.1: Animal Preparation.....	127
5.1.2.2: Data Acquisition.....	127
5.1.2.3: Regions of Interest.....	128
5.1.3: Results.....	129
5.1.4: Discussion.....	135
5.1.6: Conclusions.....	137
5.2: Vascular Disrupting Agent.....	138
5.2.1: Introduction.....	138
5.2.2: Materials & Methods.....	139
5.2.2.1: Animal Preparation.....	139
5.2.2.2 Histology.....	140
5.2.2.3: Statistical Analysis.....	140
5.2.3: Results.....	141
5.2.4: Discussion.....	151
5.2.5: Conclusions.....	154

Chapter 6: Liver Cirrhosis.....	158
6.1: Introduction.....	159
6.2: Theory.....	161
6.2.1: Cirrhosis Model.....	161
6.3: Materials & Methods.....	161
6.3.1: Animal Preparation.....	161
6.3.2: Data Acquisition.....	162
6.3.3: Statistical Analysis.....	164
6.4: Results.....	164
6.5: Discussion.....	169
6.6 Conclusions.....	171
Final Discussion:.....	174

List of Figures

Chapter 1

Figure 1.1: Anatomical image of the Liver.....	3
Figure 1.2: Gross Anatomy of the Liver.....	4
Figure 1.3: Histological Anatomy of the Liver.....	5

Chapter 2

Figure 2.1: Schematic of RF Quadrature Coil.....	16
Figure 2.2: Images of Each Step of Processing Pipeline.....	25

Chapter 3

Figure 3.1: Velocity Compensated Slice Select Gradient Schematic.....	40
Figure 3.2: Velocity Compensated Slice Select Gradient Schematic.....	43
Figure 3.3: Flow Phantom.....	46
Figure 3.4: Comparison of Images Acquired With and Without Velocity Compensation – Flow Phantom.....	47
Figure 3.5: Contrast & Standard Deviation measured in Flow Phantom. Susceptibility Maps.....	49
Figure 3.6: Comparison of Images Acquired With and Without Velocity Compensation – In-Vivo.....	51
Figure 3.7: Contrast & Standard deviation measured in blood vessel Susceptibility Maps.....	42
Figure 3.8: Comparison of SNR in 2D and 3D Magnitude Images.....	55

Figure 3.9: 2D and 3D Processing Series.....	56
Figure 3.10: Standard Deviation 2D vs. 3D	58
Figure 3.11: Liver Histology.....	61
Figure 3.12: Liver Histology (fat).....	61
Figure 3.13: ROI human brain data.....	67
Figure 3.14: Heuristic vs Physical filter – coronal orientation.....	68
Figure 3.15: Heuristic vs Physical filter – axial orientation.....	69
Figure 3.16: Field shift comparison – physical vs heuristic filter.....	71
Figure 3.17: Processing Series w/ ROI – SHARP Algorithm.....	73
Figure 3.18: TSVD Threshold Series.....	74
Figure 3.19 Contrast & Standard Deviation – SHARP Algorithm	75
Figure 3.20: ROI – TKD Algorithm	76
Figure 3.21 TKD Threshold Series	77
Figure 3.22 TKD threshold - Contrast and Standard Deviation.....	77
Figure 3.23 TKD threshold - Various Field Maps.....	79
Figure 3.24 TKD threshold - Blood Vessel & Liver Tissue Susceptibility.....	80
Figure 3.25: TKD threshold - Tissue Standard Deviation.....	51
Figure 3.26 TKD threshold - Susceptibility with Linear Fit.....	83
Figure 3.27: TKD threshold - Projected Underestimation Calculated & Literature Values.....	84
Figure 3.28: Susceptibilitymaps with and without correction.....	85
Figure 3.29: Corrected and Uncorrected Susceptibility Values.....	85

Chapter 4

Figure 4.1: Water Reference in situ.....	92
Figure 4.2: Hepatic Vein ROI.....	96
Figure 4.3: Portal vein ROI.....	96
Figure 4.4: Hepatic Artery ROI.....	97
Figure 4.5: Blood vessels with Gibbs Ringing.....	95
Figure 4.6: Standard Deviation in Water and Liver Tissue Reference ROIs.....	100
Figure 4.7: Mean Standard Deviation in Water and Liver Tissue Reference ROIs	100
Figure 4.8: Processing Series with MIPs.....	101
Figure 4.9: Mean Susceptibility in Various Liver ROIs.....	103
Figure 4.10: Histology (Perl's Iron Stain).....	104
Figure 4.11: Processing Series Hyperoxia Experiment.....	113
Figure 4.12: Normoxia and Hyperoxia MIPs.....	114
Figure 4.13: Portal and Hepatic Vein Susceptibility – Gas Challenge.....	116
Figure 4.14: Portal and Hepatic Vein SvO ₂ – Gas Challenge.....	117
Figure 4.15: Invasive vs Calculated SvO ₂	118

Chapter 5

Figure 5.1: T ₂ * Magnitude Images Displaying Liver Tumours.....	128
Figure 5.2: Processing Series - CRLM experiment.....	129
Figure 5.3: Susceptibility – Liver Tissue vs Tumour.....	130
Figure 5.4: Susceptibility – Liver Tumour – Gas Challenge.....	131
Figure 5.5: Magnitude & Susceptibility Maps – liver tumours - Gas Challenge.....	132,133
Figure 5.6: Portal & Hepatic Vein SvO ₂ – Healthy vs Disease.....	134
Figure 5.7: Processing Series - CRLM experiment – Treated Cohort.....	141

Figure 5.8: Processing Series - CRLM experiment – Control Cohort.....	142
Figure 5.9: Susceptibility – Tissue vs Tumours – Treated & Control Groups.....	143
Figure 5.10: T ₂ * Magnitude Images Displaying Liver Tumour Burden	145
Figure 5.11: H & E Stained Histology Image of Treated Liver.....	146
Figure 5.12: Susceptibility – Tumours During Gas Challenge – Treated & Control Groups	148
Figure 5.13: Susceptibility – Normoxic vs Hyperoxic – Treated and Control Cohorts.....	149
Figure 5.14: ShvO ₂ – Treated and Control Groups.....	151

Chapter 6

Figure 6.1: T ₂ * Magnitude Images Displaying ROI	163
Figure 6.2: Processing Series - cirrhosis experiment – BDL Cohort	164
Figure 6.3: Processing Series - cirrhosis experiment – Sham Cohort	165
Figure 6.4: Susceptibility – Liver Tissue – BDL vs Sham.....	165
Figure 6.5: Sham vs. BDL perls iron stained liver segment (lit).....	166
Figure 6.6: Susceptibility –Gas Challenge - BDL vs Sham	167
Figure 6.7: ShvO ₂ - BDL vs Sham	168

List of Tables

Chapter 1

Table 1.1: List of literature regarding the quantification of liver iron with MRI.....	10
---	----

Chapter 2

Table 2.1: Non-exhaustive list of QSM literature	32
---	----

Chapter 3

Table 2.1: Acquisition parameters for sec. 3.2.1.....	65
--	----

Chapter 5

Table 5.1: Summary of data presented in fig. 5.9.....	144
--	-----

Table 5.1: Summary of the results displayed in figure 6 & 7.....	148
---	-----

Chapter 6

Table 6.1: Summary of data presented in fig. 6.6.....	168
--	-----

Chapter 1

The aim of this thesis is to explore novel applications of Quantitative Susceptibility Mapping in the liver. A number of scenarios have been investigated in a preclinical context, and are discussed in chapters 4 – 6. The implementation of QSM in the preclinical liver required significant experimental work which has been detailed in chapter 3.

This chapter establishes the context of the research, discussing both micro- and macro scale liver anatomy, as well as imaging techniques currently used to image the liver, and to diagnose hepatic diseases. Finally, some of the advantages QSM can offer over current liver imaging techniques are highlighted.

Context of Research

Quantitative Susceptibility Mapping (QSM) is a novel MRI technique that uses variation in magnetic susceptibility as a contrast mechanism. While QSM is of relatively recent inception, it has spawned a rapidly growing field of research that has found a wide range of diverse applications – from quantifying changes in cerebral iron deposition caused by neurodegenerative diseases ^[1-3], to quantifying cerebral perfusion ^[4], to estimating blood oxygen saturation^[5-7]. Thus far however, much of the research in the field has explored the application of QSM to the brain in a clinical setting.

It is the aim of the experimental work carried out herein to implement QSM in the pre-clinical liver, and to investigate its subsequent application to pre-clinical models of human liver disease - namely colorectal liver metastases and liver cirrhosis.

It is the purpose of this thesis to present a thorough argument in support of the experimental work, and to justify its undertaking. This chapter will discuss the structure and function of the liver under healthy conditions, and will examine some of the modalities currently used in clinical examination. Chapter 2 will elucidate the relevant background theory, and establish the case for the use of QSM in the liver. Chapter 3 will discuss the optimisation of the acquisition and processing pipeline, while chapters 4 – 6 will present the experimental work that has been carried out to test the hypotheses put forward in the previous chapters. Finally, there will be a general discussion of the use of QSM in the liver, and an outline of work that could be carried out should the project be continued.

1.1 THE LIVER

The liver is the second largest organ in the body, and at any one time contains roughly 10% of the total blood volume. It plays a major role in blood filtration, biosynthesis and metabolism, and is responsible for the storage of a number of vitamins and minerals, most notably iron in the form of ferritin. Correct functioning of the liver is of great importance, and the diagnostic procedures available for assessing liver health and function range from invasive testing in the form

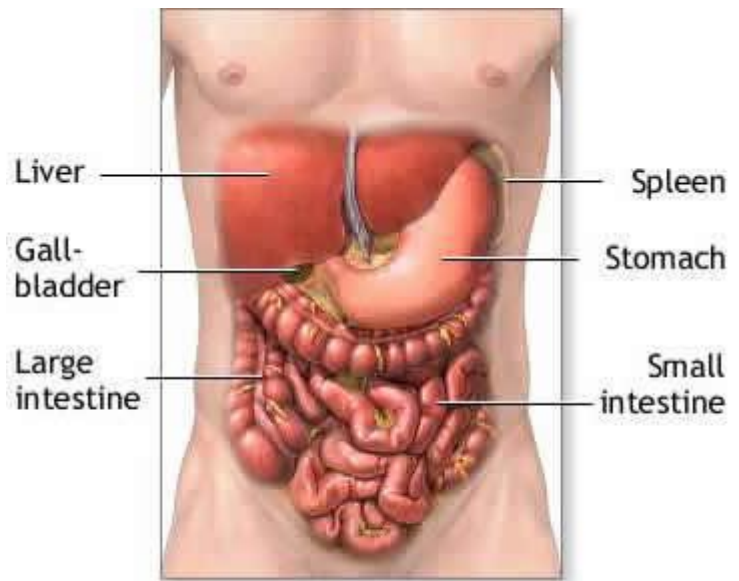


Fig 1.1: Anatomical image depicting the liver in-situ [9]

of biopsy and biochemical assay, to non-invasive imaging. The work carried out herein focusses exclusively on Quantitative Susceptibility Mapping, and it underpins all of the hypotheses presented that QSM can offer unique compositional and functional information that could aid in the diagnosis and monitoring of liver diseases. As such, let us begin our discussion with an examination of the structure and function of a healthy liver (Figure 1.1).

Under normal circumstances, the human liver can weigh up to 1.5 kg. Despite its size however, the structure of the liver is relatively simple when compared to other major organs. On a macroscopic level, the liver is divided into 4 main lobes - the right, left, caudate and quadrate, but there is little in structure and function to differentiate the lobes from one another. This lack of regional specificity within the liver imbues the organ with a number of advantages. In the first instance, it allows the liver to assume roles in systems as diverse as the digestive, endocrine, immune and circulatory. Secondly, it means that small, regional insults can be absorbed with little impact on the functionality of the entire organ, allowing it to efficiently metabolise and expel toxins. Thirdly, the uniform functionality of the tissue allows significant surgical resection in the case of chronic liver diseases.

The homogeneous structure of the liver also allows for another of its peculiar facets – its remarkable ability to regenerate. Unlike bone and skin which rely on stem cells, the regeneration of the liver tissue is due to the proliferation of existing mature cell types in the

intact portion of the organ ^[10]. A complete restoration of the liver after partial hepatectomy can take as little as 3 – 6 months ^[11], so is often a useful intervention in cases of Hepatocellular Carcinoma or Colorectal Liver Metastases. It is known however that certain disease states (e.g. cirrhosis) can undermine or inhibit the liver’s restorative properties ^[12], thus precluding certain patients from this form of treatment. As such, an accurate assessment of the liver and its function will play a major role in determining the subsequent treatment pathway.

Another attribute unique to the liver is its dual blood supply (Figure 1.2). The Hepatic Portal Vein delivers nutrient rich, partially deoxygenated blood that has passed through the gut and mesentery. It supplies roughly 75% of the total liver blood volume, but only 50% of the required oxygen. The

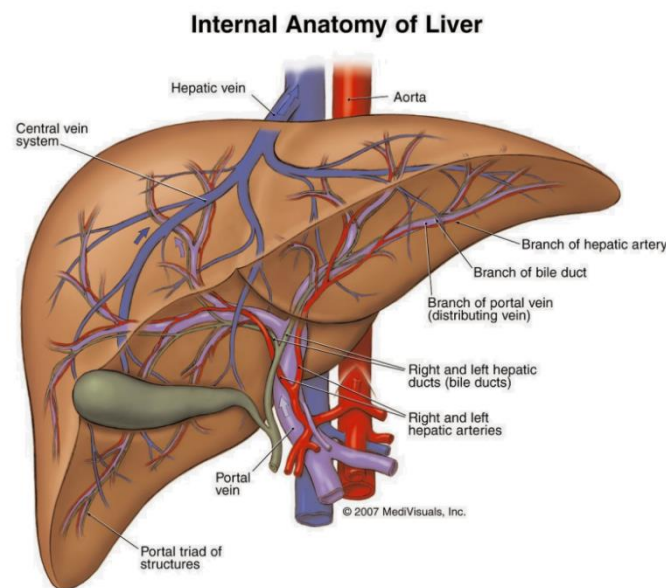


Fig 1.2: Internal anatomy of the liver depicting the blood supply [9]

The shortfall is made up by the Hepatic Artery, which delivers richly oxygenated blood from the descending aorta. Both vessels enter the liver through the porta hepatis on the inferior surface of the liver before branching into the various lobes. The blood they carry then passes through the liver tissue before draining to the hepatic veins, and finally into the inferior vena cava (IVC).

The liver cells are known as hepatocytes (Figure 1.3). These form hepatic plates – thin layers of cells roughly 1 – 2 cells thick, separated by extremely permeable capillary spaces called sinusoids. The hepatic plates are arranged into functional units called liver lobules, which consist of a large number of hepatic plates nucleated around a central vein. At the periphery of each lobule are portal triads – branches of the hepatic portal vein and hepatic artery, as well as bile canaliculi – a thin conduit through which bile is channelled from the hepatocytes. Blood enters the lobule through the portal triad and mixes in the sinusoids where

the structure of the hepatic plates maximises contact with the hepatocytes. Finally, the blood drains through the central vein, branches of which converge to form the hepatic veins.

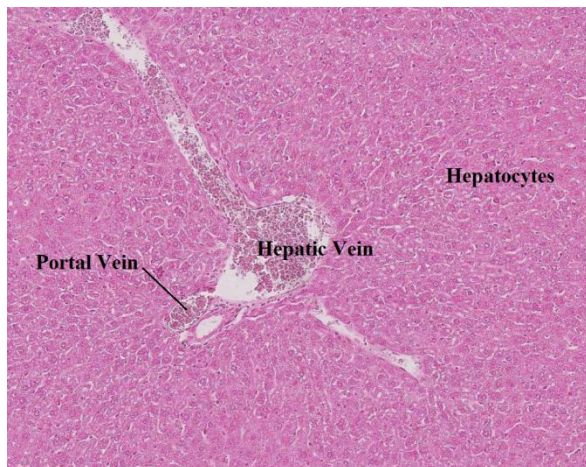
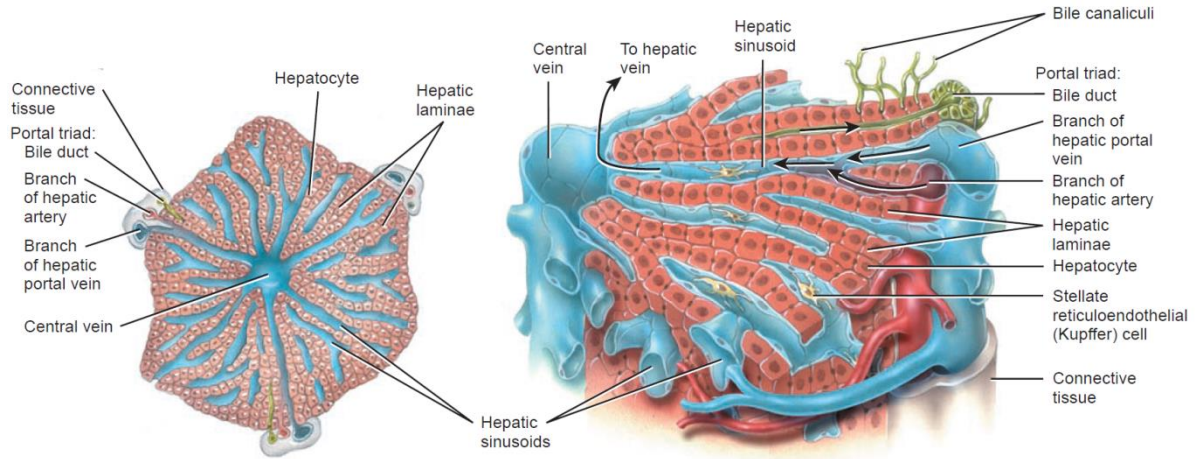


Fig 1.3a & b: Histological Anatomy of the liver^[8]

While an exhaustive list of vital functions in which the liver plays a role would be difficult to compile, some estimates put the number at several hundred ^[13]. As such, any damage or condition that impedes the normal functioning of the liver can have an extremely serious effect on the patient in whom they manifest. Liver diseases are often asymptomatic until they reach an advanced stage, and even when patients seek medical help symptoms can

be ambiguous. This difficulty is compounded by the fact that liver lesions and tumours can often be mistaken as benign (or vice versa) on standard MRI and CT images ^[14]. This may go some way to explain why liver disease is the only major cause of death still increasing year on year ^[15]. Existing non-invasive imaging techniques provide limited information beyond morphology ^[16], and so there is a strong clinical need for improvements to be made in this area. Quantitative Susceptibility Mapping may go some way to filling that void.

1.2 LIVER IMAGING

As mentioned, there are a number of modalities available when performing liver imaging. Computed tomography (CT) and ultrasound may be used to identify morphological abnormalities such as liver lesions that are the hallmarks of cirrhosis. Images acquired with a CT scanner are usually high resolution, which is important for detecting smaller lesions, but acquiring the image requires a high dose of ionising radiation to be administered to the patient. This is particularly true in the abdomen, where the effective dose of radiation is increased due to the air/tissue boundary at the lungs. This is not an issue in ultrasound imaging, but the images are extremely low resolution by comparison, and interpretation is heavily dependent on the operator.

Biopsies and serum assays give compositional and functional information respectively, but are limited by the fact that they are invasive, and are also open to sampling error. Functional information can also be derived from positron emission tomography (PET) but this too necessitates irradiation. Magnetic Resonance Imaging offers non-invasive, high resolution images, without the need for ionising radiation. As such, it is becoming the principal diagnostic modality for hepatic ailments, particularly for staging and re-staging oncological patients ^[17].

The assessment and monitoring of liver disease has benefitted greatly from the advent of MRI imaging. MRI has been used to measure liver fat fraction ^[18], gauge liver perfusion ^[19], or to measure elasticity of the liver tissue (to diagnose fibrosis) ^[20]. Relaxometry can be further enhanced in some cases by the incorporation of exogenous contrast agents such as gadolinium (Gd) ^[20] or super paramagnetic iron oxide particles (SPIOs) ^[21]. Diffusion weighted imaging (DWI) has been used to identify hepatic lesions ^[22]. Susceptibility Weighted Imaging (SWI) has been used to identify haemorrhages ^[23], and to improve the identification of liver nodules that are believed to be a precursor for hepatocellular carcinoma (HCC) ^[24]. Furthermore, there is a large body of work dedicated to the identification and

quantification of iron within the liver (see table 1 for an extensive but not exhaustive list of literature regarding the quantification of liver iron with MRI).

It is expected that the advantages offered by QSM will be extremely beneficial to the techniques currently used to image the liver. For instance, the measurements made on QSM images are independent of imaging parameters like field strength and relaxation times, allowing more robust comparisons between studies performed across different centres. Secondly, magnetic susceptibility is an intrinsic property of the tissue under examination, and it has been shown that the correlation between tissue iron content and susceptibility is stronger and more significant than with R_2^* [25]. Susceptibility mapping is sensitive to changes in the deoxyhaemoglobin content of blood [26], but unlike SWI, QSM can offer *quantitative* measurements that can be used to calculate venous oxygen saturation [6, 7, 27]. Furthermore, the contrast in QSM images is more localised than that in SWI images, giving rise to a more accurate depiction of blood vessels [25]. This may be particularly relevant for liver imaging due to the peculiar fashion in which the liver derives its blood supply, as it is well known that a number of pathologies can affect hepatic haemodynamics [16]. Additionally, it is well known that both liver regeneration and the presence of cancer can both result in an increased demand for oxygen [28, 29].

The experimental work detailed in the upcoming chapters has examined the changes in hepatic magnetic susceptibility brought about by the administration of a hyperoxic gas challenge to a healthy cohort, and has sought to apply QSM to pre-clinical models of both colorectal liver metastases (CRLM) and liver cirrhosis. The chapters that immediately follow however are a detailed discussion of the QSM background theory, and an examination of how implementation of QSM was optimised for application to the liver.

Year	Author	Title	Journal
1995	Turlin, B., et al.	<i>Increased liver iron stores in patients with hepatocellular carcinoma developed on a noncirrhotic liver</i>	Hepatology
1995	Turlin, B., et al.	<i>Increased liver iron stores in patients with hepatocellular carcinoma developed on a noncirrhotic liver</i>	Hepatology
1997	Angelucci, E.G., A.	<i>Limitations of Magnetic Resonance Imaging in Measurment of Hepatic Iron.</i>	Blood
2000	Clark, P.R. and T.G. St Pierre	<i>Quantitative mapping of transverse relaxivity (1/T(2)) in hepatic iron overload: a single spin-echo imaging methodology.</i>	Magn Reson Imaging
2000	Clark, P.R. and T.G. St Pierre	<i>Quantitative mapping of transverse relaxivity (1/T(2)) in hepatic iron overload: a single spin-echo imaging methodology.</i>	Magn Reson Imaging
2001	Fenzi, A., et al.	<i>In vivo investigation of hepatic iron overload in rats using T2 maps: quantification at high intensity field (4.7-T).</i>	J Magn Reson Imaging
2001	Fenzi, A., et al.	<i>In vivo investigation of hepatic iron overload in rats using T2 maps: quantification at high intensity field (4.7-T).</i>	J Magn Reson Imaging
2002	Carneiro, A.A., et al.	<i>Theoretical evaluation of the susceptometric measurement of iron in human liver by four different susceptometers</i>	Physiol Meas
2002	Carneiro, A.A., et al.	<i>Theoretical evaluation of the susceptometric measurement of iron in human liver by four different susceptometers</i>	Physiol Meas
2003	Brittenham, G.M., et al.	<i>Noninvasive measurement of iron: report of an NIDDK workshop</i>	Blood
2003	Clark, P.R., W. Chua-anusorn, and T.G.S. Pierre	<i>Bi-exponential proton transverse relaxation rate (R2) image analysis using RF field intensity-weighted spin density projection: potential for R2 measurement of iron-loaded liver.</i>	Magnetic Resonance Imaging
2003	Sheth, S.	<i>SQUID biosusceptometry in the measurement of hepatic iron</i>	Pediatr Radiol
2003	Clark, P.R., W. Chua-Anusorn, and T.G. St Pierre	<i>Proton transverse relaxation rate (R2) images of liver tissue; mapping local tissue iron concentrations with MRI</i>	Magn Reson Med
2004	Gandon, Y., et al.	<i>Non-invasive assessment of hepatic iron stores by MRI.</i>	The Lancet
2004	Li, T.Q., A.M. Aisen, and T. Hindmarsh	<i>Assessment of Hepatic Iron Content Using Magnetic Resonance Imaging.</i>	Acta Radiologica
2005	Wood, J.C., et al	<i>MRI R2 and R2* mapping accurately estimates hepatic iron concentration in transfusion-dependent thalassemia and sickle cell disease patients</i>	Blood
2005	Carneiro, A.A., et al.	<i>Liver iron concentration evaluated by two magnetic methods: magnetic resonance imaging and magnetic susceptometry</i>	Carneiro, A.A., et al.
2005	St Pierre, T.G., P.R. Clark, and W. Chua-Anusorn	<i>Measurement and mapping of liver iron concentrations using magnetic resonance imaging</i>	Ann N Y Acad Sci

2005	St Pierre, T.G., et al.	<i>Noninvasive measurement and imaging of liver iron concentrations using proton magnetic resonance.</i>	Blood
2006	Merkle, E.M. and R.C. Nelson	<i>Dual Gradient-Echo i-o phase hepatic MR imaging: A useful tool for evaluating more than fatty infiltration.</i>	Radiographics
2007	Storey, P., et al.	<i>R2* imaging of transfusional iron burden at 3T and comparison with 1.5T</i>	J Magn Reson Imaging
2007	Pakbaz, Z., et al.	<i>Liver Iron Measurement by SQUID Biosusceptometry Compared to Liver Biopsy: A More Accurate Definition of Optimal Iron Range.</i>	Blood
2008	Deugnier, Y., P. Brissot, and O. Loreal	<i>Iron and the liver: update 2008</i>	J Hepatol,
2008	Dereure, O., et al.	<i>Measurement of liver iron content by magnetic resonance imaging in 20 patients with overt porphyria cutanea tarda before phlebotomy therapy: a prospective study.</i>	Acta Derm Venereol
2008	Dujardin, M., et al.	<i>Indications for body MRI Part I. Upper abdomen and renal imaging</i>	Eur J Radiol
2008	Virtanen, J.M., M.E. Komu, and R.K. Parkkola	<i>Quantitative liver iron measurement by magnetic resonance imaging: in vitro and in vivo assessment of the liver to muscle signal intensity and the R2* methods</i>	Magn Reson Imaging
2009	Taouli, B., R.L. Ehman, and S.B. Reeder	<i>Advanced MRI methods for assessment of chronic liver disease.</i>	AJR Am J Roentgenol
2009	Chandarana, H., et al.	<i>Hepatic iron deposition in patients with liver disease: preliminary experience with breath-hold multiecho T2*-weighted sequence.</i>	AJR Am J Roentgenol
2009	Olthof, A.W., et al.	<i>Non-invasive liver iron concentration measurement by MRI: comparison of two validated protocols.</i>	Eur J Radiol
2009	Vag, T., et al	<i>MR imaging findings of iron overload</i>	Radiographics
2009	Fischer, R. and P.R. Harmatz	<i>Non-invasive assessment of tissue iron overload.</i>	ASH Education Program Book
2010	Lim, R.P., et al.,	<i>Quantification of hepatic iron deposition in patients with liver disease: comparison of chemical shift imaging with single-echo T2*-weighted imaging.</i>	AJR Am J Roentgenol
2011	Deugnier, Y. and B. Turlin	<i>Pathology of hepatic iron overload</i>	Semin Liver Dis
2011	Meloni, A., et al.	<i>Feasibility, Reproducibility and Reliability for the T2* Iron Evaluation At 3T in Comparison with 1.5T.</i>	Blood
2011	Meloni, A., et al.	<i>Feasibility, Reproducibility and Reliability for the T2* Iron Evaluation At 3T in Comparison with 1.5T.</i>	Blood
2012	Lv, W., et al.	<i>Value of abdominal susceptibility-weighted magnetic resonance imaging for quantitative assessment of hepatic iron deposition in patients with chronic hepatitis B: comparison with serum iron markers.</i>	J Int Med Res

2012	Hou, P., et al.	<i>A practical approach for a wide range of liver iron quantitation using a magnetic resonance imaging technique.</i>	Radiol Res Pract
2012	Virtanen, J.M., et al.	<i>Iron overload: accuracy of in-phase and out-of-phase MRI as a quick method to evaluate liver iron load in haematological malignancies and chronic liver disease.</i>	Br J Radiol
2013	Tirnitz-Parker, J.E.E., et al.	<i>Iron and Hepatic Carcinogenesis</i>	Critical Reviews in Oncogenesis
2013	Trottier, B.J., et al.	<i>Association of iron overload with allogeneic hematopoietic cell transplantation outcomes: a prospective cohort study using R2-MRI-measured liver iron content.</i>	Blood
2014	Hernando, D., et al.	<i>Quantification of liver iron with MRI: state of the art and remaining challenges</i>	J Magn Reson Imaging

Table 1.1: List of literature regarding the quantification of liver iron with MRI

References

1. Acosta-Cabronero, J., et al., *In vivo quantitative susceptibility mapping (QSM) in Alzheimer's disease*. PLoS One, 2013. **8**(11): p. e81093.
2. Lotfipour, A.K., et al., *High resolution magnetic susceptibility mapping of the substantia nigra in Parkinson's disease*. J Magn Reson Imaging, 2012. **35**(1): p. 48-55.
3. van Bergen, J.M.G., et al., *Quantitative Susceptibility Mapping Suggests Altered Brain Iron in Premanifest Huntington Disease*. American Journal of Neuroradiology, 2016. **37**(5): p. 789-796.
4. Xu, B., et al., *Quantification of cerebral perfusion using dynamic quantitative susceptibility mapping*. Magn Reson Med, 2015. **73**(4): p. 1540-8.
5. Hsieh, M.C., et al., *Quantitative Susceptibility Mapping-Based Microscopy of Magnetic Resonance Venography (QSM-mMRV) for In Vivo Morphologically and Functionally Assessing Cerebromicrovasculature in Rat Stroke Model*. PLoS One, 2016. **11**(3): p. e0149602.
6. Ozbay, P.S., et al., *Effect of respiratory hyperoxic challenge on magnetic susceptibility in human brain assessed by quantitative susceptibility mapping (QSM)*. NMR Biomed, 2015. **28**(12): p. 1688-96.
7. Fan, A.P., et al., *Regional quantification of cerebral venous oxygenation from MRI susceptibility during hypercapnia*. Neuroimage, 2015. **104**: p. 146-55.
8. Tortora G. J and D.H. J, *Principles of Anatomy and Physiology*. 14th ed. 2014, New York, NY: HarperCollins College.
9. India, L.T. 2017 [cited 2017; Available from: <http://www.livertransplantsindia.com/liver-liver-diseases.php>.
10. Michalopoulos, G.K., *Liver Regeneration*. Science, 1997. **276**(5309): p. 60-66.
11. Nagasue, N., et al., *Human Liver Regeneration after Major Hepatic Resection*. Hum Liv Regen, 1986. **206**(1): p. 30 - 39.
12. Horiguchi, N., E.J.N. Ishac, and b. gAO, *Liver regeneration is suppressed in alcoholic cirrhosis: correlation with decreased STAT3 activation*. Alcohol, 2007. **41**(4): p. 271 - 280.
13. Fan, Z., et al., *Blood Oxygen Level-Dependent Magnetic Resonance Imaging of the Human Liver: Preliminary Results*. Journal of Computer Assisted Tomography, 2010. **34**(4): p. 523-531.
14. Vilgrain, V., M. Lagadec, and M. Ronot, *Pitfalls in Liver Imaging*. Radiology, 2016. **278**(1): p. 34 - 51.
15. *Facts About Liver Disease - British Liver Trust*. 2017; Available from: <https://www.britishlivertrust.org.uk/about-us/media-centre/facts-about-liver-disease/>.
16. Barash, H., et al., *Functional magnetic resonance imaging monitoring of pathological changes in rodent livers during hyperoxia and hypercapnia*. Hepatology, 2008. **48**(4): p. 1232-41.
17. Maniam, S. and J. Szklaruk, *Magnetic resonance imaging: Review of imaging techniques and overview of liver imaging*. World J Radiol, 2010. **2**(8): p. 309-22.
18. Sharma, P., et al., *Measurement of liver fat fraction and iron with MRI and MR spectroscopy techniques*. Diagn Interv Radiol, 2014. **20**(1): p. 17-26.
19. Kashitani, N., et al., *Portal blood flow in the presence or absence of diffuse liver disease: measurement by phase contrast MR imaging*. Abdom Imaging, 1995. **20**(197 - 200): p. 197.
20. Low, R.N., *Abdominal MRI advances in the detection of liver tumours and characterisation*. The Lancet Oncology, 2007. **8**(6): p. 525-535.

21. Choi, J.S., et al., *Comparison of multi-echo and single-echo gradient-recalled echo sequences for SPIO-enhanced liver MRI at 3 T*. Clin Radiol, 2010. **65**(11): p. 916-23.
22. Kandpal, H., et al., *Respiratory-triggered versus breath-hold diffusion-weighted MRI of liver lesions: comparison of image quality and apparent diffusion coefficient values*. AJR Am J Roentgenol, 2009. **192**(4): p. 915-22.
23. Li, R.K., et al., *Using a 2D multibreath-hold susceptibility-weighted imaging to visualize intratumoral hemorrhage of hepatocellular carcinoma at 3T MRI: correlation with pathology*. J Magn Reson Imaging, 2012. **36**(4): p. 900-6.
24. Dai, Y., et al., *Improving detection of siderotic nodules in cirrhotic liver with a multi-breath-hold susceptibility-weighted imaging technique*. J Magn Reson Imaging, 2011. **34**(2): p. 318-25.
25. Sirlin, C.B. and S.B. Reeder, *Magnetic resonance imaging quantification of liver iron*. Magn Reson Imaging Clin N Am, 2010. **18**(3): p. 359-81, ix.
26. Zhang, J., et al., *Quantitative mapping of cerebral metabolic rate of oxygen (CMRO₂) using quantitative susceptibility mapping (QSM)*. Magn Reson Med, 2015. **74**(4): p. 945-52.
27. Shmueli, K., et al., *Magnetic susceptibility mapping of brain tissue in vivo using MRI phase data*. Magn Reson Med, 2009. **62**(6): p. 1510-22.
28. Shimizu, H., et al., *Changes in hepatic venous oxygen saturation related to the extent of regeneration after partial hepatectomy in rats*. Am J Surg, 1999. **178**(5): p. 428 - 431.
29. Edrei, Y., et al., *Vascular Profile Characterization of Liver Tumors by Magnetic Resonance Imaging Using Hemodynamic Response Imaging in Mice*. Neoplasia, 2011. **13**(3): p. 244-IN5.

Chapter 2

This chapter discusses in detail the background theory of QSM. The relationship between the phase of the T_2^* -weighted signal is established, and is followed by a discussion of the general processing steps required to calculate a susceptibility map from raw phase data. There subsequently follows a detailed description of the various algorithms that have been chosen in this instance to perform the necessary processing steps. Finally, there is a discussion of QSM in general, and an argument for its use in liver imaging.

Background Theory

Magnetic resonance imaging (MRI) uses radio-frequency (RF) magnetic waves to probe the physicochemical environment of hydrogen protons within a subject. RF energy is absorbed and subsequently re-emitted by a subject under examination, and the emitted signals provide physiological information that can be used to form an image. So far, the majority of MRI applications involve monitoring the magnitude of the signal at each point in a region of interest. Differences in the rates of signal relaxation give rise to image contrast, and by careful selection of the acquisition parameters the resulting image can be sensitised to a variety of time constants that impart information on the tissues being examined.

The MRI signal is complex, meaning that in addition to magnitude information, the phase of the signal at each point is also recorded. This information is often discarded in the interests of efficient use of computer memory, but it has been shown recently that the phase of T2*-weighted data - when correctly processed - can yield useful physiological information [2]. MRI phase-based imaging can produce high contrast to noise ratio (CNR) images that are more sensitive to some physiological information than standard magnitude MRI imaging [3].

The phase of the T2*-weighted gradient echo (GRE) MRI signal is sensitive to variations in the magnetic field induced within a subject undergoing an MRI scan [4]. These variations are due to changes in the magnetic susceptibility throughout the biological tissue under examination, as well as shim imperfections and background field effects. Recently it has been shown that the phase distribution can be related to the underlying magnetic susceptibility of the subject through a magnetic dipole kernel [5]. This has led to a new field of research called Quantitative Susceptibility Mapping.

Quantitative Susceptibility Mapping is a processing technique that produces images with exquisite anatomical detail, and, furthermore allows the relative quantification of magnetic susceptibility throughout a volume of interest (VOI) [6]. From this, information about the composition of the tissue can be inferred, providing clinically relevant information based on intrinsic properties of the tissue under interrogation [7, 8].

So far, the majority of the research into susceptibility mapping has focussed on neurological applications [9-12], wherein the technique promises to be extremely useful in the study of a wide range of neurodegenerative disorders such as Parkinson's disease [13], Alzheimer's disease [14], and Multiple Sclerosis [15]. There are, however a large number of

processes and pathologies that can affect physiological magnetic susceptibility, meaning the technique is not confined to the brain. The iron contained in blood for example, or calcifications that may accompany some forms of cancer mean that susceptibility mapping has the potential to find a wide range of non-neurological clinical use. As such, it is the aim of the work undertaken hence to investigate the use of QSM in pre-clinical applications, focussing primarily on the liver.

2.1 PHASE

Phase based MRI techniques provide a means with which to measure variations in the magnetic field induced in a subject undergoing an MRI scan ^[2]. There are a number of magnetically active components present in biological systems. As such, for purposes described here, volumes of interest within the system can be thought of as susceptibility distributions.

When an otherwise homogeneous magnetic field passes through a susceptibility distribution, it gives rise to a characteristic field pattern. The phase of a GRE signal provides the means with which to measure variations within the field, and susceptibility mapping allows quantification of the underlying susceptibility distribution based on the recorded phase. Inferences can then be made regarding the composition of the tissue. As such, let us examine the origin of MRI phase data and its relationship to magnetic susceptibility. It should be noted that the susceptibility effects discussed throughout this body of work pertain specifically to those caused by magnetically active constituents of biological tissue that result in distortions of the B_0 field. These are distinct from susceptibility *artefacts*, which cause distortion of the linear field gradients, resulting image misregistration.

MRI phase imaging is performed using a T2*-weighted gradient-recalled echo acquisition sequence. The T2*-weighted signal contains components from two relaxation mechanisms – pure T2, and T2' ^[16]. Pure T2 decay is caused by dipole-dipole interactions that result in irreversible dephasing of the transverse magnetic signal. T2' decay is a reversible effect caused by physiological magnetic susceptibility variation, as well as main magnetic field inhomogeneity, and chemical shift ^[17]. It is the latter that is of interest when performing phase imaging. Hence a gradient echo sequence is used, as a spin echo will cancel the T2' effects.

MRI signals are commonly detected in quadrature. Quadrature coils consist of 2 concentric RF pick-up coils that are oriented at 90° to each other (fig. 2.1). They detect the signal simultaneously in both the x- and y- directions. Magnitude MRI utilises the modulus of the signal:

$$S_{\text{mod}} = \sqrt{(S_x^2 + S_y^2)} \quad [1]$$

Conversely, phase MRI measures the change in the angle of orientation of the magnetisation vector, and is independent of the magnitude response:

$$\phi = \arctan (S_x / S_y) \quad [2]$$

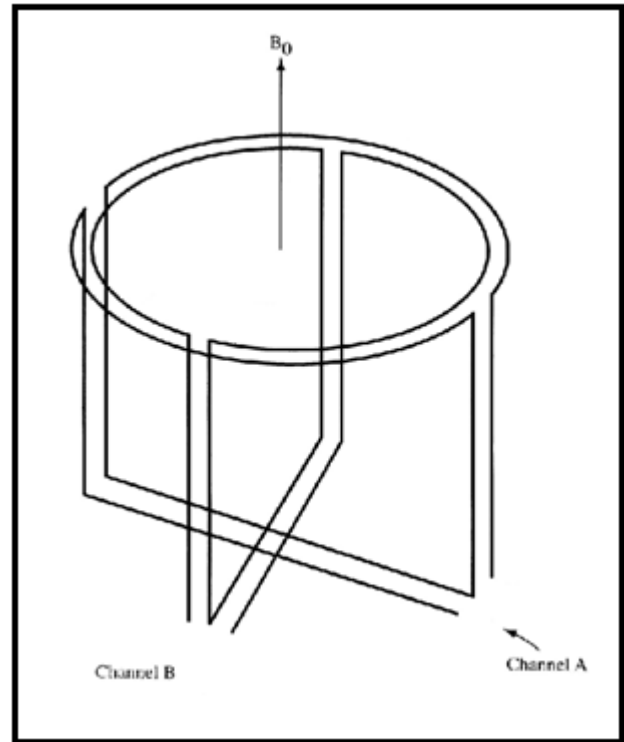


Fig 2.1: Schematic of RF quadrature coil ^[1]

The Larmor frequency (ω) is equal to the product of the gyromagnetic ratio of the protons (hydrogen in this case) and the main magnetic field:

$$\omega = \gamma \cdot B_0 \quad [3]$$

The phase of a T2*-weighted signal can be expressed as the product of the Larmor frequency and time:

$$\phi = \phi_0 + \omega \cdot TE \quad [4]$$

where ϕ_0 is the initial phase offset and TE is the echo time, i.e. the time the signal is measured. The difference in phase between two regions can be expressed as:

$$\Delta\phi = \phi_0 + \Delta\omega \cdot TE \quad [5]$$

$$\Delta\omega = \gamma \cdot \Delta B \quad [6]$$

And, (neglecting chemical shift effects):

$$\Delta B = g \cdot \Delta\chi \cdot B_0 \quad [7]$$

where g accounts for the geometry of the tissue, and χ is the volume magnetic susceptibility. Changes in the magnetic field due to shim imperfections and air-tissue interfaces are neglected as they will be suppressed during post-processing^[18]. As such, variation in the phase of the T2*-weighted signal will reflect distortions of the magnetic field.

Recent theoretical work has shown that the magnetic susceptibility of an irregular object can be calculated from the magnetic field distribution that results as the response of the object to a static magnetic field^[5]. T2*-weighted phase provides a means with which to measure the magnetic field distribution.

2.2 MAGNETIC SUSCEPTIBILITY

Magnetic susceptibility is the degree to which an object becomes magnetised when exposed to a magnetic field^[19]:

$$M = \chi H \equiv \chi (B_0 / \mu_0) \quad [8]$$

Paramagnetic materials – those with a susceptibility greater than one – enhance the strength of a magnetic field that passes through them. Diamagnetic materials, whose susceptibility is less than one have the opposite effect. As such, an object held in a static magnetic field will distort the field according to its susceptibility distribution.

The distorted field can be interpreted as the convolution of the susceptibility distribution with a unit dipole response, and its description gives rise to a complicated function. Convolution theorem allows this to be expressed in the Fourier domain as a simple point-wise multiplication^[20]:

$$\Delta B_z(\mathbf{k}) = B_0 \chi(\mathbf{k}) \left(\frac{1}{3} - \cos^2 \beta \right) \quad [9]$$

where $\Delta B_z(\mathbf{k})$ is the measured field in the z-direction in k-space, and β is the angle between the \mathbf{k} -vector and the static magnetic field such that^[5]:

$$\frac{1}{3} - \cos^2 \beta = \frac{1}{3} - \frac{k_z^2}{K^2} \quad [10]$$

where k_z is the \mathbf{k} -vector in the z-direction, and K is the magnitude of the \mathbf{k} -vector. Re-writing eqn. 9 and solving for χ :

$$\chi(\mathbf{k}) = \frac{\Delta B_z(\mathbf{k})}{B_0} / \left(\frac{1}{3} - \frac{k_z^2}{K^2} \right) \quad [11]$$

This equation allows the calculation of a susceptibility distribution from a measured magnetic field. The simplest solutions take advantage of convolution theorem, allowing the deconvolution of the distribution with the dipole response to be performed as a simple point-wise division in k-space. Taking the inverse Fourier transform of the result gives the susceptibility distribution in real space.

2.3 CALCULATION OF SUSCEPTIBILITY MAP

The input data to the susceptibility calculation is T2*-weighted phase data. This gives a measure of the distortion of the static B_0 field caused by the susceptibility distribution of the sample, known as a field map. As mentioned however, the distortions of the magnetic field are due to contributions from a number of sources ^[4]. The field contributions of interest must be extracted from the raw phase data in order to calculate a useful susceptibility map. The raw data is further confounded by the fact that phase can only be measured between the finite limits of $\pm \pi$. Hence, large changes in susceptibility result in aliasing that must also be removed from the data prior to the susceptibility calculation. As such, there are three main steps involved when calculating a susceptibility map: Phase unwrapping, background field suppression, and finally the susceptibility calculation.

2.3.1 Phase Unwrapping

Phase unwrapping is the name given to the process of removing the aliasing caused by the finite limits of phase. When values of phase exceed the boundaries of $\pm \pi$, they “wrap” back to the origin and pass through their initial value repeatedly over time. In phase images this results in a series of light and dark bands across the image. Phase wrapping is a complication in a number of disciplines and is well known problem. There are numerous freely available algorithms that will perform spatial phase unwrapping ^[21-23]. Multi-echo MRI images can also be unwrapped temporally ^[9, 24].

2.3.2 Background Field Suppression

A large portion of the literature regarding susceptibility mapping has been devoted to separating the extraneous phase contributions from those of interest ^[6, 25-27]. The approaches can roughly be divided into two main groups: Heuristic and physical.

The sub-division of background suppression algorithms is essentially based on assumptions made about the background field. The underlying assumption inherent in the heuristic approaches is that the background field manifests itself as large, spatially slowly varying phase undulations across the image. As such, removal of the low-spatial frequency components from the image will suppress the background field. This leaves in-tact the high spatial frequency components of the signal, which are assumed to be the phase variations caused by the susceptibility distribution throughout the regions of interest ^[4].

Physical methods are more sophisticated, and use complex algorithms to manipulate the mathematical properties of the signal to separate the contributions to the phase data. It has been shown repeatedly that the physical approaches to background field suppression supply data that are superior to those derived by heuristic means ^[6, 20, 25]. Heuristic approaches can only remove the background field if it is spatially slowly varying, which may not be the case ^[19]. Physical solutions remove even high spatial frequency background field components while preserving contrast ^[6, 20]. Hence, as the field of susceptibility mapping progresses, physical approaches are becoming the standard methods of background field suppression ^[8, 14, 28].

The resultant images - known as field maps - depict the field shifts caused by variation in physiological magnetic susceptibility, and provide users with a contrast mechanism that is independent of the magnitude of the signal. The images have a high contrast to noise ratio, and this type of phase imaging is a pre-cursor to SWI and susceptibility mapping ^[2, 29].

The anatomical accuracy of the field maps is undermined by the non-local relationship between phase shifts and susceptibility variations ^[9]. Secondly, the measured phase shifts (and hence contrast) are dependent on the angle of the anatomical feature to the magnetic field ^[20]. As such, there was strong impetus to overcome these difficulties. The solutions were provided by susceptibility mapping.

2.3.3 Susceptibility Calculation

The calculation of magnetic susceptibility from a field map is an ill-posed inverse problem. The reason becomes clear from a closer look at the inversion calculation:

$$\chi(\mathbf{k}) = \frac{\Delta B_z(\mathbf{k})}{B_0} / \left(\frac{1}{3} - \frac{k_z^2}{K^2} \right) \quad [12]$$

As the values on the right hand side of the denominator approach 1/3, the numerator is divided by values that approach zero. As such, the susceptibility values approach infinity, resulting in severe streaking artefacts and noise amplification in the susceptibility map ^[27]. The ambiguous values of the dipole kernel lie at the “magic angle”, a conic surface in k-space that lies at $\sim 54.7^\circ$ to B_0 ^[9]. Circumventing the inverse problem has been the focus of a number of studies, and several solutions have been explored.

The most reliable way of calculating a susceptibility map is to oversample the data by scanning the subject at several angles with respect B_0 ^[11]. The images are then co-registered, and any values that are ambiguous at one orientation are compensated for in the others. While this allows the calculation of an artefact free susceptibility map, re-orienting the subject within the confined space in the bore of the scanner is not always possible, particularly in patients with restricted movement. Furthermore the scan time is increased by the number of acquisitions that are needed, the accuracy of the images is dependent on the registration algorithm, and it is now thought that magnetic susceptibility is anisotropic ^[30]. As such, multi-orientation acquisitions are not practicable solutions to the inverse problem.

Clinical use of susceptibility mapping will most likely depend on those calculated from single orientation (SO) acquisitions. As such, SO solutions to the inverse problem almost always involve supplying *a priori* information to the inversion algorithm to compensate for ambiguity in the inversion kernel. Image space approaches usually involve providing information on organ shape to impose constraints on a minimisation function which is then solved iteratively ^[31-33]. These have been shown to calculate high quality susceptibility maps but can be computationally cumbersome, sometimes taking up to several hours to perform the inversion ^[27].

Alternately, there are a number of k-space based approaches to performing the inversion calculation ^[4, 9, 20]. K-space inversion algorithms take advantage of convolution theorem which allows operations to be performed as simple point-wise multiplication or

division in k-space. These are the simplest approaches to performing the inversion, and differ from real-space algorithms in that instead of supplying spatial information, the *a priori* data attempts to mitigate the problem by correcting, substituting or removing the ill-conditioned regions of the data before transformation back into image space. The resulting susceptibility maps are of lower quality than those calculated in image space ^[27], and there is an inherent trade-off between image quality and fidelity to the measurement (contrast) when deciding the boundaries of the ill-conditioned data. The advantages however lie in the simplicity of the algorithms, and the fact that the time to perform the calculation is of the order of seconds ^[9].

2.3.4 Algorithms

There is a large variety of algorithms available for performing each operation in the QSM processing pipeline. As mentioned previously, each comes with its own advantages and drawbacks, and careful selection of algorithms is necessary for each undertaking. For example, it has been shown that heuristic methods of background field suppression deal poorly with unwanted high spatial frequency contributions, and the time taken to perform some inversion operations may not be suitable when dealing with very large data sets. Conversely, heuristic background field suppression can be useful if the experiment aims to examine small structures, and if an extremely high quality susceptibility map is required then a more cumbersome inversion may be necessary.

The algorithms employed in the pipeline used for this body of work were a Laplacian based SHARP algorithm, which performs both phase unwrapping and background field suppression in a single step, and a Thresholded K-space Division (TKD) algorithm to perform the inversion calculation. These were chosen as it was found that they provided good quality images while minimising processing time. There follows a discussion of how each performs its respective operation.

2.3.5 SHARP algorithm

The approach to background field suppression used throughout the experimental work presented here is known as the Sophisticated Harmonic Artefact Reduction for Phase images (SHARP), which relies on the properties of a Laplacian operator to remove the unwanted phase contributions within a user defined ROI ^[6].

The measured magnetic field within a region of interest can be thought of as the summation of contributions from external (i.e. unwanted) and internal sources:

$$\mathbf{B}^{\text{tot}} = \mathbf{B}^{\text{ext}} + \mathbf{B}^{\text{int}} \quad [13]$$

The internal contributions are the result of variations in magnetic susceptibility within the ROI. They are orders of magnitude smaller than the external contributions, and so to map the susceptibility within the ROI the two must be separated. SHARP background field suppression techniques are based on the assumption that phase contributions from outside the ROI are harmonic throughout the region, i.e. that they give rise to functions that satisfy that Laplace equation; whereas those generated by sources from within the region of interest are anharmonic ^[34]. As such, the second order derivative of the external contributions (i.e. the background field) within the ROI (as calculated via the Laplace equation) will equal zero:

$$\nabla^2 \mathbf{B}^{\text{ext}} = 0; \quad [14]$$

where ∇^2 is the Laplacian operator. Hence:

$$\nabla^2 \mathbf{B}^{\text{tot}} = \nabla^2 \mathbf{B}^{\text{int}} \quad [15]$$

Solving this equation can be accomplished by taking advantage of the spherical mean value (SMV) theorem which states that a harmonic function is preserved when convolved with any non-negative, radially symmetric, normalised function. This allows separation of the respective field contributions, and hence isolation of the field shifts of interest ^[6]. In practice, this is done in three steps:

- 1: Convolution of the data set with a spherical kernel;
- 2: Masking the results to define the internal and external field contributions;
- 3: Deconvolution with the spherical kernel.

Convolution and deconvolution are performed in Fourier space as simple point-wise multiplication and division respectively.

The edges of the region of interest can prove troublesome however, as during convolution the spherical kernel incorporates values from outside the defined ROI, thus violating the SMV theorem^[34]. This results in false extreme values around the outline of the subject in the processed images, which are unacceptable sources of noise when performing susceptibility mapping. One simple solution to this problem is to erode the binary mask applied in the second step, thus eliminating the problem areas from the processed phase data^[35].

A further confounding factor when performing SHARP based processing is the presence of anharmonic contributions to B^{ext} caused by the initial phase offset at $TE = 0$. Mitigation of this source of noise can be accomplished by relaxing the condition that states that the unwanted contributions to the measured magnetic field are entirely harmonic throughout the ROI. This is done by truncated singular value decomposition (TSVD) of the deconvolution^[6].

In practice, TSVD is carried out by providing *a priori* information to the algorithm. As the values of the spherical kernel approach zero, the values of the inverse kernel used for deconvolution become unacceptably large. TSVD essentially truncates the inverse kernel such that its values are set to zero whenever they fall outside a user defined threshold^[35]. This is explored experimentally in chapter 3 (sec. 3.2.1.1).

2.3.6 Laplacian phase unwrapping

The SHARP algorithm can be modified such that it can be applied directly to wrapped phase data^[35], performing both phase unwrapping and background field suppression in tandem. To do this, the algorithm incorporates a solution offered by Schofield and Zhu^[36] that shows that the unwrapped phase can be derived directly from the wrapped phase by recognising certain trigonometric properties. Hence the unwrapped phase is equal to:

$$\nabla^2 \varphi_{\text{unwr}} = (\cos \varphi_{\text{wr}} \cdot \nabla^2 \sin \varphi_{\text{wr}}) - (\sin \varphi_{\text{wr}} \cdot \nabla^2 \cos \varphi_{\text{wr}}) \quad [16]$$

where φ_{unwr} is the unwrapped phase and φ_{wr} is the wrapped phase^[37]. The result of the calculation is then deconvolved with the Laplacian operator to yield an unwrapped,

background field suppressed phase image. As before, the convolution and deconvolution operations are carried out in k-space.

The combination of SHARP and Laplacian phase unwrapping was carried out in this instance by performing the three steps required by the SHARP algorithm using the following 3D dimensional kernel:

$$\text{First plane } \begin{bmatrix} 0 & 0 & 0 \\ 0 & 1/6 & 0 \\ 0 & 0 & 0 \end{bmatrix} \quad \text{Second plane } \begin{bmatrix} 0 & 1/6 & 0 \\ 1/6 & -1 & 1/6 \\ 0 & 1/6 & 0 \end{bmatrix} \quad \text{Third plane } \begin{bmatrix} 0 & 0 & 0 \\ 0 & 1/6 & 0 \\ 0 & 0 & 0 \end{bmatrix}$$

The construction of this operator is based on the discrete form of the Laplacian equation in three dimensions ^[34], and returns an unwrapped, background field suppressed image.

2.3.7 Thesholded k-space Division

The simplest inversion method is the thresholded k-space division (TKD) algorithm ^[9]. In order to solve the inverse problem the algorithm simply removes ambiguous values from the inversion kernel once a user defined threshold value is reached. The values are then replaced with the threshold value ^[9]. This is the fastest inversion algorithm ^[27] and is easy to implement, however the removal of information compromises the accuracy of the susceptibility values ^[35]. Careful selection of the threshold is extremely important, as removal of too much information compromises the susceptibility values (and hence image contrast), but including too much ambiguity compromises the image quality by increasing the severity of the streaking and noise amplification ^[9, 20, 35] (see chap. 3, sec. 3.2.2.1) The simplicity and speed of the TKD algorithm makes it an attractive solution to the inverse problem, and it has already been used in a number of clinical studies ^[13, 38, 39]. In addition to this, there have been attempts to derive a correction factor for images of the brain at 3T to counteract the systemic underestimation of susceptibility values caused by thresholding ^[35].

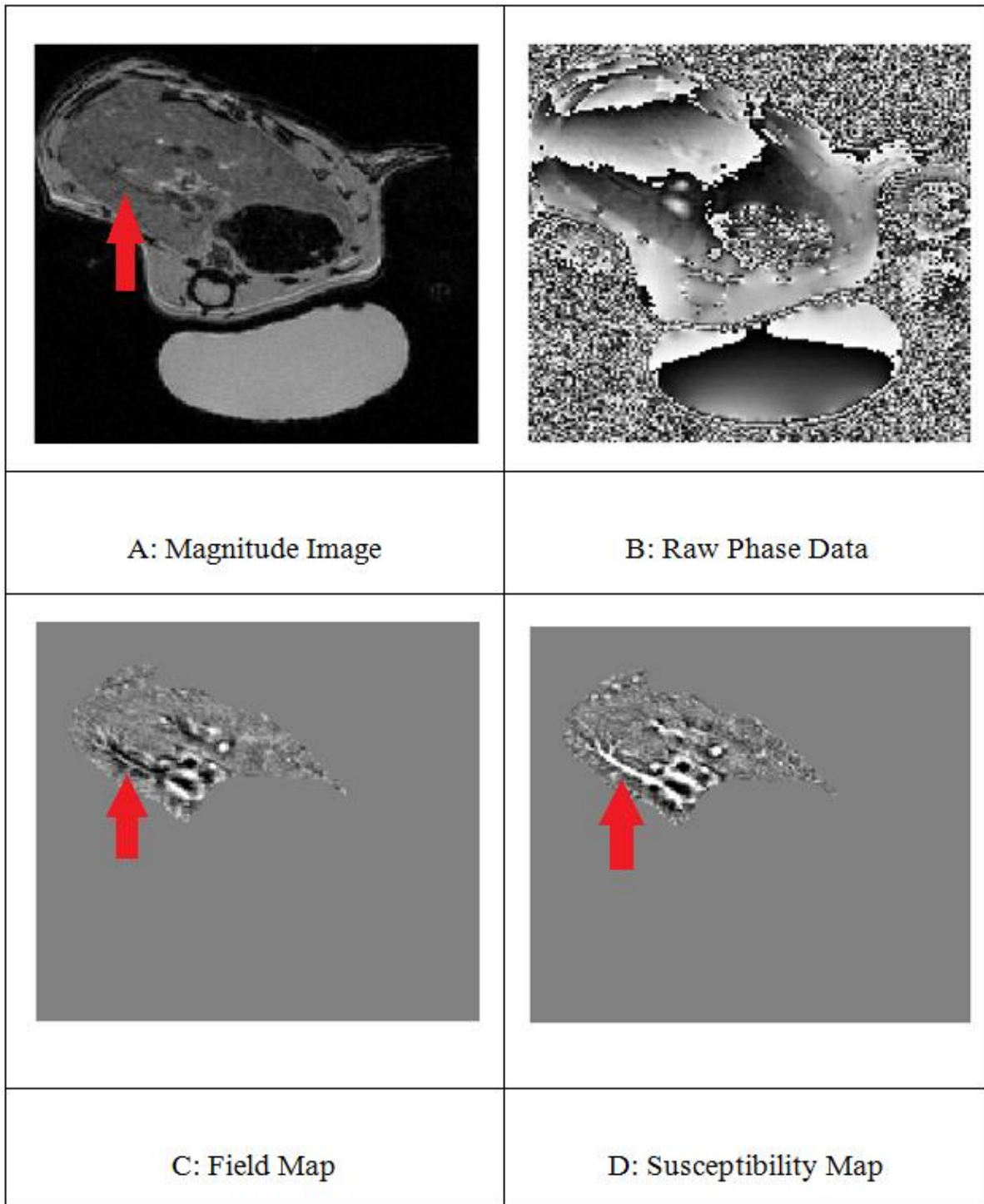


Fig 2.2 A – D: Images depicting each step of the processing pipeline. **A:** Magnitude Image w/ water reference, **B:** Raw Phase data w/ water reference, **C:** Segmented, unwrapped, background corrected field map (SHARP), **D:** Susceptibility Map (TKD inversion). Note the blood vessel (red arrow) in the susceptibility map is more visible than on the field map due to the localised contrast.

2.4 QUANTITATIVE SUSCEPTIBILITY MAPPING

While still in relative infancy, susceptibility mapping promises to be an extremely beneficial addition to the clinical MRI techniques that are currently available. The non-invasive measurement of magnetic susceptibility has been sought across a number of disciplines for a number of reasons. For example: biosusceptometry has been used to investigate liver iron stores ^[40], drug delivery systems ^[41], and in the treatment of liver diseases such as thalassemia ^[42]. As such, the extension of susceptometry to MRI seems a natural progression.

Susceptibility weighted imaging (SWI) is a phase based MRI technique that is seen as the progenitor of QSM. SWI involves the derivation of a positive or negative phase mask which is used to enhance contrast in magnitude images ^[3]. It is reasonably well established as a clinical technique, and has been used in the brain to examine changes in cerebral iron deposition ^[43], to enhance cerebral vascular structures ^[44, 45], and to evaluate brain lesions ^[46]. In addition to this there have been numerous studies that have implemented SWI in abdominal organs ^[47-49]. While SWI is a useful clinical tool, there are a number of inherent drawbacks when compared to QSM.

The phase masks used in SWI are derived from field maps, so the contrast is both non-local and dependent on the orientation of the object to the magnetic field ^[9, 50]. This is overcome by the inversion procedure in QSM, so does not present an issue in susceptibility maps. Secondly, susceptibility weighted images can only show positive *or* negative shifts in susceptibility, whereas susceptibility maps can display both on the same image. This allows differentiation between blood products and calcifications for example ^[8]. Thirdly, susceptibility weighted images are not quantitative, and so while they can highlight differences in deoxyhaemoglobin concentrations in the blood, or iron in the brain, comparison between cohorts is far less precise.

There have been a number of clinical applications explored with QSM. Initial investigations focussed on quantifying the changes in focal iron deposits in the brain associated with a variety of neurodegenerative disorders, including Parkinson's ^[51] and Alzheimer's disease ^[14]. Some of these studies have since progressed to mid-sized (~50 patients) longitudinal clinical trials ^[52, 53].

It has been shown that QSM is sensitive to changes in myelination that are associated with the onset of Multiple Sclerosis (MS), and it has even been suggested that QSM may be more sensitive than R_2^* at the earliest stages of the disease ^[51]. More recently, there has been a degree of interest generated in using QSM to estimate changes in the deoxyhaemoglobin content of blood. It is known that the susceptibility of blood is linearly related to its deoxyhaemoglobin content ^[54], and that changes in deoxyhaemoglobin are directly indicative of changes in blood oxygen saturation.

Deoxyhaemoglobin (dHb) is paramagnetic, however when oxygen binds to haemoglobin it has a profound effect on the magnetic signature of the molecule, turning paramagnetic dHb into diamagnetic oxyhaemoglobin (Hb). QSM has afforded a novel way to exploit this difference, and has given rise to a number of studies attempting to estimate changes blood oxygen saturation (SO_2) from measured differences in susceptibility. For example, it has been shown recently that QSM can differentiate between cerebral venous blood under normoxic and hyperoxic conditions, which could play a role in detecting differences brought about by neurological pathophysiology ^[39, 55]. Other studies have sought to use QSM to quantify the Cerebral Metabolic Rate of Oxygen ($CMRO_2$) on a global and regional basis - an important tool for assessing metabolic changes associated with strokes, tumours, and some neurodegenerative disorders ^[56-58]. It is this area of research that is of particular interest for application to the liver. Table 1 at the end of the chapter contains an extensive but not exhaustive list QSM literature.

2.5 QSM in the liver

The use of phase imaging in the liver is not a new phenomenon. SWI has been the subject of a number of papers that have aimed to examine a diverse range of disease states. For instance, it was found in a feasibility study that decreases in the liver-to-muscle signal intensity ratio as measured on a susceptibility-weighted image correlated strongly with increasing grades of liver fibrosis ^[59]. In another study it was found that SWI was better at identifying certain morphological features that are associated with hepatocellular carcinoma (e.g. pseudo-capsules, haemorrhage) than conventional MR imaging ^[60], and in a study focussing on liver cirrhosis it was found that SWI provided the most sensitive method to detect the siderotic regenerative nodules associated with the disease ^[61].

The aim of the work carried out in this thesis focusses entirely on pre-clinical models. While there have been attempts to implement QSM in the pre-clinical kidney, the work was ex-vivo^[62]. Implementation of QSM in an in-vivo pre-clinical liver has never been performed before, and will offer a number of advantages over clinical imaging. Firstly, pre-clinical imaging can be carried out at high field strengths, allowing high resolution images to be acquired with excellent SNR. All of the experiments conducted presently were performed using a 9.4T MRI scanner. Secondly, models of human diseases can be induced in pre-clinical subjects, allowing a thorough comparison of healthy and disease cohorts. Thirdly the burden of ethics is significantly lower for performing pre-clinical trials, allowing far more experimental procedures to be carried out on the test subjects. The latter is particularly prevalent when attempting to implement and develop the application of novel imaging techniques.

We are particularly interested in the ability of QSM to quantify changes in blood oxygen saturation. As discussed, the liver derives its blood supply in a unique manner, and under normal conditions there is a balance between the blood supplied by the portal vein and hepatic artery. Disruption of this balance is well known to be indicative of a number of disease states^[63, 64], and deterioration of hepatic homeostasis is associated with a high morbidity rate. We believe that this creates an opportunity to study liver pathologies using QSM, as it has been shown that QSM correlates more strongly with iron than comparable techniques such as R_2^* imaging^[9]. Furthermore, the quantitative nature of QSM allows not only the observation of changes in blood oxygen, but also the calculation of changes in the absolute value of SvO_2 that show good agreement with invasively measured values. This has been shown in cerebral blood the literature^[55], and will be shown here in chapter 4 (sec 4.2.4.).

Colorectal liver metastases (CRLM), for example, are secondary cancers that have spread from the colon. The condition is associated with poor prognosis, and there have previously been a number of MRI studies focussed on CRLM. Haemodynamic response imaging (HRI) for example has explored the use of endogenous contrast in the form of BOLD imaging to improve the diagnosis of CRLM^[65], as well as to assess the changes in the vascular profile of tumours^[66]. The advantage offered by QSM in this instance is that susceptibility mapping is independent of imaging parameters such as field strength, and overcomes the directional dependence of R_2^* mapping and SWI. It has been shown that as the tumours grow, they receive blood primarily from the hepatic artery^[63, 67]. It will be

shown that the difference in the deoxyhaemoglobin concentration of blood in the portal vein and hepatic artery means that it is possible to differentiate between tumours and healthy liver tissue, and, furthermore, that it is possible to use QSM in conjunction with a gas challenge to assess the vascularity and oxygenation status of the tumours (chapter 5).

Similarly, liver cirrhosis is caused by a chronic scarring of the liver tissue. This reduces the functionality of the hepatocytes, and causes a deterioration of the elasticity of the tissue. As a result, the blood pressure in the portal vein is rendered insufficient, and the blood cannot enter the hepatic plates. In order to prevent hypoxia, the blood supplied by the arterial source is increased, thus increasing the amount of oxygenated blood supplied to the liver. Furthermore, hepatic siderosis is a known facet of cirrhosis ^[61]. The ability to use QSM to assess the extent of cirrhosis based on changes in liver iron and tissue oxygenation will be investigated in chapter 6.

The sensitivity of phase-based MR imaging techniques to variations in physiological susceptibility means that they are well placed to examine hepatic diseases, and it is thought that QSM can offer a number of further advantages. For example, it has been shown that QSM correlates more strongly with iron stores than R_2^* measurements ^[9], and the localised nature of the contrast means that the images aren't beset by the blooming artefacts known to affect SWI and R_2^* images ^[9]. Furthermore, it has been shown in the literature that the quantitative nature of QSM allows the calculation of venous oxygen susceptibility (SvO_2) ^[55]. While cerebral SvO_2 has been the focus of a number of experiments, it is relatively underused in the liver, even though several studies have shown it to be an eminently useful parameter ^[68-70]. On this basis it is hypothesised that QSM will prove to be an advantageous addition to existing hepatic imaging techniques. The latter half of this thesis contains a number of novel applications of QSM, however the highly experimental nature of the work necessitates extensive optimisation of both data acquisition and QSM image processing. This will be the focus of the upcoming chapter.

Author	Year	Title	Journal
Liu, T.	2010	Unambiguous identification of superparamagnetic iron oxide particles through quantitative susceptibility mapping of the nonlinear response to magnetic fields	Magn Reson Imaging
Li, W.	2011	Quantitative susceptibility mapping of human brain reflects spatial variation in tissue composition	Neuroimage
Klohs, J.	2011	Detection of cerebral microbleeds with quantitative susceptibility mapping in the ArcAbeta mouse model of cerebral amyloidosis	J Cereb Blood Flow Metab
Schweser, F.	2012	Quantitative susceptibility mapping for investigating subtle susceptibility variations in the human brain	Neuroimage
Liu, J.	2012	Morphology enabled dipole inversion for quantitative susceptibility mapping using structural consistency between the magnitude image and the susceptibility map	Neuroimage
Langkammer, C.	2012	Quantitative susceptibility mapping (QSM) as a means to measure brain iron? A post mortem validation study	Neuroimage
Bilgic, B.	2012	MRI estimates of brain iron concentration in normal aging using quantitative susceptibility mapping	Neuroimage
Liu, T.	2012	Accuracy of the morphology enabled dipole inversion (MEDI) algorithm for quantitative susceptibility mapping in MRI	IEEE Trans Med Imaging
Wong, R.	2012	Visualizing and quantifying acute inflammation using ICAM-1 specific nanoparticles and MRI quantitative susceptibility mapping	Ann Biomed Eng
Wang, S. et. al.	2013	Hematoma volume measurement in gradient echo MRI using quantitative susceptibility mapping	Stroke
Deistung, A.	2013	Quantitative susceptibility mapping differentiates between blood depositions and calcifications in patients with glioblastoma	PLoS One
Acosta-Cabronero, J.	2013	In vivo quantitative susceptibility mapping (QSM) in Alzheimer's disease	PLoS One
Xie, L.	2013	Quantitative susceptibility mapping of kidney inflammation and fibrosis in type 1 angiotensin receptor-deficient mice	NMR Biomed
Zheng, W.	2013	Measuring iron in the brain using quantitative susceptibility mapping and X-ray fluorescence imaging	Neuroimage
Lim, I. A.	2013	Human brain atlas for automated region of interest selection in quantitative susceptibility mapping: application to determine iron content in deep gray matter structures	Neuroimage
Deistung, A.	2013	Toward in vivo histology: a comparison of quantitative susceptibility mapping (QSM) with magnitude-, phase-, and R2*-imaging at ultra-high magnetic field strength	Neuroimage
Wang, S.	2013	Noise Effects in Various Quantitative Susceptibility Mapping Methods	IEEE Trans Biomed Eng
Li, W.	2014	Integrated Laplacian-based phase unwrapping and background phase removal for quantitative susceptibility mapping	NMR Biomed
Balla, D. Z.	2014	Functional quantitative susceptibility mapping (fQSM)	Neuroimage
Xu, B.	2014	Flow compensated quantitative susceptibility mapping for venous oxygenation imaging	Magn Reson Med
Liu, C. et. al.	2015	Quantitative Susceptibility Mapping: Contrast Mechanisms and Clinical Applications	Tomography
Ozbay, P. S.	2015	Effect of respiratory hyperoxic challenge on magnetic susceptibility in human brain assessed by quantitative susceptibility mapping (QSM)	NMR Biomed
Sun, H.	2015	Validation of quantitative susceptibility mapping with Perls' iron staining for subcortical gray matter	Neuroimage

Zhang, J.	2015	Quantitative mapping of cerebral metabolic rate of oxygen (CMRO ₂) using quantitative susceptibility mapping (QSM)	Magn Reson Med
Xu, B.	2015	Quantification of cerebral perfusion using dynamic quantitative susceptibility mapping	Magn Reson Med
Wang, Y.	2015	Quantitative susceptibility mapping (QSM): Decoding MRI data for a tissue magnetic biomarker	Magn Reson Med
Sun, H.	2015	Quantitative susceptibility mapping using single-shot echo-planar imaging	Magn Reson Med
Sharma, S. D.	2015	Quantitative susceptibility mapping in the abdomen as an imaging biomarker of hepatic iron overload	Magn Reson Med
Dimov, A. V.	2015	Joint estimation of chemical shift and quantitative susceptibility mapping (chemical QSM)	Magn Reson Med
Deng, W.	2015	Iterative projection onto convex sets for quantitative susceptibility mapping	Magn Reson Med
Haacke, E. M.	2015	Quantitative susceptibility mapping: current status and future directions	Magn Reson Imaging
Barbosa, J. H.	2015	Quantifying brain iron deposition in patients with Parkinson's disease using quantitative susceptibility mapping, R ₂ and R ₂ '	Magn Reson Imaging
Liu, C.	2015	Susceptibility-weighted imaging and quantitative susceptibility mapping in the brain	J Magn Reson Imaging
Dong, J	2015	Simultaneous phase unwrapping and removal of chemical shift (SPURS) using graph cuts: application in quantitative susceptibility mapping	IEEE Trans Med Imaging
Reichenbach, J. R.	2015	Quantitative Susceptibility Mapping: Concepts and Applications	Clin Neuroradiol
Schweitzer, A. D.	2015	Quantitative susceptibility mapping of the motor cortex in amyotrophic lateral sclerosis and primary lateral sclerosis	AJR Am J Roentgenol
Murakami, Y.	2015	Usefulness of quantitative susceptibility mapping for the diagnosis of Parkinson disease	AJNR Am J Neuroradiol
Schweser, F. et. al.	2016	Foundations of MRI phase imaging and processing for Quantitative Susceptibility Mapping (QSM)	Z Med Phys
Hsieh, M. C.	2016	Quantitative Susceptibility Mapping-Based Microscopy of Magnetic Resonance Venography (QSM-mMRV) for In Vivo Morphologically and Functionally Assessing Cerebromicrovasculature in Rat Stroke Model	PLoS One
Du, G.	2016	Quantitative susceptibility mapping of the midbrain in Parkinson's disease	Mov Disord
Zhang, Y.	2016	Longitudinal change in magnetic susceptibility of new enhanced multiple sclerosis (MS) lesions measured on serial quantitative susceptibility mapping (QSM)	J Magn Reson Imaging
Chang, S.	2016	Quantitative Susceptibility Mapping of Intracerebral Hemorrhages at Various Stages	J Magn Reson Imaging
Kudo, K.	2016	Oxygen extraction fraction measurement using quantitative susceptibility mapping: Comparison with positron emission tomography	J Cereb Blood Flow Metab
Moon, Y.	2016	Patterns of Brain Iron Accumulation in Vascular Dementia and Alzheimer's Dementia Using Quantitative Susceptibility Mapping Imaging	J Alzheimers Dis
Stuber, C.	2016	Iron in Multiple Sclerosis and Its Noninvasive Imaging with Quantitative Susceptibility Mapping	Int J Mol Sci
van Bergen, J.M.G.	2016	Quantitative Susceptibility Mapping Suggests Altered Brain Iron in Premanifest Huntington Disease	American Journal of Neuroradiology
Xie, L.	2016	Dynamic contrast-enhanced quantitative susceptibility mapping with ultrashort echo time MRI for evaluating renal function	Am J Physiol Renal Physiol

Zhang, Y.	2016	Quantitative Susceptibility Mapping and R2* Measured Changes during White Matter Lesion Development in Multiple Sclerosis: Myelin Breakdown, Myelin Debris Degradation and Removal, and Iron Accumulation	AJNR Am J Neuroradiol
Tan, H.	2016	Quantitative Susceptibility Mapping in Cerebral Cavernous Malformations: Clinical Correlations	AJNR Am J Neuroradiol
Wei, H.	2017	Joint 2D and 3D phase processing for quantitative susceptibility mapping: application to 2D echo-planar imaging	NMR Biomed
Santin, M. D.	2017	Reproducibility of R2 * and quantitative susceptibility mapping (QSM) reconstruction methods in the basal ganglia of healthy subjects	NMR Biomed
Lauzon, M. L.	2017	Quantitative susceptibility mapping at 3 T: comparison of acquisition methodologies	NMR Biomed
Sharma, Samir D.	2017	MRI-based quantitative susceptibility mapping (QSM) and R2* mapping of liver iron overload: Comparison with SQUID-based biomagnetic liver susceptometry	Magnetic Resonance in Medicine
Straub, S.	2017	Suitable reference tissues for quantitative susceptibility mapping of the brain	Magn Reson Med
Hsieh, M. C.	2017	Investigating hyperoxic effects in the rat brain using quantitative susceptibility mapping based on MRI phase	Magn Reson Med
Straub, Sina	2017	Potential of quantitative susceptibility mapping for detection of prostatic calcifications	Journal of Magnetic Resonance Imaging

Table 2.1: Non-exhaustive list of QSM literature.

References

1. Sunyu, S. and I. Toshiba America Mri, *Quadrature detection coil for interventional MRI*. 2001.
2. Duyn, J., et al., *High field MRI of brain cortical substructure based on signal phase*. PNAS, 2007. **104**(28): p. 11796 - 11801.
3. Haacke, E.M., et al., *Susceptibility weighted imaging (SWI)*. Magn Reson Med, 2004. **52**(3): p. 612-8.
4. Haacke, E.M., et al., *Imaging iron stores in the brain using magnetic resonance imaging*. Magn Reson Imaging, 2005. **23**(1): p. 1-25.
5. Marques, J.P. and R. Bowtell, *Application of a Fourier-based method for rapid calculation of field inhomogeneity due to spatial variation of magnetic susceptibility*. Concepts in Magnetic Resonance Part B: Magnetic Resonance Engineering, 2005. **25B**(1): p. 65-78.
6. Schweser, F., et al., *Quantitative imaging of intrinsic magnetic tissue properties using MRI signal phase: an approach to in vivo brain iron metabolism?* Neuroimage, 2011. **54**(4): p. 2789-807.
7. Tan, H., et al., *Quantitative Susceptibility Mapping in Cerebral Cavernous Malformations: Clinical Correlations*. AJNR Am J Neuroradiol, 2016. **37**(7): p. 1209-15.
8. Deistung, A., et al., *Quantitative susceptibility mapping differentiates between blood depositions and calcifications in patients with glioblastoma*. PLoS One, 2013. **8**(3): p. e57924.
9. Shmueli, K., et al., *Magnetic susceptibility mapping of brain tissue in vivo using MRI phase data*. Magn Reson Med, 2009. **62**(6): p. 1510-22.
10. Schweser, F., et al., *Quantitative susceptibility mapping for investigating subtle susceptibility variations in the human brain*. Neuroimage, 2012. **62**(3): p. 2083-100.
11. Liu, T., et al., *Calculation of susceptibility through multiple orientation sampling (COSMOS): a method for conditioning the inverse problem from measured magnetic field map to susceptibility source image in MRI*. Magn Reson Med, 2009. **61**(1): p. 196-204.
12. Chen, Z., et al., *An optimised framework for reconstructing and processing MR phase images*. Neuroimage, 2010. **49**(2): p. 1289-300.
13. Lotfipour, A.K., et al., *High resolution magnetic susceptibility mapping of the substantia nigra in Parkinson's disease*. J Magn Reson Imaging, 2012. **35**(1): p. 48-55.
14. Acosta-Cabronero, J., et al., *In vivo quantitative susceptibility mapping (QSM) in Alzheimer's disease*. PLoS One, 2013. **8**(11): p. e81093.
15. Liu, C., et al., *High-field (9.4 T) MRI of brain dysmyelination by quantitative mapping of magnetic susceptibility*. Neuroimage, 2011. **56**(3): p. 930-8.
16. Reichenbach, J.R., et al., *Theory and Application of Static Field Inhomogeneity Effects in Gradient Echo Imaging*. Journal of Magnetic Resonance Imaging, 1997. **7**(2): p. 266 - 279.
17. Chavhan, G.B., et al., *Principles, Techniques, and Applications of T2*-based MR Imaging and Its Special Applications*. RadioGraphics, 2009. **29**(5): p. 1433-1449.
18. Haacke, E.M., et al., *Susceptibility-weighted imaging: technical aspects and clinical applications, part I*. AJNR Am J Neuroradiol, 2009. **30**(1): p. 19-30.
19. Schenck, J.F., *Role of Mag Sus in MRI magnetic compatability of 1st and 2nd kind*. Med Phys, 1996. **23**(6): p. 815 - 850.

20. Wharton, S., A. Schafer, and R. Bowtell, *Susceptibility mapping in the human brain using threshold-based k-space division*. Magn Reson Med, 2010. **63**(5): p. 1292-304.
21. Jenkinson, M., *Fast, automated, N-dimensional phase-unwrapping algorithm*. Magnetic Resonance in Medicine, 2003. **49**(1): p. 193-197.
22. Abdul-Rahman, H.S., et al., *Fast and robust three-dimensional best path phase unwrapping algorithm*. Applied Optics, 2007. **46**(26): p. 6623-6635.
23. Witoszynskij, S., et al., *Phase unwrapping of MR images using Phi UN--a fast and robust region growing algorithm*. Med Image Anal, 2009. **13**(2): p. 257-68.
24. Schweser, F., *Phase Processing for QSM*. Proc. from 2nd workshop on MRI phase contrast and QSM, 2013.
25. Liu, T., et al., *A novel background field removal method for MRI using projection onto dipole fields (PDF)*. NMR Biomed, 2011. **24**(9): p. 1129-36.
26. Denk, C. and A. Rauscher, *Susceptibility weighted imaging with multiple echoes*. J Magn Reson Imaging, 2010. **31**(1): p. 185-91.
27. Wharton, S. and R. Bowtell, *Whole-brain susceptibility mapping at high field: a comparison of multiple- and single-orientation methods*. Neuroimage, 2010. **53**(2): p. 515-25.
28. Deng, W., et al., *Iterative projection onto convex sets for quantitative susceptibility mapping*. Magn Reson Med, 2015. **73**(2): p. 697-703.
29. Hammond, K.E., et al., *Development of a robust method for generating 7.0 T multichannel phase images of the brain with application to normal volunteers and patients with neurological diseases*. Neuroimage, 2008. **39**(4): p. 1682-92.
30. Li, W., et al., *Magnetic susceptibility anisotropy of human brain in vivo and its molecular underpinnings*. Neuroimage, 2012. **59**(3): p. 2088-97.
31. de Rochefort, L., et al., *Quantitative MR susceptibility mapping using piece-wise constant regularized inversion of the magnetic field*. Magn Reson Med, 2008. **60**(4): p. 1003-9.
32. de Rochefort, L., et al., *Quantitative susceptibility map reconstruction from MR phase data using bayesian regularization: validation and application to brain imaging*. Magn Reson Med, 2010. **63**(1): p. 194-206.
33. Kressler, B., et al., *Nonlinear regularization for per voxel estimation of magnetic susceptibility distributions from MRI field maps*. IEEE Trans Med Imaging, 2010. **29**(2): p. 273-81.
34. Li, L. and J.S. Leigh, *High-precision mapping of the magnetic field utilizing the harmonic function mean value property*. J Magn Reson, 2001. **148**(2): p. 442-8.
35. Schweser, F., et al., *Toward online reconstruction of quantitative susceptibility maps: superfast dipole inversion*. Magn Reson Med, 2013. **69**(6): p. 1582-94.
36. Schofield, M.A. and Y. Zhu, *Fast phase unwrapping algorithm for interferometric applications*. Optics Letters, 2003. **28**(14): p. 1194-1196.
37. Deistung, A., et al., *Toward in vivo histology: a comparison of quantitative susceptibility mapping (QSM) with magnitude-, phase-, and R2*-imaging at ultra-high magnetic field strength*. Neuroimage, 2013. **65**: p. 299-314.
38. Schafer, A., et al., *Direct visualization of the subthalamic nucleus and its iron distribution using high-resolution susceptibility mapping*. Hum Brain Mapp, 2012. **33**(12): p. 2831-42.
39. Ozbay, P.S., et al., *Effect of respiratory hyperoxic challenge on magnetic susceptibility in human brain assessed by quantitative susceptibility mapping (QSM)*. NMR Biomed, 2015. **28**(12): p. 1688-96.
40. Sheth, S., *SQUID biosusceptometry in the measurement of hepatic iron*. Pediatr Radiol, 2003. **33**(6): p. 373-7.

41. Ferrari, P.C., et al., *A novel automated alternating current biosusceptometry method to characterization of controlled-release magnetic floating tablets of metronidazole*. Drug Dev Ind Pharm, 2014. **40**(8): p. 1123-31.
42. Neilson, P., et al., *Using SQUID biomagnetic liver susceptometry in the treatment of thalassemia and other iron loading diseases*. Transfusion Science, 2000. **23**: p. 527 - 258.
43. Haacke, E.M., et al., *Correlation of putative iron content as represented by changes in R2* and phase with age in deep gray matter of healthy adults*. J Magn Reson Imaging, 2010. **32**(3): p. 561-76.
44. Rauscher, A., et al., *Noninvasive assessment of vascular architecture and function during modulated blood oxygenation using susceptibility weighted magnetic resonance imaging*. Magn Reson Med, 2005. **54**(1): p. 87-95.
45. Ge, Y., et al., *Diminished visibility of cerebral venous vasculature in multiple sclerosis by susceptibility-weighted imaging at 3.0 Tesla*. J Magn Reson Imaging, 2009. **29**(5): p. 1190-4.
46. Radwan, M.M., et al., *Role of magnetic susceptibility weighted imaging in evaluation of brain lesions*. Alexandria Journal of Medicine, 2011. **47**(4): p. 299-308.
47. Mie, M.B., et al., *Susceptibility weighted imaging (SWI) of the kidney at 3T--initial results*. Z Med Phys, 2010. **20**(2): p. 143-50.
48. Lv, W., et al., *Value of abdominal susceptibility-weighted magnetic resonance imaging for quantitative assessment of hepatic iron deposition in patients with chronic hepatitis B: comparison with serum iron markers*. J Int Med Res, 2012. **40**(3): p. 1005-15.
49. Tao, R., et al., *Characterizing hepatocellular carcinoma using multi-breath-hold two-dimensional susceptibility-weighted imaging: comparison to conventional liver MRI*. Clin Radiol, 2012. **67**(12): p. e91-7.
50. O'Gorman, R.L., et al., *Optimal MRI methods for direct stereotactic targeting of the subthalamic nucleus and globus pallidus*. Eur Radiol, 2011. **21**(1): p. 130-6.
51. Langkammer, C., et al., *Quantitative susceptibility mapping (QSM) as a means to measure brain iron? A post mortem validation study*. Neuroimage, 2012. **62**(3): p. 1593-9.
52. *QSM and Regional DCE MRI Permeability Using GOCART Technique - Full Text View - ClinicalTrials.gov*. 2017; Available from: <https://www.clinicaltrials.gov/ct2/show/NCT03091803>.
53. *Longitudinal Quantitative Susceptibility Mapping (QSM) in Alzheimer 's Disease - Full Text View - ClinicalTrials.gov*. 2017; Available from: <https://clinicaltrials.gov/ct2/show/NCT02752750>.
54. Pauling, L. and C.D. Coryell, *The Magnetic Properties and Structure of Hemoglobin, Oxyhemoglobin and Carbonmonoxyhemoglobin*. Proc Natl Acad Sci, 1936. **22**: p. 210 - 216.
55. Hsieh, M.C., et al., *Investigating hyperoxic effects in the rat brain using quantitative susceptibility mapping based on MRI phase*. Magn Reson Med, 2017. **77**(2): p. 592-602.
56. Fan, A.P., et al., *Regional quantification of cerebral venous oxygenation from MRI susceptibility during hypercapnia*. Neuroimage, 2015. **104**: p. 146-55.
57. Zhang, J., et al., *Quantitative mapping of cerebral metabolic rate of oxygen (CMRO2) using quantitative susceptibility mapping (QSM)*. Magn Reson Med, 2015. **74**(4): p. 945-52.
58. Xu, B., et al., *Flow compensated quantitative susceptibility mapping for venous oxygenation imaging*. Magn Reson Med, 2014. **72**(2): p. 438-45.

59. Balassy, C., et al., *Susceptibility-weighted MR imaging in the grading of liver fibrosis- a feasibility study*. Radiology, 2013. **270**(1): p. 149 - 158.
60. Chen, W., et al., *Susceptibility-weighted imaging for the noncontrast evaluation of hepatocellular carcinoma: a prospective study with histopathologic correlation*. PLoS One, 2014. **9**(5): p. e98303.
61. Dai, Y., et al., *Improving detection of siderotic nodules in cirrhotic liver with a multi-breath-hold susceptibility-weighted imaging technique*. J Magn Reson Imaging, 2011. **34**(2): p. 318-25.
62. Xie, L., et al., *Quantitative susceptibility mapping of kidney inflammation and fibrosis in type 1 angiotensin receptor-deficient mice*. NMR Biomed, 2013. **26**(12): p. 1853-63.
63. Breedis, C. and G. Young, *The blood supply of neoplasms in the liver*. Am J Pathol, 1954. **30**(5): p. 969 - 985.
64. Jin, F., et al., *Carbogen Gas-Challenge BOLD MR Imaging in a Rat Model of Diethylnitrosamine-induced Liver Fibrosis*. Radiology, 2010. **254**(1): p. 129 - 137.
65. Edrei, Y., et al., *Quantitative functional MRI biomarkers improved early detection of colorectal liver metastases*. J Magn Reson Imaging, 2014. **39**(5): p. 1246-53.
66. Edrei, Y., et al., *Vascular Profile Characterization of Liver Tumors by Magnetic Resonance Imaging Using Hemodynamic Response Imaging in Mice*. Neoplasia, 2011. **13**(3): p. 244-IN5.
67. Ramasawmy, R., et al., *Separation of arterial and portal blood supply to mouse liver and tumour tissue using pseudo-Continuous Arterial Spin Labelling*. Proc Intl Soc Mag Reson Med, 2015. **23**: p. 0532.
68. Katsuramaki, T., et al., *Monitoring perioperative hepatic venous oxygen saturation ShvO2 in hepatectomy - Changes of ShvO2 in Hemorrhagic Shock*. J Hep Bil Pancr Surg, 1997. **4**: p. 351 - 355.
69. Shimizu, H., et al., *Changes in hepatic venous oxygen saturation related to the extent of regeneration after partial hepatectomy in rats*. Am J Surg, 1999. **178**(5): p. 428 - 431.
70. Yoshioka, S., et al., *Hepatic Venous Hemoglobin Oxygen Saturation Predicts Regenerative Status of Remnant Liver after Partial Hepatectomy in Rats*. Hepatology, 1998. **27**(5): p. 1349 - 1353.

Chapter 3

Chapter 3 outlines the implementation of QSM in the preclinical liver, and is divided into two sections. The first section (3.1) pertains to the acquisition of the data, detailing the various parameters selected for the acquisition sequence, as well as modifications to the sequence such as flow compensation, that were found to be necessary. Chapter 3.1 also contains some preliminary experimental work, including susceptibility maps calculated from data acquired from a pre-clinical liver in-vivo, as well as a justification for acquiring 2D vs 3D data in the experiments exploring novel applications that follow. Finally there is a brief discussion of the influence of liver fat on QSM images in this context.

The second section (3.2) pertains to the processing of the data, and outlines the experimental work undertaken to empirically optimise the series of algorithms required to calculate a susceptibility map from raw T_2^* -weighted phase data, and, furthermore, characterises the impact that the interaction between the algorithms has on the final image. Lastly, a novel method to compensate for the inherent underestimation of susceptibility values calculated using the selected inversion algorithm is presented.

OPTIMISATION

3.1 Acquisition

With the exception of a handful of papers ^[3, 4], research into the use of susceptibility mapping has so far focussed exclusively on the brain, and there are even fewer studies exploring preclinical models ^[5-7]. The novelty of the work undertaken as part of this thesis necessitated a degree of optimisation before QSM could successfully be implemented in a preclinical liver. For example, it was found that the large vessels and high degree of blood flow in the liver required modification of the acquisition sequence to mitigate artefacts. Secondly, while the particular processing pipeline selected for the main experiments that follow has been shown to yield clinically relevant data in the brain ^[8, 9], implementation in a preclinical liver at high field strengths required a degree of calibration of the various algorithms. As such, the following chapter aims to justify the data acquisition procedure and processing pipeline that was be used for the remainder of the experiments detailed in the upcoming chapters.

3.1.1 Acquisition parameters

The fidelity of a susceptibility map to the physiological environment it represents relies on the input of high quality data to the inversion algorithm. This is particularly true when using TKD inversion, as it is prone to noise amplification which can have deleterious effects on the measurements derived from the images. It is, however equally important to minimise the length of time each animal is under anaesthetic. As such, selection of acquisition parameters must strike a careful balance between maximising SNR and minimising acquisition time. Some parameters need to be tailored to individual mice or specific studies, but others can be standardised for all experiments. There follows a brief discussion of the acquisition parameters employed in the experiments that follow.

3.1.1.1 Echo Time

Quantitative Susceptibility Maps are derived from the phase (φ) of GRE data, which is equal to:

$$\varphi = \varphi_0 + \gamma \cdot B \cdot TE \quad [1]$$

where φ_0 is the initial phase offset, γ is the gyromagnetic ratio of the (hydrogen) protons, B is the local magnetic field, and TE is the echo time. Of these, the first two are constants and the second is effectively the measurand, so from a data acquisition standpoint the echo time is the experimentally defined parameter which enables control of the signal.

Optimising the echo time is an important consideration when performing QSM, as contrast in the final image will depend on the extent of the distinction between tissues based on their respective phase. Phase evolves over time, and increasing the time between excitation and acquisition will allow small differences in susceptibility to become apparent. Conversely, for reasons that will be discussed below, it is imperative that the field map has a high signal to noise ratio (SNR). When magnitude SNR is greater than ~ 3 , the noise in a phase image is inversely proportional to the magnitude SNR^[10]. As such, it is also desirable to minimise the echo time in order to boost SNR. There is general agreement in the literature that an echo time equal to the T_2^* value of the tissue offers the optimal compromise^[11]. The T_2^* value of a healthy mouse liver was measured using a multi-GRE technique. Briefly, a multi-echo image of a healthy mouse liver was acquired at 9.4T. A T_2^* map of the liver was calculated by first calculating the logarithm of the exponential T_2^* decay at each point in the image. A linear fit was then performed on a voxel-wise basis, and the slope of the linear fit was taken to be the T_2^* -value at each point. The mean value in a region liver tissue was then taken as the T_2^* value of the tissue, and was found to be ~ 4 ms at 9.4T. This process is depicted in figure 3.1. This is the echo time used for all of the main experiments that follow.

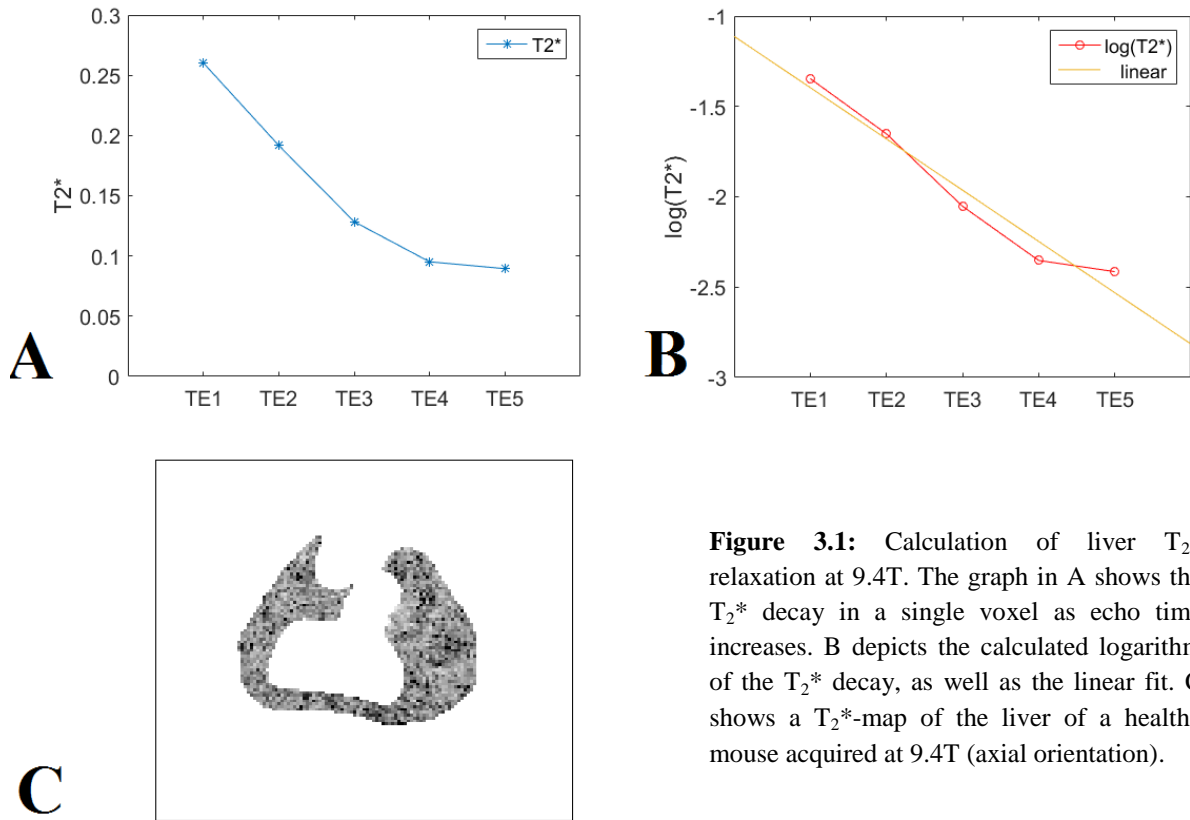


Figure 3.1: Calculation of liver T_2^* relaxation at 9.4T. The graph in A shows the T_2^* decay in a single voxel as echo time increases. B depicts the calculated logarithm of the T_2^* decay, as well as the linear fit. C shows a T_2^* -map of the liver of a healthy mouse acquired at 9.4T (axial orientation).

3.1.1.2 Respiratory gating

All in-vivo acquisitions were respiratory-gated. This was done by monitoring the animals breathing rate with a pressure sensitive respiratory monitor (SA Instruments, Stony Brook, NY, USA) while they were in the scanner. Data were acquired only during a flat region of the respiratory cycle (i.e. between breaths) in order to avoid respiratory related motion artefacts in the image.

3.1.1.3 Repetition Time & Flip Angle

The T1 of the liver at 9.4T is relatively long ($>1s$)^[12] compared to lower field strengths. In order to minimise T1 influence on the acquired images, each was acquired at a repetition time of 1s. In order to maximise magnitude SNR a flip angle of 70° was chosen as it is close to the Ernst angle for the above TR and T1 values.

3.1.1.4 Resolution & Averages

Only the z-component of the magnetic field will differ significantly from zero in response to the susceptibility distribution^[13]. As such, the number of sampling points will be specified by the number of slices in an axial oriented acquisition. These must be sufficiently numerous to give a reasonable facsimile of the distorted field. It was found that 60 – 100 slices of 200 μm thickness (mice), or 300 μm thickness (rats) would cover the entire liver at a sufficient resolution. These slice thicknesses was chosen as they are the upper limit of resolution achievable with this scanner under these circumstances.

It was shown in a phantom experiment detailed in the literature that a voxel aspect to slice thickness ratio above 1:2 resulted in a deviation from the expected susceptibility, which was ascribed to partial volume effects^[14]. As such, the matrix size in the phase and frequency encode directions employed throughout the experimental work were selected such that the voxels were isotropic, and were tailored to the FOV required to ensure each individual animal was entirely contained within the image.

The number of signal averages acquired for the animals in each study was dependent on their tolerance of the anaesthetic. As such, signal averages were limited to 4 for disease cohorts. This was doubled for healthy young animals.

3.1.2 FLOW COMPENSATION

Flow compensation is a well-known modification of MRI acquisition sequences that improves the quality of images when first order laminar flow is present in an area under examination. During a standard acquisition, a signal is excited with a resonant RF pulse. Magnetic gradients are applied for spatial localisation (i.e. phase encoding and read

dephasing), and a “readout” gradient is then applied at a predetermined time such that the isochromats rephase, and the echo is realised. This however is true only in the case of *static* isochromats. Any non-stationary spin packet, e.g. those within the blood vessels, will not rephase upon read-out, resulting in magnitude signal loss.

The effect is equally detrimental to phase images. The phase of the GRE signal is essentially a measure of the extent of the precession of the isochromats at a given (echo) time. Isochromats accumulating extra phase as they move through magnetic gradients will distort local field estimations, leading to erroneous susceptibility measurements. Flow compensation involves modifying the acquisition sequence by adding extra gradients that are designed to ensure all of the isochromats rephase upon readout.

Initial applications of QSM were mostly concerned with assessing changes in the focal centres of iron in the brain, and so were not affected by blood flow. Advances in the field however have given rise to a number of QSM applications for which flow compensation has been crucial. For instance, QSM venography has been applied to a preclinical model of stroke ^[7], which involved the detection of small cerebral blood vessels. The image distortion caused by blood flow would most likely prove detrimental in this scenario. Equally, there have been a number of studies attempting to quantify cerebral venous oxygen saturation (SvO₂) through susceptibility measurements ^[9, 15, 16]. Accurate estimation of SvO₂ depends on the linear relationship of deoxyhaemoglobin content and magnetic susceptibility, and in the presence of uncompensated flow this linearity is severely undermined ^[16].

The blood vessels contained within the liver are extremely abundant and large relative to those in the brain, meaning that there are large volumes of blood entering, leaving and passing through the liver during the acquisition sequence. As such, a series of short experiments were carried out to assess the necessity of flow compensation in the liver. There follows a brief discussion of the implementation of flow compensation in this instance, and an analysis of its effect on the Quantitative Susceptibility Maps derived thereafter.

3.1.2.1 Implementation

The effect a gradient has on the precession of an isochromat during the course of a pulse sequence can be described by its moment. Positive and negative gradients will have opposing effects, and the extent to which they do will depend on their strength and duration.

In order to ensure all spins rephase at the desired echo time, the area under the positive and negative curves described by each gradient waveform must sum to zero. Gradient Moment Nulling (GMN) refers to the technique that ensures that this condition is met.

Gradient moments can be nulled to varying degrees, referred to as orders. Zeroth-order moment nulling ensures that all stationary spins rephase at the desired echo time, and is included in virtually all pulse sequences. The situation becomes more complex when a ROI contains both stationary *and* moving spins, and it is the objective of higher order moment nulling to ensure that the total phase dispersion is zero for *all* spins at the echo time whether they are stationary or not. As such, first-order nulling is pertinent to spins that move through the gradient at a constant velocity, second order nulling refers to spins moving at a constant acceleration, and so on. GMN is performed by including extra lobes on a gradient waveform of sufficient strength, duration and polarity such that all spins up to the desired order will rephase upon read-out.

In the interests of clarity, let us examine a velocity compensated slice select gradient, where lobe 1 is the refocussing gradient, and lobe 2 is the velocity compensating gradient (fig 3.1).

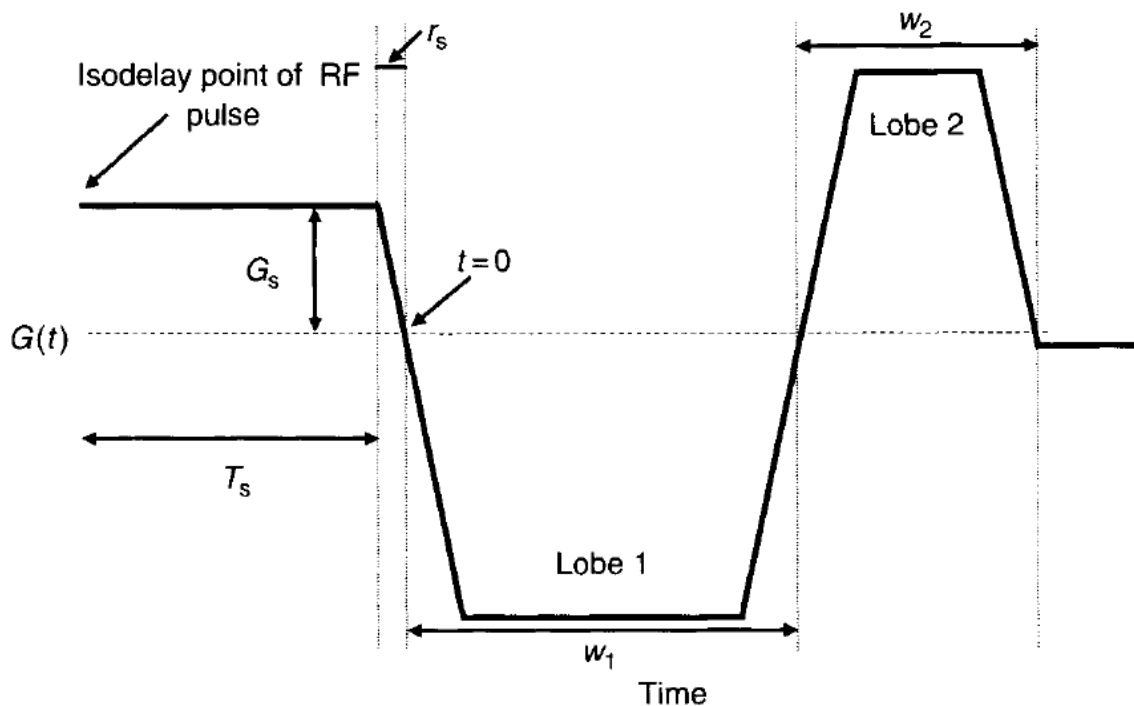


Fig 3.2: A velocity compensated slice select gradient^[1].

The amplitude and duration of the slice select gradient are represented by G_s and T_s respectively, the widths of the lobes are $w_{1,2}$, and r_s is the gradient ramp time. The goal of the exercise is to calculate the widths, amplitudes and shape of the unknown lobes 1 & 2, such that the net area under the waveform is equal to zero, i.e. that:

$$A_1 = A_2 + A_s \quad [2]$$

where A denotes the absolute value of the area under each lobe, and A_s is the area from the RF isodelay point to the end of the slice selection lobe (i.e. $t = 0$).

Manipulation of the gradient waveform requires modification of the programme that dictates the sequence protocol. Each gradient is treated separately, so compensation can be applied to each cardinal direction individually, or any combination thereof. To ensure the extra lobes are of the appropriate size etc., they are described by a series of equations that incorporate information from the sequence protocol, and calculate the required amplitude and duration accordingly. So, for example, A_2 in eqn. 1 can be calculated using the equation (as derived in Bernstein)^[1]:

$$A_2 = \frac{-hr + \sqrt{(hr^2) + 2(hrA_s + A_s^2 + 2hm_s)}}{2} \quad [3]$$

where h is the maximal gradient amplitude, r is the minimal rise time from 0 to h , and m_s is the absolute value of the first moment of the slice select lobe. The variables h , r , are directly calculated during the execution of the sequence, and both m_s and A_s can be calculated from sequence parameters. The variables A_2 and A_s can then be used to calculate A_1 (eqn. 1), and the gradients of lobes 1 & 2 can be calculated such that their net area sums to zero, thus nulling the 1st moment of the sequence. Similar equations allow the calculation of gradients that will null the first moment of the frequency and phase-encode gradients. For the experimental work below, flow compensation was applied in all three directions, so the sequences are said to be fully first-order flow compensated.

The Agilent scanner used for these experiments offers two possible options when implementing GMN. The first is to programme the acquisition such that the individual gradient waveforms run in a sequential fashion. While this is easy to implement from a

programming point of view, the extra lobes come with a time penalty that may increase the echo and repetition times to an unacceptable degree.

The second option is to take advantage of the gradient kernel programming capability built into the Agilent paradigm. Instead of running each gradient sequentially, this removes the blocking constraints imposed on the sequence, and allows individual waveforms to arbitrarily overlap. The individual waveforms are combined into a single compound gradient shape, which has the effect reducing the minimum echo and repetition times. Upon implementation it was found that the required echo time necessitated programming the acquisition sequence in kernel form.

Implementation of flow compensation was done in two stages. The first stage was conducted entirely on a flow phantom, as this allowed on-line sequence development without the use of animals. Once it was established that the sequence could successfully compensate for laminar flow, in-vivo animal data was acquired with and without flow compensation in order to gauge the effect on the subsequent susceptibility maps.

3.1.2.2 Stage I – Flow Phantom

The flow phantom was constructed in-house, and consisted of a 15 ml falcon tube filled with agar (figure 3.3). A hole was cut in the top and bottom of the falcon tube, through which a thin flexible plastic pipe was inserted such that the direction of the pipe was parallel to that of the falcon tube. The pipe was connected at either end to a water bath and pump that were outside the scan room so that when the pump was turned on water flowed at a constant rate in a closed system.

The tube was positioned in the scanner such that the flow was perpendicular to the main magnetic field. The dataset consisted of 3 GRE acquisitions:

Acq 1: No flow, no flow compensation

Acq 2: Flow, no flow compensation

Acq 3: Flow, flow compensated sequence.

The acquisition parameters were as such: $B_0 = 9.4\text{T}$, $TR = 1000\text{ ms}$, $TE = 8.9\text{ ms}$, $FA = 70^\circ$, $FOV = 30 \times 30 \times 23\text{ mm}$, $Matrix = 128 \times 128 \times 50$, $Voxel = 234 \times 234 \times 460\text{ }\mu\text{m}$, $bandwidth = 50\text{ kHz}$, $average = 1$.

Susceptibility maps were calculated from the raw phase data of each acquisition using the SHARP and TKD algorithms discussed in chapter 2. Images were examined by visual inspection, and susceptibility was measured in the agar and in the pipe. The susceptibility shift is quoted in ppb, and is the difference in susceptibility between the two regions. The standard deviation of the susceptibility within the pipe is also compared as a measure of the success of the flow compensation.

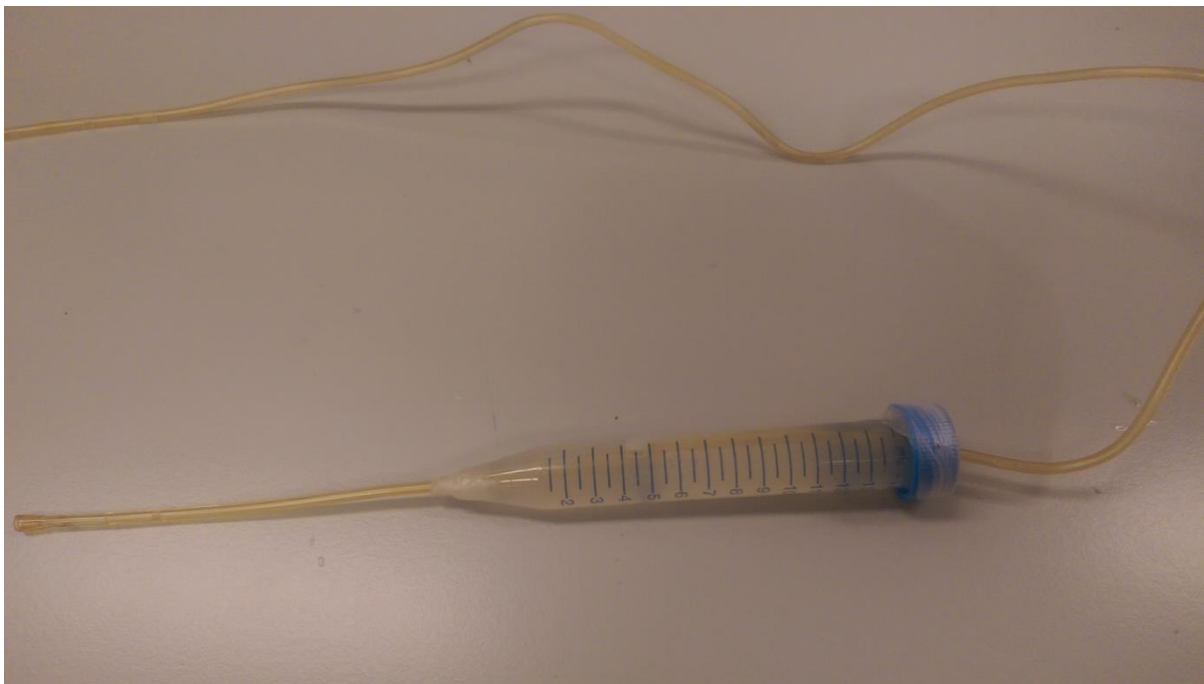


Figure 3.3: Photograph of flow phantom.

3.1.2.2.1 Stage I – Results

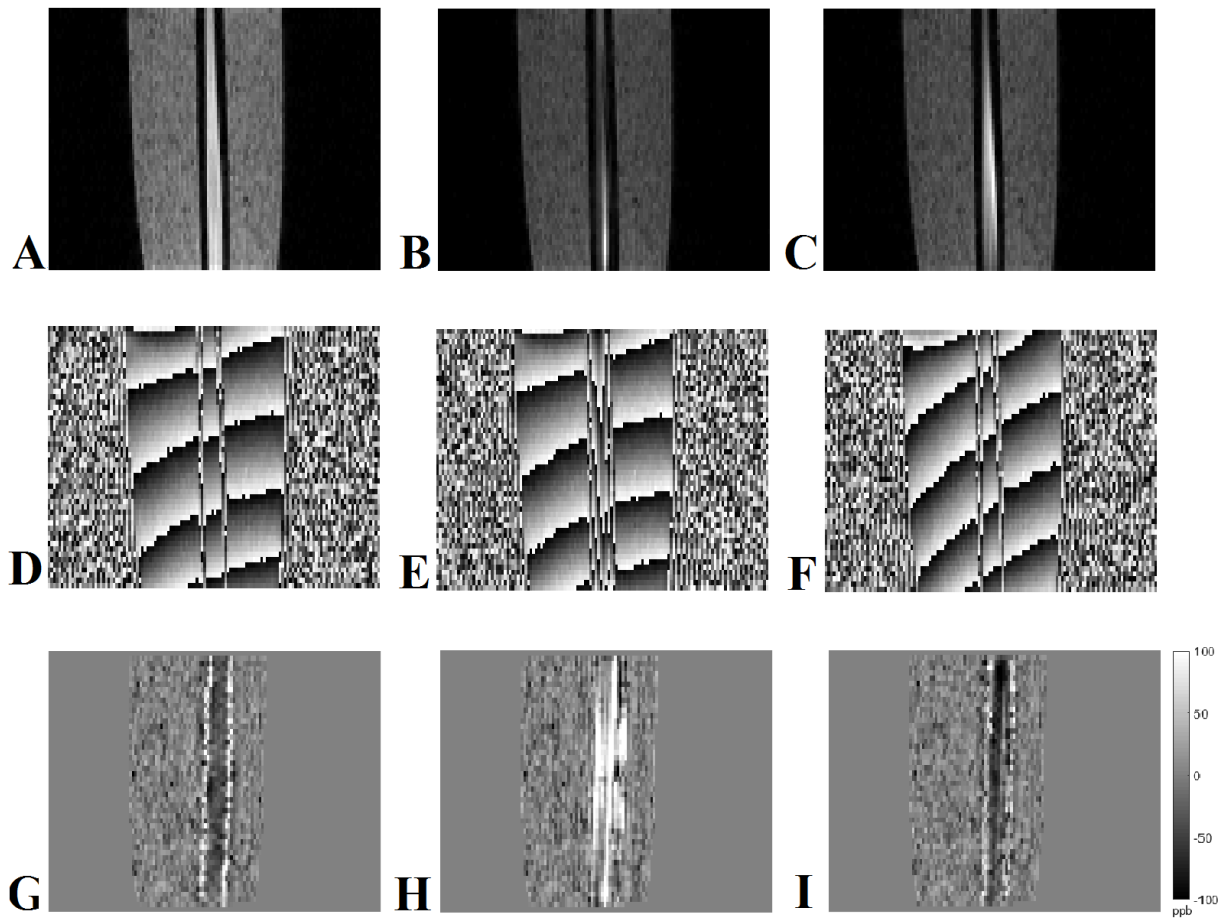


Figure 3.4 A- I: Images from data acquired with no flow (A, D, G), flow but no compensation (B, E, H), and flow with compensation (C, F, I). The top row contains magnitude images from each acquisition, the second row is the raw phase data, and the third row contains the corresponding susceptibility maps.

Figure 3.4 shows a trio of images from each dataset. Columns 1 – 3 are populated by Acq. 1- 3 respectively. The top row contains magnitude images, the second row contains the corresponding phase images, and the bottom row contains the subsequent susceptibility maps. All images are shown in sagittal orientation

In the magnitude image with no flow, the water is hyperintense from the top to the bottom of the image with respect to the agar. In the image with no flow compensation the water and the agar are of almost the same intensity, while in the image with flow compensation the water is also hyperintense, but the contrast seems to drop off slightly at the top and bottom of the image.

The raw phase images are contained in the second row (D - F). As discussed in chapter 2 section 2.3.1 the pixel values in a raw phase image are expressed between the finite limits of $\pm \pi$. As such, when the values of phase exceed this limit, they “wrap” back to the origin, resulting in a series of bright and dark bands throughout the image. The effect is clearly visible in figure 3.4, and a comparison of the phase wraps gives an insight into the effectiveness of the flow compensated sequence. In the first image (D), in which there is no flow, the phase wraps form a continuous band across the entirety of the phantom, as expected. In the second, uncompensated image (E), there is a break in the phase wraps as they pass through the section of the phantom that contained the flowing water. The reason for this is that the isochromats contained in the water pipe did not rephase at the echo time, as they have accumulated extra phase while passing through the various gradients. Conversely, in the compensated phase image (E), the phase wraps manifest as unbroken lines that pass across the entire phantom, as the modification to the sequence has resulted in the correct rephasing of the majority of the isochromats at the correct time.

The resultant susceptibility maps are contained in the third row (G – I). In the no-flow image (G), the susceptibility of the water in the pipe is slightly hypointense with respect to the agar that surrounds it (see figure 3.5). By comparison, the water in the susceptibility map calculated from the uncompensated data is hyperintense. Again this is attributed to the distortion of the phase as the moving isochromats passed through the various imaging gradients. As expected, the water in the compensated image (G) is hypointense, in reflection of the first image. The water in image G however is slightly more hypointense than in the first image. This may be attributed to non-laminar flow at the edges of the pipe that has not been entirely compensated for by the sequence.

The graph in figure 3.5 A shows the shift in measured susceptibility between the water and agar for each acquisition. The susceptibility of the water in the uncompensated image is measured as paramagnetic (i.e. > 0), while in the others it is diamagnetic. The susceptibility of the water in the flow compensated image is slightly more diamagnetic than the water in the no flow image. According to the literature, the magnetic susceptibility of both water and agar is very similar ^[17], so it is unclear why in this instance the water appears to be slightly diamagnetic by comparison. The difference is ~ 30 ppb, and it may be that the water in the phantom contains some impurities (i.e. calcium) which would explain the discrepancy.

The graph in figure 3.5B shows the standard deviation of the susceptibility measured in the water in each data set. As expected, the standard deviation in the uncompensated image is the highest. The SD in the compensated image is slightly higher than that in the image with no flow. The differences between the compensated and no flow images may be due to non-laminar flow that is not compensated for by first order gradient moment nulling.

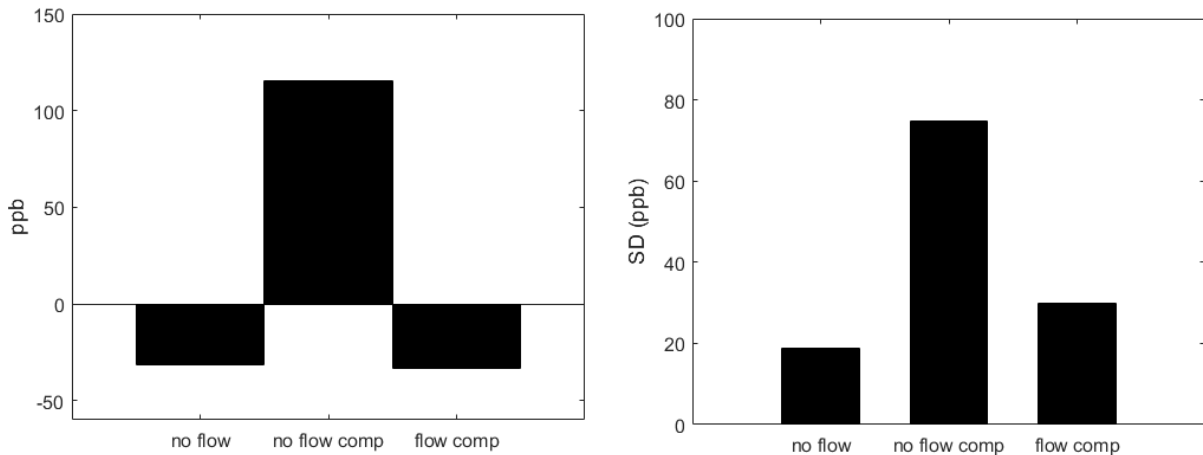


Figure 3.5 A & B: Graphs depicting the contrast measured in each of the susceptibility maps displayed in figure 2 (A) and the standard deviation of the susceptibility measured in the water in the same images (B).

3.1.2.2.2 Stage I – Conclusions

It is clear from the above that the presence of flow during the acquisition will have a noticeable effect on the resultant images, and a detrimental effect on the susceptibility maps and the values measured therein. It is also shown that first-order flow compensation was successfully implemented, and that it goes some way to mitigating the errors introduced by flow. It must be noted however that the compensation is imperfect; some residual flow artefact remains, which may be a systemic source of error throughout the experiments. Inclusion of higher order compensation would however push the echo time to an unacceptable value, so it was decided that first order compensation was the optimal choice.

3.1.2.3 Stage II – In-vivo acquisition

Once the efficacy of the flow-compensated acquisition sequence was established, in-vivo data was acquired to determine the effect of flow compensation on a susceptibility map that was more representative of data that would be acquired during the main experiments in the upcoming chapters.

GRE data was acquired from a healthy CD1 mouse (6 -8 weeks old). The subject was anaesthetised using 4% isoflurane in 100% O₂. During scanning, respiratory rate was monitored and maintained at ~50 - 70 breaths p/m by varying isoflurane concentration between 1.5 and 3%. Data were acquired while the mouse was administered medical air, by means of a respiratory gated sequence on a 9.4T scanner (Agilent Technologies).

The acquisition parameters were as such: **Flow compensated acquisition:** TR = 1000 ms, TE = 4 ms, FA = 70°, FOV = 25.6 x 25.6 x 16 mm, Matrix = 128 x 128 x 80, Voxel = 200 µm isotropic, bandwidth = 50 kHz, average = 4. **Standard acquisition:** TR = 1231 ms, TE = 4.712 ms, FA = 70°, FOV = 25.6 x 25.6 x 16 mm, Matrix = 128 x 128 x 80, Voxel = 200 µm isotropic, bandwidth = 50 kHz, average = 4.

Data was manually segmented using ITK-snap^[18] and susceptibility maps were calculated from raw phase data using the SHARP and TKD algorithms. Images were assessed by visual inspection, and the magnetic susceptibility was measured in a large blood vessel, and in the liver tissue. The difference in susceptibility between each region was taken as a measure of image contrast, and the standard deviation of the measured susceptibility in the blood vessel quoted as a measure of image quality.

3.1.2.3.1 Stage II – Results

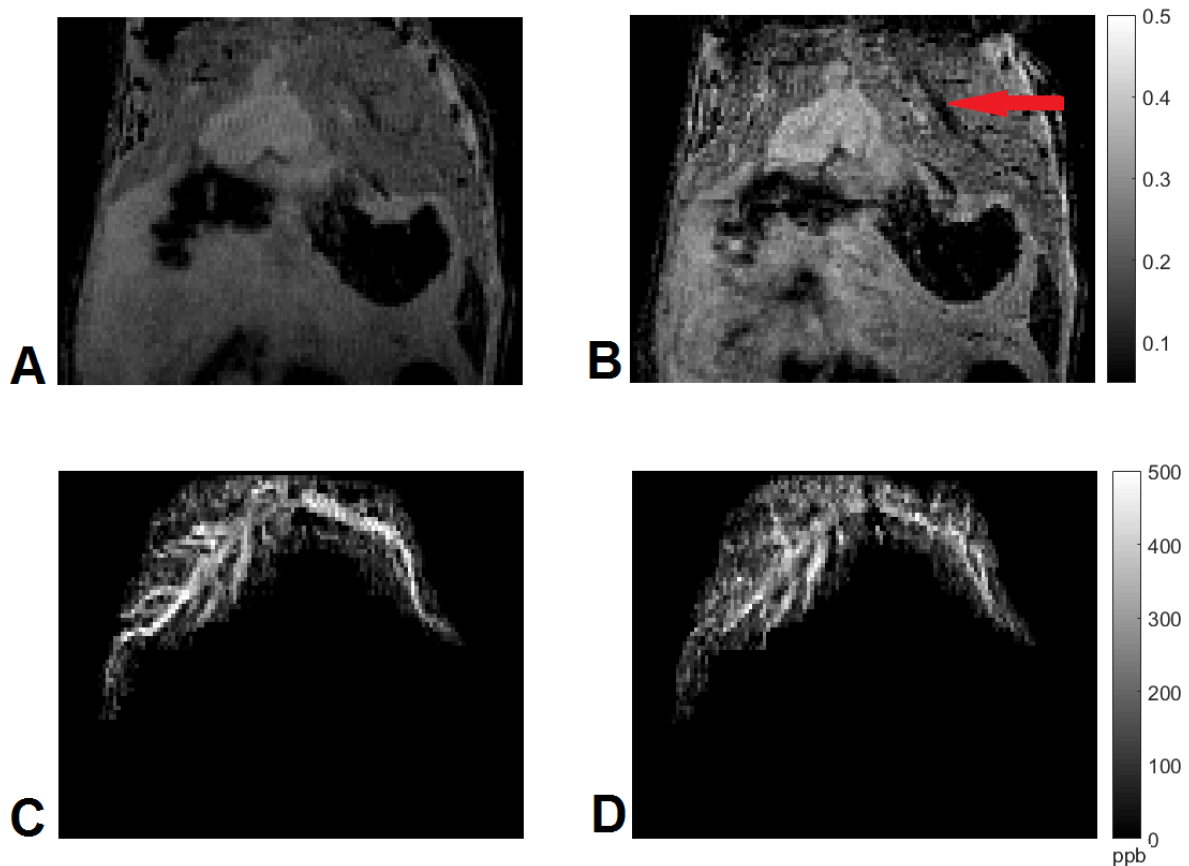


Figure 3.6 A- D: In-vivo images of mouse liver (sagittal orientation) acquired with (A, C), and without (B, D) flow compensation. The top row contains magnitude images, and the bottom row contains Maximum Intensity Projections over a 2 mm area of the corresponding susceptibility maps. The red arrow draws attention to the prominence of a large blood vessel in the uncompensated image.

Figure 3.6 (top row) shows single slice magnitude images of the mouse liver (sagittal orientation) acquired with (left) and without (right) flow compensation. The second row contains maximum intensity projections (MIP) over 2 mm (10 slices) of the susceptibility maps calculated from the same data set.

The image quality of the magnitude image acquired with the flow compensated sequence is superior to the image acquired with the standard sequence as evidenced by the fact that contrast in the liver volume is more homogeneous, and there is less signal dropout, particularly towards the superior section of the organ. Additionally, the large blood vessel

that is visible on the right hand side of the uncompensated image (red arrow) is less conspicuous in the flow compensated image. This is because the acquisition sequence has reduced signal drop out due to flow artefact.

The MIPs displayed in the second row of figure 3.6 also display obvious differences. The delineation of the blood vessels in the flow compensated image is far superior to that in the uncompensated image. Furthermore, the vessels in the uncompensated image appear more diffuse, which will have implications for the susceptibility measured not only in the blood vessels, but also in the surrounding tissue.

Figure 3.7 shows a series of graphs that depict differences in the susceptibility measured in the blood vessel and liver tissue. Graph A shows that the contrast between the 2 regions is higher in the flow compensated image due to the superior delineation of the blood vessels – when the signal from the blood vessels is diffuse, it contaminates the signal from the adjacent regions thus undermining the measurement. Graph B shows that the standard deviation is higher in the susceptibility in the blood vessel in the uncompensated image. This is as expected, and is due to flow artefact.

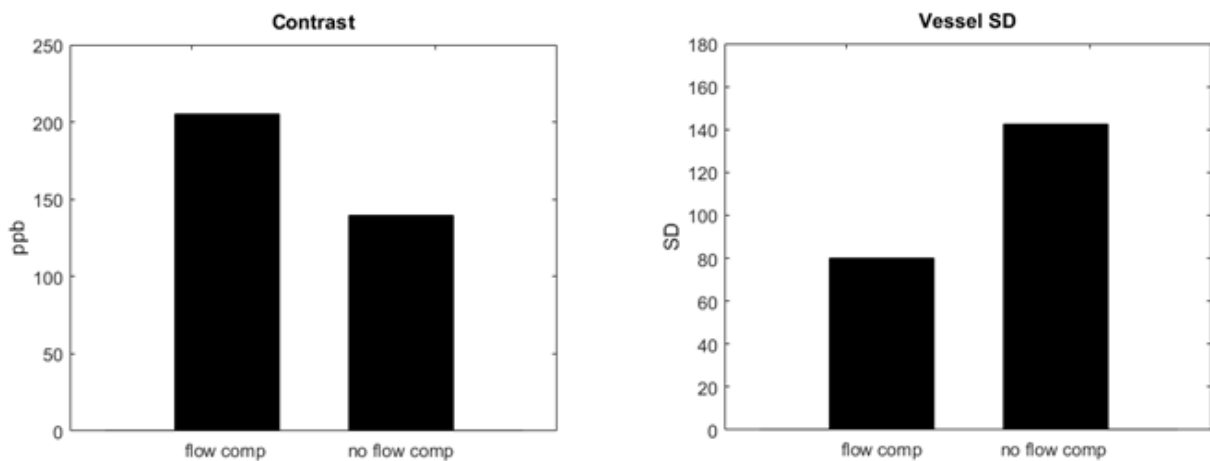


Figure 3.7 A & B: Graphs depicting a comparison between the contrast (A) and the standard deviation of the susceptibility measured in a large blood vessel (B) in images acquired with and without flow compensation.

3.1.2.3.2 Stage II – Conclusions

It is clear from the above that first order flow compensation improves the quality of QSM images and measurements. The delineation between the blood vessels and tissue is vastly improved, as is image contrast. Additionally, the susceptibility measured in the blood vessels is less noisy when flow compensation is included in the imaging sequence. This is highly desirable, as susceptibility changes are of the order of parts per billion, and so could easily be obscured by noise.

From this set of experiments it is concluded that first order flow compensation is extremely beneficial when performing in-vivo QSM on the liver. As such, all results discussed in the remainder of the thesis will be derived from images acquired with a first order flow compensated sequence.

3.1.3 2D vs 3D images

When performing susceptibility mapping in the brain, it is usual to acquire data using a 3D GRE acquisition sequence, the reasons cited in the literature being that 3D acquisitions offer superior SNR, and that 2D acquisitions may introduce phase inconsistencies among adjacent slices ^[19]. It is also noted in the same review however that 2D data are also compatible with QSM, and it has been suggested in an SWI study of the liver that a 3-dimensional acquisition sequence is not suitable for abdominal imaging, due to the long acquisition times and the large B_0 variations encountered when doing so^[20].

There are a number of recent examples in which the application being explored has necessitated calculating susceptibility maps from 2D GRE data. These are instances which require fast acquisitions, such as in the case of functional QSM ^[21] or for use in patients that are unable to remain still for the duration of the scan ^[22]. The latter is particularly prevalent, as the most well developed application of QSM is to assess changes in focal iron deposition in the brains of Parkinson's or Huntington's disease sufferers.

In order to assess the suitability of each acquisition sequence for use in the preclinical liver, 2D and 3D GRE data was acquired of an excised mouse liver at 9.4T. As mentioned, it is important to minimise the time each subject spends in the scanner, and optimisation of the acquisition parameters selected must involve a trade-off between maximising SNR and

minimising scan time. As such, the acquisition parameters of the 3D sequence were manipulated to ensure that the scan time required by both sequences was the same, such that a comparison can be drawn between the (magnitude) SNR in both images, and the quality of the susceptibility maps calculated from each data set.

3.1.3.1 Methods

2D and 3D GRE data was acquired from a non-fixed, freshly excised mouse liver that was immersed in Fomblin. The acquisition parameters were as such:

2D: $B_0 = 9.4T$, $TR = 1000$ ms, $TE = 4$ ms, $FA = 70^\circ$, $FOV = 25.6 \times 20 \times 16$ mm, Matrix = $128 \times 100 \times 80$, Voxel = $200 \times 200 \times 200\mu\text{m}$, bandwidth = 50 kHz, average = 8, acquisition time: 13m 20s.

3D: $B_0 = 9.4T$, $TR = 100$ ms, $TE = 4$ ms, $FA = 8^\circ$, $FOV = 25.6 \times 20 \times 24$ mm, Matrix = $128 \times 100 \times 100$, Voxel = $200 \times 200 \times 200\mu\text{m}$, bandwidth = 100 kHz, average = 8, acquisition time: 13m 20s.

The masks required for QSM processing, and regions of interest were manually segmented on the magnitude images using ITK-snap^[18]. ROIs consisted of a region of liver tissue that did not contain any obvious large blood vessels, and a region of the image within the FOV but outside the sample in order to measure the image noise.

Susceptibility maps were calculated from raw phase data using the SHARP and TKD algorithms. Signal to noise was calculated using the following equation:

$$\text{SNR} = 0.655 \cdot S/\sigma \quad [4]$$

Where S is the magnitude signal in a region of the object being imaged, and σ is the standard deviation of the noise, measured in the aforementioned region. The standard deviation of the susceptibility measured in the liver tissue is also quoted as a measure of image quality.

3.1.3.2 Results

Figure 3.8 shows the magnitude SNR measured in the 2D and 3D datasets respectively. Unsurprisingly given the acquisition parameters, the SNR in the 2D image (37.92) is higher than in the 3D image (31.74). Increasing the receive bandwidth lowers the acquisition time but increases the amount of noise sampled with the signal. Secondly, the flip angle with which the 3D data was acquired was not the at the Ernst angle ($\sim 25^\circ$ at this TR for tissues with this T_1), also contributing to reducing the SNR by reducing the signal.

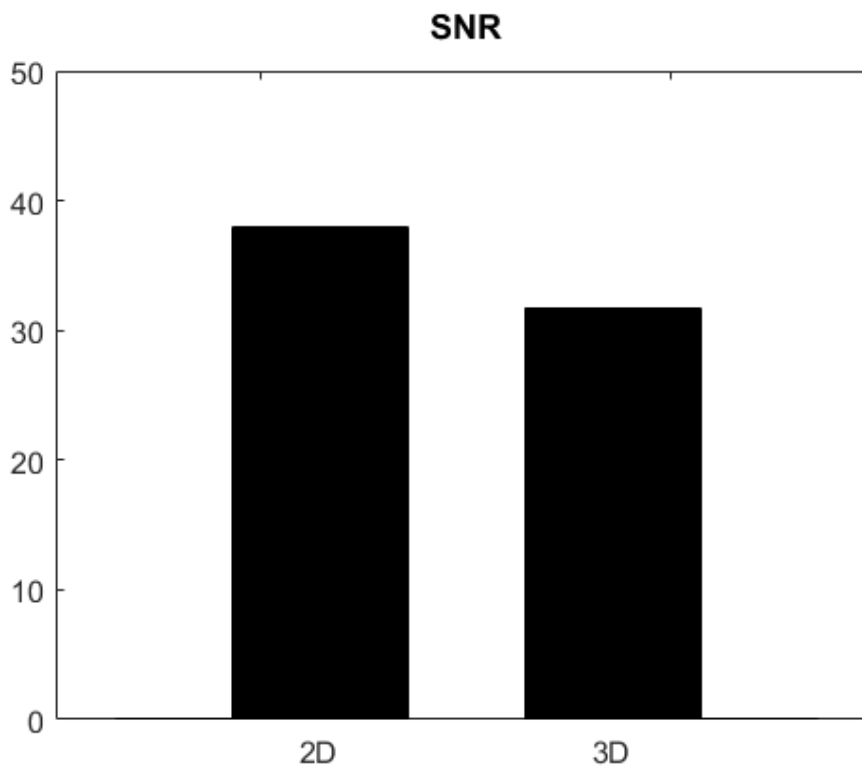


Fig 3.8: Graph depicting difference in Signal to Noise ratio as measured in 2D and 3D magnitude data.

Figure 3.9 shows the T_2^* -weighted magnitude, raw phase, field maps, and susceptibility maps acquired with both 2D (left) and 3D (right) acquisition sequences. For the purposes of display, the raw phase data has been masked such that only the sample is displayed.

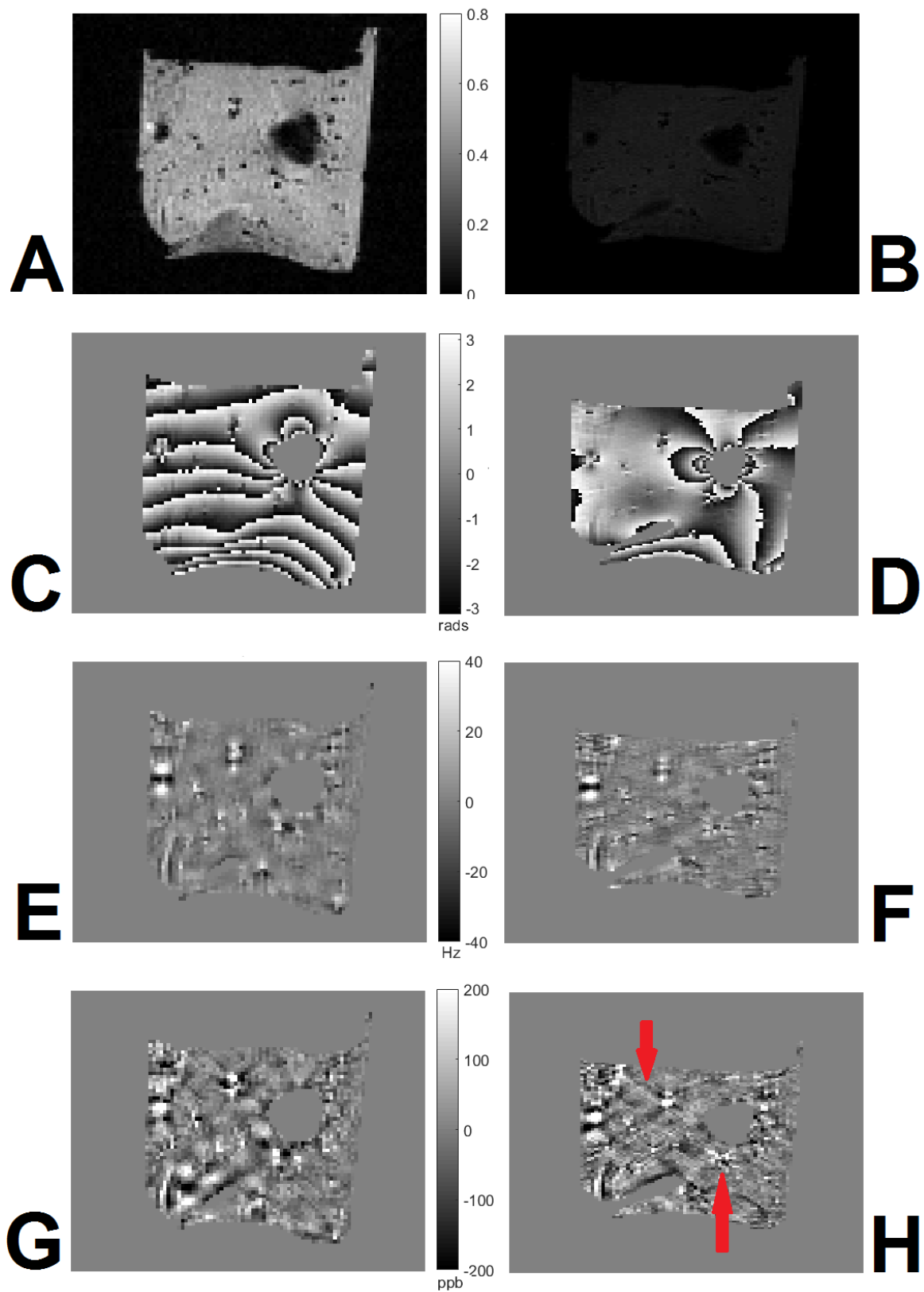


Fig 3.9 A- H: T2*-weighted magnitude images (A,B), raw phase (C,D), frequency maps (E,F), and susceptibility maps (G,H), of 2D (left hand column), and 3D (right hand column) data. The red arrows in (H) indicate the streaking artefact caused by noise in the data supplied to the TKD algorithm.

As expected, the signal in the 2D magnitude image (A) is far superior to that in the 3D image (B) due to the reasons discussed in the previous paragraph. A comparison of the raw phase data (C & D) shows that the phase lines are more dense and numerous on the 2D image (C). It is unclear why this is the case, but may have something to do with the differences in which the data is acquired. During 2D acquisitions, each slice is excited in isolation, and the data from that slice is then acquired. During 3D acquisitions, the entire image volume is excited, and an extra phase encoding gradient is applied in the “slice” direction such that it is spatially encoded. The difference in how each of these gradients are applied during their respective acquisition sequence may explain the differences in phase wraps in the raw images. In any case, this will not have any effect on the susceptibility map calculated from either data set as the phase wraps will all be removed during processing. More importantly, there was no evidence in the 2D image of any broken, or “open-ended” fringe lines that may be indicative of phase inconsistencies, and can adversely affect the phase unwrapping process^[23].

The frequency maps displayed in E & F show that in both cases the phase wraps and background field contributions have been successfully removed by the SHARP algorithm. The dipole patterns that are visible in the images are due to the presence of blood vessels. The tissue visible between the dipoles in each image is less homogeneous in the 3D data. This may be due to increased noise.

The quality of the susceptibility map calculated from the 2D data (G) is superior to that from the 3D data (H). The streaking artefact caused by the TKD algorithm is more prominent in the 3D susceptibility map (red arrows). This is most likely due to the increased noise in the image, and will negatively impact any quantitative measurements.

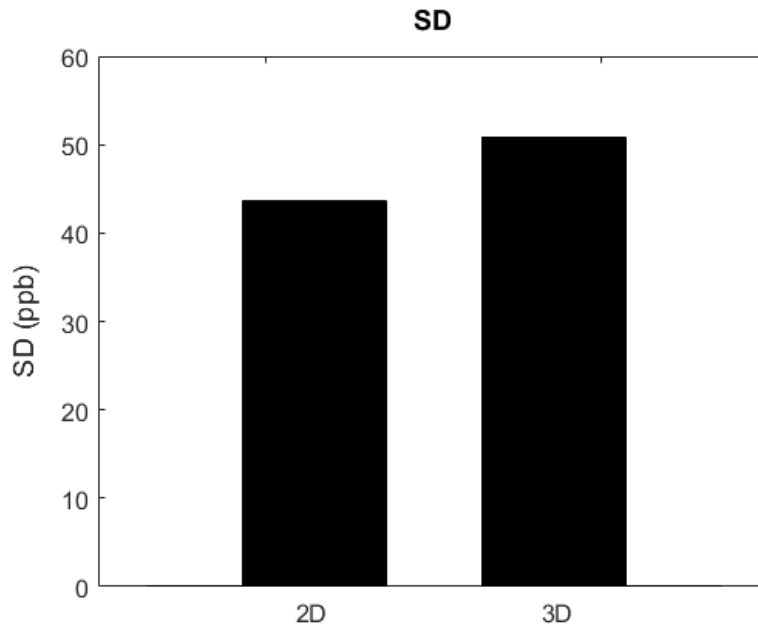


Fig 3.10: The standard deviation in ppb on the measurement of susceptibility taken from the 2D and 3D images respectively. The higher SD in the 3D image is caused by more prominent streaking artefacts in the susceptibility map.

The negative impact of the artefacts in the susceptibility is confirmed numerically in figure 3.10, which displays the standard deviation on a measurement taken in the liver tissue of each image, which is quoted as a measure of image quality. It is clear that the SD on the measurement of the 3D image (50.88) is greater than that of the 2D image (43.66).

3.1.3.3 Discussion

The results of this experiment are borne out of a very preliminary dataset acquired in the early stages of the project. Nevertheless, the results are broadly indicative of the differences between 2D and 3D susceptibility maps in the context of pre-clinical abdominal imaging. As the data was ex-vivo, the B_0 inhomogeneities caused by the large air-tissue interfaces in the abdomen were not encountered, allowing the study to focus explicitly on the trade-off between SNR and acquisition time.

As mentioned, noise in a phase image is proportional to the noise in the corresponding magnitude image^[10]. While it would be possible to optimise the 3D acquisition sequence used here - by reducing the receive bandwidth for example, improving data acquisition to the point at which the SNR in the 3D dataset was significantly higher than in the 2D dataset would

almost certainly involve a time penalty, particularly so if respiratory-gating is introduced to the sequence.

The reduction in scan time brought about by 2D acquisitions is an attractive prospect for many applications. For instance, QSM-fMRI has been the subject of investigation^[21], and recently a processing method has been developed that allows the calculation of QSM images from 2D-EPI data^[24]. In that instance it was shown that quantitative results derived from 2D susceptibility maps are consistent with those derived from 3D susceptibility maps. Additionally, reduced scan time allows a higher throughput when dealing with cohorts of multiple subjects, which is advantageous in both research and clinical scenarios.

3.1.3.4 Conclusion

The scan time required to acquire 3D data can be reduced by adjusting some acquisition parameters, but this comes at the expense of reducing the SNR in the magnitude images, which negatively impacts the subsequent susceptibility maps.

Based on the above, it was deemed that 2D acquisitions provide data that is of sufficient quality to perform susceptibility mapping in the pre-clinical liver at high fields, and any improvement in SNR that could be brought about by a lengthy 3D acquisition is less desirable than reducing the scan time required for each animal.

3.1.4 Mouse liver fat fraction

The influence of fat is a topic not usually discussed in the context of QSM images, the reason being that the majority of applications focus on the brain. When performing QSM in organs outside the head however, the contribution of fat to the MRI signal must be considered.

Chemical shift is a well-known phenomenon in MR imaging, and refers to the difference in resonant frequencies of two nuclei due to their local environments. It is most commonly seen in regions that contain fat. Chemical shift is electronic in nature, and occurs when the electron cloud around protons contained in a fat molecule produce a local, induced

magnetic field that opposes B_0 . As such the electron cloud produces a shielding effect that reduces the magnetic field experienced by the protons, effectively resulting in a diamagnetic response to the applied field.

Less well known however is the effect that fat will have on QSM images. The contrast in images derived from T_2^* -weighted phase data is brought about by differences in the phase angle of the magnetic vector of the acquired signal at each point in the image. These differences are due to local variations in the main magnetic field (B_0) caused by regional susceptibility differences in the tissue under examination. As such, if a voxel contains both water and fat, it is probable that the fat will have the effect of undermining the susceptibility shift caused by paramagnetic components of the tissue that may be of interest (e.g. iron), or, conversely, causing an overestimation of the contribution of any diamagnetic substances that may be present.

In order to ascertain the levels of fat present in the livers of the mice examined in later chapters, the histological images obtained as part of the respective studies were visually inspected for the presence of fat (figure 3.11). These were compared to images from a study in the literature that focussed on mouse models of non-alcoholic fatty liver disease (NAFLD), in which large lipid droplets are clearly visible ^[2] (figure 3.12). In addition, another study that aimed to compare a variety of MRI fat quantification techniques found histologically that the liver fat content of wild type mice was 0.53 ± 0.19 %, compared to 23.03 ± 2.59 % found in obese mice ^[25]. Furthermore, upon visual inspection no mis-registration artefacts, indicative of the presence of fat, were visible on any of the acquired magnitude images.

At time of writing, there have been two papers published that have sought to address the problem of chemical shift in the context of QSM imaging, both of which have involved complex modifications of the processing protocol. As the amount of fat present in the livers of the mice examined was negligible, implementing a chemical shift correction in the data processing protocol was deemed unnecessary.

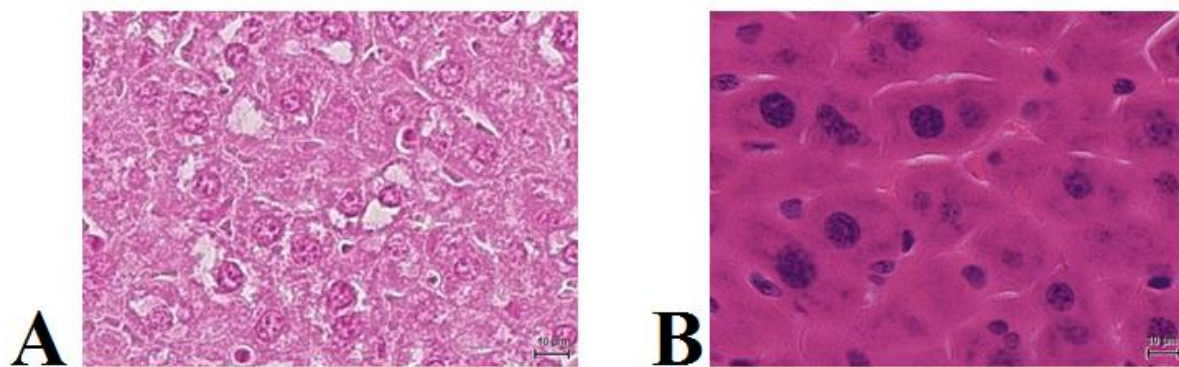


Fig 3.11 A & B: H & E stained histological images of livers from a healthy mouse (A) and a mouse with tumours (B) from the studies described in chapter 4 and chapter 5 respectively. No lipid droplets are visible in either image.

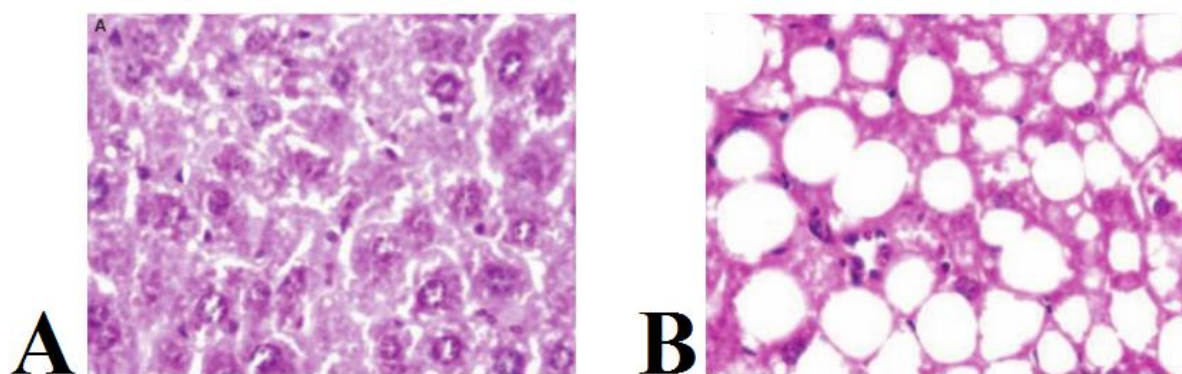


Fig 3.12 A & B: Images taken from literature^[2]. H & E stained histological images of livers from a healthy mouse (A) and a mouse fed a high fat/fructose diet (B). Large lipid droplets are clearly visible in the second image, indicating the presence of a high degree of fat in the liver.

3.2 Processing

As discussed in chapter 2, calculation of a susceptibility map requires three main steps – phase unwrapping, background field suppression, and inversion. There are a number of algorithms that can perform each stage of the process, and it was decided that the experiments conducted herein would employ a SHARP algorithm to perform both phase unwrapping and background field suppression, and a TKD algorithm to perform the inversion calculation.

This particular processing pipeline was chosen because it has been previously been shown to work well in practice^[26], it is relatively easy to implement and optimise for novel applications, and it can generate a susceptibility map from raw data in a matter of seconds^[8]. To the best of our knowledge, implementing QSM to study the pre-clinical liver has never before been performed. Within each processing pipeline there are a number of variables that must be matched to the application. For example, it was found upon initial implementation that the combination of high field strength and the unique geometry of the liver – in particular the location and size of the air/tissue interfaces of the abdomen – required careful calibration of the SHARP algorithm. By the same token, *all* inversion algorithms require optimisation upon initial implementation. This process was performed on an empirical basis, and the speed with which these algorithms perform their respective functions allowed an exploration of the effect that each of these variables – and their interaction - had on the resultant susceptibility map. Once established, this pipeline had the added advantage of allowing large volumes of data to be processed relatively quickly.

The following section highlights the steps taken to optimise the selected processing pipeline for calculating an in-vivo susceptibility map from raw GRE phase data acquired from a mouse liver at 9.4T. The first experiment details a comparison of a heuristic and physical (homodyne and SHARP) background field suppression algorithms discussed in chapter 2 (sec. 2.3.2) in order to bolster the argument that the SHARP filter is more suitable for liver imaging. The second step was incremental adjustment of the TSVD threshold of the SHARP algorithm such that the raw data is unwrapped and the background field contributions are sufficiently suppressed. It was also necessary at this point to mitigate the artefacts at the edge of the image by adjusting the erosion of the binary mask. The second step was to adjust the threshold of the TKD algorithm such that the resulting susceptibility maps retained a reasonable degree of contrast, but displayed minimal inherent streaking artefact.

The data selected for the first experiment (sec. 3.2.1) is human brain data acquired at a very preliminary stage of the project. Otherwise, the data selected for the optimisation procedure was that of a healthy mouse, considered to be broadly representative of the data acquired for the main experiments that follow. The acquisition parameters are as such: $B_0 = 9.4\text{T}$, $TR = 1000\text{ ms}$, $TE = 4\text{ ms}$, $FA = 70^\circ$, $FOV = 32 \times 32 \times 12\text{ mm}$, $Matrix = 160 \times 160 \times 60$, $Voxel = 200\text{ }\mu\text{m}$ isotropic, $bandwidth = 50\text{ kHz}$, $average = 8$. The acquisition sequence was respiratory gated and first order flow compensated in all directions. Binary masks were manually drawn in ITK-SNAP^[18], and all post processing was performed in Matlab (version 2015b, The MathWorks, Natick, MA). As all of the main experiments involve administering a hyperoxic gas challenge, it was necessary to consider images acquired under both medical air and pure oxygen in the optimisation procedure.

3.2.1: Heuristic vs Physical Background Field Suppression

This first experiment investigates the argument that physical background field removal algorithms are superior to heuristic algorithms when preparing data that is to be input to the susceptibility algorithm. Field maps will be calculated from human brain data, and comparisons will be drawn between data processed with a homodyne filter (heuristic), and a SHARP based algorithm (physical).

The same raw $T2^*$ -weighted phase data will be processed with both algorithms. The resultant field maps will be compared visually, and the mean frequency values from different brain regions will be compared to each other and to literature values.

There follows first a brief description of the background theory of the homodyne filter. For the theory regarding the SHARP algorithm, the reader is referred to chap. 2 sec. 2.3.5.

3.2.1.1 Homodyne filtering

Homodyne filtering is a type of synchronous detection, and falls into the heuristic category of approaches to background field suppression. The underlying assumption of the technique is that the complex T_2^* -weighted signal can be interpreted as consisting of high spatial frequency components that we wish to examine, modulated by an undesired low spatial frequency background. To extract the component that is of interest the signal must be demodulated, requiring a demodulation reference. This can be isolated from the original signal by low pass filtering (LPF), such that the reference will encompass the low spatial frequency background field. Demodulation is then carried out by performing complex division of the original by the filtered signal. This removes the unwanted low spatial frequency component, but leaves in-tact the high spatial frequency phase variations of interest. In addition to this, as the calculation is carried out in the complex plane, phase wraps are also removed [27].

There is a trade-off involved when performing homodyne filtering: The band-pass of the filter must be of sufficient width that the demodulation reference is an adequate representation of the unwanted phase variation, while at the same time narrow enough to preserve the contrast between large structures. This trade off becomes readily apparent when trying to mitigate the problems associated with phase imaging. It can be seen from eqn. 4 (chap. 2 sec. 2.1) that the contrast in a phase image is dependent on field strength, and can be manipulated by careful selection of echo time. Equally, both phase wraps and background field effects are exaggerated by increases in field strength or echo time, becoming higher spatial frequency components of the image. This increases the overlap between wanted and unwanted signal, making the respective contributions harder to separate. Hence an increase in echo time will necessitate filter with a wider bandwidth, however the contrast gained by virtue of the increased echo time can in some cases compensate for this.

K-space is filled such that the high spatial frequency components of the image that make up the sharp details, such as the edges, are mapped to the outside of k-space. Conversely, the low-spatial frequency components – those responsible for contrast - are mapped to the centre. As such, filtering was carried out by performing a Fourier transform of the image, and then multiplying the result by a 3D Gaussian function. This preserved the values at the centre of k-space, while minimising the values in the outer region. The data was then inverse Fourier transformed to yield a low pass filtered image, and the demodulation

was carried out by complex division in the image domain. Finally, the homodyne filtered images were multiplied by a sufficiently eroded binary brain mask to remove edge effects. The brain mask was extracted from the magnitude data using the BET tool in the FSL package ^[28].

The bandpass of the filter can be discussed in terms of the full width half maximum (FWHM) of the Gaussian function. It is quoted in terms of the number of points in the x-direction of k-space (k_x) as $\Delta k_x = \text{FOV}_x^{-1}$. The filter has been designed such that it will act on the same spatial frequencies in all three directions in k-space.

A FWHM of 60 voxels in the k_x direction was used to filter the complex data. The filter width was determined empirically by visual inspection of the filtered images ^[27].

3.2.1.2 Data Acquisition

Scans were performed on a 3T scanner (Magnetom, Siemens Healthcare, Germany). A multi-echo (5) T_2^* -weighted 3D GRE coronal acquisition was performed. The image acquired at TE_4 (19.68 ms) was chosen for examination as it has been determined in a previous experiment on the same data set (not shown) that this image provides the best balance between SNR and contrast after filtering. Parameter values are presented in table 3.1

Parameter	Value
TR / TE_1 / TE_5 (ms)	30 / 4.92 / 24.6
ΔTE (ms)	4.92
Flip Angle ($^\circ$)	20
FOV (mm)	178.86 x 192 x 220
Voxel size (mm)	0.859 x 2 x 0.859
Number of averages	1
Receiver BW (Hz/px)	400

Table 3.1: Acquisition parameters for sec. 3.2.1

3.2.1.3 ROI

Regions of interest (figure 3.13) were placed in:

- White matter in the primary motor area ^[29, 30].
- Grey matter in the primary motor area ^[29, 30].
- The putamen, an iron rich structure in the base of the forebrain ^[31].
- CSF in the ventricles ^[31].

These regions were chosen as they are often used throughout the literature to gauge the usefulness of phase based images. Briefly, grey matter (GM) has been shown to contain more iron than white matter (WM). WM contains myelin, which is slightly diamagnetic. As such, the mean frequency shift between grey and white matter has been used as a measure of contrast in field maps ^[29, 30]. The putamen is an iron rich deep brain structure, so will be readily apparent on a calculated susceptibility map. As the calculated susceptibility maps contain no areas of known absolute susceptibility, the measured susceptibility values must be quoted relative to a reference. CSF is thought to contain very little iron, and so will have a susceptibility close to that of water. As such, it is often used as the reference for susceptibility measurements in the literature ^[31]. Susceptibility values are quoted as the difference in measurements. ROIs were hand drawn on the magnitude image acquired at the first echo using ITK-SNAP ^[32].

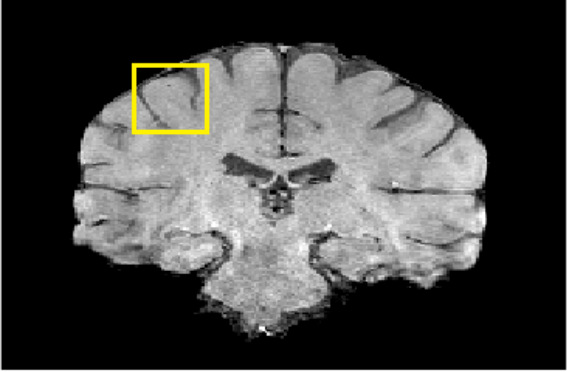
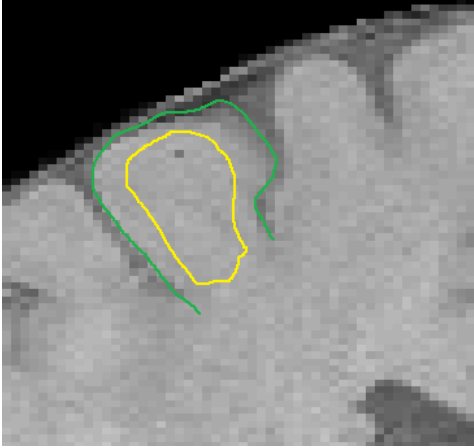
<p>A: Motor region of cortex</p>	<p>B: Close up of motor region delineating white (yellow) and grey (green) matter</p>
	
	
<p>C: Putamen</p>	<p>D: CSF in the ventricles</p>

Fig 3.13: Regions of interest, as drawn on magnitude T2*-weighted images.

3.2.1.4 RESULTS

The images displayed in figure 3.14 and 3.15 show the magnitude, raw phase, homodyne and SHARP filtered field maps in coronal and axial planes. It is clear from the field maps that phase based imaging provides contrast of iron rich areas of the brain that is not evident on the magnitude data. The highlighted region in the SHARP field map in figure 3.14 is where we would expect to find the red nucleus and substantia nigra, two iron rich deep brain nuclei. It is also clear however that the contrast is non-local and depends on the orientation of the structure to the main magnetic field.

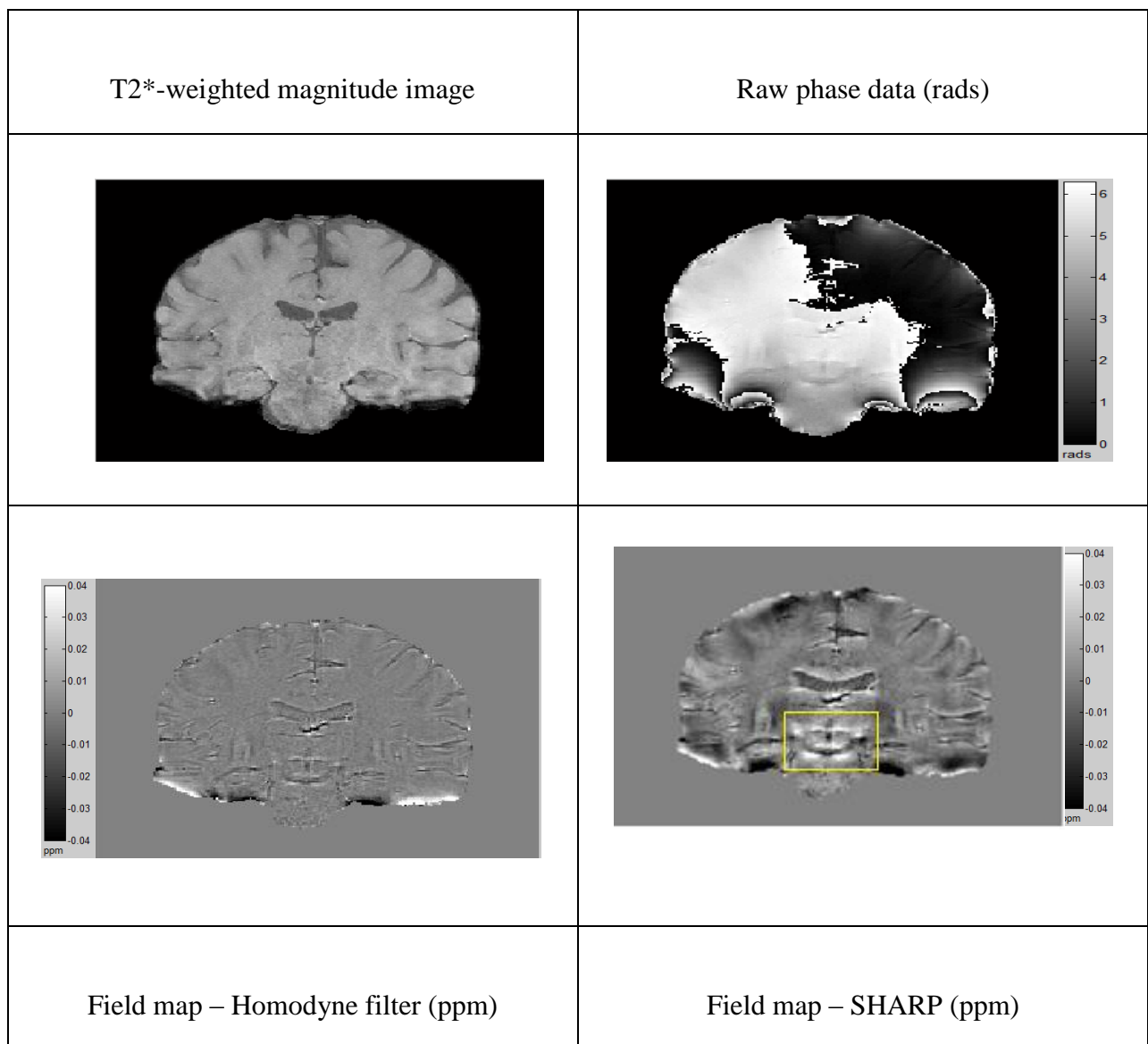


Fig 3.14: Coronal images. Magnitude, raw phase and field maps calculated with a homodyne filter and SHARP algorithm respectively. The highlighted region in the SHARP derived field map shows the region that contains iron rich structures

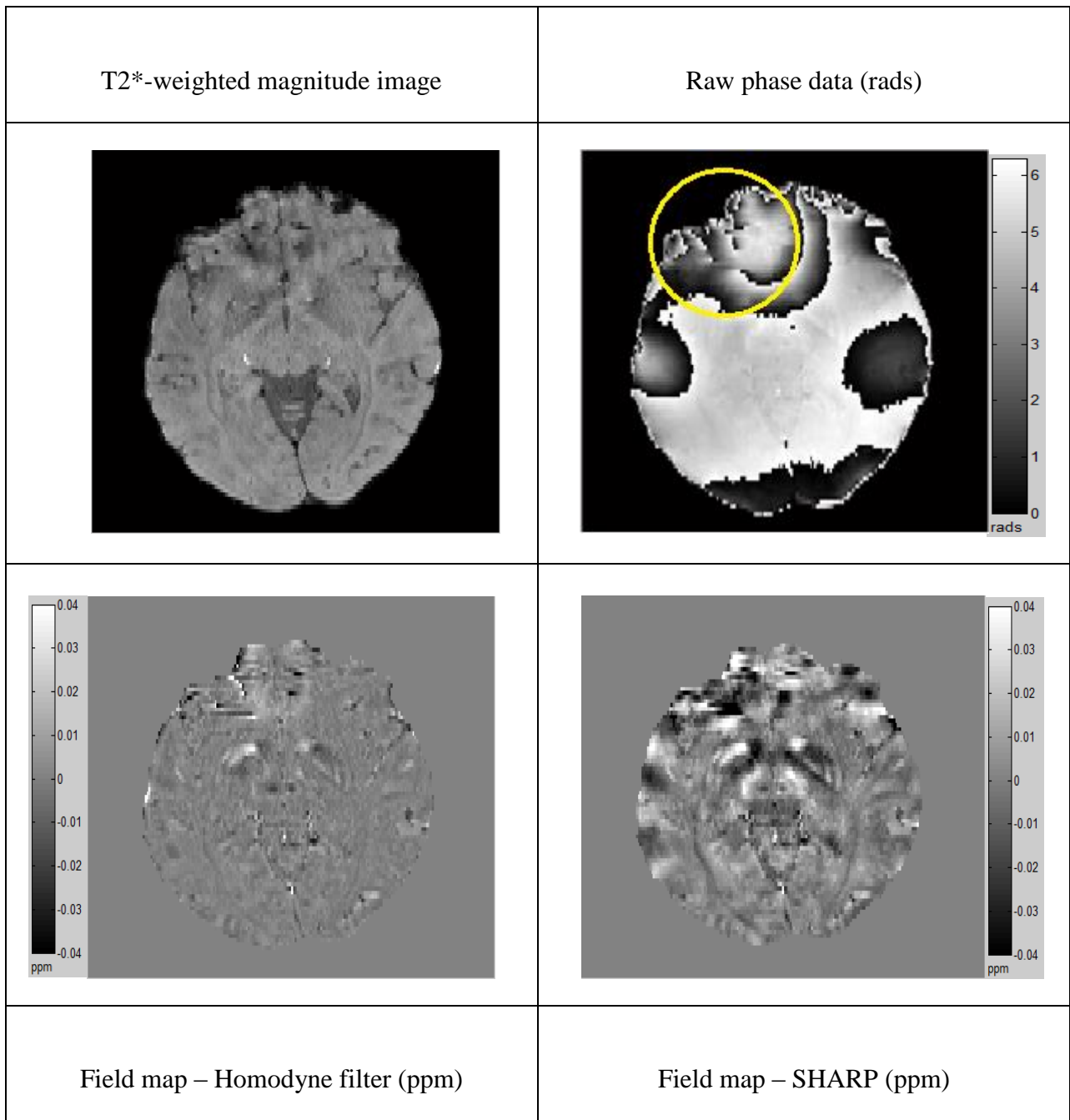


Fig 3.15: Axial images of the data displayed in fig. 3.14. The highlighted region in the raw phase image shows phase discontinuities in the area adjacent to the sinus.

Both homodyne and SHARP algorithms removed phase wraps and suppressed the background field to an extent that is sufficient for susceptibility calculation, but it is equally clear that the field maps derived by the SHARP algorithm provide superior contrast to the homodyne filtered images. Both algorithms struggled to remove the unwanted field effects in the area that is adjacent to the sinuses (figure 3.15). This area is known to cause particular difficulty when processing phase images due to the steep susceptibility gradient at the tissue / air interface. The effect can even be seen as a slightly darker region of the magnitude image. In this data set, this region appears to cause particular difficulty for the processing algorithms due to the presence of phase discontinuities (highlighted region in figure 3.15). Phase discontinuities are incomplete phase wraps and are thought to be caused by the algorithm responsible for the combination of the multi-channel phase data^[33]. It is thought these can be mitigated by using the SENSE rather than the GRAPPA algorithm^[33].

The graphs in figure 3.16 display the absolute field shift between grey and white matter in the motor region. Graph 3.16 A confirms that the measured field shift and hence image contrast is superior in the SHARP filtered image. Graph 3.16 B compares the field shift measured in the SHARP images to similar values from the literature measured on systems with different field strengths^[29, 30]. As expected, the contrast increases with field strength.

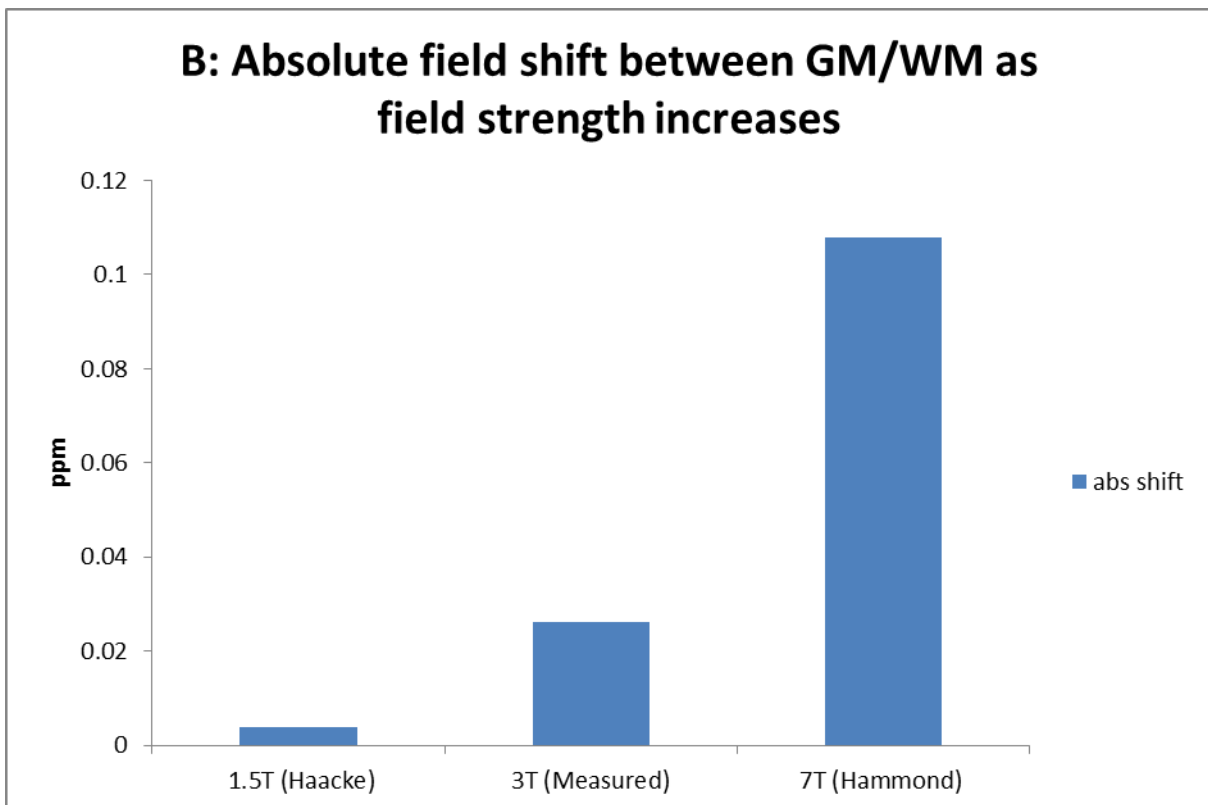
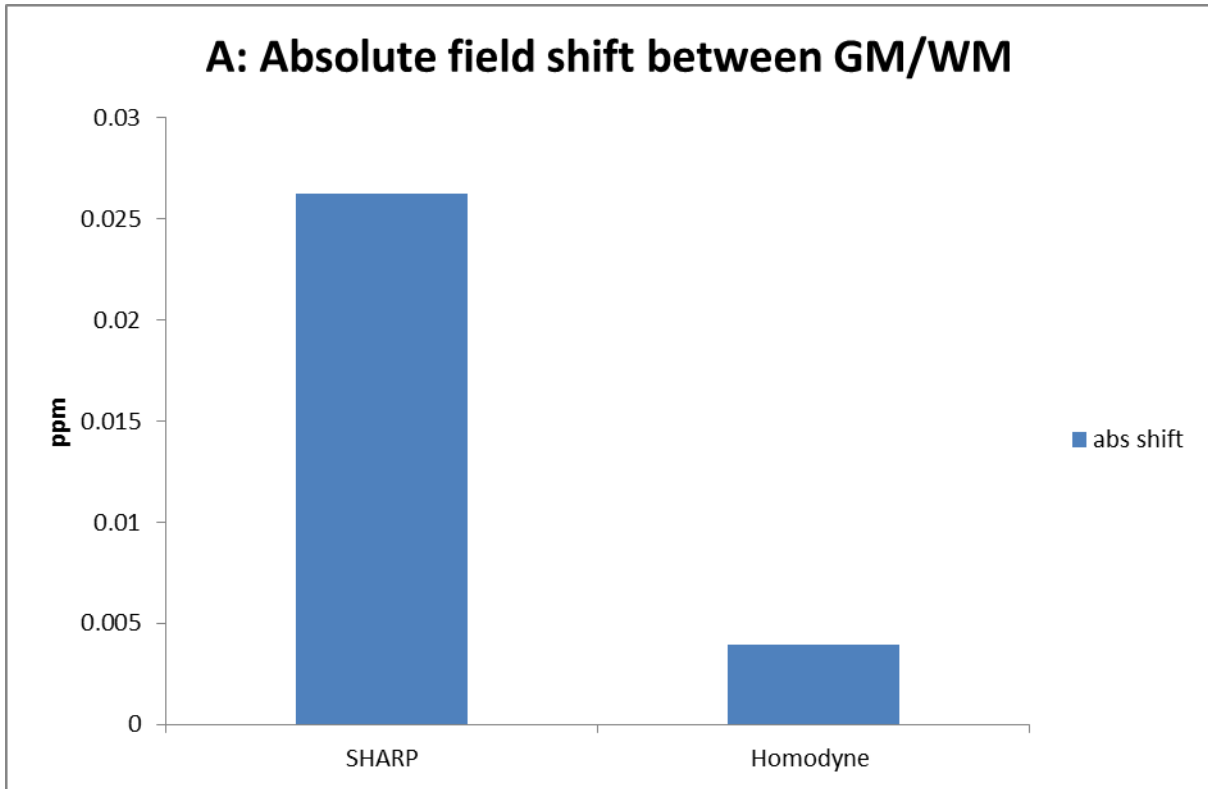


Fig 3.16 A & B: Graph A displays the measured absolute field shift between the grey and white matter in the motor region. Graph B shows the measured field shift in the SHARP processed data compared to values from the literature measured at different field strengths[29, 30] .

3.2.1.5 CONCLUSIONS

It was shown that physical approaches to data processing produce superior input data for the susceptibility algorithm, but that useable susceptibility maps can be calculated from the data derived via heuristic means.

3.3.1 : SHARP algorithm

Figure 3.17 shows the magnitude image of the area within the subject's liver that contains the region of interest (red box). Figures 3.17 B & C show the corresponding raw phase image (for display purposes masked such that only the liver is shown) and SHARP processed field map, the latter of which will be the subject of the measurement. Figure 3.17 C depicts the regions of interest in green (tissue) and red (vessel), and has been scaled to Hz, such that image contrast – measured as the mean frequency shift between the liver tissue and a large vessel - could be discussed in terms of the optimisation protocol. All images shown were derived from the data set acquired while the subject was breathing pure O₂, as the observed background field was much more pronounced under these conditions. It is thought that this is because O₂ is a paramagnetic molecule, so its administration may have had a greater effect on the susceptibility gradient between the lungs and the liver.

Previous studies have implemented this pipeline in the brain with TSVD threshold values that range from 0.016^[8] to 0.2^[9]. For this work, the TSVD threshold was incrementally increased from 0.006 – 0.04. The resulting field maps were visually inspected to determine sufficient suppression of the background field^[31]. The number of times the mask was eroded was then increased incrementally from 1 – 3 until the edge artefacts were deemed adequately removed (see below).

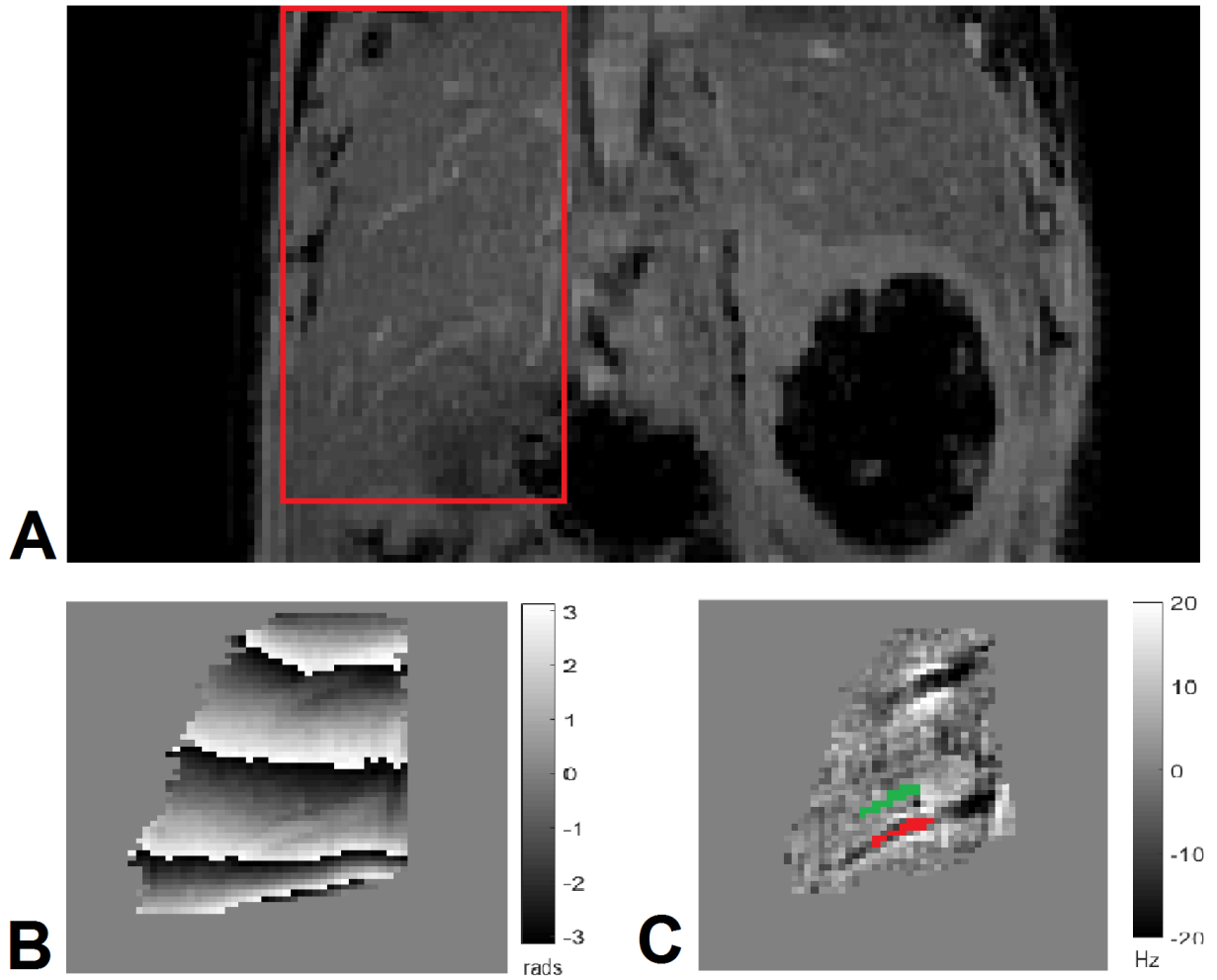


Figure 3.17 A – C: (A) T2*-weighted magnitude image of in-vivo mouse liver (coronal orientation). The highlighted area containing the ROIs is magnified in the bottom row. (B) Corresponding region of raw phase image. (Image has been masked for clarity during display) (C) Corresponding field map displaying vessel (red) and liver tissue (green) regions of interest.

3.3.1.1: SHARP results

As mentioned in chapter 2 (sec. 2.3.2), background field effects most obviously manifest as large scale contrast undulations throughout the image. As such, it can be seen from figure 3.18 that the characteristic hypo- and hyperintensities (yellow arrows) indicative of external field contributions to the image are reduced as the TSVD threshold is increased. Conversely, the edge effects (green arrows) – caused by an idiosyncrasy of the SHARP algorithm (chap. 2 sec. 2.3.5) - remain largely unchanged. These are eliminated as the mask is eroded to a greater degree.

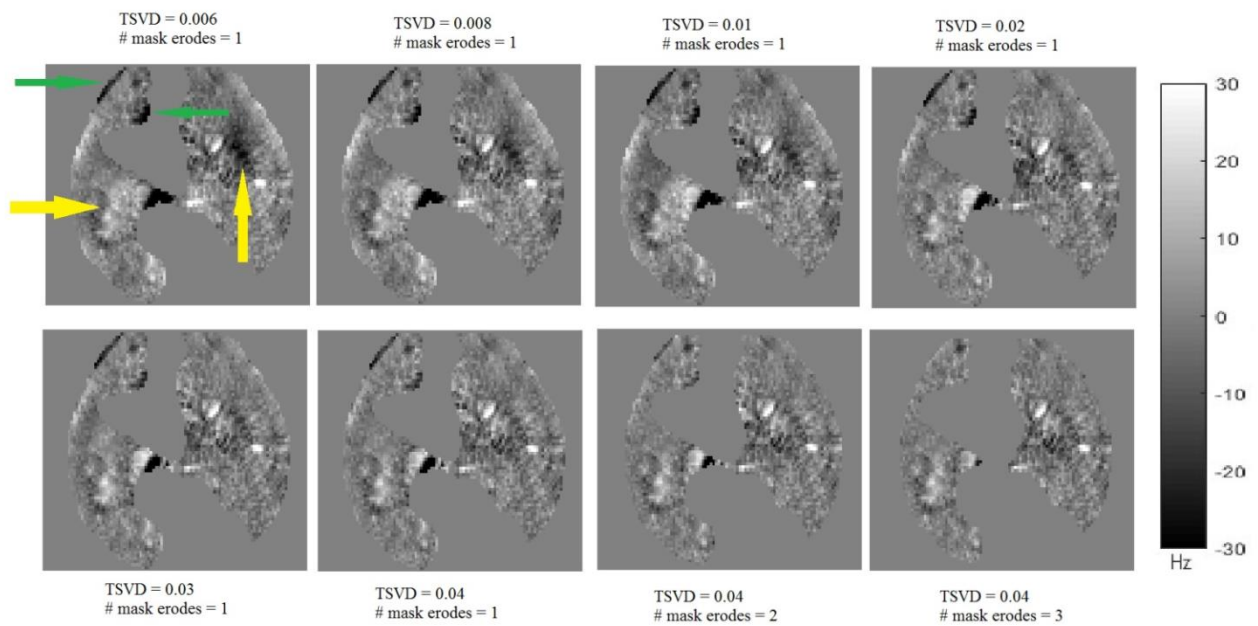


Figure 3.18: Field map of mouse liver (axial orientation) calculated using the SHARP algorithm. Series shows the reduction in background field contributions (yellow arrows) and edge effects (green arrows) as the TSVD regularisation threshold and degree of mask erosion are increased respectively.

The graphs in figure 3.19 show the image contrast and standard deviation within each ROI as the algorithm is optimised. Image contrast increased with the TSVD threshold. The reason for this is that as the relatively large contributions to the image that constitute the background field are removed, the underlying contrast brought about by field shifts within the organ of interest is revealed. There is a slight reduction in contrast as the number of times the mask is eroded is increased due to the removal of the extreme values around the edge of the image.

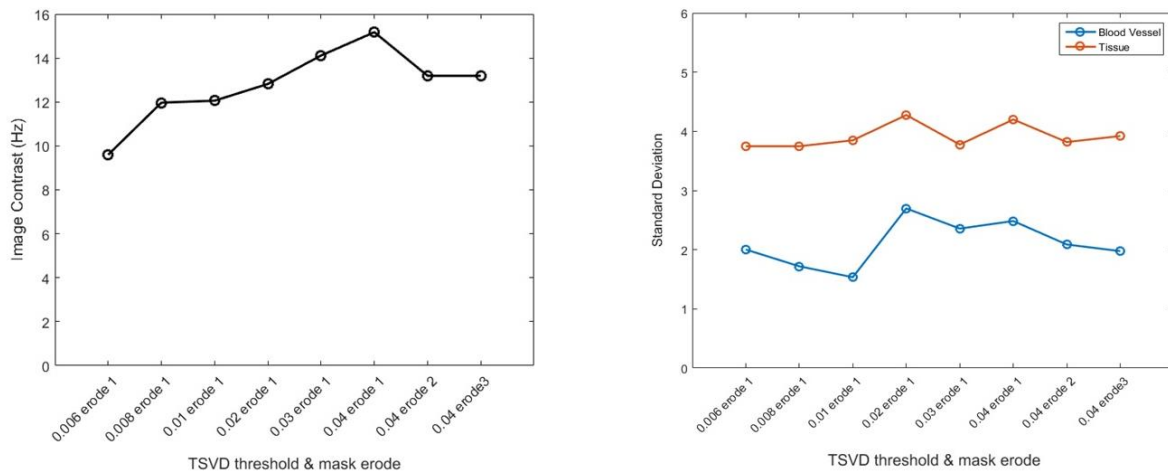


Figure 3.19: Graphs depicting the measured contrast (left) and standard deviation in the ROIs (right) as the SHARP algorithm is optimised

Images were visually assessed in all instances. The criteria for acceptance was removal of any large scale contrast undulations that are indicative of background field effects. Equally, the removal of edge effects was deemed sufficient when there were no obvious signs of abrupt contrast changes around the edges of the liver in the images. The progression of this removal process is depicted in figure 3.18. It was deemed that a TSVD threshold of **0.04** with a mask eroded **3** times resulted in adequate suppression of the background field effects and removal of edge artefacts from the field map. As such, raw data processed with these thresholds was used as the input data for the susceptibility algorithm.

3.2.3: Thresholded K-space (TKD) Algorithm

There is also a large degree of variability in the regularisation threshold value selected for the TKD algorithm in previous studies. Values ranging from 0.2 – 0.5 were found agreeable in the literature ^[26]. Presently, the threshold was incrementally increased from 0.008 to 1. Images were examined by visual inspection, and the difference in mean susceptibility between the liver tissue and a large vessel (figure 3.20) was used to numerically gauge image contrast in terms of the optimisation procedure.

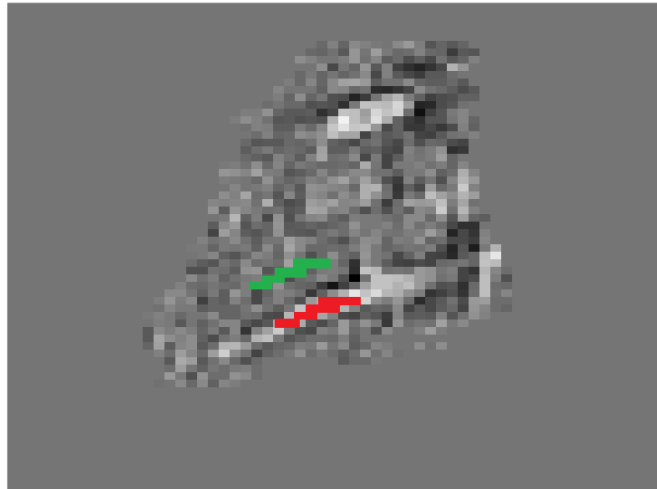


Figure 3.20: Quantitative Susceptibility Map of mouse liver (coronal orientation), displaying large blood vessel (red) and liver tissue (green) ROIs.

Additionally, and in similar fashion to previous studies, the standard deviation of the susceptibility within the tissue ROI was used to assess the severity of the streaking artefact inherent to the TKD algorithm ^[26].

3.2.3.1: TKD results

Figure 3.21 shows a series of representative susceptibility maps calculated with increasing thresholds. As expected, there is a strong positive correlation between image quality and TKD threshold. This is due to the fact that as the threshold is lowered it allows more ambiguity into the susceptibility calculation, resulting in greater noise amplification. Conversely, as the threshold is increased more *a priori* information is supplied to the calculation, resulting in a decrease in image contrast.

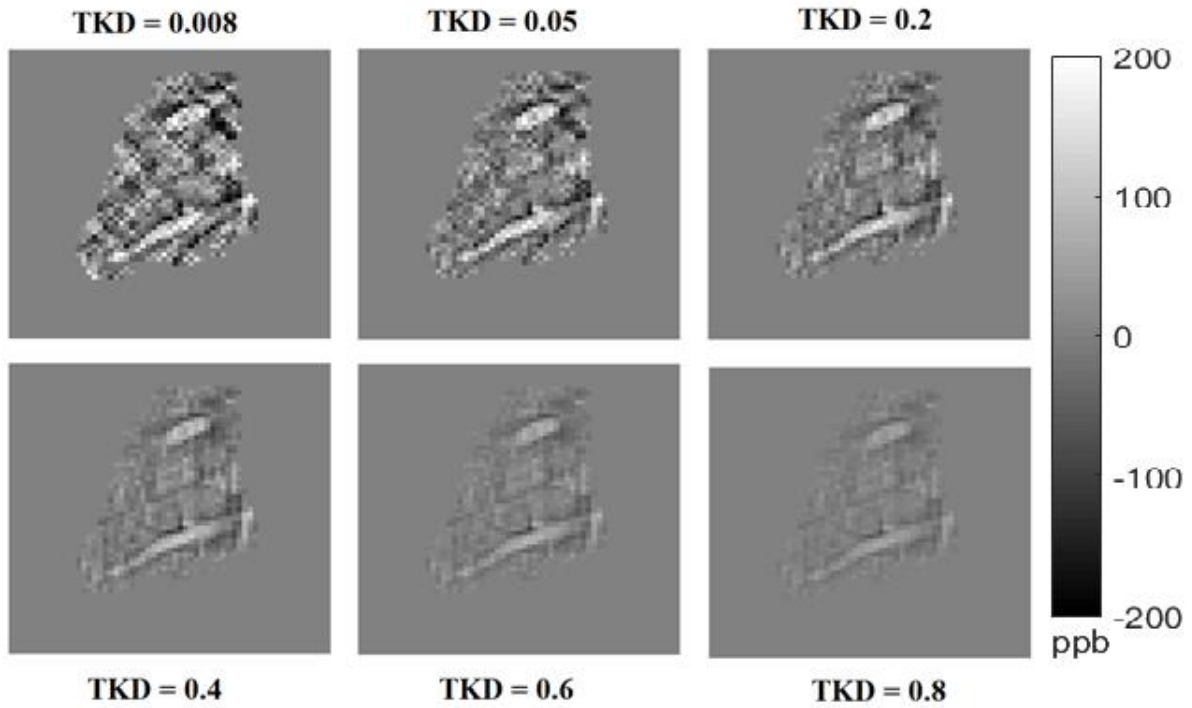


Figure 3.21: Series of Quantitative Susceptibility Maps depicting changes in image quality and contrast as the TKD threshold is increased

This is confirmed numerically in figure 3.22. The graph in 3.21 A shows an almost linear decrease in image contrast as the TKD threshold is increased. Equally, 3.21 B shows an almost linear decrease in the standard deviation of the values within the liver tissue ROI as the threshold is increased. Optimisation of the TKD algorithm requires striking a balance between reducing the image artefact while retaining adequate contrast. In this instance, a TKD threshold value of **0.2** was deemed to meet these criteria.

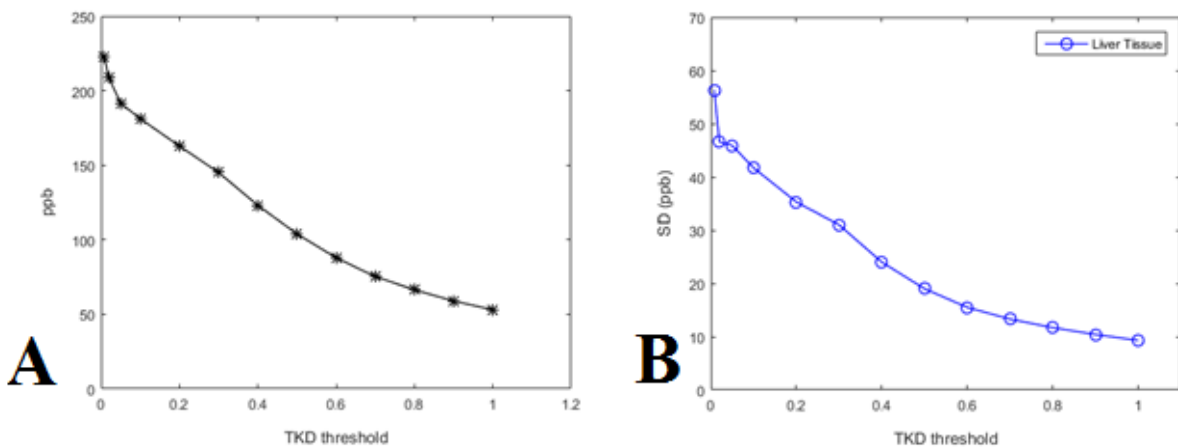


Figure 3.22: Graphs depicting image contrast (A) and SD in the liver tissue ROI (B) as the TKD threshold is increased

3.2.4: Interaction between Algorithms

In order to ensure a thorough analysis of the processing pipeline, an investigation was carried out on the impact that the interaction between the SHARP and TKD algorithms have on the final susceptibility map. The same raw data was processed with the SHARP algorithm three times with variations in the TSVD threshold and degree of mask erosion:

Field Map 1: TSVD = 0.04, # mask erodes = 1;

Field Map 2: TSVD = 0.04, # mask erodes = 3;

Field Map 3: TSVD = 0.08, # mask erodes = 3;

Susceptibility maps were then calculated from each field map using the TKD algorithm with the same range of regularisation thresholds examined in the previous section (i.e. 0.008 - 1). Images were subject to visual inspection, and contrast was calculated as before. Again, the SD of the susceptibility values in the tissue ROI was used to gauge the severity of the streaking artefact.

3.2.4.1: Results

Figure 3.23 shows a representative susceptibility map calculated from each dataset and a graph showing the how image contrast in each changes as the TKD threshold is increased. There is little difference in contrast between each of the data sets, however the data processed with the highest TSVD threshold consistently has the lowest contrast of the three. Of the other 2, the data set subject to a greater degree of mask erosion displayed higher contrast at low values of the TKD threshold. Contrast in each image decreases by an average of $11.99 \pm 3.39\%$, $12.74 \pm 2.35\%$ and $12.95 \pm 2.52\%$ per 0.1 increment of the TKD threshold for field maps A, B, and C respectively.

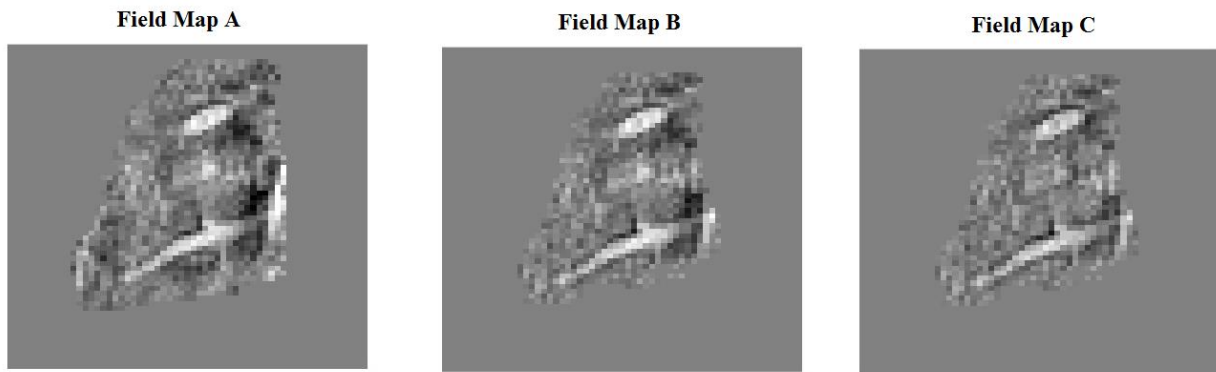
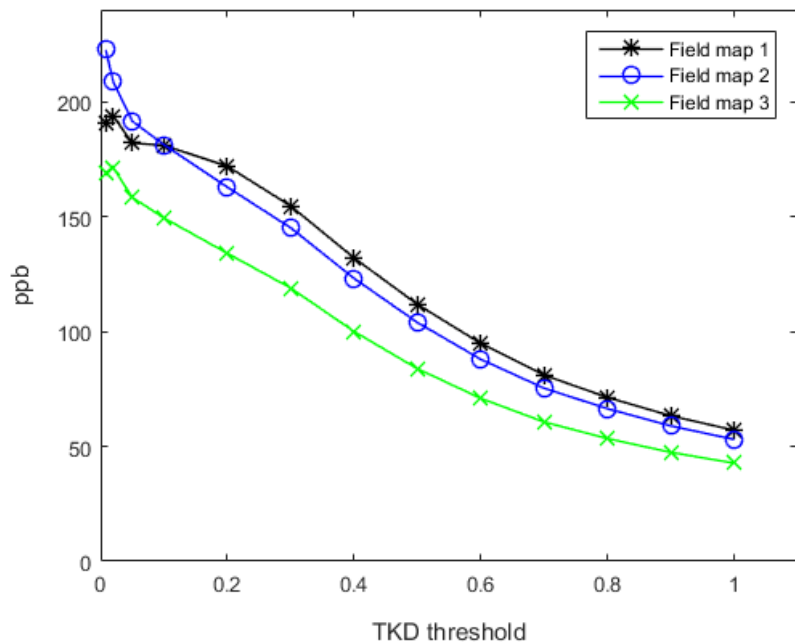


Figure 3.23: Top: Series of quantitative susceptibility maps of mouse liver (coronal orientation) depicting the differences to the final image brought about by changes in input data to the inversion calculation. Images calculated with TKD algorithm, threshold = 0.2. **Bottom:** Graph depicting changes in image contrast measured in susceptibility maps for each field map, as the TKD threshold is increased.



The graphs in figure 3.24 depict the progression of the measured susceptibility values in the liver tissue and blood vessel respectively as the TKD threshold is increased. The susceptibility values measured in the blood vessel decrease gradually with each increment of the TKD threshold, but there is little difference between the values measured in each image at each point. As expected, each tends to zero as the regularisation value is increased. As before, the values in the image processed with the highest TSVD threshold is consistently the closest to the zero point.

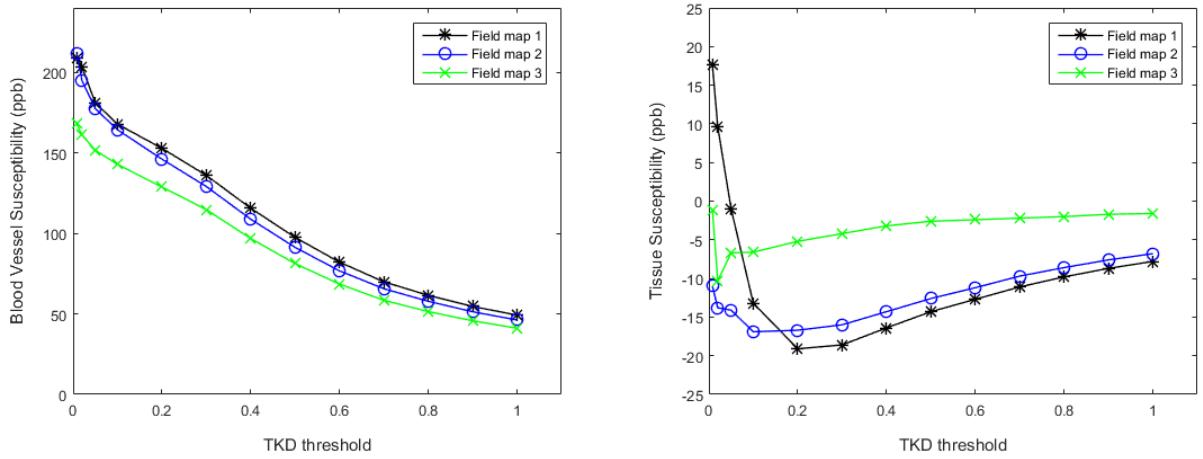


Figure 3.24: Graphs depicting the changes in measured susceptibility in the blood vessel (left) and liver tissue (right), for each input data as the TKD threshold is increased.

The susceptibility measured in the liver tissue is more sensitive to the number of times the mask has been eroded than to the TSVD threshold when the TKD regularisation is at a low value (i.e. < 0.2). As the TKD threshold is increased however the values from the data set with the same TSVD threshold are almost identical. Again, the values in the image processed with the highest TSVD threshold are consistently the closest to the zero point. As the TKD threshold is increased, the contrast in all images is increasingly undermined. The convergence of all susceptibility values on the zero point is demonstrative of this.

The graph in figure 3.25 shows the progression of the SD measured in the liver tissue as the TKD threshold is increased, and is presented as a measurement of the streaking artefact in the susceptibility maps. As expected, the SD has an inverse relationship with the regularisation threshold, and there is virtually no difference between data sets for most increments. At low values of the TKD threshold the data set processed with the highest TSVD value is higher than the others, indicating a slight sensitivity of the TKD algorithm.

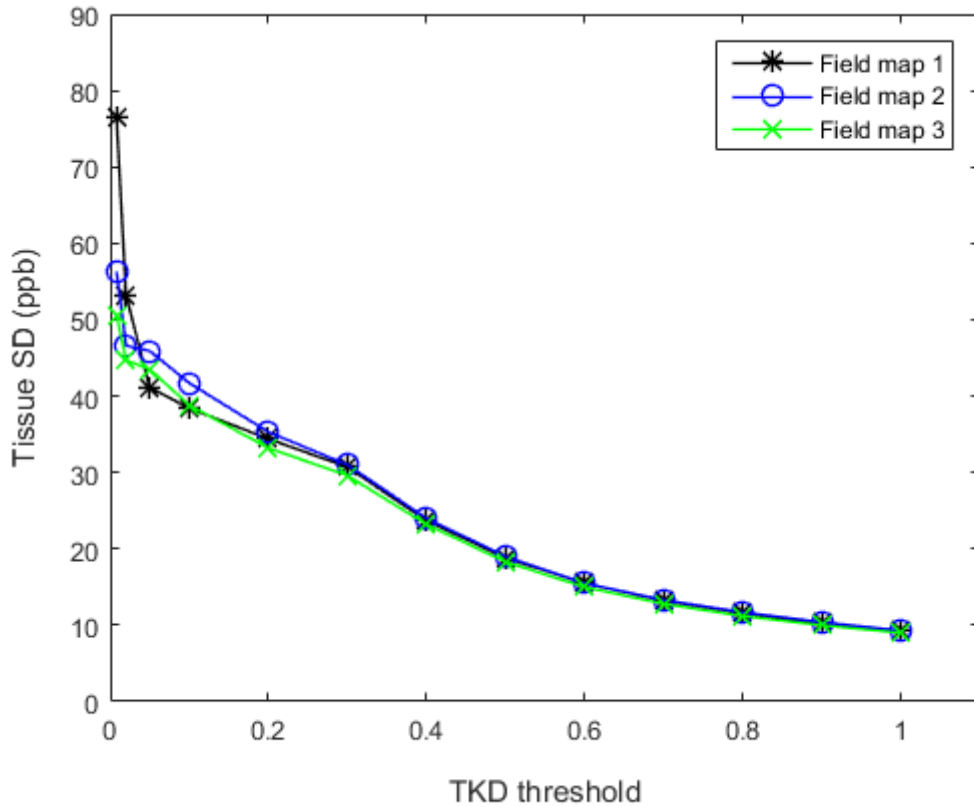


Figure 3.25: Graph depicting changes in the standard deviation of the susceptibility values measured in the liver tissue for each field map as the TKD threshold is increased.

3.2.4.2: Conclusions

The above experiment explored the interaction between the various algorithms that are to be used to process the data for the main experiments carried out as part of this body of work. Image quality (given by the standard deviation on measurements from ROIs), and image contrast were examined. The expected trade-off between image quality and fidelity was observed. It was found that the TSVD threshold and number of times that the mask was eroded during the SHARP processing step have some effect on image contrast, however it was also found that the factor most affecting image contrast was the amount of information supplied to the inversion algorithm via the threshold value.

3.2.5: TKD Systemic Underestimation

While it is true that the derivation through careful processing of a pristine field map from raw data is a crucial component of the susceptibility mapping process, it can be seen from the above that the differences in measured susceptibility values calculated from the various field maps is of the order of tens of parts per billion. It is equally clear that once a field map has been deemed a suitable substrate for inversion, the largest influence on the susceptibility measurements when using the TKD method is the TKD regularisation threshold.

The systemic underestimation of susceptibility values in images calculated using the TKD method is a well-known problem ^[8, 26], and is an inherent property of the algorithm. As shown above, each 0.1 increment of the regularisation threshold results in a ~12% change in susceptibility values. This comes about because the regularisation of the algorithm involves replacing very small values of the deconvolution kernel with a value equal to the regularisation threshold. As such, the division of the field map in k-space is performed in this region with inflated values ^[8].

The effect is almost linear with the TKD threshold, and is consistent across the entire image. As such, one simple solution to the problem is the inclusion of a simple multiplicative factor when carrying out the inversion calculation ^[8]. The study in which this solution was presented detailed a rigorous comparison between a TKD susceptibility map and a one calculated from multi-echo data via the COSMOS method. This enabled the derivation of a curve that expressed the degree of underestimation for each increment of the TKD regularisation threshold (figure 3.27 B). This was then compared to theoretically predicted values of underestimation. While it was shown that this successfully mitigated the underestimation engendered by the algorithm, the purpose of the exercise was to demonstrate its applicability to human brain imaging, and as such may not be pertinent at high field strength in a preclinical liver.

The solution to the underestimation issue proposed herein is to perform linear regression on the series of values measured within an ROI as the TKD regularisation threshold is increased. As such, the intercept of the fitted line will be the mean susceptibility within the ROI if the regularisation threshold was 0. This can then be used to estimate the underestimation of susceptibility values, and to subsequently calculate a correction factor for the image.

The data selected was that used in previous sections. The raw data was processed with the SHARP algorithm (TSVD threshold = 0.04, #msk erodes = 3). TKD threshold values were incrementally increased from 0.008 – 1, and the mean susceptibility measured in the blood vessel ROI (figure 3.20) was selected as the measurement on which to perform the regression.

3.2.5.1: Results

The graph in figure 3.26 shows the progression of the measured value as the TKD threshold is increased, and the results of the linear least squares fit. The intercept of the regression line with the y-axis was observed at a value of 185.81 ppb. Figure 3.27 shows the projected underestimation plotted against the TKD regularisation threshold as derived from the results of the linear regression, and the graph depicting the same from Scheweser 2013^[8]. The table 1 shows the calculated correction factor for each increment of the TKD threshold.

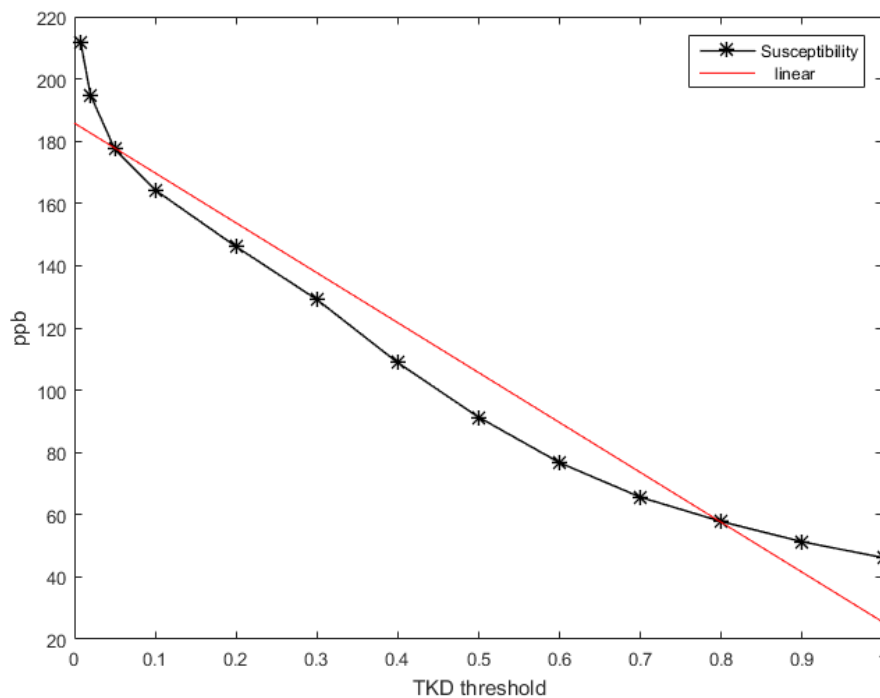
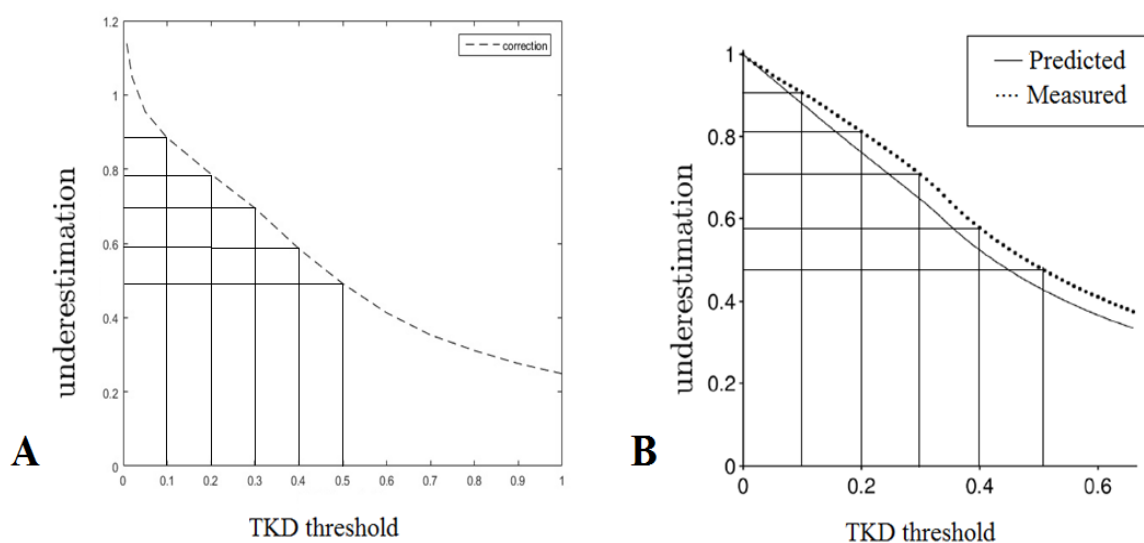


Figure 3.26: Graph depicting changes in susceptibility measured in the blood vessels within the liver as the TKD threshold is increased, and the results of a linear regression performed on the measured values. The y-intercept of the regression indicates the predicted susceptibility value in the ROI when the TKD threshold is 0.



TKD threshold	Underestimation
0.008	1.138798
0.02	1.048383
0.05	0.954739
0.1	0.884237
0.2	0.786287
0.3	0.694796
0.4	0.585544
0.5	0.491362
0.6	0.412787
0.7	0.353049
0.8	0.31107
0.9	0.276088
1	0.248641

Figure 3.27: (A) Graph depicting the projected underestimation for each TKD threshold value as calculated from the results of the linear regression. (B) Graph depicting the projected underestimation from Schweser (2013)

Figure 3.28 shows an image from a susceptibility map calculated with an inversion threshold of 0.2, with and without the inclusion of the correction factor. There is an improvement in contrast in the image in which the underestimation has been mitigated. This is confirmed numerically in the graph shown in figure 3.29, which depicts the progression of the mean susceptibility value measured within the blood vessel as the TKD threshold is increased in the corrected and uncorrected susceptibility maps respectively. As expected, the negative correlation between susceptibility values and TKD regularisation threshold has been mitigated.

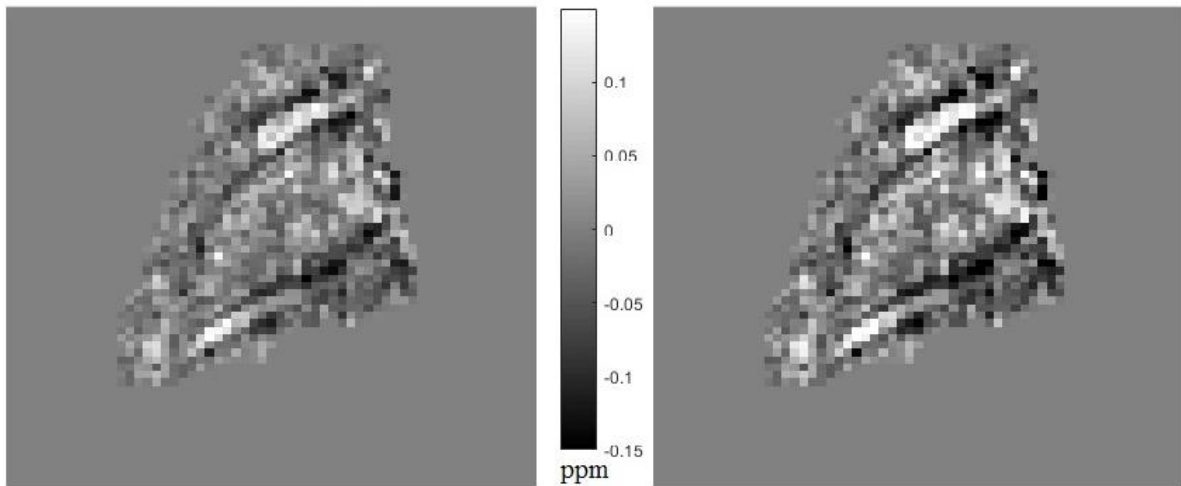


Figure 3.28: Quantitative Susceptibility Maps calculated from identical field maps using TKD inversion. Image on the right has been calculated with algorithm including the correction factor. Note the difference in contrast between the images.

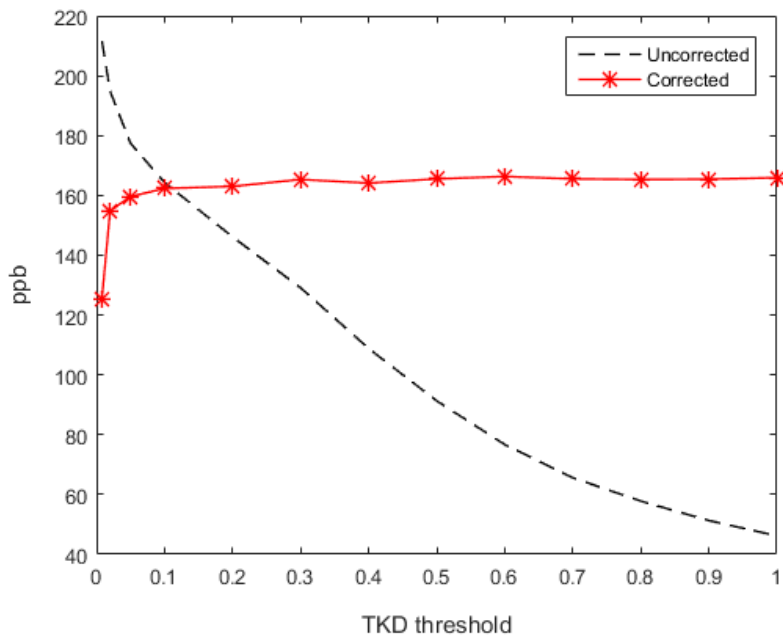


Figure 3.29: Graph depicting the difference in susceptibility values between the corrected and uncorrected images measured in the blood vessel as the TKD threshold is increased.

3.2.5.2: Discussion and Conclusions

While there were no explicitly reported numerical values accompanying the graph in the Schweser et. al. (2013), there appears to be good agreement between the underestimation calculated by both methods. It has been shown previously that the correction factor derived from the curve in the literature can compensate for the systemic underestimation inherent to the TKD algorithm^[8]. This has been confirmed numerically above (figure 3.29).

There are a number of advantages to using the TKD algorithm when calculating a susceptibility map by comparison to other inversion algorithms. For example, it has been shown that iterative inversion methods can take up to several hours to perform the necessary calculations^[34]. The speed of the TKD algorithm means that it is well suited to investigating novel applications of QSM, and it has been shown that the images derived by means of TKD inversion retain the advantages that QSM has over other similar techniques^[34].

While the correction factor derived above shows good agreement with that in the literature, it should also be noted that the underestimation values in the literature were derived by using a multi-orientation (MO) acquisition susceptibility map as a gold standard (i.e. the COSMOS method). While this is a common practice when performing susceptibility mapping, it is known that there are limitations to the accuracy of the images calculated via the COSMOS method (see chapter 2). While no measurement is absolutely perfect, any thorough study that employs TKD must at the very least acknowledge the shortcomings of the algorithm, and would preferably make an attempt to mitigate the problem. As such, the appropriate correction factor as estimated above will be included in the inversion calculation for the experiments performed henceforth. The acquisition and processing factors with which QSM will be performed in the following chapters is contained in table 2 below.

Quantitative Susceptibility Mapping is a rapidly developing, and relatively new field of research which can broadly be split into two main groups – those that seek to improve the accuracy of the processing pipeline, and those that endeavour to discover new applications. As with any field of research, both pathways will develop in tandem, informing and encouraging each other. The work carried out hence is of the latter variety.

Acquisition		
	Parameter	Value
	B_0 (T)	9.4
	TR (ms)	1000
	TE (ms)	4
	FA	70
	FOV (mm)	TBC (as discussed)
	Matrix	TBC (as discussed)
	Vox (μm)	200 isotropic
	BW (kHz)	50
	#avg	TBC (as discussed)
Processing		
Algorithm	Variable	Value
SHARP	TSVD Threshold	0.4
SHARP	Mask Erosion	X 3
TKD	TKD threshold	0.2
TKD	Algorithm Correction Factor	185.81 ppb

Table 2: Summary of empirically derived acquisition and processing parameters that will be used for the remainder of the experimental work presented in this thesis

References

1. Bernstein, M.A., K.F. King, and X.J. Zhou, *CHAPTER 10 - CORRECTION GRADIENTS*, in *Handbook of MRI Pulse Sequences*. 2004, Academic Press: Burlington. p. 292-362.
2. Levene, A.P., et al., *Quantifying hepatic steatosis – more than meets the eye*. *Histopathology*, 2012. **60**(6): p. 971-981.
3. Sharma, P., et al., *Measurement of liver fat fraction and iron with MRI and MR spectroscopy techniques*. *Diagn Interv Radiol*, 2014. **20**(1): p. 17-26.
4. Sharma, S.D., et al., *MRI-based quantitative susceptibility mapping (QSM) and R2* mapping of liver iron overload: Comparison with SQUID-based biomagnetic liver susceptometry*. *Magnetic Resonance in Medicine*, 2017. **78**(1): p. 264-270.
5. Xie, L., et al., *Quantitative susceptibility mapping of kidney inflammation and fibrosis in type 1 angiotensin receptor-deficient mice*. *NMR Biomed*, 2013. **26**(12): p. 1853-63.
6. Hsieh, M.C., et al., *Investigating hyperoxic effects in the rat brain using quantitative susceptibility mapping based on MRI phase*. *Magn Reson Med*, 2017. **77**(2): p. 592-602.
7. Hsieh, M.C., et al., *Quantitative Susceptibility Mapping-Based Microscopy of Magnetic Resonance Venography (QSM-mMRV) for In Vivo Morphologically and Functionally Assessing Cerebromicrovasculature in Rat Stroke Model*. *PLoS One*, 2016. **11**(3): p. e0149602.
8. Schweser, F., et al., *Toward online reconstruction of quantitative susceptibility maps: superfast dipole inversion*. *Magn Reson Med*, 2013. **69**(6): p. 1582-94.
9. Ozbay, P.S., et al., *Effect of respiratory hyperoxic challenge on magnetic susceptibility in human brain assessed by quantitative susceptibility mapping (QSM)*. *NMR Biomed*, 2015. **28**(12): p. 1688-96.
10. Gudbjartsson, H. and S. Patz, *Rician Distribution of Noisy MRI data*. *Magnetic Resonance in Medicine*, 1995. **34**(910 - 914): p. 910.
11. Haacke, E.M., et al., *Quantitative susceptibility mapping: current status and future directions*. *Magn Reson Imaging*, 2015. **33**(1): p. 1-25.
12. Ramasawmy, R., et al., *Separation of arterial and portal blood supply to mouse liver and tumour tissue using pseudo-Continuous Arterial Spin Labelling*. *Proc Intl Soc Mag Reson Med*, 2015. **23**: p. 0532.
13. Marques, J.P. and R. Bowtell, *Application of a Fourier-based method for rapid calculation of field inhomogeneity due to spatial variation of magnetic susceptibility*. *Concepts in Magnetic Resonance Part B: Magnetic Resonance Engineering*, 2005. **25B**(1): p. 65-78.
14. Haacke, E.M., et al., *Susceptibility mapping as a means to visualize veins and quantify oxygen saturation*. *Journal of Magnetic Resonance Imaging*, 2010. **32**: p. 663 - 676.
15. Fan, A.P., et al., *Quantitative oxygenation venography from MRI phase*. *Magn Reson Med*, 2014. **72**(1): p. 149-59.
16. Xu, B., et al., *Flow compensated quantitative susceptibility mapping for venous oxygenation imaging*. *Magn Reson Med*, 2014. **72**(2): p. 438-45.
17. Bakker, C.J.G. and R. de Roos, *Concerning the preparation and use of substances with a magnetic susceptibility equal to the magnetic susceptibility of air*. *Magnetic Resonance in Medicine*, 2006. **56**(5): p. 1107-1113.
18. Yusekevitch, P.A., *ITK-SNAP*. 2015.

19. Liu, C., et al., *Quantitative Susceptibility Mapping: Contrast Mechanisms and Clinical Applications*. Tomography, 2015. **1**(1): p. 3-17.
20. Balassy, C., et al., *Susceptibility-weighted MR imaging in the grading of liver fibrosis- a feasibility study*. Radiology, 2013. **270**(1): p. 149 - 158.
21. Balla, D.Z., et al., *Functional quantitative susceptibility mapping (fQSM)*. Neuroimage, 2014. **100**: p. 112-24.
22. Sun, H. and A.H. Wilman, *Quantitative susceptibility mapping using single-shot echo-planar imaging*. Magn Reson Med, 2015. **73**(5): p. 1932-8.
23. Rauscher, A. and S. Witoszynskij, *Processing Concepts and SWI Filtered Phase Images*, in *Susceptibility Weighted Imaging in MRI*. 2011, John Wiley & Sons, Inc. p. 89-101.
24. Wei, H., et al., *Joint 2D and 3D phase processing for quantitative susceptibility mapping: application to 2D echo-planar imaging*. NMR Biomed, 2017. **30**(4).
25. Peng, X.-G., et al., *Quantification of liver fat in mice: comparing dual-echo Dixon imaging, chemical shift imaging, and 1H-MR spectroscopy*. Journal of Lipid Research, 2011. **52**(10): p. 1847-1855.
26. Shmueli, K., et al., *Magnetic susceptibility mapping of brain tissue in vivo using MRI phase data*. Magn Reson Med, 2009. **62**(6): p. 1510-22.
27. Denk, C. and A. Rauscher, *Susceptibility weighted imaging with multiple echoes*. J Magn Reson Imaging, 2010. **31**(1): p. 185-91.
28. Jenkinson, M., *Fast, automated, N-dimensional phase-unwrapping algorithm*. Magnetic Resonance in Medicine, 2003. **49**(1): p. 193-197.
29. Haacke, E.M., et al., *Establishing a baseline phase behavior in magnetic resonance imaging to determine normal vs. abnormal iron content in the brain*. J Magn Reson Imaging, 2007. **26**(2): p. 256-64.
30. Hammond, K.E., et al., *Development of a robust method for generating 7.0 T multichannel phase images of the brain with application to normal volunteers and patients with neurological diseases*. Neuroimage, 2008. **39**(4): p. 1682-92.
31. Schweser, F., et al., *Quantitative imaging of intrinsic magnetic tissue properties using MRI signal phase: an approach to in vivo brain iron metabolism?* Neuroimage, 2011. **54**(4): p. 2789-807.
32. Yushkevich, P.A., et al., *User-guided 3D active contour segmentation of anatomical structures: significantly improved efficiency and reliability*. Neuroimage, 2006. **31**(3): p. 1116-28.
33. Haacke, E.M., et al., *Susceptibility weighted imaging (SWI)*. Magn Reson Med, 2004. **52**(3): p. 612-8.
34. Wharton, S. and R. Bowtell, *Whole-brain susceptibility mapping at high field: a comparison of multiple- and single-orientation methods*. Neuroimage, 2010. **53**(2): p. 515-25.

Chapter 4

Chapter 4 presents the first implementation of QSM in the mouse liver with the optimised acquisition and data processing protocols. This chapter contains two experiments. The aims of the first experiment were to establish the case for using an external susceptibility reference, to examine a variety of regions of interest in the liver in terms of susceptibility, and to demonstrate the robustness of the acquisition and processing protocols.

The aims of the second experiment were to examine the use of QSM to assess changes in venous oxygen saturation in the portal and hepatic veins, as modulated by a hyperoxic gas challenge. Data was acquired from a cohort of health mice ($n = 10$) under both normoxic and hyperoxic conditions. Susceptibility was measured on QSM images in the aforementioned regions, and was used to calculate the venous oxygen saturation in both. Finally, the values calculated from the susceptibility of the hepatic vein were compared to invasively measured values.

4.1 QSM with optimised pipeline

4.1.1 Introduction

Once it had been ascertained that calculating a susceptibility map of a pre-clinical liver was feasible, data from a small cohort of healthy mice were acquired and processed with the optimised protocols established in the previous chapter. The aim of this experiment was threefold – to establish the case for the use of an external reference against which susceptibility values could be measured; to explore the suitability of various regions of interest from a QSM standpoint; and to demonstrate the robustness of the imaging protocol by examining the precision of the measurements made within a cohort.

4.1.1.1 Susceptibility Reference

Susceptibility mapping is said to be a *semi*-quantitative technique, as the phase (φ) of a GRE signal from which the image is calculated, is equal to:

$$\varphi = \varphi_0 + \gamma B TE \quad [1]$$

where φ_0 is the initial phase value, γ is the gyromagnetic ratio of the protons, B is the local magnetic field, and TE is the echo time. The initial phase value, also referred to as the induction field offset, is an unknown property, and, as such, the values derived from the image are not absolute, so must be discussed as being relative to a reference point common to all images in a dataset.

When performing QSM in the brain it is generally agreed that susceptibility values should be quoted relative to the cerebrospinal fluid (CSF) located in the ventricles^[1], though other references are also used (e.g. white matter). These are imperfect solutions however. In the first instance, it is impossible to quantify intra-subject variability, though it is highly likely that this will be a source of error^[1]. Secondly, reference ROI's are often manually segmented, so can be mistakenly contaminated by values from non-reference tissues (e.g. the choroid plexus^[2]). Furthermore, it has been shown recently that the susceptibility of the reference tissue can be affected by the independent variables of the experimental protocol (e.g. administration of gases^[3]).

Performing QSM in the liver presents challenges for identifying a reference ROI. In comparison to the brain, the liver is an amorphous structure, and is relatively homogeneous. As such it is difficult to select an internal reference that is conspicuous enough not only to be identified repeatedly in the same animal, but is clear and unambiguous in an entire study cohort. This difficulty is compounded by the fact that the anatomical position of the liver results in significant movement over the course of the respiratory cycle.

The solution suggested here is the inclusion of a sample of distilled water in the scanner with each subject (figure 4.1). This has the advantage of being easily identified, eliminates intra-subject and intra-experiment variability, and, although the ROI is still manually segmented, the large homogeneous nature of the sample reduces dramatically the possibility of contamination by human error.

4.1.1.2 Regions of interest

The homogeneous nature of the liver also presents challenges when first attempting to identify regions for examination. Unlike the brain which contains well-defined focal points of accumulated iron (e.g. red nuclei, substantia nigra etc.), there is no clear, recognisable differentiation between regions of the liver. It has been shown previously however that QSM is sensitive to fluctuations in the deoxyhaemoglobin content of blood^[3-5]. As such, it was decided that the most obvious areas to focus on were the major blood vessels of the liver, and a section of liver tissue. The regions of interest that were selected for examination were the Portal Vein (PV), the Hepatic Vein (HV), the Hepatic Artery (HA), and a region of liver tissue that did not contain any obvious blood vessels.

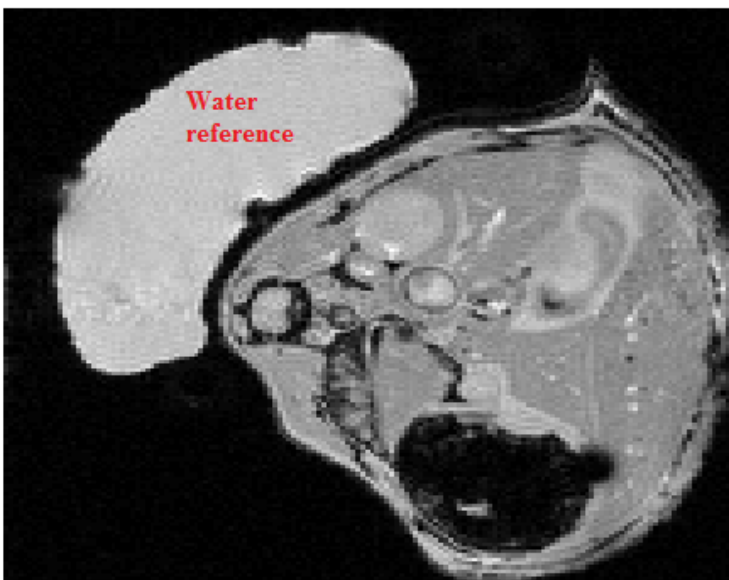


Fig. 4.1: Magnitude image, axial orientation, healthy mouse with water reference.

4.1.1.3 Precision and Robustness

The calculation of a susceptibility map involves processing raw data with a series of complex algorithms, each of which must be optimised according to the requirements of the application and anatomical location. Once the acquisition protocol and processing pipeline had been optimised for use in the pre-clinical liver, it was decided that image quality and the precision of susceptibility measurements must be assessed before the technique could be reliably applied to disease models. As such, data were acquired and susceptibility maps were calculated using the protocols that have been discussed in chapter 3.

4.1.2 Materials and Methods

4.1.2.1 Animal Preparation

All animal studies were performed in accordance with the UK Home Office Animals Science Procedures Act (1986). 5 healthy CD1 mice (female 8 – 12 weeks) were scanned with a 9.4T MRI scanner (Agilent Technologies, Santa Clara, CA, USA) using a 39-mm-diameter bird cage coil for signal transmission and reception (RAPID Biomed, Rimpar, Germany).

Each animal was anaesthetised using 4% isoflurane in 100% O₂. Data were acquired while each subject was administered a mixture of pure O₂ and isoflurane at a rate of 0.5 ltr / min. for the duration of the scan. Respiratory rate was constantly monitored using a pressure pad (SA instruments, Stony Brook, NY USA) and maintained at ~40 - 80 breaths per minute by varying isoflurane concentration between 1.5 and 3%. Rectal temperature was maintained at $37.5 \pm 0.5^{\circ}\text{C}$ using a warm water circulation system.

4.1.2.2 Data Acquisition

The data acquired were single echo, fully first order flow compensated, respiratory gated, T₂*-weighted 2D GRE acquisitions. Scan parameters were as follows:

B₀ = 9.4T, TR = 1000 ms, TE = 4 ms, FA = 70°, Voxel = 200 μm isotropic, bandwidth = 50 kHz, average = 8.

FOV was adjusted to accommodate each animal, and the matrix size was adjusted to ensure the voxel dimensions were as above.

4.1.2.3 QSM processing

Quantitative susceptibility maps were calculated from the raw phase data. A binary mask was manually drawn around the entire liver in each magnitude image using ITK-SNAP^[6]. The corresponding phase data were unwrapped and background field suppression was performed using the SHARP algorithm^[7] (TSVD threshold = 0.04, # mask erode = 3).

Susceptibility inversion was carried out using the Thresholded K-Space Division (TKD) algorithm^[8]. The threshold of the TKD kernel was set to ± 0.2 , such that absolute values outside of this range were set to the threshold value with the appropriate sign depending on the position of the voxel within the kernel. A correction factor of 1.26 (i.e. $1 / 0.786$) was included in the deconvolution operation of the TKD algorithm, as previously discussed. All post processing was performed in Matlab (version 2015b, The Math Works, Natick, MA).

4.1.2.4 External Reference

In order to establish the homogeneity and precision of the measurement taken from the water reference in the susceptibility map, an ROI was manually segmented from each magnitude image using ITK-SNAP^[6]. The standard deviation of the voxels in each ROI was examined, as well as the mean value and SD for the entire set of measurements. For comparison, similar measurements were taken from a region of liver tissue located as far as possible from any large vessels.

4.1.2.5 Regions of interest

Regions of interest were manually segmented on each magnitude image using ITK-SNAP^[6], and corresponded to large branches of the portal vein (PV), the hepatic vein (HV), and the hepatic artery (HA). A segment of liver tissue that was as remote as possible from any large veins was also included for examination.

Each region of interest was identified as follows:

Hepatic vein (figure 4.2 A & B): Branches of the hepatic veins are quite large, and as they carry blood with a high concentration of deoxyhaemoglobin usually appear hypointense on GRE magnitude images. As such, they are relatively easy to identify, and if visually traced through the image volume will connect to the inferior vena cava (IVC), which is itself easily identifiable as the largest vessel in the image.

Portal Vein (figure 4.3 A & B): Branches of the portal vein are smaller than the hepatic vein, and are slightly more difficult to identify. As they are *supplying* blood to the liver, the vessel walls are usually much thicker than those of the hepatic vein, and they can be identified as hyperintense areas on the GRE magnitude image. When visually traced through the image volume they connect to the main branch of the portal vein, which is the second largest vessel in the image, and is located close to the IVC.

Hepatic artery (figure 4.4 A, B & C): The hepatic artery is extremely small with respect to the other vessels, and at the resolution of the images examined here is often the size of a single voxel in the x-y plane. It appears as a small, hypointense dot towards the inferior portion of the image, and can be identified as it branches off the coeliac trunk, located below the liver and perpendicular to the direction of the hepatic artery (i.e. it lies upon the y-axis of an axial image).

It was found that the hepatic artery was more easily identifiable if the magnitude image is inverted (i.e. each voxel is multiplied by -1), such that the vessel appears as hyperintense. During segmentation, image contrast can be manipulated such that the HA can be easily identified and traced through the image volume.

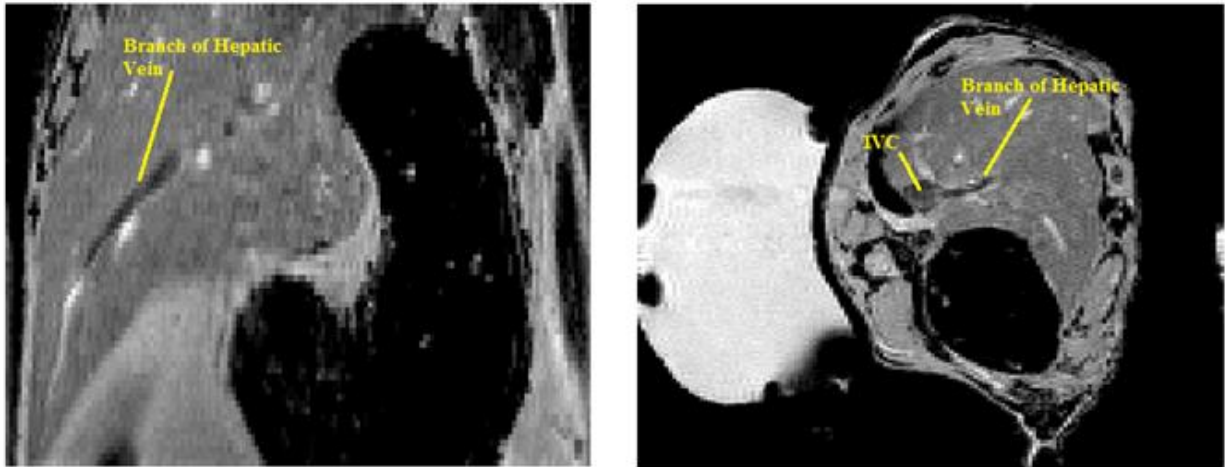


Fig 4.2: Magnitude image of a healthy mouse liver in sagittal (A) and axial (B) orientation, displaying branches of the hepatic vein and the IVC.

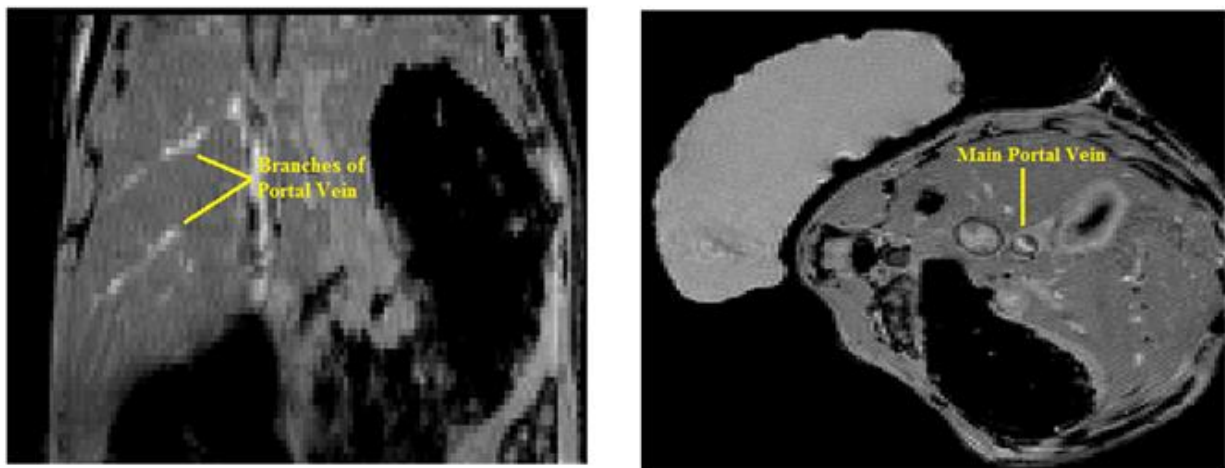
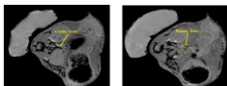


Fig 4.3: Magnitude image of a healthy mouse liver in sagittal (A) and axial (B) orientation, displaying branches of the portal vein and the main portal vein



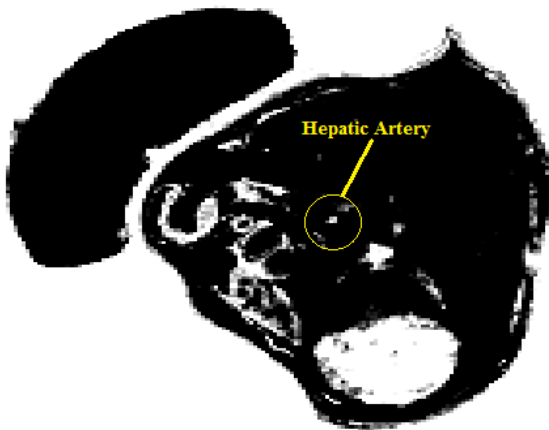
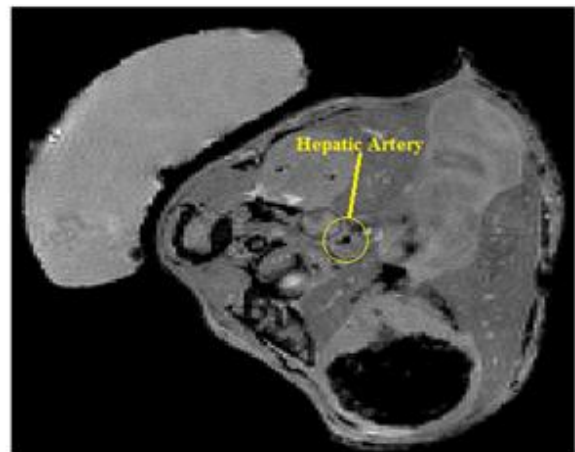
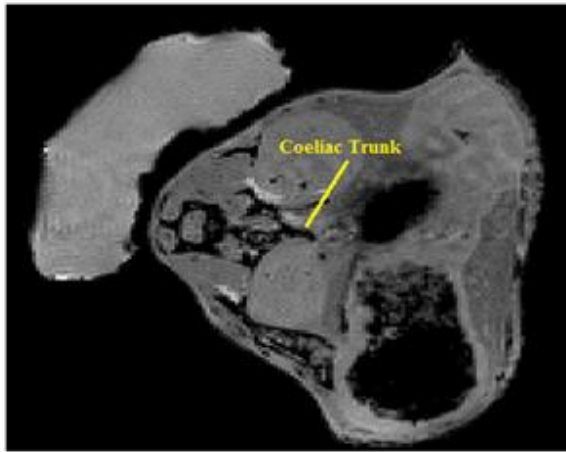


Fig 4.4 A, B & C: Magnitude image of a healthy mouse liver in axial orientation, displaying the coeliac trunk (A), the hepatic artery (B), and an inverted image (C) displaying the hepatic artery as hyperintense with respect to the rest of the liver

4.1.2.6 Precision and Robustness

All images were visually assessed in order to gauge their quality and to detect any artefacts. Magnetic susceptibility was measured in the aforementioned regions of interest, and is quoted as the susceptibility shift with respect to the water sample. Lastly, the standard deviation of each ROI is taken as an indication of the precision of each measurement^[9]. The precision of each measurement will also be the criteria used to gauge the suitability of the regions of interest that have been selected for examination.

In addition to MRI data, histology was performed on a selection of liver samples to assess the iron content of the liver tissue.

4.1.2.7 QSM in blood vessels

Taking measurements from blood vessels can be problematic in QSM images. Gibbs ringing, caused by the under-sampling of high spatial frequencies in the image causes an oscillation of contrast at sharp signal intensity transitions in the image. This is known to happen at the interface between blood vessels and tissue in susceptibility maps. This is depicted in fig 4.5 A ^[10], which shows a 2 dimensional profile plot across a cylinder – representative of a blood vessel - in a numerical phantom. It can be seen that the artefact causes erroneous negative values at the boundary of the object, noted in the study to be up to $\pm 85\%$ of the input susceptibility value. In reality, this manifests as a ring of negative values around blood vessels in a susceptibility map (fig 4.5B).

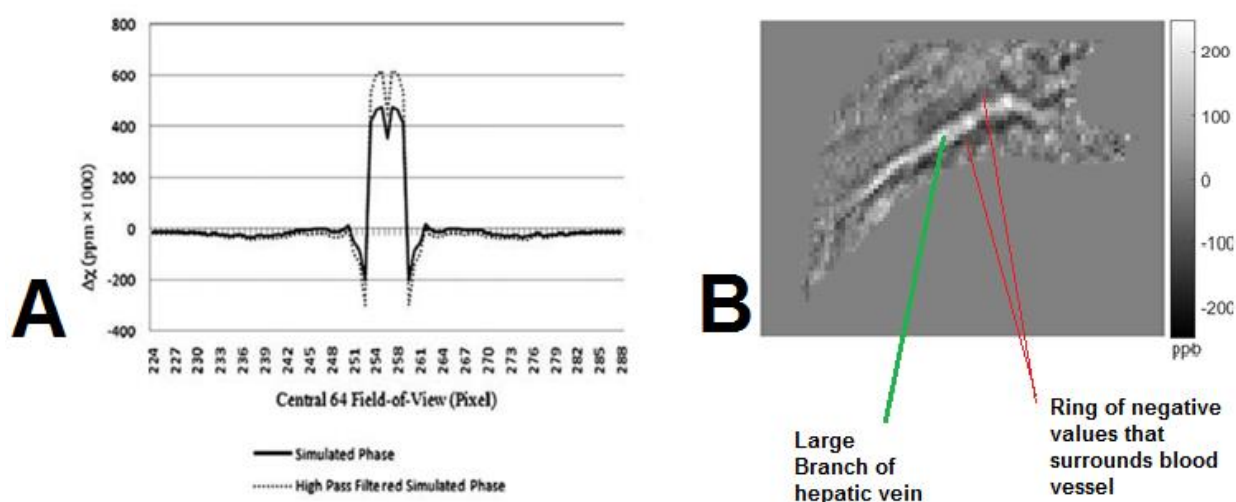


Fig 4.5 A & B: (A) Taken from Haacke et. al. (2010)^[1] Displays the results of a numerical susceptibility phantom that has been subject to inversion. The cylinder in the image represents a blood vessel, and the image demonstrates the artefact that arises due to Gibbs ringing when areas of sharp contrast are inverted. (B) Susceptibility map taken from one of the data sets examined here, depicting a large branch of the hepatic vein featuring the negative susceptibility values that surround it.

The difficulty is compounded by partial volume effects. In the voxels that lie at the vessels boundary, the phase inside and outside the vessel will be integrated across the voxel. In the magnitude image this leads to blood vessels appearing thicker than they are - the so-called “blooming” artefact. This can be problematic when segmenting ROIs within the blood

vessel, and also means that the phase in these voxels will be an inaccurate estimate of the true value.

One solution put forward in the literature is to only accept susceptibility values within blood vessels that are in the top 20th percentile of those within the region of interest^[11], thus reducing the chances that the measured values lie at the border between the blood vessel and tissue, and so confounded by either error. As such, this will be the criteria of acceptance of a measured value within a blood vessel region.

4.1.2.8 Histology

Animals were culled immediately after scanning. Livers were excised and stored in 10% neutral buffered formalin. Standard Perl's iron staining was carried out on livers from three subjects in order to evaluate the iron content of the liver tissue.

4.1.3 Results

4.1.3.1 External Reference

Figure 4.6 shows the mean and standard deviation of the individual measurements taken from the QSM images in regions of the external water reference and liver tissue respectively. As discussed, values measured on a susceptibility map necessitate a reference against which to be measured. As such, the mean values quoted below are themselves meaningless, but the variation measured within each ROI (i.e. SD) gives a measure of the homogeneity of the measured susceptibility within each region, and the SD of the mean values of each ROI within the dataset allows evaluation of the precision of the measurement. The susceptibility measurements made in experiments rely heavily on both of these parameters. Inhomogeneities brought about by the acquisition or processing procedures will introduce noise in subsequent measurements. As the expected changes are of the order of parts per billion, erroneous variation could obscure changes in susceptibility that are indicative of experimentally dependent variables. Equally, imprecise measurements could undermine differences between cohorts.

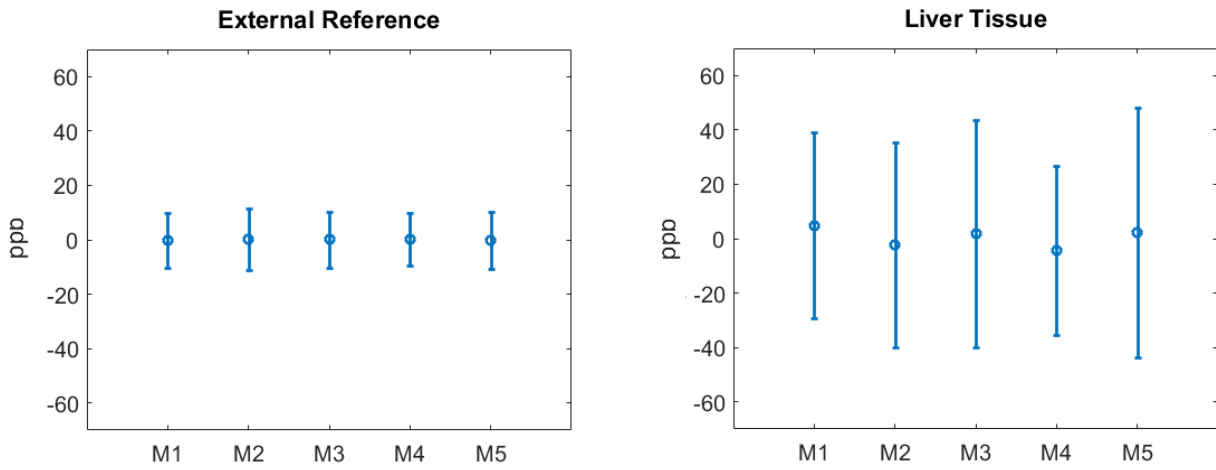


Fig 4.6: Comparison of the standard deviation of susceptibility measurements measured in regions of the external water reference (left) and liver tissue (right). This is given as a measure of the homogeneity of the values in each region.

The values taken from the water reference in each image are -0.0319 ± 10.1 ppb, 0.0254 ± 11.3 ppb, 0.0356 ± 10.3 ppb, 0.1950 ± 9.6 ppb, -0.1860 ± 10.6 ppb. Conversely, the values taken from the liver tissue are 4.8663 ± 34.17 ppb, -2.0963 ± 37.65 ppb, 2.0269 ± 41.8 ppb, -4.2519 ± 30.98 ppb, 2.2597 ± 45.8 ppb.

Figure 4.7 shows the mean and standard deviation of the above values. The standard deviation is quoted as a measure of the precision of the measurement. The mean and standard deviation of the values are 0.0076 ± 0.1372 ppb, and 0.5609 ± 3.66 ppb for the water and liver ROIs respectively.

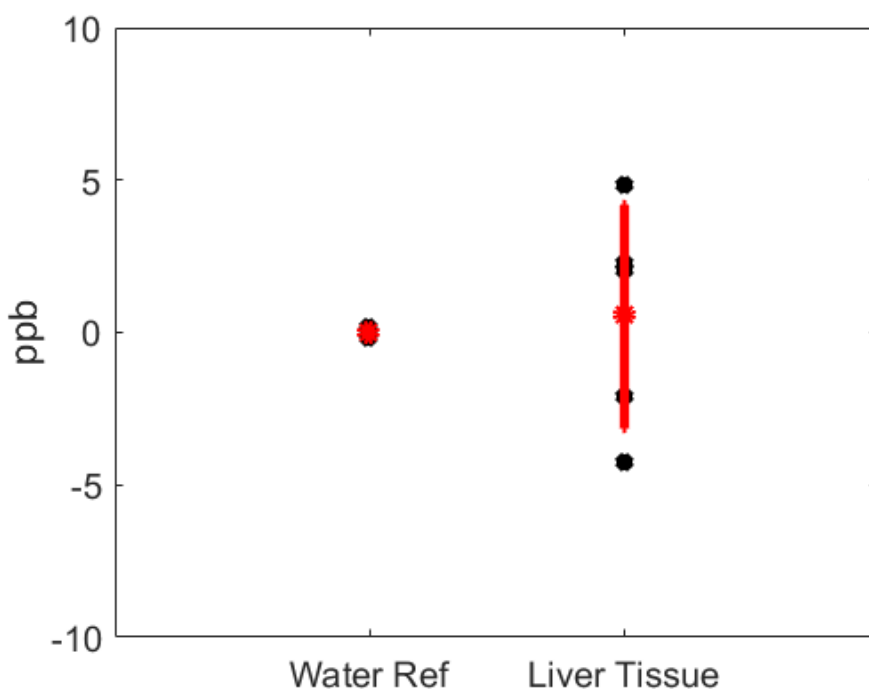


Fig 4.7: Comparison of the standard deviation of the mean susceptibility values measured in the water reference and liver tissue. This is given as a measure of the precision of the measurement. There is greater variation in the values measured in the liver tissue, assumed to be due to compositional variation between subjects.

4.1.3.2 Precision and Robustness

Figure 4.8 shows representative slices of the magnitude (A), raw phase data (masked for display purposes, such that only the liver is visible in the FOV) (B), frequency map (C), and susceptibility map (D). The images are from the dataset of a single subject.

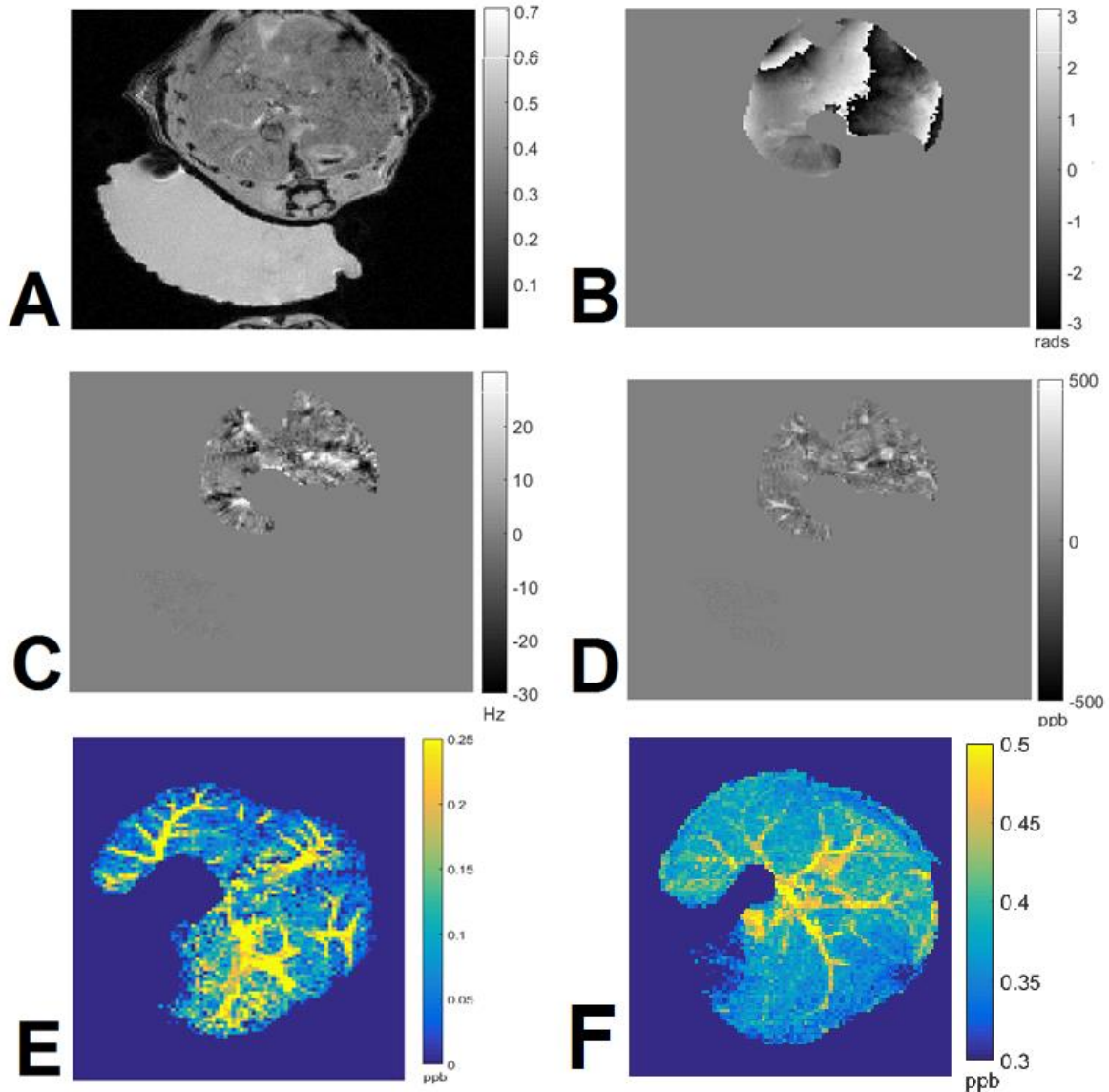


Fig 4.8 A- F: Representative images taken from the dataset of one subject. All images are taken from the same region. (A) T₂*-weighted magnitude image. (B) Raw phase data (masked for display purposes). (C) Frequency map. (D) Susceptibility map. (E) Maximum Intensity Projection (MIP) of susceptibility map (12 slices, 2.4 mm segment). (F) MIP of magnitude image taken from same region as (E).

All images were visually inspected at each point in the processing pipeline. Inspection of the magnitude and raw phase images showed that the data had been successfully reconstructed. Furthermore, there were no obvious artefacts in the phase data that indicated any phase distortions or inconsistencies which may have had a negative impact of the subsequent processing steps. Inspection of the field map (C) showed that the SHARP algorithm had successfully unwrapped the raw phase data, and that the background field had been removed to an adequate degree. Again, there were no obvious artefacts that would have had a negative impact on the inversion calculation. The susceptibility map was inspected upon completion of the inversion. The streaking artefact was minimal, and there were no obvious signs of artefacts or excessive noise which may have influenced the images or the quantitative values that were to be measured. This procedure was carried out for the data from all subjects.

Once it had been ascertained that the calculation of the susceptibility map had been successful, a maximum intensity projection (MIP) of a region of the susceptibility map (12 slices, 2.4 mm segment, coronal orientation) was composed is displayed in figure 4.8 E. To allow a comparison of the information offered by susceptibility maps and magnitude data, a MIP over the same region of the magnitude image is shown in figure 4.8 F.

In order to demonstrate the precision of the quantitative measurements taken from the images, as well as the suitability of the regions of interest, the mean susceptibility and standard deviation of each set of measurements are displayed in figure 4.9. Values from each region are quoted as relative to the water reference. Mean values in each region were as follows: PV: 226.4 ± 65.44 ppb, HV: 293.33 ± 46.92 ppb, HA: 274.4 ± 188.9 ppb, tissue: 0.55 ± 3.79 ppb.

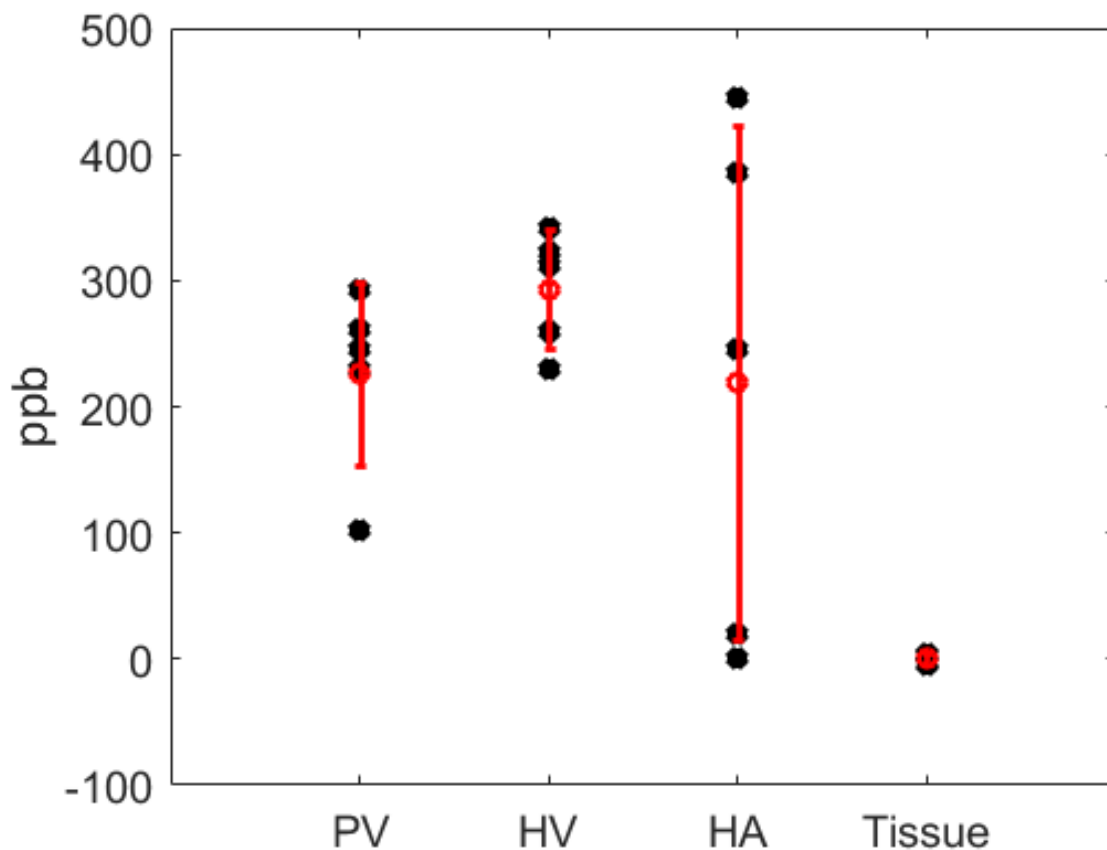


Fig 4.9: Graph displaying mean susceptibility values and standard deviation measured in each of the regions of interest. The variation in measurements from each region are used as a criteria by which to gauge the suitability of the region for examination

Figure 4.10 shows a series of representative images of a histological sample at increasing magnification. Also included for comparison is a reference image from the literature that has been subject to the same stain^[12]. The reference image is taken from a mouse model of haemochromatosis, a disorder that is characterised by excess iron deposition in the liver parenchyma. The difference in terms of iron deposition between the healthy and reference images is quite pronounced, to the extent that the healthy samples contain very little iron by comparison.

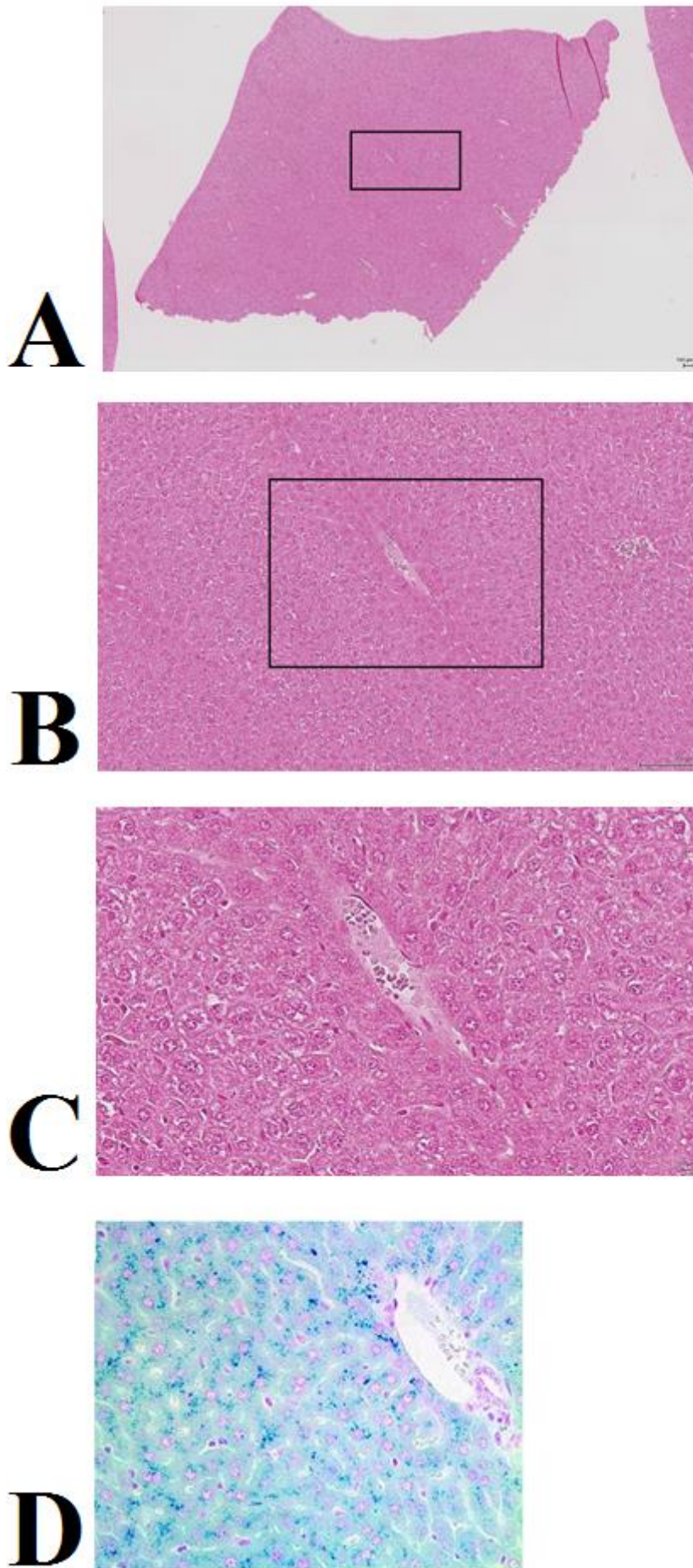


Fig 4.10 A - D: Representative images of histological samples from healthy mouse livers subject to Perl's iron stain. Images are from the same sample displayed at increasing magnification – x2.43 (A), x13.35 (B), and x35.15(C). Also included is a reference image from the literature to allow comparison to an iron overloaded image (D). It should be noted that there is a marked difference in the staining of the healthy and reference samples

4.1.4 Discussion

The variability of the reference against which susceptibility is measured in QSM experiments is often not discussed in the literature, however it is widely acknowledged that there will be a degree of variability between subjects, and even individual scans. It has been shown recently that the variability of the reference value depends on the reference tissue that is chosen. In the (human) brain, CSF has been shown to have the smallest variability (mean susceptibility 10 ± 14 ppb), while in the same study, the mean susceptibility of the white matter ranged from 6 ± 20 ppb to 28 ± 23 ppb depending on the location in which it was measured^[1]. As such, standardisation of the susceptibility reference is an important factor when trying to maximise the benefit of the quantitative nature of QSM.

In that regard, the external reference used in this experiment was a successful inclusion to the experimental set-up. As discussed in the literature, the reference against which susceptibility is measured should be independent of experimental variables, easy to depict and delineate, and easily identifiable across a wide range of subjects^[1]. The external reference meets all of the criteria. Furthermore, the sample displays excellent homogeneity and precision when compared to the liver tissue as measured here, but also by comparison to the CSF measurement in the study cited above.

The inclusion of the reference into the set-up is extremely simple; however the drawback is that the FOV must be increased to accommodate its inclusion in the image. This should not present too great a problem however - the sample used here was quite large relative to the subject but could easily be made smaller depending on the constraints of the experiment. While the CSF may be a suitable reference when performing cerebral QSM in humans, the expansion of the field into abdominal imaging will require the use of an easily identifiable reference that gives rise to repeatable measurements. The external water reference included here provides one possible solution.

The images displayed in figure 4.8 exemplify the steps taken to calculate a susceptibility map, and the rigour of the inspection of the images that takes place at every point during the process. Improper reconstruction of the images can result in aberrations in the raw phase data such as open-ended fringe lines which are detrimental to the unwrapping process, thus undermining the final susceptibility map. Equally, the frequency maps that are the result of the SHARP algorithm must be inspected for any residual phase wraps, background field contributions or edge effects that would introduce excessive noise in the

final susceptibility map. Finally, the susceptibility map is inspected for any artefacts that may have occurred during the inversion, including excessing streaking which may undermine the measurements taken from the images. The purpose of performing this experiment was to discern whether the protocols that were optimised in the previous chapter could be applied to a number of datasets such that high quality susceptibility maps could be calculated repeatedly and consistently. In that regard the exercise was a success.

The blood vessels displayed in 4.8 (E) are the hepatic veins. Hepatic veins carry a relatively high proportion of deoxyhaemoglobin so are paramagnetic, and, hence, hyperintense with respect to the liver tissue. As such, they feature prominently on the MIP of the susceptibility map. Conversely, the portal veins are hyperintense relative to the surrounding liver tissue due to the thickness of the vessel walls (as discussed sec. 4A.2.5). As such, the portal veins feature more prominently on the MIP of the magnitude image. This shows that susceptibility mapping can provide information that is not available on a standard GRE magnitude image.

The susceptibility of the blood in the hepatic vein is more paramagnetic than that in the portal vein (fig. 4.9), which is indicative of the fact that the blood being carried away from the liver (i.e. in the hepatic vein) contains a higher concentration of deoxyhaemoglobin than the blood entering the liver. It was expected that the difference in susceptibility between the two on this basis would have been more pronounced, but this may be because the blood in the portal vein already contains an appreciable concentration of dHb, having already passed through the gut and mesentery. Furthermore, the blood in the HV contains a mixture of contributions from the portal and hepatic veins, so trying to predict a relationship between the portal and hepatic vein without considering the hepatic artery may be difficult.

The susceptibility of the blood in the hepatic artery appears more paramagnetic than that in the portal vein. This was not expected, as arteries carry richly oxygenated blood. As such, it is expected that the susceptibility of the arterial blood would register as diamagnetic with respect to that in the portal vein. As mentioned above, the hepatic artery is an extremely small vessel, with a diameter that is often the size of a single voxel under this imaging protocol. As such, it may be the case that partial volume effects at the edge of the vessel – unavoidable at the resolution of the images – may have resulted in erroneous values with relatively large variation between subjects.

It would be an interesting experiment in any future work that lead on from this thesis to attempt to use the aorta as a reference against which to measure the susceptibility of the large hepatic veins. Given the linearity of the relationship between susceptibility and blood deoxyhaemoglobin content this may allow the calculation of a decrease in blood oxygen concentration without the use of an external standard. This would however necessitate the assumption that the blood in the aorta was 100% oxygenated, which may not be the case in each animal, and so could introduce systematic errors. Furthermore, measuring the susceptibility in the aorta would require both cardiac and respiratory gating, thus introducing additional complexity into both data acquisition and image reconstruction, as well as increasing the required scan time for each subject.

The magnetic susceptibility of the tissue is almost identical to that of the water reference. It was expected that the iron in the liver would have resulted in the liver tissue registering as paramagnetic with respect to water, but as is indicated by the histology it would appear that there is very little iron present in the livers of the subjects examined. Taking this into consideration it is conceivable that the liver tissue is of roughly the same susceptibility as water, as that will be the main magnetically active constituent of the organs composition. An interesting proof of concept experiment would be a comparison between the susceptibility measured in the liver tissue of healthy subjects and those from a disease model that resulted in liver iron overload (e.g. haemochromatosis). The lack of availability of such a model in our lab would have required implementing the disease model ourselves, requiring ethical and licensing approval, and as such was outside of the realistic time limits of the PhD. This could however be considered as an experiment in future, now that QSM acquisition and processing pipelines are established for use in a pre-clinical model.

The precision of the measurements across the cohort is illustrated by the standard deviation in each ROI. This is taken as an indication of the suitability of each region for examination with QSM under the imaging protocol employed here. The SD of the measurements in the portal and hepatic veins are lower than that in the hepatic artery. Again, this is due to the size of the various ROIs, and the ease with which they can be segmented. The PV and HV are much larger, and values can be quoted with a greater degree of confidence that the measurements are not contaminated by values from outside the intended ROI, or are affected by partial volume effects that are present at the vessel wall. This is not possible with the HA, and is reflected in the relatively high standard deviation of the measurement across the cohort. Based on the results presented here, it appears that the HA is

not a suitable region of interest for study under this imaging protocol. It may be possible if the resolution of the images was increased, but this would come at a cost to scan time and/or SNR.

The robustness of the experimental protocol would have benefitted from scanning the same mouse a number of times in succession, and measuring the susceptibility in the same area to assess the repeatability of the measurement. This is difficult in the liver however, as it moves and it's amorphous nature makes it difficult to examine precisely the same region again and again. This difficulty could have introduced systematic errors into the measurement and undermined the exercise.

4.1.5 Conclusion

The water reference that accompanied each animal in the scanner was a successful addition to the imaging protocol. It provided a robust reference point against which to measure the susceptibility values, it was easily identifiable each image, and as it is external was not influenced by the experimental protocol. As such it will be included in all of the data sets examined hence.

It is shown above that it is possible to calculate high quality susceptibility maps of a healthy pre-clinical liver that allows repeatable measurements in a number of differentiable regions. Based on the evidence presented herein, it is shown that the portal and hepatic veins, as well as the liver tissue are suitable regions for examination under this imaging protocol, however the hepatic artery is not.

4.2: Hyperoxic Gas Challenge

4.2.1 Introduction

It was shown in the previous section that it is possible to use Quantitative Susceptibility Mapping to estimate the magnetic susceptibility of blood in large branches of the liver vasculature. It was also shown in figure 4.8 (E) that hepatic veins feature more prominently than portal veins on MIPs of QSM images. The reason for this is that as the blood passes through the liver, oxygen is being metabolised, meaning the deoxyhaemoglobin content of the blood is higher as it leaves the liver through the hepatic vein. The susceptibility of the blood is linearly related to its deoxyhaemoglobin content^[1], which, in turn, is indicative of the oxygen content of the blood.

The assessment of venous blood susceptibility using QSM has been the focus of several studies in recent years, as the measurement can be used to calculate Venous Oxygen Saturation (SvO_2)^[2-4]. Studies have been performed in both pre-clinical^[4] and clinical scenarios^[2, 3]. It has been shown that QSM is sensitive to changes in deoxyhaemoglobin brought about by a hyperoxic gas challenge^[3, 4], can be used to measure the Cerebral Metabolic Rate of Oxygen Consumption ($CMRO_2$)^[1], and can even quantify *regional* venous oxygenation in the brain^[2]. To date however, all of the work has been carried out in the cerebral vasculature. It is the hypothesis explored here that this can be extended to the liver.

Hepatic Venous Oxygen Saturation ($ShvO_2$) is an indicator of the hepatic oxygen supply-demand ratio^[5], and has been the focus of a number of studies. Several in particular have investigated $ShvO_2$ in patients that have undergone surgical procedures, as this may have important implications for their postoperative care^[6]. For instance, it was found that after Fontan operations – a palliative procedure performed on children – monitoring $ShvO_2$ in the immediate post-operative period could predict the occurrence and severity of subsequent acute liver dysfunction^[7]. Furthermore, it was shown in a preclinical study that $ShvO_2$ in rats that have undergone partial hepatectomy could be used to gauge the regeneration status of the remnant portion^[6, 8].

Previously, measurement of $ShvO_2$ has been performed invasively by means of catheterisation. This increases the risk of infection and thrombosis, making it unsuitable for some patients. Quantitative Susceptibility Mapping may offer the ability to assess $ShvO_2$

non-invasively, which could have a positive impact on the post-operative care and assessment of those who have undergone treatment.

To test the hypothesis, a hyperoxic gas challenge was administered to a cohort of healthy mice, such that the deoxyhaemoglobin content of the blood was manipulated in a controlled fashion. Susceptibility was measured in a large branch of the hepatic vein in each subject under both normoxic and hyperoxic conditions. Susceptibility measurements were then used to calculate $ShvO_2$ under each condition. Magnetic susceptibility and SvO_2 were also measured and calculated respectively in a branch of the portal vein, as it is expected that the differences brought about by the gas challenge will also manifest here. The magnitude of the change brought about by the gas challenge should be the same in both blood vessels provided the rate of oxygen metabolism remains the same under each condition. This is assumed to be the case. Finally, venous oxygenation was measured invasively in the inferior vena cava in order to provide validation for the calculations.

4.2.2 Theory

4.2.2.1 Magnetic susceptibility of blood

The magnetic properties of the haemoglobin molecule are dependent on its oxygenation state^[9]. Haemoglobin consists of 4 globin subunits, each of which contains a haem molecule consisting of iron (Fe(II)) surrounded by a porphyrin ring^[10]. Both molecular O_2 and Fe(II) contain unpaired electrons, and as such are paramagnetic. When Oxygen binds to haemoglobin however, the product is a singlet state with an equal number of spin up and spin down electrons, and so is diamagnetic. Upon dissociation both revert to their previous state, and are once again paramagnetic^[11].

Venous blood oxygen saturation is, effectively, the percentage of haemoglobin binding sites that are occupied, and so is directly measurable by susceptometry. While there is also a small amount of O_2 dissolved in the plasma (~2% under resting conditions), and it is possible for carbon-monoxide to bind to haemoglobin, these are negligible under normal circumstances, and so have little impact on the overall susceptibility of the blood. Carbominohaemoglobin – the compound that forms when CO_2 binds to haemoglobin, accounting for ~10% of CO_2 transported by the blood – is also paramagnetic, so will not result in an underestimation of $ShvO_2$.

4.2.2.2 Calculating ShvO₂

The susceptibility difference between blood and water can be related to SvO₂ by the following:

$$\Delta\chi_{\text{blood} - \text{water}} = \Delta\chi_{\text{do}} \cdot \text{Hct} \cdot (1 - \text{SvO}_2) \quad [1]$$

where $\Delta\chi_{\text{do}} = 2.26$ ppm (SI) is the difference in susceptibility between fully oxygenated and deoxygenated blood^[12], and Hct is the fraction of blood composed of haematocrit, assumed in this instance to be 0.4^[4].

In the study cited above the equation relates SvO₂ to the susceptibility shift between the vein and surrounding tissue. As shown in the previous section the difference in susceptibility between liver tissue and the water reference is negligible, but as the water reference is less likely to be confounded by inter-subject variability, all calculations will be performed using the water sample as the reference point.

4.2.3 Methods

4.2.3.1 Animal Preparation

All animal studies were performed in accordance with the UK Home Office Animals Science Procedures Act (1986). 10 healthy CD1 mice (female 8 – 12 weeks) were scanned with a 9.4T MRI scanner (Agilent Technologies, Santa Clara, CA, USA) using a 39-mm-diameter bird cage coil for signal transmission and reception (RAPID Biomed, Rimpar, Germany).

Gasses were administered through a nose cone at a rate of 0.5 ltr/min. Images were acquired under normoxic conditions as the subject was administered medical air (21% O₂/balance Nitrogen), and again under hyperoxic conditions as the subject was administered 100% O₂. 10 minutes were allowed between gasses to allow the animal to acclimatise. All other animal preparation was as discussed in chapter 4.1.

Data acquisition, QSM processing and ROI segmentation were all performed as discussed previously.

4.2.3.2 Blood Gas Measurement

In order to quantify the degree of hyperoxia induced by the gas challenge, blood gases were measured invasively in 3 mice with a blood gas analyser. Mice were anaesthetised and blood was extracted from a portion of the inferior vena cava (IVC) within the liver, under ultrasound guidance. The procedure was carried out under normoxic and hyperoxic conditions for each mouse. Data were acquired on a RAPIDLab 348EX blood gas system (Siemens), and 10 minutes were allowed following a change in administered gas to allow the animal to acclimatise before sampling. Samples were transferred from the syringe to a 2 μ l heparinised glass tube, and then to the blood gas analyser.

4.2.3.3 Statistical Analysis

Parameter estimates were compared using a Wilcoxon matched-pairs signed rank test, in which a difference was considered statistically significant for $p < 0.05$.

4.2.4 Results

Figure 4.11 depicts an array representative images from a single subject. Shown are a single slice of the magnitude, the corresponding raw phase (masked for display), the frequency map, and the susceptibility map. Each image depicts the same slice from each image. Both normoxic (left column) and hyperoxic (right column) states are shown.

In the magnitude images (A & B) the hepatic veins feature less prominently on the hyperoxic images. The reason for this is that the administration of pure O_2 reduces the deoxyhaemoglobin content of the blood. This in turn reduces T_2^* dephasing and associated signal loss. Additionally hyperoxia is known to have a vasoconstrictive effect, so it may also be the case that the blood vessels themselves are less dilated. There were no obvious artefacts in any of the magnitude images that would have indicated adverse conditions for performing susceptibility mapping.

The phase images (C & D) acquired under either state are very similar to each other – both contain the same number of phase wraps, which appear in broadly the same place in the image. Again there was no indication of phase inconsistencies (e.g. broken phase wraps) that

may have indicated improper data reconstruction or uncompensated blood flow artefacts which may impact negatively on the susceptibility maps.

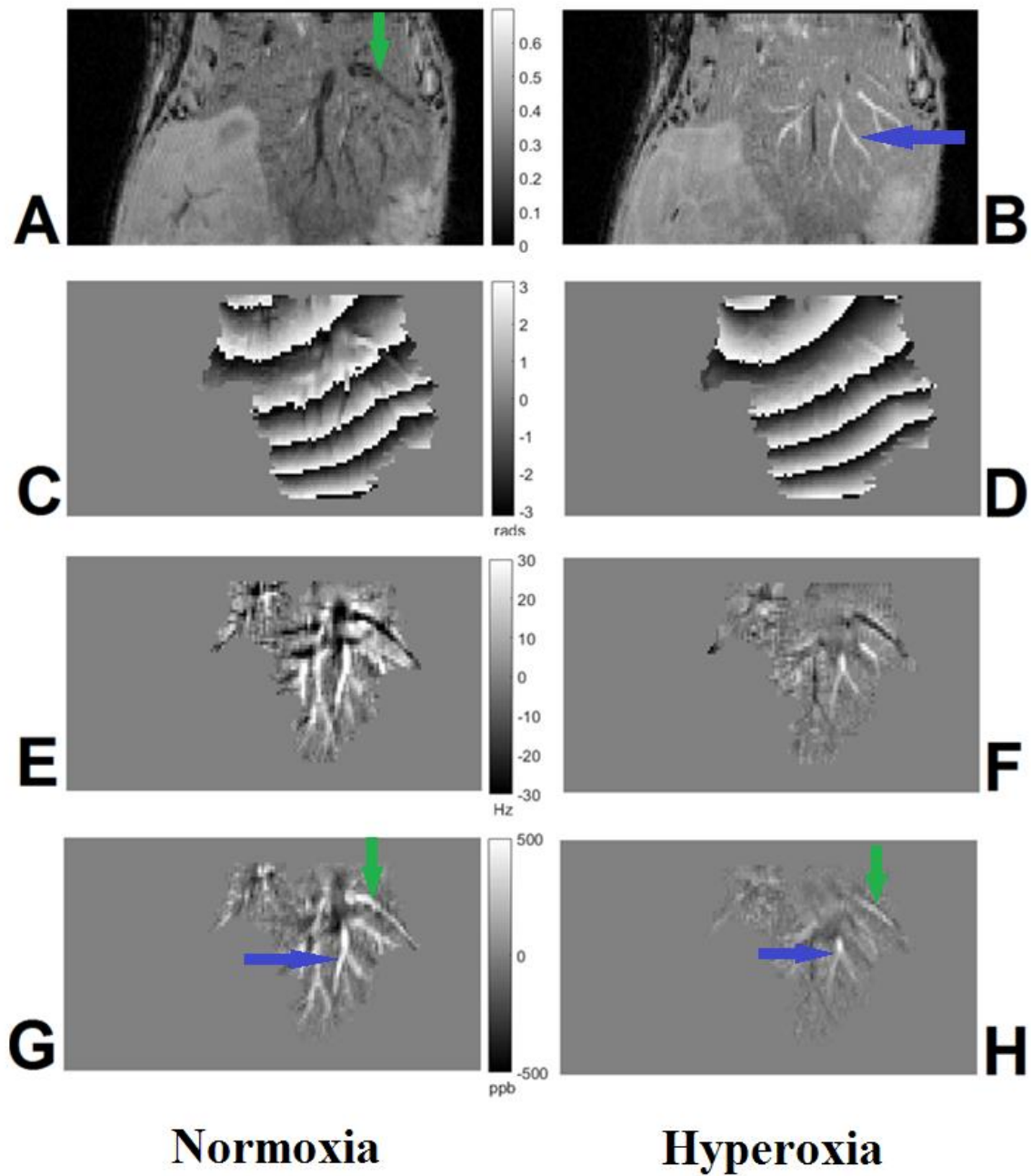


Fig 4.11 A - H: Magnitude images (A, B), raw phase (C, D), frequency maps (E, F) and susceptibility maps (G, H) from data acquired under normoxic and hyperoxic conditions. Both portal and hepatic veins feature on the QSM images (blue and green arrows respectively), while only the hepatic vein appears on the normoxic magnitude image and only the portal vein appears on the hyperoxic magnitude image.

The frequency maps calculated from the raw phase data are depicted in E & F. Blood vessels appear more prominently in the normoxic image (E), than in the hyperoxic image. This is due to the fact that the greater deoxyhaemoglobin content of the blood under normoxic condition causes a greater perturbation of the B_0 field, resulting in a more prominent manifestation on the phase image. The bright and dark areas which are particularly obvious in (E) are the characteristic dipole patterns of susceptibility variations on phase images, and exemplify the orientation dependence and non-local contrast of phase imaging.

The normoxic and hyperoxic susceptibility maps are shown in images (G) and (H) respectively. As expected, the blood vessels feature more prominently on the normoxic image. Interestingly, branches of both the portal vein (blue arrows) and hepatic vein (green arrows) are visible on the QSM images, whereas on the magnitude images, the hepatic vein is only prominent on the normoxic image, and the portal vein is only prominent on the hyperoxic image. There were no obvious artefacts on the susceptibility maps.

The change in susceptibility brought about by the gas challenge is highlighted in figure 4.12, which features maximum intensity projections of a segment of the susceptibility maps (11 slices, 2.2 mm segment.) As expected, the blood vessels appear more prominently on the normoxic image.

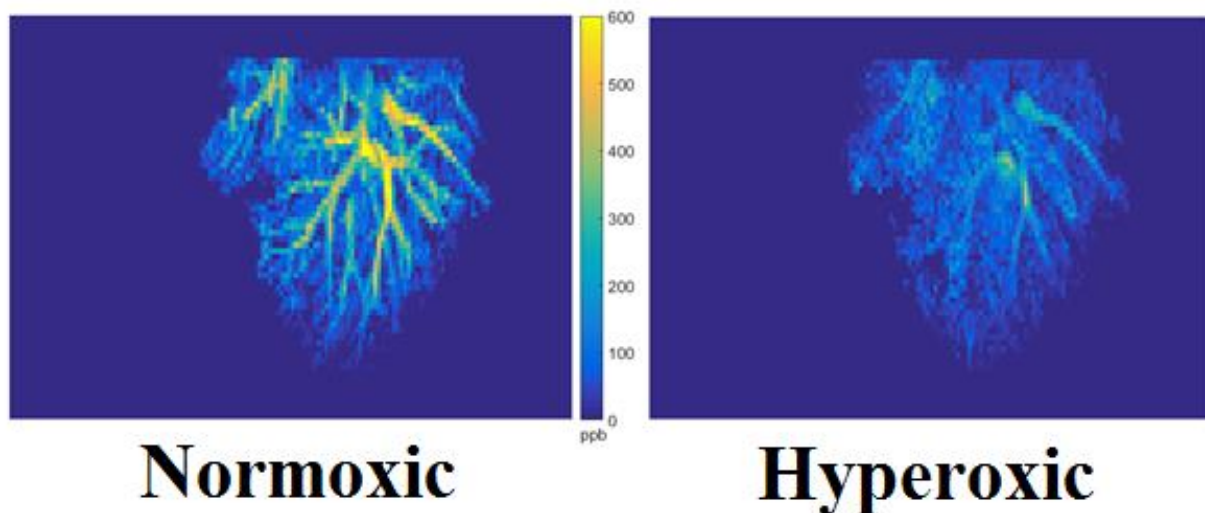


Fig 4.12: Maximum Intensity Projections over 2.2 mm segment of a representative mouse liver under normoxic and hyperoxic conditions. Large branches of the hepatic and portal veins are clearly visible in each image. Note that the vessels are brighter with respect to the liver tissue in the normoxic image compared with the hyperoxic image, indicating a more paramagnetic susceptibility. This is due to the increased concentration of deoxyhaemoglobin in the blood under normoxia.

Figure 4.13 illustrates the changes in magnetic susceptibility in the hepatic (A) and portal (B) veins under both normoxic and hyperoxic conditions respectively. A significant diamagnetic shift in mean susceptibility ($p < 0.01$) was detected in the hepatic vein under hyperoxic conditions. Susceptibility decreased from 427.9 ± 161.2 ppb to 234.5 ± 80.5 ppb under normoxic and hyperoxic conditions respectively. Similarly, the mean susceptibility in the portal vein decreased significantly from 383.6 ± 134.3 ppb under normoxia to 248.7 ± 161.8 ppb under hyperoxia ($p < 0.05$).

A significant increase in venous oxygen saturation was detected in both vessels under hyperoxic conditions. This is depicted in figure 4.14. In the hepatic vein (A), mean $ShvO_2$ increased by 21.39% from $52.67 \pm 17.83\%$ to $74.06 \pm 8.9\%$ ($p < 0.01$), and in the portal vein (B) $SpvO_2$ increased by 14.93% from $57.57 \pm 14.85\%$ to $72.5 \pm 17.9\%$.

Figure 4.15 shows a comparison of $ShvO_2$ as calculated from the QSM data, and the blood gas measured invasively via the IVC. The invasive measurement showed a mean increase of 26.14% in blood oxygenation, from $52.83 \pm 9.78\%$ to $78.97 \pm 11.45\%$. The difference was not statistically significant.

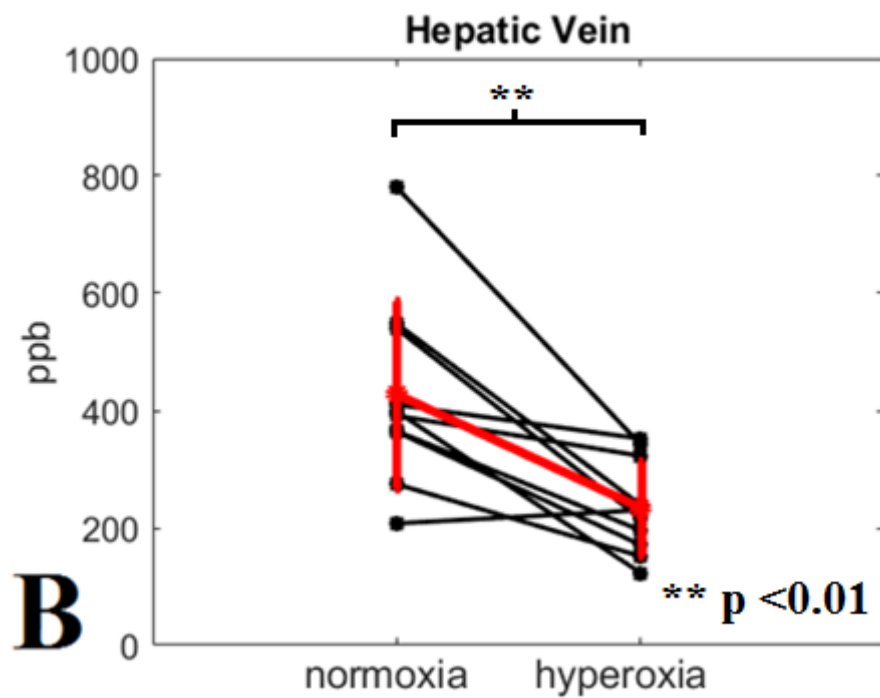
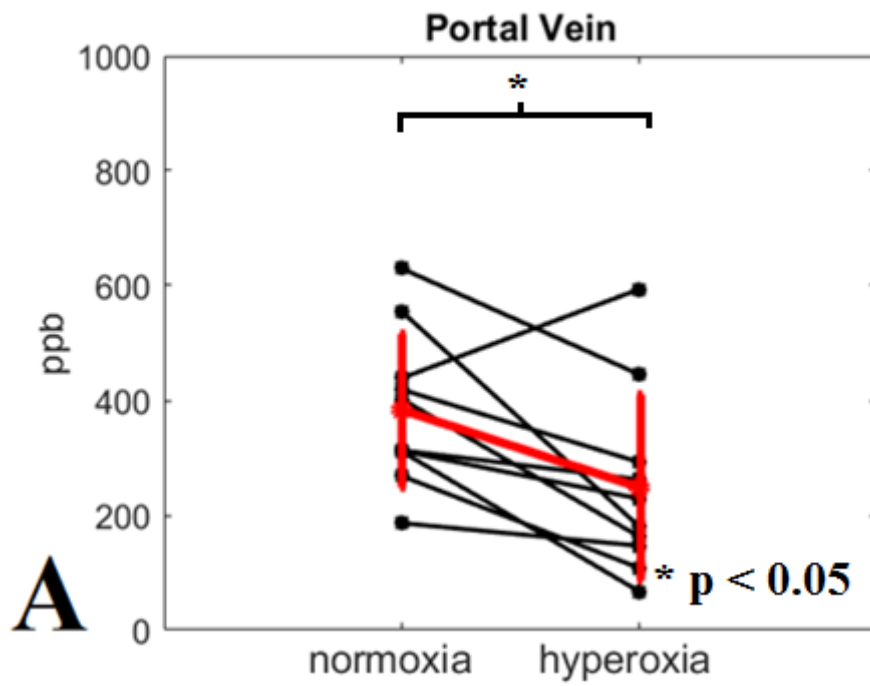


Fig 4.13 A & B: Graphs showing the change in susceptibility (ppb) in the portal (A) and hepatic (B) veins. There is a statistically significant shift in susceptibility in response to hyperoxia in both regions (* $p < 0.05$ – PV, ** $p < 0.01$ - HV).

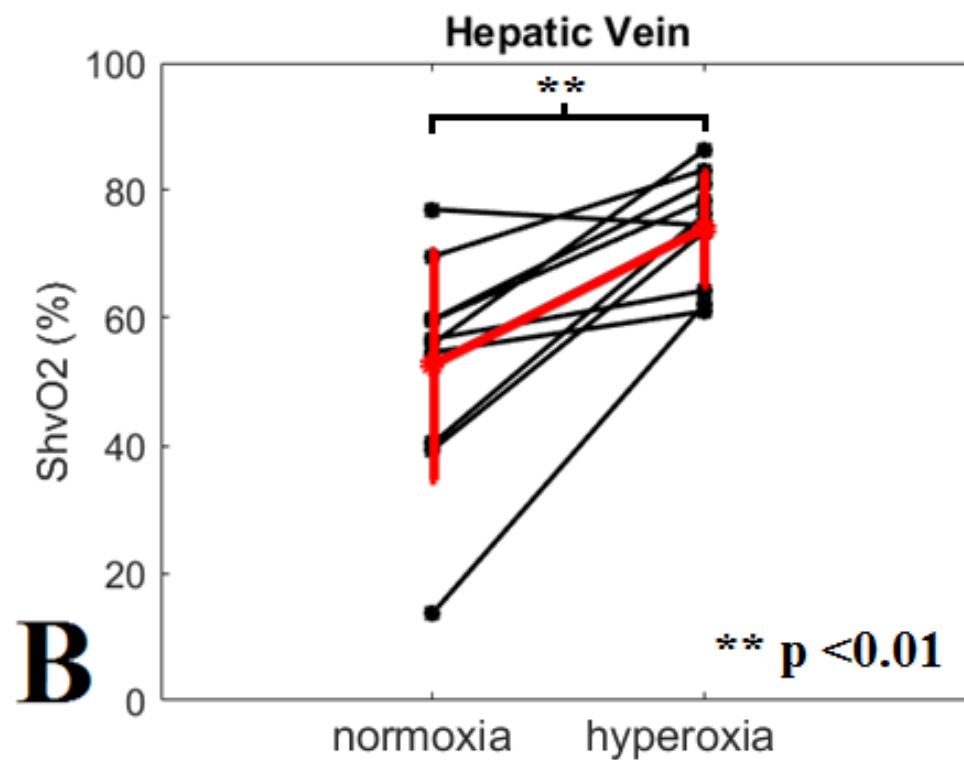
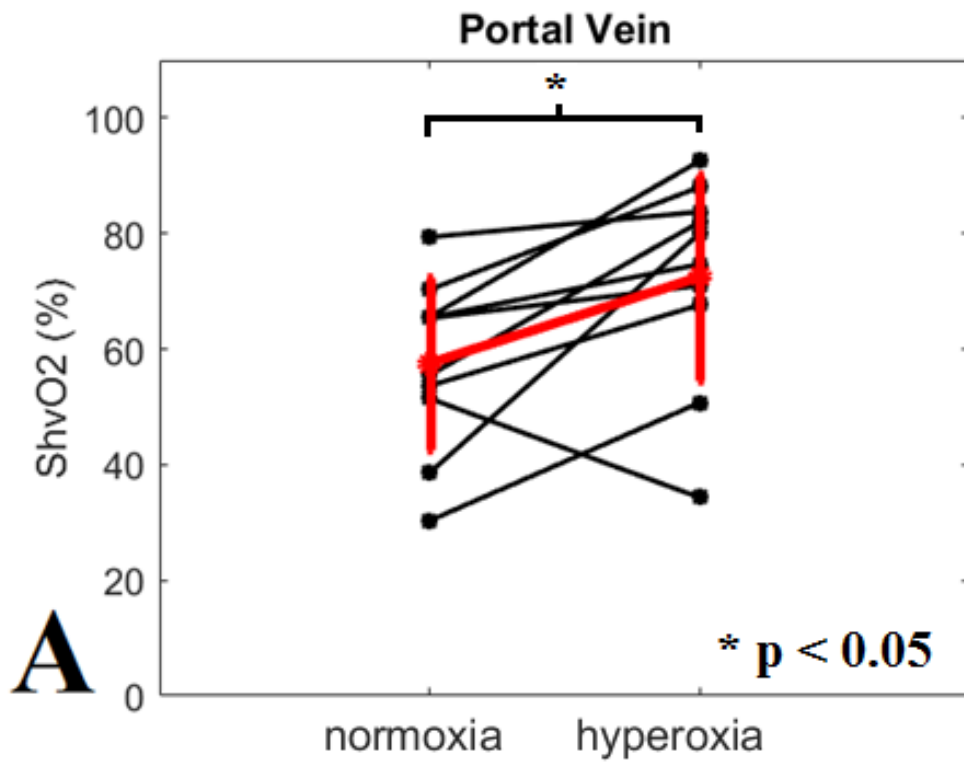


Fig 4.14 A & B: Graphs showing the change in venous oxygen saturation in the portal (A) and hepatic (B) veins. There is a statistically significant increase in response to hyperoxia in both regions. (* $p < 0.05$ – PV, ** $p < 0.01$ - HV).

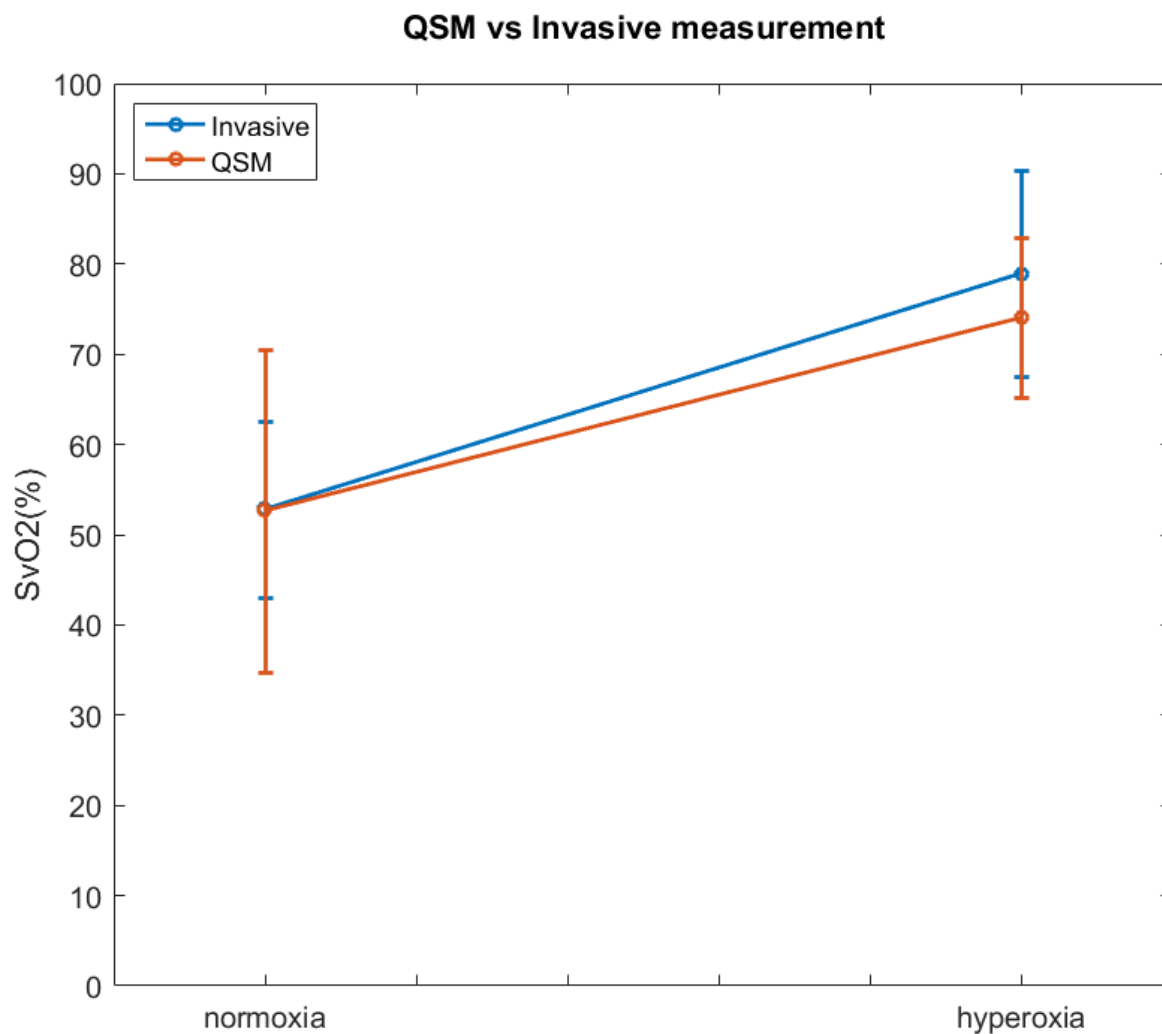


Fig 4.15: Graphs showing the change in venous oxygen saturation in the hepatic vein - calculated from the QSM data, and the IVC – measured invasively from using the blood gas analyser. The difference measured invasively is not statistically significant but there is excellent agreement between the two datasets.

4.2.5 Discussion

The ability to non-invasively perform venous oximetry in the liver could have important clinical implications. For instance, thanks to improvements in diagnostic radiology, patient selection and operative technique, partial hepatectomy has increasingly become a more viable treatment option in cases of hepatic lesions, both malignant and benign. It is known that the regenerating liver places an increased metabolic burden on patients that have undergone the procedure, and it has been shown previously that $ShvO_2$ reflects the metabolic status of the remnant liver^[6, 8]. The advent of QSM means that the ability to relate magnetic susceptibility to $ShvO_2$ offers a way to assess this in a non-invasive and repeatable fashion.

In the present study, we employed QSM to assess changes in hepatic venous oxygen saturation modulated by a hyperoxic gas challenge. This is the first report that examines the ability of QSM to assess oxygen changes in the major hepatic vessels, and it is shown that it is possible to detect statistically significant differences in blood oxygenation in response to hyperoxia.

It is known that exposure to hyperoxic conditions will reduce the deoxyhaemoglobin concentration of venous blood. This has been confirmed presently by invasive measurement. QSM uses deoxyhaemoglobin as a native contrast agent, so it logically follows that under hyperoxic conditions there would be a reduction in contrast between the hepatic vein and the surrounding tissue when compared to an image acquired under normoxia. This is shown in figures 4.11 (G & H) and 4.12.

The diamagnetic shift in response to the gas challenge shown in figure 4.13 substantiates the effect depicted in figure 4.11 (G & H). The difference in susceptibility brought about by the gas challenge in both the portal and hepatic vein is statistically significant, but there is also a high degree of variability between subjects. This is most likely due to natural variation in metabolic rates between subjects.

The SvO_2 changes in figure 4.14 are within realistic physiological boundaries. Previous studies that have calculated SvO_2 from QSM measurements in the cerebral vasculature have reported a ~10% increase from ~88% to ~99% in response to hyperoxia^[4]. The absolute values measured here are much lower. It should be noted however that the blood from which these measurements have been taken has already passed through the gut and mesentery before reaching the liver, so it is expected that blood oxygenation would be lower

than that measured in the brain. Furthermore, the effect of the gas challenge measured here is greater than that measured in the brain, but again, this may be a function of the fact that the venous blood the liver receives is partially deoxygenated, and so the effects of hyperoxia on hepatic blood may be greater than in the brain.

There is no statistically significant difference between the portal and hepatic veins in terms of SvO_2 under hyperoxic or normoxic conditions. As the hepatic vein is downstream from the portal vein it was expected that the deoxyhaemoglobin concentration would be higher than in the PV, and that this relationship would remain constant over the course of the experiment. There are reports in the literature of the effective arterialisation of portal venous blood in rats in response to hyperoxia – i.e. $SpvO_2$ increased from ~53% under normoxia to ~93% under hyperoxia in healthy control animals^[13]. While the normoxic $SpvO_2$ value is comparable to the measurement made in our experiment, the increase under induced hyperoxia is far greater than we have observed, but may go some way to explaining the relationship between blood oxygenation between the two vessels under hyperoxia. It is difficult to draw any conclusions from this however without data from the hepatic artery.

The ability to non-invasively perform venous oximetry in the liver could have important clinical implications. Hepatic venous oxygen saturation is an eminently useful metric, and has been used to assess hepatic oxygen kinetics in studies with respective focusses as diverse as haemodialysis^[22], acute and chronic heart failure^[23], and hepatic ischemic/reperfusion injuries^[24, 25]. Furthermore, thanks to improvements in diagnostic radiology, patient selection and operative technique, partial hepatectomy has increasingly become a more viable treatment option in cases of hepatic lesions, both malignant and benign. It is known that the regenerating liver places an increased metabolic burden on patients that have undergone the procedure, and it has been shown previously that $ShvO_2$ reflects the metabolic status of the remnant liver^[15, 17]. The advent of QSM means that the ability to relate magnetic susceptibility to $ShvO_2$ offers a way to assess this in a non-invasive and repeatable fashion.

4.2.6 CONCLUSIONS

The present study clearly demonstrates that it is possible to measure changes in blood oxygen saturation in the portal and hepatic veins on the basis of susceptibility. Furthermore, it has been shown that the susceptibility measurement can be used to calculate venous blood oxygen saturation in the major hepatic vessels, and that the calculated values reflect physiologically realistic ones. Venous oxygen saturation calculated from measurements of susceptibility in the hepatic vein have been validated by invasive blood gas measurements, and there was good agreement between the measurements.

References

1. Straub, S., et al., *Suitable reference tissues for quantitative susceptibility mapping of the brain*. Magn Reson Med, 2017. **78**(1): p. 204-214.
2. Haacke, E.M., et al., *Quantitative susceptibility mapping: current status and future directions*. Magn Reson Imaging, 2015. **33**(1): p. 1-25.
3. Ozbay, P.S., et al., *Effect of respiratory hyperoxic challenge on magnetic susceptibility in human brain assessed by quantitative susceptibility mapping (QSM)*. NMR Biomed, 2015. **28**(12): p. 1688-96.
4. Haacke, E.M., et al., *In vivo measurement of blood oxygen saturation using magnetic resonance imaging a direct validation of the blood oxygen level-dependent concept in functional brain imaging*. Hum Brain Mapp, 1997. **5**: p. 341 - 346.
5. Hsieh, M.C., et al., *Investigating hyperoxic effects in the rat brain using quantitative susceptibility mapping based on MRI phase*. Magn Reson Med, 2017. **77**(2): p. 592-602.
6. Yusekevitch, P.A., *ITK-SNAP*. 2015.
7. Schweser, F., et al., *Toward online reconstruction of quantitative susceptibility maps: superfast dipole inversion*. Magn Reson Med, 2013. **69**(6): p. 1582-94.
8. Shmueli, K., et al., *Magnetic susceptibility mapping of brain tissue in vivo using MRI phase data*. Magn Reson Med, 2009. **62**(6): p. 1510-22.
9. Tang, J., et al., *SWIM: Susceptibility Mapping as a Means to Visualize Veins and Quantify Oxygen Saturation*, in *Susceptibility Weighted Imaging in MRI*. 2011, John Wiley & Sons, Inc. p. 461-485.
10. Haacke, E.M., et al., *Susceptibility mapping as a means to visualize veins and quantify oxygen saturation*. Journal of Magnetic Resonance Imaging, 2010. **32**: p. 663 - 676.
11. Fan, A.P., et al., *Regional quantification of cerebral venous oxygenation from MRI susceptibility during hypercapnia*. Neuroimage, 2015. **104**: p. 146-55.
12. Huang, F.W., et al., *A mouse model of juvenile hemochromatosis*. J Clin Invest, 2005. **115**(8): p. 2187-91.
13. Zhang, J., et al., *Quantitative mapping of cerebral metabolic rate of oxygen (CMRO₂) using quantitative susceptibility mapping (QSM)*. Magn Reson Med, 2015. **74**(4): p. 945-52.
14. Katsuramaki, T., et al., *Monitoring perioperative hepatic venous oxygen saturation ShvO₂ in hepatectomy - Changes of ShvO₂ in Hemorrhagic Shock*. J Hep Bil Pancr Surg, 1997. **4**: p. 351 - 355.
15. Yoshioka, S., et al., *Hepatic Venous Hemoglobin Oxygen Saturation Predicts Regenerative Status of Remnant Liver after Partial Hepatectomy in Rats*. Hepatology, 1998. **27**(5): p. 1349 - 1353.
16. Takano, H., et al., *Monitoring of hepatic venous oxygen saturation for predicting acute liver dysfunction after Fontan operations*. The Journal of Thoracic and Cardiovascular Surgery. **108**(4): p. 700-708.
17. Shimizu, H., et al., *Changes in hepatic venous oxygen saturation related to the extent of regeneration after partial hepatectomy in rats*. Am J Surg, 1999. **178**(5): p. 428 - 431.
18. Jain, V., et al., *Investigating the magnetic susceptibility properties of fresh human blood for noninvasive oxygen saturation quantification*. Magn Reson Med, 2012. **68**(3): p. 863-7.

19. Ge, Y., R.I. Grossman, and E.M. Haacke, *Susceptibility Weighted Imaging in Multiple Sclerosis*, in *Susceptibility Weighted Imaging in MRI*. 2011, John Wiley & Sons, Inc. p. 249-264.
20. Jensen, K.P. and U. Ryde, *How O₂ binds to heme: reasons for rapid binding and spin inversion*. J Biol Chem, 2004. **279**(15): p. 14561-9.
21. Hughes, S.J., et al., *Effect of inspired oxygen on portal and hepatic oxygenation effective arterialization of portal blood by hyperoxia*. Cell Transplantation, 2004. **13**: p. 801 - 808.
22. Rokyta, J.R., et al., *Effects of continuous venovenous haemofiltration-induced cooling on global haemodynamics, splanchnic oxygen and energy balance in critically ill patients*. Nephrology Dialysis Transplantation, 2004. **19**(3): p. 623-630.
23. MATSUDA, H., et al., *Analysis of Acute and Chronic Heart Failure in View of Hepatic Oxygen Supply-Demand Relationship Using Hepatic Venous Oxygen Saturation: SYMPOSIUM ON PATHOPHYSIOLOGY AND SEVERITY OF HEART FAILURE IN THE ASPECT OF CIRCULATORY INSUFFICIENCY*. Japanese circulation journal, 1989. **53**(2): p. 175-179.
24. Kretzschmar, M., A. Krüger, and W. Schirrmeyer, *Hepatic ischemia-reperfusion syndrome after partial liver resection (LR): hepatic venous oxygen saturation, enzyme pattern, reduced and oxidized glutathione, procalcitonin and interleukin-6*. Experimental and Toxicologic Pathology, 2003. **54**(5-6): p. 423-431.
25. Katsuramaki, T., et al., *Changes in Hepatic Venous Oxygen Saturation in Hepatic Warm Ischemia/Reperfusion Injury in Pigs*. Surgery Today, 2000. **30**(4): p. 343-351.

Chapter 5

Chapter 5 details two experiments. The first demonstrates the first application of QSM to a preclinical model of colorectal liver metastases (CRLM). Data was acquired in a cohort of mice that had been inoculated with CRLM ($n = 10$). Magnetic susceptibility was measured in both the healthy liver tissue and in the liver tumours. Secondly, a comparison was made between the susceptibility of the liver tumours under normoxic and hyperoxic conditions. Thirdly, the venous oxygen saturation was calculated from susceptibility measurements taken from the hepatic vein under normoxic conditions, and was compared to that of a cohort of healthy mice.

The aim of second experiment was to determine the ability of QSM to assess the efficacy of a Vascular Disrupting Agent (VDA), a novel chemotherapeutic agent. A cohort of mice ($n = 10$) that had been inoculated with SW1222 colorectal cancer cells were scanned immediately before, and 72 hours after the drug was administered to half of the animals. Hyperoxia was induced in all mice during both scanning sessions, and susceptibility maps were calculated under both hyper- and normoxic conditions. Susceptibility was measured in the healthy liver tissue and tumours under normoxic conditions, and in the tumours under both hyper- and normoxic conditions, at both time points. A comparison was also made between the venous oxygen saturation of the hepatic vein, as calculated from the measured susceptibility of both groups at both time points.

5.1 QSM and Colorectal Liver Metastases

5.1.1 Introduction

Though still considered a novel technique, Quantitative Susceptibility Mapping has shown considerable potential in terms of clinical use. As discussed in chapter 2, the application of QSM has been investigated in the context of a broad assortment of clinical conditions, ranging from neurodegenerative disorders ^[1-4], to volumetric measurement of haematomas ^[5], to a variety of experiments examining various facets of cerebral venous oxygenation ^[6-10]. To date however, the application of QSM to cancer research has been limited to a handful of studies, and within those has been confined to the identification of iron and calcium deposits in tumour volumes ^[11, 12].

In the previous chapter, the differences between oxygenated and partially deoxygenated blood were discussed in terms of magnetic susceptibility, and it was shown that QSM could differentiate between normoxic and hyperoxic blood in both the portal and hepatic veins. It is well known that cancer cells require a rich supply of oxygenated blood to service their enhanced metabolic requirements ^[13], and in this chapter the hypothesis will be extended to investigate the application of QSM to a preclinical model of colorectal liver metastases.

Colorectal cancer is the 4th most common cancer in the UK, accounting for 12% of all new cancer diagnoses ^[14]. It is most common in older age groups, and the median 5-year survival rate for those diagnosed between the ages of 60 – 69 is ~67%, a figure which decreases with age. It is estimated that of those diagnosed, between 50 - 70% will develop secondary tumours in the liver, known as colorectal liver metastases (CRLM). CRLM have a negative effect on prognosis, reducing the 5 year median survival rate to ~5% ^[15]. As with all cancers, early detection and intervention are critical for improving outcome.

Hepatic resection, often in combination with either pre- or post-surgical chemotherapy is the only curative treatment available for CRLM ^[16]. As few as 20% of patients diagnosed with CRLM will qualify for surgical intervention, but of those that do, 5-year survival has been reported to range from 37 – 58%. The remaining patients must be assessed for palliative care options. Imaging plays a vital role in the diagnosis and assessment of patients with CRLM, and there are a number of modalities available at each stage of the treatment cycle.

Ultrasound (US), for example, has been shown to improve tumour detection intra-operatively, identifying additional tumours in 16% of patients in one study ^[17]. The limited size of the visual field however generally precludes US imaging from pre-operative assessment ^[18]. Similarly, FDG-PET can identify malignant lesions with extremely high accuracy ^[19], but its diagnostic value can be undermined by the increased uptake of FDG by tissues suffering from inflammation ^[20]. High resolution, contrast enhanced, computed tomography (CT) is the most widely used modality for pre- and post-operative assessment and monitoring of CRLM, however it has been shown that MRI has a higher sensitivity to sub-centimetre lesions ^[21], and it is generally recommended that CT findings should be integrated with those from other imaging modalities before any significant changes to therapeutic strategy are introduced^[20]. As such, it is clear from the literature that no one imaging modality can act as a panacea.

Beyond identification and morphological assessment of CRLM, there are some techniques that give information concerning the haemodynamics and vasculature of tumours. Gadolinium and iodinated contrast agents can be intravenously administered during MRI and CT protocols respectively to assess tumour blood flow, and there have been attempts in the literature to characterise the vascular profile of liver tumours using BOLD MRI in conjunction with gas challenges ^[13].

The ability to assess changes in tumour oxygenation has important implications for the selection of oncological treatment pathways, and a non-invasive technique that produces reliable and reproducible results could find broad use in a clinical setting. Hyperoxia is a well-known tumour radiosensitiser that works by increasing the amount of dissolved oxygen in plasma in order to allow the diffusion of oxygen into chronically hypoxic regions of tumours ^[22]. It was shown in the previous chapter that QSM could provide functional information regarding changes in blood oxygenation in the branches of the major hepatic blood vessels. In this chapter, the hypothesis is extended to ascertain information regarding the oxygenation status of colorectal liver metastases.

This study aimed to test three hypotheses in a preclinical (mouse) model of colorectal liver metastases. The first was that it is possible to differentiate between healthy liver tissue and tumours on the basis of susceptibility, as the tumours receive greater amounts of oxyhaemoglobin from the hepatic artery than normal liver tissue ^[13, 23, 24]. The second was that QSM can be used to detect changes in the susceptibility of the tumours that are indicative

of changes in oxygenation status. In order to test this, the susceptibility of the tumours was measured under the administration of pure O₂. This was then compared to baseline susceptibility measured under normoxic conditions. Finally the third hypothesis was that the increased metabolic demand placed on the liver by the tumours will manifest in the hepatic venous oxygen saturation (ShvO₂). To examine this, ShvO₂ was calculated from the susceptibility measured in the hepatic vein of the mice with tumours, and was compared to that of the healthy mice examined in the previous experiment. Data acquired from a small cohort of mice of the same species as the disease cohort that had *not* been inoculated with cancer cells was also included for completeness.

5.1.2 Materials & Method

5.1.2.1 Animal Preparation

All animal studies were performed in accordance with the UK Home Office Animals Science Procedures Act (1986). Severe combined immunodeficiency (SCID) mice (n = 10) were inoculated with 1×10^6 SW1222 CRLM cells via intrasplenic injection^[25]. A splenectomy was then performed immediately post-injection. Mice were scanned 19 days post-surgery. The healthy cohort were CD1 wild type mice (WT, n = 10), and the third cohort were uninoculated SCID mice (n = 2). The small size of the third cohort precluded their inclusion in any statistical analysis.

Gasses were administered through a nose cone at a rate of 0.5 ltr/min. Normoxic data was acquired as the subjects were administered medical air (21% O₂/balance Nitrogen), while hyperoxic data was acquired under the administration of 100% O₂. 10 minutes were allowed between gasses to allow the animal to acclimatise. All other animal preparation was as discussed in chapter 4.

5.1.2.2 Data Acquisition

The data acquired were single echo, fully first order flow compensated, respiratory gated, T₂*-weighted 2D GRE acquisitions. Scan parameters were as follows:

$B_0 = 9.4T$, $TR = 1000$ ms, $TE = 4$ ms, $FA = 70^\circ$, Voxel = $200 \mu\text{m}$ isotropic, bandwidth = 50 kHz, average = 4.

FOV was adjusted to accommodate each animal, and the matrix size was adjusted to ensure the voxel dimensions were as above.

QSM processing (sec. 4.1.2.3), venous oxygen saturation (SvO_2) calculations (sec. 4.2.2.2) and statistical comparisons (sec. 4.2.3.3) were as performed previously.

5.1.2.3 Regions of Interest

Liver tumours were identified as hyperintense regions on the T_2^* -weighted magnitude data (figure 5.1 - highlighted). Multiple tumours were identified in each animal and were manually segmented *en masse* in each image, such that the values quoted for the tumours represent the combined mean value measured in all identified tumours for each animal. Regions of healthy liver tissue were also segmented manually from areas that were as remote as possible from tumours or large branches of the hepatic vessels. All other ROI's were identified and segmented as discussed previously (sec. 4A.2.5).

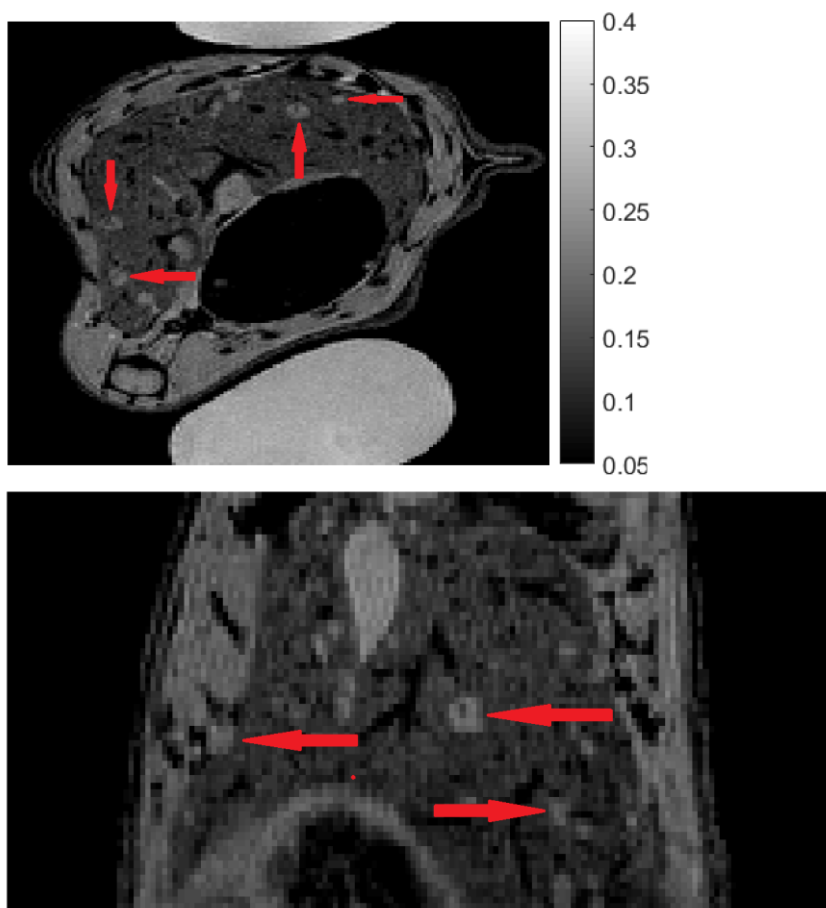


Fig 5.1: Representative coronal (top) and sagittal (bottom) orientation T_2^* -weighted magnitude images displaying the liver tumours (red arrows) that appear as hyperintensities relative to the healthy liver tissues.

5.1.3 Results

The images in figure 5.2 are a representative slice from a magnitude image (A), the corresponding raw phase image (masked for display purposes) (B), the corresponding frequency map (C), and the corresponding susceptibility map (D), from a single mouse with tumours. There was nothing in the magnitude image that would have indicated any respiration, flow, or reconstruction artefact that could have negatively impacted on the subsequent processing procedure. The raw phase data showed no evidence of artefacts or phase discrepancies that could have undermined the unwrapping and background field removal process that they were to be subjected to. The SHARP algorithm successfully unwrapped the phase image, and removed the background field contributions to the measured magnetic field (C). In the particular frequency map displayed there are still some visible edge effects that were not removed by the mask erosion process (red arrows). It was expected that these would not have any major impact on the susceptibility map. Upon carrying out the inversion this proved to be the case, and there were no major streaking artefacts visible in the susceptibility map (D). It was found that the contrast from the blood vessels was entirely localised, as expected. The images displayed are representative of the entire cohort, and the inspections that they have been subjected to were carried out for each image of every subject.

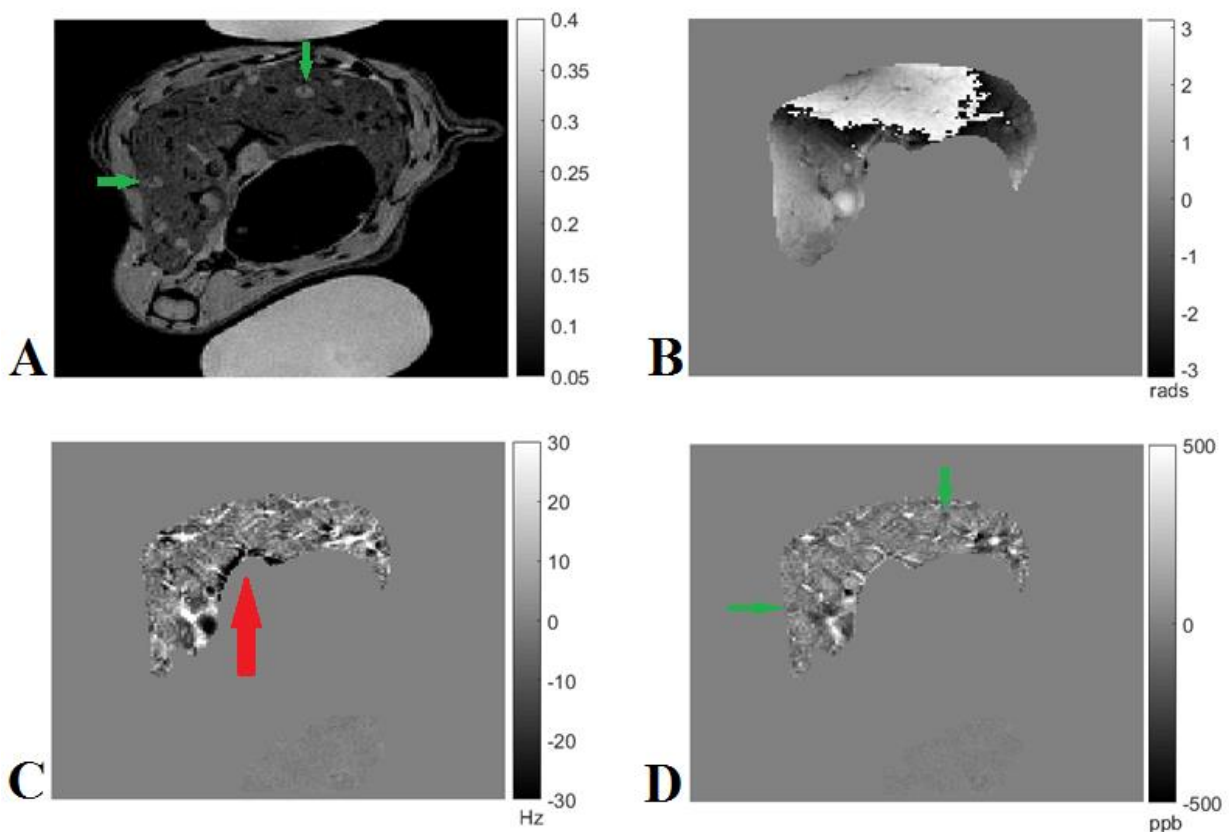


Fig 5.2 A - D: T₂*-weighted magnitude image (A), corresponding raw phase image (B), frequency map (C) and calculated susceptibility map (D) of a single mouse, representative of the entire dataset examined here.

Some of the tumours displayed in figure 5.2 have been highlighted in the magnitude and corresponding susceptibility map (green arrows A & D). As mentioned, these appear as hyper-intense on the T_2^* -weighted magnitude images, however on susceptibility maps appear as slightly hypo-intense regions relative to the healthy liver tissue, and are difficult to detect. The reason for this is that relative to other regions (e.g. venous blood vessels), the B_0 field perturbation caused by the tumours is quite small, and so they generate little contrast on QSM images.

The graph in figure 5.3 depicts the difference in mean susceptibility between the healthy liver tissue and the tumours of all of the subjects under normoxic conditions. The susceptibility of the tissue and tumours is 1.38 ± 2.76 ppb and -33.54 ± 18.5 ppb respectively. The tumours are significantly more diamagnetic than the surrounding healthy liver tissue ($p < 0.0001$), thus confirming the first experimental hypothesis. It is expected that this is due to the increased amount of oxyhaemoglobin received by the tumours due to their increased arterial blood supply.

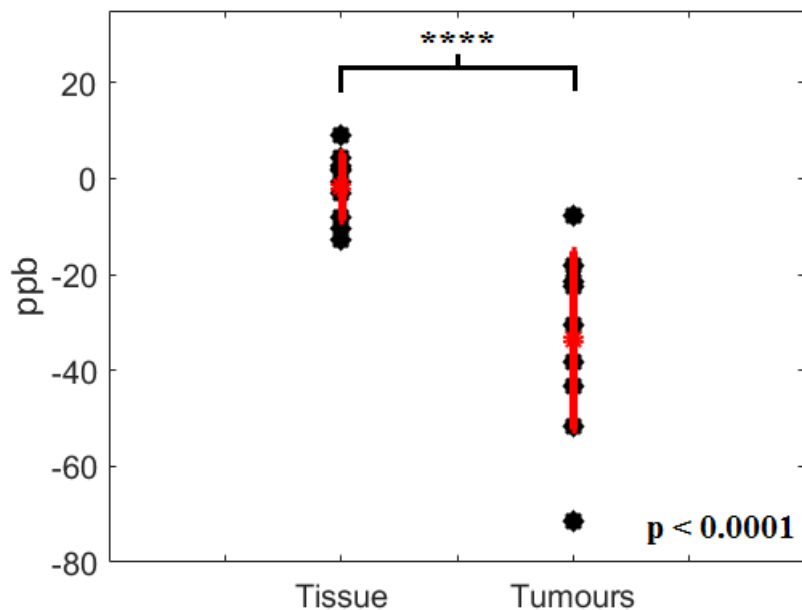


Fig 5.3: Graph displaying the difference in mean susceptibility (ppb) between healthy liver tissue and liver tumours. Tumours are significantly more diamagnetic than the liver tissue. This is ascribed to the increased arterial component of their blood supply.

Figure 5.4 illustrates the behaviour of the tumours under hyperoxic and normoxic conditions as measured on a susceptibility map, and shows that the tumours are significantly more *paramagnetic* under hyperoxic conditions ($p < 0.01$). The susceptibility under hyper- and normoxia is -15.63 ± 10.72 ppb and -33.54 ± 18.5 ppb respectively. The result is counter-intuitive, as it was shown in the previous experiment (chap. 4.2) that the administration of pure O_2 results in a diamagnetic shift in the susceptibility of the blood in the blood vessels, and it was expected that the same effect would be observed in the tumours. This suggests that the susceptibility of the tumours is not entirely governed by the deoxyhaemoglobin content of the blood.

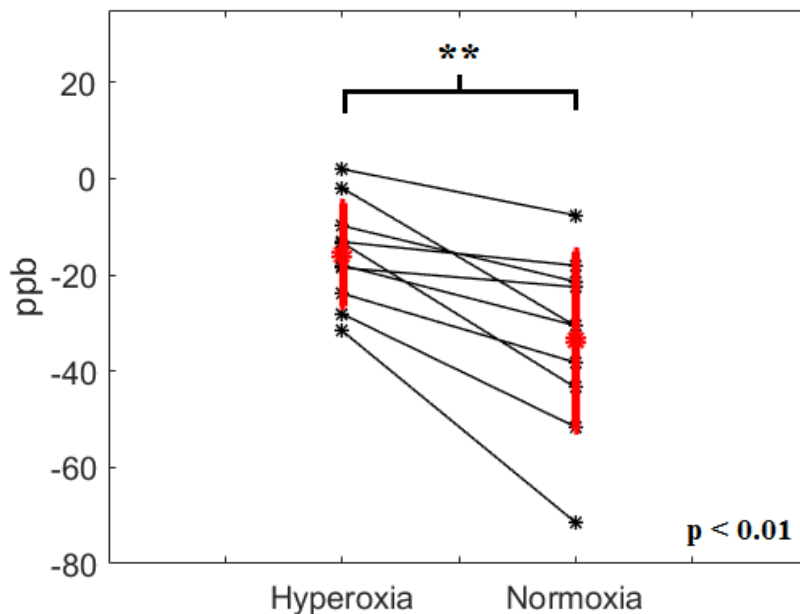


Fig 5.4: Graph displaying the mean susceptibility of the liver tumours under both hyperoxic and normoxic conditions. The administration of pure O_2 results in a significant paramagnetic shift from normoxic susceptibility.

The images in figure 5.5A & B show the effect of the administration of pure O_2 as detected by the T_2^* -weighted magnitude images (A) and the corresponding susceptibility maps (B). Normoxic images are included for comparison, and hyperoxic and normoxic images are indicated in each by H & N respectively. Also included are magnified images of a single tumour (magnified areas indicated by blue boxes). There is a clear increase in magnitude signal intensity in response to the administration of oxygen relative to the normoxic images. The effect was observed in both the healthy liver tissue and the tumour. This was as expected.

Conversely, there was little change in signal intensity in response to hyperoxia observed in the susceptibility maps (5.5B). Again, the tumours are difficult to detect and are indicated by blue arrows in the close up image. The images of the tumours are slightly more hypo-intense when acquired under normoxic conditions, confirming that they are more paramagnetic under O₂ administration. There is little difference in the signal intensity of the liver tissue, however the blood vessels are more hyperintense in the normoxic image due to the increased levels of deoxyhaemoglobin.

Magnitude Images

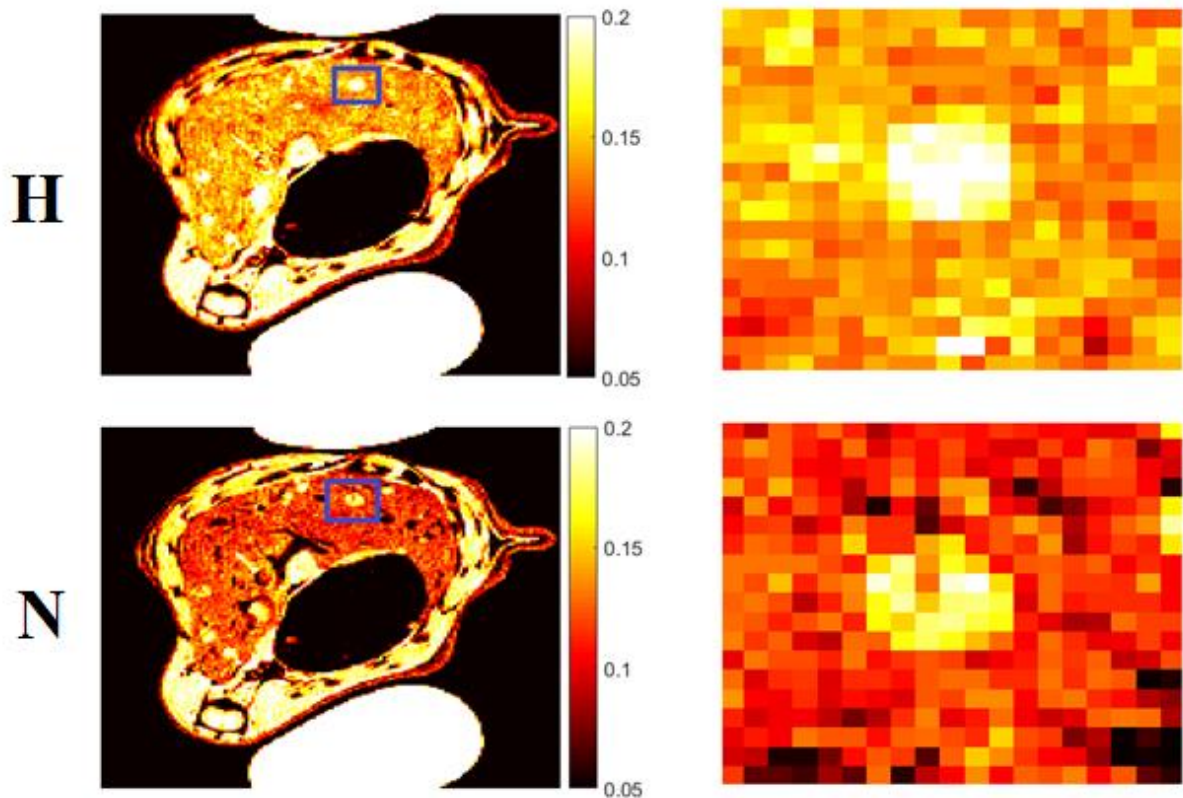


Fig 5.5A: Coronal orientation T_2^* -weighted magnitude images of the liver of a representative mouse with tumours, under hyperoxic (H) and normoxic (N) conditions. The left had column contains magnified images of a single tumour (highlighted by the blue box in the left hand images). The administration of pure O₂ results in enhancement of the T_2^* weighted signal in both the healthy liver tissue and liver tumours.

Susceptibility maps

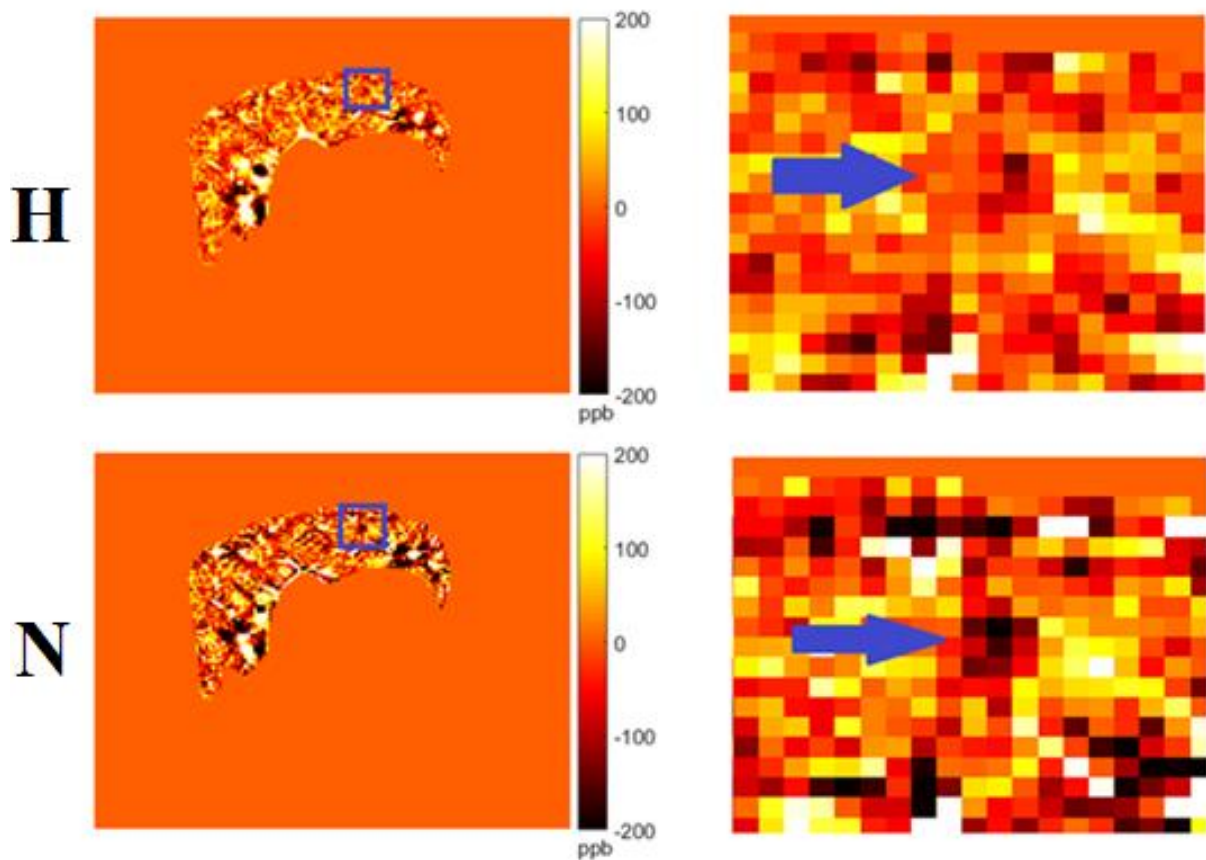


Fig 5.5B: Coronal orientation susceptibility maps calculated from the corresponding phase data of the magnitude images in 5A. The administration of oxygen has little effect on the contrast visible in the liver tissue. In addition, the tumours are difficult to detect relative to the magnitude images, however appear as slightly hypointense regions, indicating that they are diamagnetic with respect to the surrounding liver tissue.

The graphs in figure 5.6 shows the venous blood saturation measured under normoxic conditions in the portal (A) and hepatic (B) veins of the mice with tumours and the healthy cohort from the previous chapter. Also included is the SvO₂ of the uninoculated mice. There was no significant difference between the cohorts measured in the portal vein, however the oxygen saturation of the blood in the hepatic vein was significantly lower in the mice with tumours when compared to the wild types ($p < 0.05$). As the effect was not observed in the portal vein, this would indicate that the effect is not systemic, and is instead caused as the blood passes through the liver. It is expected that this can be attributed to the increased metabolic requirements of the liver tumours. Although statistical analysis was not possible for the uninoculated mice, the mean oxygen saturation in both regions was higher than that in the other groups. While it is difficult to draw any meaningful conclusion from a cohort of

two mice, this lends credence to the argument that the diminished oxygen observed in the mice with tumours is related to the increased oxygen needs of the tumours.

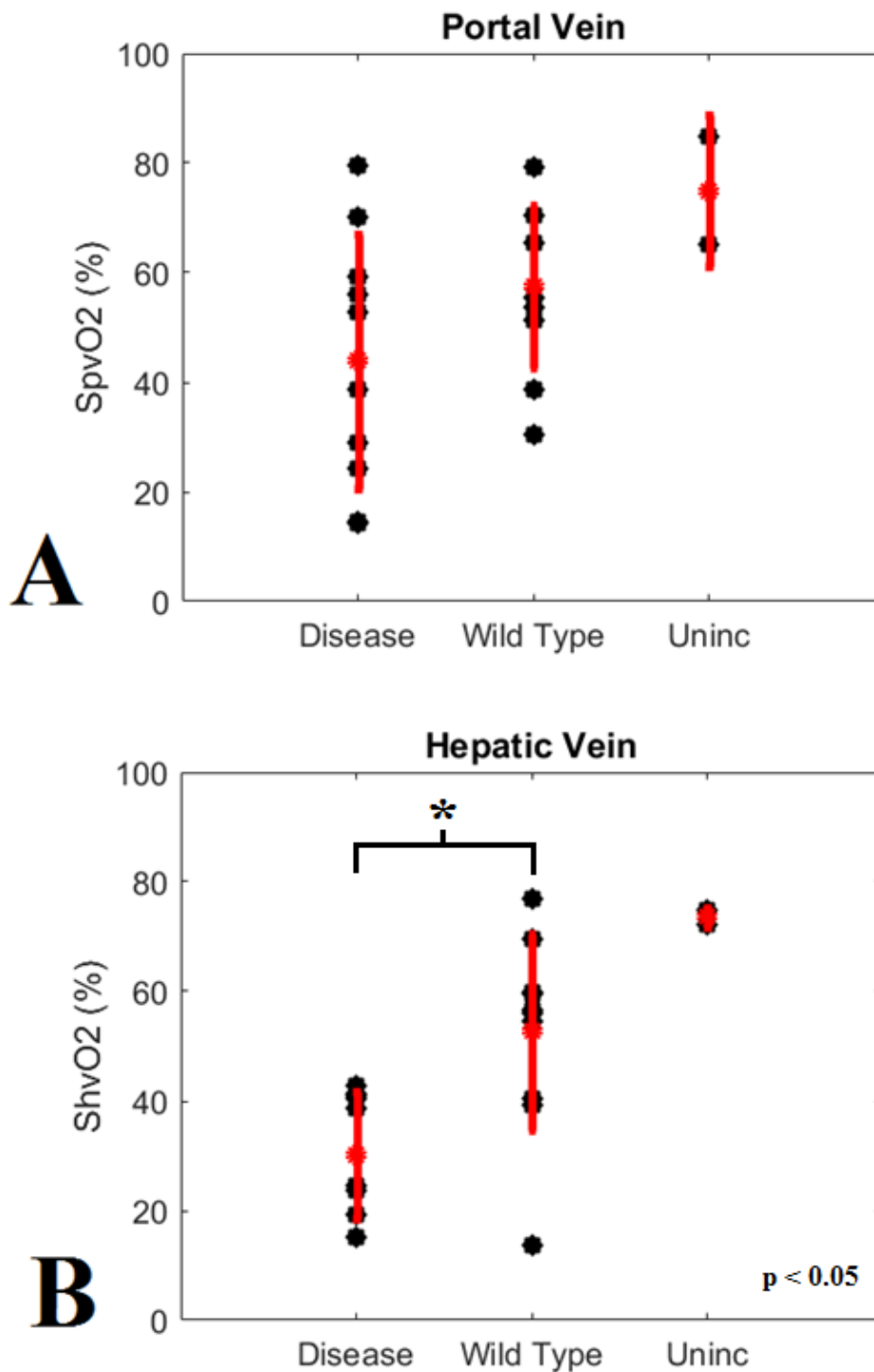


Fig 5.6 A & B: Graphs displaying the difference in venous blood oxygen saturation between the mice with tumours, healthy wild type, and uninoculated (uninc) SCID mice as calculated from susceptibility measured in the blood in the portal vein (A) and the hepatic vein (B). The blood in the hepatic vein of the mice with tumours contained significantly less oxygen than the healthy cohort. This is attributed to the tumour burden of the liver.

5.1.4 Discussion

Hypoxia is known to be one of the main limiting factors in the efficacy of cancer treatment for a number of reasons. For instance, oxygen molecules stabilise the DNA damage caused by the reactive oxygen species that result from the radiolysis of water molecules ^[26]. In the absence of oxygen the damage is readily reversible, meaning a higher dose of radiation is required to ensure adequate effect. Secondly, a well oxygenated tumour is indicative of a healthy blood supply, which increases the likelihood that chemotherapeutic agents will reach their intended target. Thirdly, it is well known that hypoxia results in genotypic mutations in tumour cells, increasing their malignant potential ^[27].

As recently as the 1990s, tumour hypoxia was assessed in clinical studies by means of polarographic needles, and, while useful in demonstration, the invasive nature of the procedure prevented its inclusion in regular clinical assessment ^[26]. Improvements in imaging in recent decades however have meant that hypoxia can now be measured using alternative, non-invasive approaches, which has opened the possibility of routine assessment of tumour oxygenation.

The inclusion of hypoxia imaging in regular diagnostic protocol brings with it a number of advantages. Firstly, the non-invasive nature of imaging allows longitudinal monitoring of individual patients. Secondly, previous clinical analyses have shown that there is a large degree of heterogeneity among tumours, and even within and between the same tumour types ^[27]. Hypoxia imaging allows customisation of treatment plans – for instance in the form of conformal radiotherapy, or combinations of radio- and chemotherapy. Furthermore, hypoxia imaging would allow assessment of methods designed to alleviate hypoxia. In this study, QSM has been successfully applied to a preclinical model of colorectal liver metastases. It has been shown that it is possible to derive clinically relevant information regarding blood oxygenation in the context of liver cancer from QSM images, and is the first such application of Quantitative Susceptibility Mapping.

The graph shown in figure 5.3 displays the difference in susceptibility between the healthy liver tissue and the tumours under normoxic conditions. The tumours are significantly more diamagnetic than the healthy liver tissue, and this has been ascribed to arterial blood supplied to the tumours. While it is possible that the susceptibility of the tumours relative to the surrounding tissue may be due to physical differences between the regions – for example tumours are known to be far less vascular than normal tissue, and the cells of which the

tumours are composed are of a different type to liver cell – this seems unlikely, as it has been shown in the literature ^[13, 23, 24] that CRLM derive blood predominantly from the hepatic artery, and is show in fig. 4.13 and fig. 5.4 that the susceptibility of both blood and tumours can be manipulated by the administration of oxygen. As such, it is thought that the susceptibility of the tumours is predominantly affected by the blood that is supplied to them.

It has been shown repeatedly that the effect of oxygen administration manifests in T_2^* -weighted magnitude images of healthy liver tissue and tumours as an increase in signal intensity. This is clearly visible in the images displayed in fig. 5.5A, and has been well documented in the literature ^[28-31]. The reason given for this is that the administration of O_2 reduces the presence of paramagnetic deoxyhaemoglobin, and, by extension, the local B_0 field inhomogeneities that increase the rate of T_2^* relaxation ^[22].

As such, the effect of O_2 administration on the susceptibility of the tumours observed here is somewhat counter-intuitive. It was expected that the decrease in deoxyhaemoglobin brought about by hyperoxia would have resulted in a diamagnetic shift in susceptibility in the tumours, whereas the opposite was observed. It may be, however, that the paramagnetic shift observed here indicates the presence of O_2 that is unbound, i.e. dissolved in the plasma.

As discussed previously (sec 4B.2.1), oxygen, when bound to haemoglobin, results in a *diamagnetic* molecule, and, as shown in the previous chapter, the administration of O_2 causes a diamagnetic shift in the susceptibility of venous blood due to a systemic decrease in deoxyhaemoglobin. Arterial blood on the other hand is almost entirely saturated. As such, inducing hyperoxia results in an increase in the amount of O_2 dissolved in the plasma ^[22, 32]. Unbound O_2 is a *paramagnetic* molecule, and, as the tumours examined here receive a large proportion of blood from the hepatic artery, it may be the case that the paramagnetic shift in susceptibility observed in response to hyperoxia is due to the increased influx of unbound O_2 that diffuses into the tumour.

The discrepancy between the magnitude and QSM results is intriguing, as the two seem to directly contradict each other. One possible explanation however may be related to mechanistic differences between phase and magnitude image contrast. It is noted in the literature that bulk susceptibility (as measured by QSM) is more directly related to tissue composition than T_2^* (or R_2^*) measurements, as changes in the latter can more accurately be thought of as measures of local field inhomogeneities ^[33]. It is noted elsewhere that the dephasing which results in the T_2^* effect only occurs when a phase dispersion exists across a

voxel, and that tissues that have uniform distributions of susceptibility will exhibit a phase effect but no T_2^* response [34]. As such, it may be the case that hyperoxic gasses have a uniform effect across the tumours to the extent that field inhomogeneities are reduced (thus increasing T_2^*), but still result in an increase in the delivery of (paramagnetic) O_2 . If this is the case, it further exemplifies one of the advantages QSM has over standard magnitude imaging i.e. that QSM can differentiate between para- and diamagnetism, whereas T_2^* is only sensitive to field (in)homogeneity, and as such tissue composition by proxy.

The difference in hepatic venous blood saturation between the mice with tumours and healthy wild type mice from the previous chapter could have significant clinical potential. The images in both cases were acquired under normoxic conditions so their acquisition necessitates little more than a single standard T_2^* scan. Future experimental work could be to perform a longitudinal study in order to characterise the correlation between tumour burden and $ShvO_2$. Once this is established, it opens the possibility of using QSM to non-invasively diagnose or monitor liver cancer, differentiate between benign and malignant lesions, or even to gauge the efficacy of treatment regimes.

The main drawback of QSM in the context of liver cancer as observed here is the difficulty with which tumours are identified on the susceptibility maps. As such, QSM can only provide complimentary information to the magnitude data, however the breadth and clinical potential of the functional information derived from susceptibility maps more than compensated for this shortcoming.

5.1.6 Conclusions

The results presented here have shown that QSM can differentiate between healthy liver tissue and liver tumours in a preclinical model of colorectal liver metastases. It has also been shown that QSM is sensitive to changes in tumour oxygenation brought about by the administration of pure O_2 in the same model. Lastly, it was shown that QSM measurements can be used to detect changes in hepatic venous blood oxygenation that are indicative of liver cancer.

5.2 VDA EXPERIMENT

5.2.1 Introduction

Colorectal liver metastases (CRLM) are, by definition, a secondary cancer. As such, treatment strategies are complex and multi-faceted ^[18]. Ultimately, the only available treatment that will allow long-term survival is removal by surgical resection ^[35], however surgery can only be performed in the context of the entire treatment regime ^[16]. For example, treatment of the primary cancer will require intervention in the form of surgery, chemo- or radiotherapy, or some combination thereof, and may take place before or after treatment of the metastases. Secondly, patients may present with tumours that are initially unresectable, requiring pre-operative chemo- or radiotherapy to downstage the tumours to resectable status ^[16]. Furthermore, only a relatively small percentage of patients will qualify for surgical intervention, but those that do not can still benefit from palliative care designed to inhibit growth, and minimise the spread of further tumours.

Imaging plays a vital role during the treatment of CRLM. CT is the most commonly used modality for assessing the treatment response of metastatic liver tumours, due to its wide availability and excellent spatial resolution. Traditionally, morphological changes (i.e. shrinkage) of the tumour have been used to assess treatment efficacy. As therapies become more sophisticated however, there is a growing body of evidence to suggest that tumour size does not always adequately correlate with treatment outcome ^[36]. Bevacizumab, for example, is an anti-vascular endothelial growth factor (anti-VEGF) antibody which works by inhibiting the growth of new blood vessels, but does not immediately lead to the reduction of tumour mass. In situations such as these, functional imaging plays a much more important role.

It is possible to derive functional information from both CT and MR techniques through the use of contrast agents. Iodine or gadolinium based agents (for CT and MRI respectively) can be administered intravenously prior to imaging, in order to assess the vascular characteristics of tumours ^[37]. Furthermore, there are myriad MRI techniques such as diffusion-weighted and BOLD MRI that can impart information regarding pathophysiology, heterogeneity, and may also predict clinical outcomes ^[36].

Oxi4503 is a combretastatin-derived chemotherapeutic drug known as a vascular disrupting agent (VDA). It works by preventing the formation of microtubules within endothelial cells, which precipitates morphological abnormalities as the cells replicate. This

causes an increase in vascular permeability, leading to the collapse of the vascular wall. Ultimately, the tumour undergoes necrosis due to an acute reduction of its blood supply^[38]. Oxi4503 has been shown in the literature to have a deleterious effect on a number of diverse tumour types^[38-40], including a preclinical model of colorectal liver metastases^[41, 42]. It acts quickly within tumours, having a profound effect immediately after administration^[41]. However, as with bevacizumab, its effects may not have an immediate impact on tumour morphology. Previously, the efficacy of Oxi4503 was assessed in CRLM by means of histology, stereology, and laser Doppler flowmetry, wherein it was shown that treated tumours displayed significant necrosis and a decrease in tumour blood flow relative to the surrounding tissue^[42].

In the previous chapter, the response of colorectal liver metastases to hyperoxia was examined using QSM, and it was established that by altering the oxygen concentration of the blood, changes could be detected in the magnetic susceptibility of the tumours. Secondly, it was shown that the hepatic venous oxygen saturation of mice with liver tumours was significantly lower than that of healthy wild type mice, which was ascribed to the increased metabolic demands of the cancer.

The aim of this chapter is to examine whether QSM can be used to assess the efficacy of the vascular disrupting agent Oxi4503. It was hypothesised that the change observed in the susceptibility of the tumours in response to hyperoxia necessitates a functioning tumour vasculature. As such, a disruption of the tumour vasculature by Oxi4503 will undermine the effect induced by the gas challenge to which QSM is sensitive. Furthermore, it was hypothesised that the destruction of the tumour vasculature would reduce the metabolic burden on the liver, and that this would be reflected in the oxygen saturation of the hepatic venous blood.

5.2.2 Methods

5.2.2.1 Animal Preparation

All animal studies were performed in accordance with the UK Home Office Animals Science Procedures Act (1986). Severe combined immunodeficiency (SCID) mice (n = 10) were inoculated with 1×10^6 SW1222 CRLM cells via intrasplenic injection^[25]. A splenectomy was then performed immediately post-injection.

This was a longitudinal study during which data was acquired at 2 distinct time-points. The cohort was divided into a treated ($n = 5$) and control ($n = 5$) group, and the initial scan took place 19 days post-surgery. Immediately after this, the treated group was administered 40 mg/kg of Oxi4503 via tail vein injection. Subsequently, all animals were rescanned 72 hours later.

Hyperoxia was induced in all animals during both scan sessions via the administration of 100% O₂, and data was acquired under hyperoxic and normoxic conditions, with 10 minutes allowed between each gas to allow the animals to acclimatise. Gases were administered through a nose cone at a rate of 0.5 ltr/min.

The data acquired during scan sessions 1 & 2 will be referred to as pre- and post-treatment respectively for the treated group, and as control 1 and control 2 respectively for the control group.

Otherwise, animal preparation (chap. 4A sec 4A.2.1), data acquisition (chap. 5A sec. 5A.2.2), QSM processing (chap. 4 sec. 4A.2.3), region of interest identification (chap. 5A sec. 5A.2.3) and venous oxygen saturation calculation (chap. 4B sec. 4B.2.2) were performed as discussed previously. As in all experimental chapters, magnetic susceptibility measurements are quoted with respect to the external water reference that was included with each subject in the scanner.

5.2.2.2 Histology

Animals were culled immediately after the second scanning session. The livers were excised and stored in 10% neutral buffered formalin. Standard Hemotoxylin & Eosin staining was carried out on all livers from both the treated and untreated animals in order evaluate the morphological changes brought about by administration of the VDA.

5.2.2.3 Statistical Analysis

Parameter estimates were compared using either a Wilcoxon matched pairs signed rank test or a Mann-Whitney test for paired and unpaired data respectively. A difference was considered statistically significant for $p < 0.05$.

5.2.3 Results

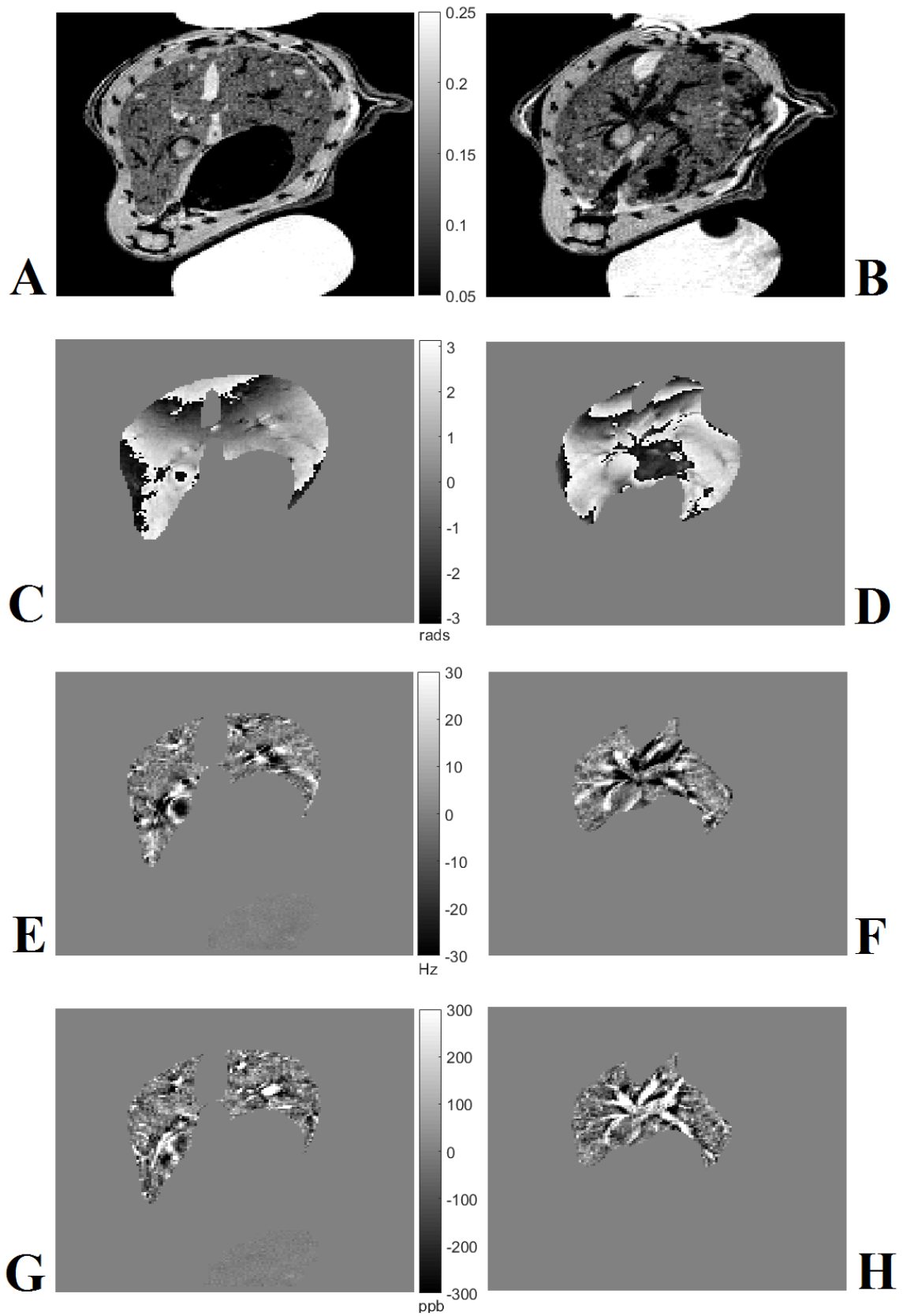


Figure 5.7 A - H: T₂*-weighted magnitude (A,B), raw phase (C, D), frequency map (E, F), and susceptibility map (G, H) of single mouse from the **treated** cohort, acquired during scan sessions 1 (left) and scan session 2 (right)

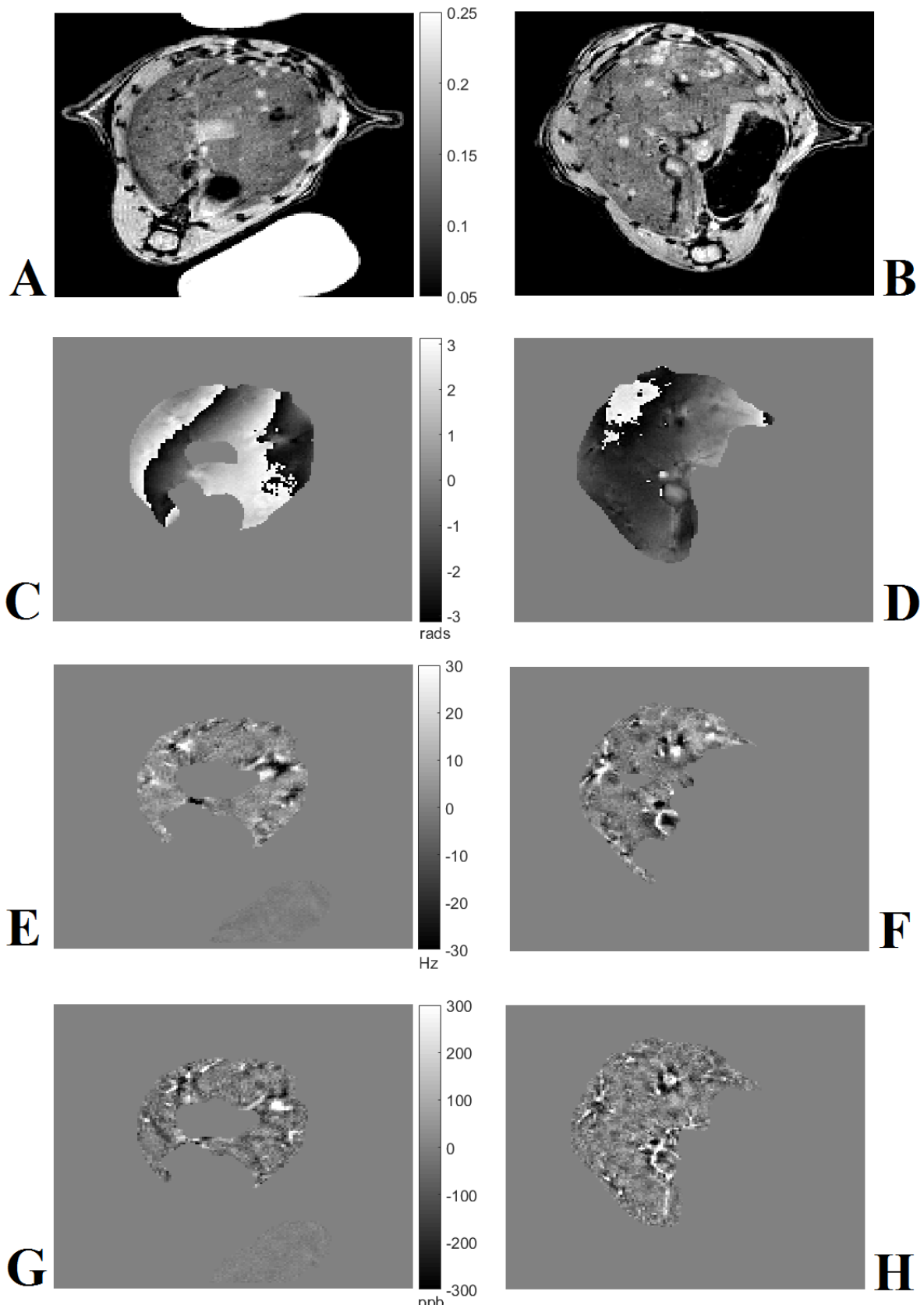


Figure 5.8 A - H: T₂*-weighted magnitude (A,B), raw phase (C, D), frequency map (E, F), and susceptibility map (G, H) of single mouse from the **control** cohort, acquired during scan sessions 1 (left) and scan session 2 (right)

Figures 5.7 & 5.8 contain representative images from the treated (figure 5.7) and control (figure 5.8) groups. Images A, C, E, and G were acquired during the first scan session, and images B, D, F, and H are the images of the same subject from the second session in each. All images were subject to the same inspection that was detailed in previously (Chap. 5A sec. 5A.3). The raw phase data did not contain any obvious artefacts that could have confounded QSM processing, the SHARP algorithm successfully unwrapped and removed the background field from the raw phase data, and the susceptibility inversion was carried out successfully by the TKD algorithm in all cases.

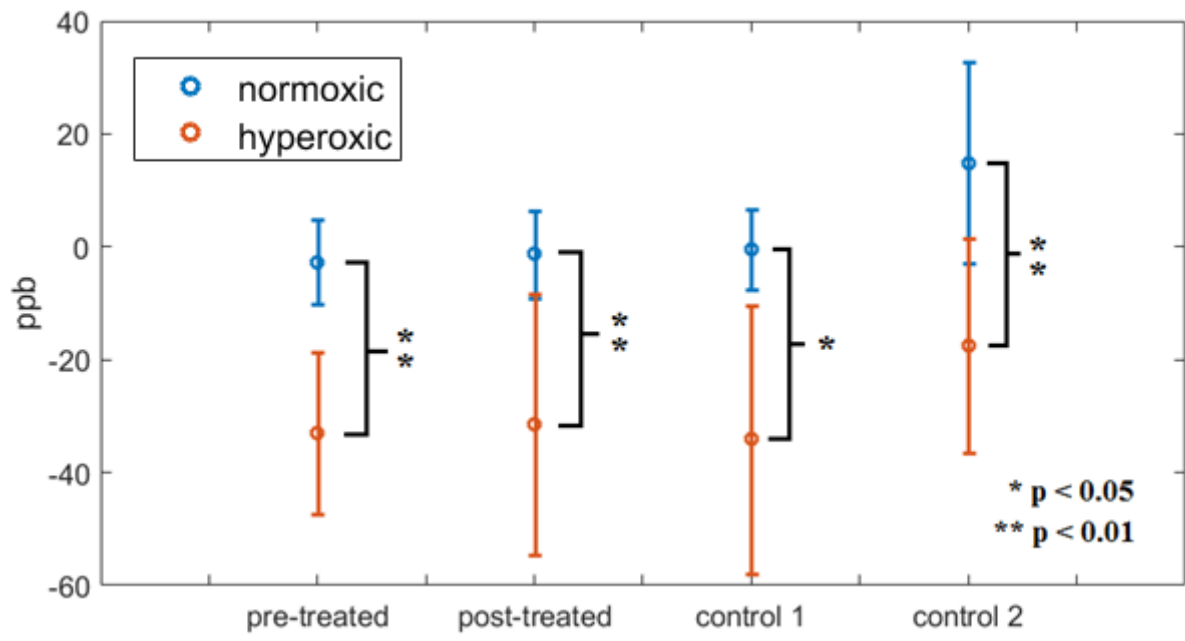


Figure 5.9: Magnetic susceptibility (ppb) of the healthy liver tissue and liver tumours in both groups, at both time-points, under normoxic conditions. The susceptibility of the liver tumours is significantly more diamagnetic than the liver tissue in all cases.

	Healthy Tissue (ppb)	Tumours (ppb)
Pre-treated	-2.64005 ± 7.42	-33.02 ± 21.32
Post-treated	-1.25544 ± 7.73	-31.54 ± 23.16
Control 1	-0.50172 ± 7.16	-34.17 ± 26.41
Control 2	14.88 ± 17.76	-17.5 ± 18.97

Table 5.1: Summary of data presented in fig. 5.9

Figure 5.9 depicts the susceptibility of the liver tumours and healthy liver tissue under normoxic conditions for both groups at both time points. Results are summarised in table 1. In all cases, the susceptibility of the liver tumours was significantly more diamagnetic than the healthy liver tissue. This was as expected given the results of the previous chapter (5.1). There were no significant differences between any group for either region of interest. The susceptibility of the healthy tissue in the control group at the second time point is more paramagnetic than in the other groups, or in any other experiment that has been presented as part of this thesis. This measurement may be artefactual – the tumour burden of some of the animals in this group at this time-point was so large that selecting an ROI that contained only healthy liver tissue was extremely difficult. It is entirely possible that the region in some of the subjects contained large blood vessels, which would account for the relatively paramagnetic susceptibility. This is depicted in figure 5.10, which shows the T_2^* -weighted magnitude images of several mice from the control group acquired at the first time point (left) and the second time-point (right), under normoxic conditions. It is clear that the tumour burden increased to an extreme degree in some cases (e.g. image pair A).

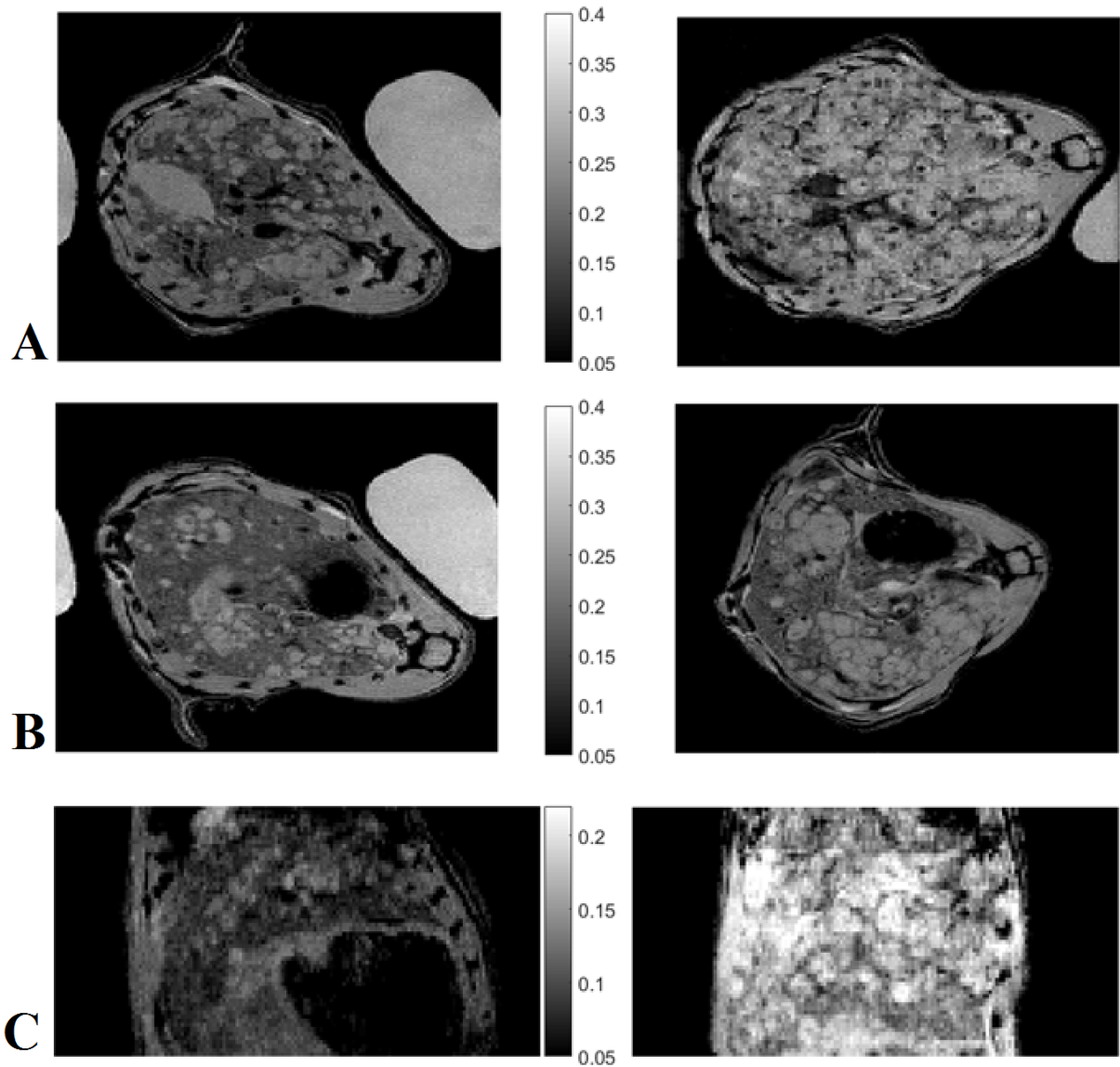
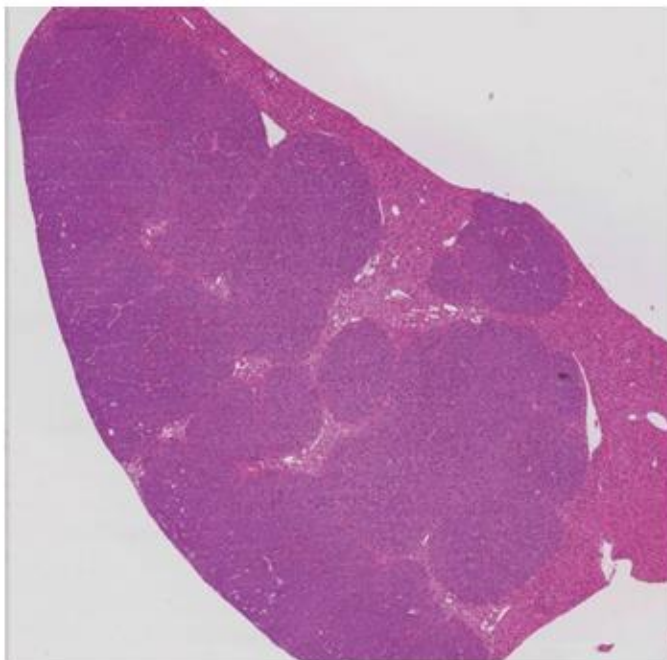


Figure 5.10 A- C: T₂*-weighted magnitude images in axial (A & B) and sagittal (C) orientation, showing extreme tumour burden of control group. Image pairs A, B & C are from 3 mice acquired during the scan sessions 1 & 2

A**B****Figure 5.11 A & B:**

(A) H & E stained histology of liver slice of treated mouse showing necrosis, viable tumour remnant, and tumours unaffected by treatment. Green Arrows: Successfully treated tumours, Yellow Arrows: Viable ring of tumour cells, Grey Arrows: Tumours unaffected by VDA

(B):) H & E stained histology of liver slice of untreated mouse shown for comparison

Figure 5.11 A shows a H&E stained histological image of one liver specimen from the treated group (A) and untreated group (B). As mentioned, the animals were culled immediately after the second MR acquisition. It can be seen from image (A) that the VDA has successfully acted on several of the large tumours (green arrows). The destruction of the tumours is incomplete however, and there is a ring of viable cells visible at their periphery (yellow arrows). This is well documented in the literature, and is attributed to the fact that the tumour periphery is fed by surrounding vessels of the host tissue, which are less susceptible to the effects of the drug ^[38]. For comparison, image B shows a H&E stained histological image of a slice of liver from the untreated group. There is no evidence of the necrosis at the centre of advanced tumours that indicates the result of the administration of the VDA.

Many of the smaller tumours appear unaffected by the treatment (grey arrows). The reason for this may be that the VDA selectively acts on tumour neo-vasculature, which is only necessitated by the tumour after it reaches a certain size ^[41]. It is possible that the tumours which were micro-metastases at the time the drug was administered were sustained by the healthy vasculature of the liver tissue, and continued to grow until the animal was culled. Conversely, it is noted in the literature that the impact of the VDA is immediate, and its effect peaks at ~24 hours after administration, after which time the vasculature begins to regenerate^[41]. The data acquired at the second time-point in this experiment was at 72 hours after the administration of the drug, which may have been enough time to abrogate some of the damage done by the drug.

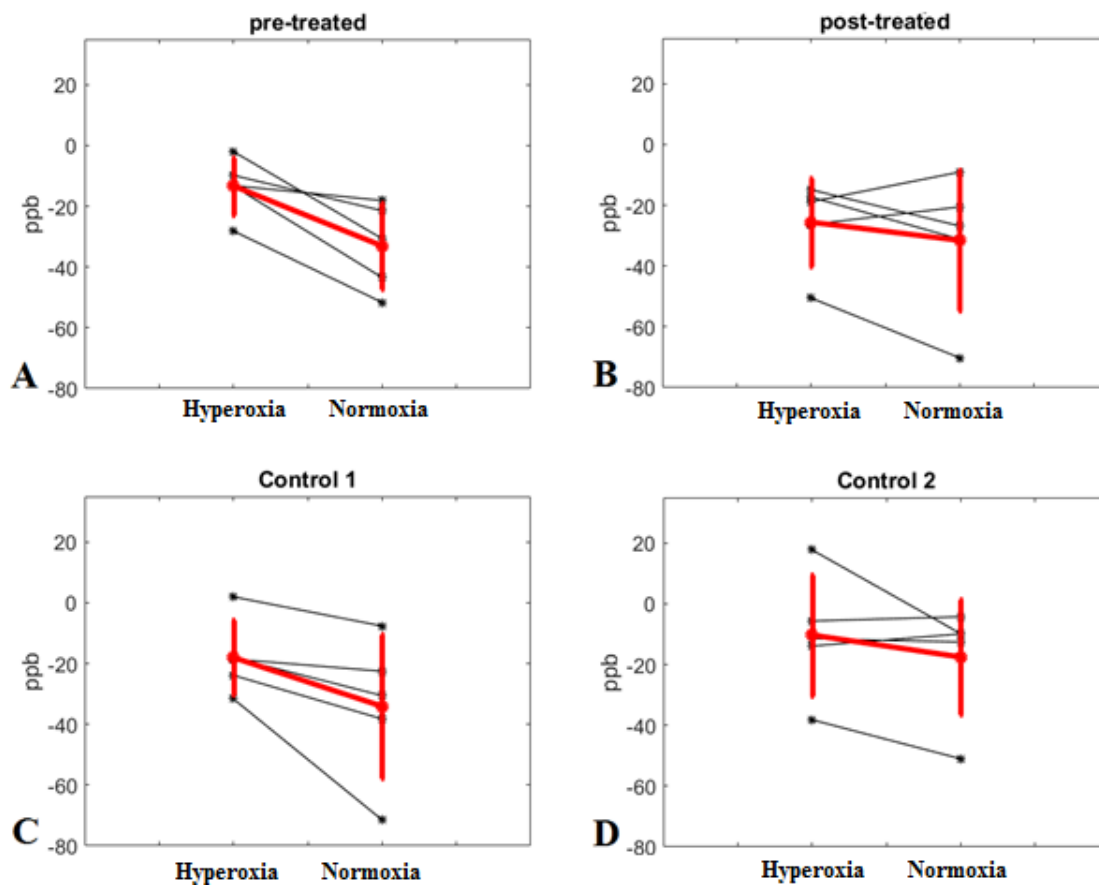


Figure 5.12 A - D: Susceptibility response of the tumours to hyperoxia and normoxia. Results from the first scan session are displayed on the left (A, C), and the corresponding results from the second session are on the right (B, D).

	Hyperoxia (ppb)	Normoxia (ppb)	Difference (ppb)
Pre-treated	-13.26 ± 9.49	-33.02 ± 21.32	19.76
Post-treated	-25.55 ± 14.6	-31.54 ± 23.16	5.99
Control 1	-18.0 ± 12.44	-34.17 ± 26.41	16.17
Control 2	-10.27 ± 20	-17.5 ± 18.97	7.23

Table 5.2: Summary of the results displayed in figure 6 & 7.

Figure 5.12 shows the susceptibility of the tumours in both groups at both time points under hyperoxia and normoxia. The data is summarised in table 2. None of the differences brought about by the gases are significant in any group, however there are some interesting similarities and differences between the groups that merit some discussion. The susceptibility of the tumours calculated from data acquired during the first scan session (A, C) is more paramagnetic under hyperoxia in all cases. Again this is as expected, and it is hypothesised that this is due to the increased influx of paramagnetic, unbound O₂ molecules that diffuse into the tumours from the hepatic artery.

The measurements taken from the data acquired at the second time-point (B, D) are less clear. The mean shift in susceptibility in response to the gases was reduced in both cases by comparison to the first scan session, and the susceptibility of the tumours of the control group (D) was more paramagnetic under *both* gases than any of the other groups.

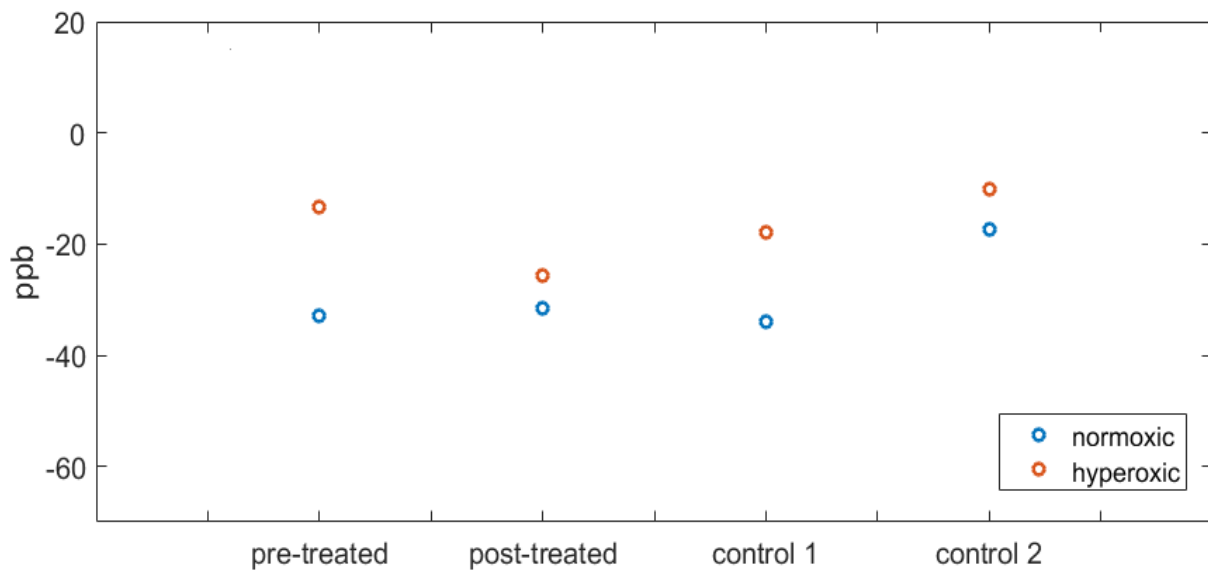


Figure 5.13: Susceptibility response of the tumours to hyperoxia and normoxia displayed on one graph to allow direct comparison between groups. Error bars have been omitted in the interests of clarity.

In order to allow a direct comparison between the results of the gas challenge, the data is presented on a single graph showing the mean susceptibility of the tumours under both hyperoxia and normoxia (Figure 5.13). The mean susceptibility of the tumours under hyper- and normoxic states is similar for both groups at the first time-point (pre-treated, control 1). The susceptibility of each under normoxia is -33.02 ppb and -34.17 ppb for the pre-treated and control 1 subjects respectively, and the *difference* in susceptibility between hyper- and normoxia is 19.76 ppb and 16.17 ppb respectively. This suggests that the treatment and control groups were well matched during the first scan session.

The paramagnetic shift in response to hyperoxia is reduced in the tumours of the post-treated group. Again, the difference in susceptibility brought about by hyperoxia is not statistically significant, but the reduced response of the tumours may be indicative of the effects of the VDA.

This response to hyperoxia is also reduced in control 2, and the susceptibility of the tumours under both normoxic and hyperoxic conditions is more paramagnetic than in the other mice. One possible reason is that the tumour burden in some of the mice was so extensive that the blood supply to the tumours was restricted (figure 5.10). This would have the effect of reducing the delivery of both oxyhaemoglobin and unbound oxygen, thus reducing the diamagnetism of the tumours under normoxic conditions, and undermining the effects of the gas challenge.

Figure 5.14 shows the venous oxygen saturation calculated from the mean susceptibility measured in the hepatic vein of both groups at each time point. The differences between the groups are not statistically significant, but the data suggests that there is a slight increase in the oxygen saturation of the treated group after the drug has been administered. Again, the small size of the groups makes it difficult to draw any conclusion from the results.

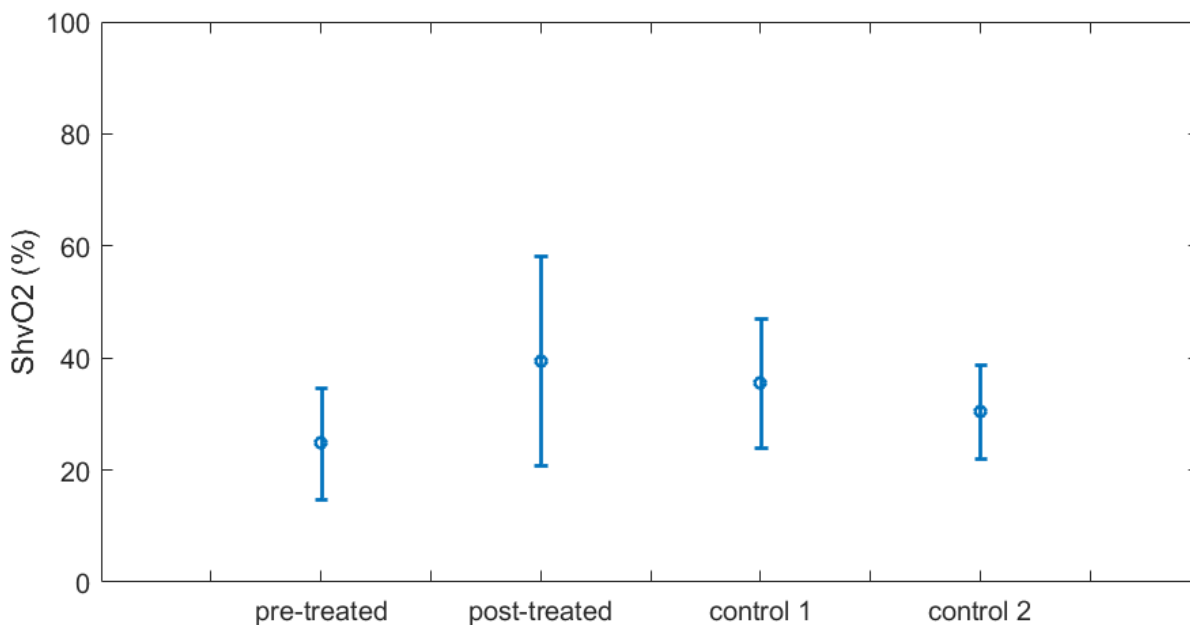


Figure 5.14: ShvO₂ (%) calculated from the measured susceptibility of the blood in the hepatic vein under normoxic conditions. There were no significant differences between the groups or timepoints.

5.2.4 Discussion

The capacity of combretastatins to destroy tumour vasculature has been known about for some time. Oxi4503 is a second generation VDA that has repeatedly been shown to have a deleterious effect on the vasculature of a range of preclinical tumour models, including head and neck squamous cell carcinomas ^[39], KHT sarcomas ^[38], and colorectal liver metastases ^[41, 42]. The efficacy of Oxi4503 has previously been assessed with a range of disparate imaging modalities, however each has drawbacks that may limit their use in various scenarios.

For example, microvascular casting has been used to allow visualisation of the effect of the drug on the vasculature ^[42], but requires the tumours to be excised, usually post-mortem, thus disallowing longitudinal assessment. Similarly, photoacoustic imaging has indicated necrosis at the centre of a treated subcutaneous xenograft ^[43], but the depth penetration currently available with photoacoustic imaging means its use is limited, particularly when attempting to image large, dense organs like the liver. Other studies have used bioluminescent imaging (BLI), or Gd-enhanced MRI to assess changes in tumour

vascularity. Both of these require the use of exogenous contrast agents, rendering them unsuitable for certain cohorts of patients. The advantages offered by QSM are that functional information pertaining to the tumour vasculature can be obtained non-invasively through the effects of deoxyhaemoglobin. The use of an endogenous contrast agent makes it a viable option for a broader cohort of patients, and means that repeated scans can be carried out with little risk to the patient.

The results of gas challenge were inconclusive. There were no significant differences in the susceptibility of the tumours under hyperoxia when compared to normoxia, and there were no significant differences in the susceptibility of the tumours between any group. It was assumed that the VDA would have destroyed the blood vessels supplying the oxygenated blood from the hepatic artery, thus affecting the normoxic susceptibility of the post-treated group, as well as reducing the paramagnetic shift caused by hyperoxia (as was observed). It was shown however that the normoxic susceptibility of the pre- and post- treatment tumours was very similar (table 2).

A major limitation of this study was the fact that the mice were imaged at 72 hours after the administration of the drug. The results of the histology have confirmed the presence of necrosis in some of the tumours that were clearly affected by the administration of the VDA, however it also shows that the smaller tumours were unaffected, and, furthermore, that a peripheral ring of viable tumour remained where the drug did take effect. It is shown in the literature that the effects of the drug manifest most strongly 24 hours after administration^[41], after which point the tumours can begin to regenerate as the drug affects less strongly the cells at the periphery of the tumours. This phenomenon is clearly visible in the fig 5.11. Furthermore, it is equally clear that some of the tumours were unaffected by the drug, which may be due to the fact that micrometastases will most likely be unaffected by the VDA due to the lack of neo-vasculature in small, young tumours. As such, it is possible that the 72 hour time window allowed these micrometastases to continue to grow. Both of these factors would have a negative effect on the experimental variable it was hoped to measure using QSM. The experimental protocol would be greatly improved by imaging the mice 24 hours after the drug was administered.

The difference between the treated and control groups at the second time point (post-treated and control 2) may have been undermined by the extreme tumour burden of the control group (figure 5.10). Chronic hypoxia limits the diffusion of oxygen to cells that are

distal from the blood vessels, and acute hypoxia restricts the flow of blood into the tumours. Both conditions are exacerbated by an increased tumour load, and could also have had the effect of confounding the results. Both of these situations could have been avoided if the second scan session had been performed at an earlier time-point.

The differences between the groups in terms of ShvO₂ were equally inconclusive. While the data suggests that there was some divergence between the pre- and post-treated animals, the underpowered nature of the study has limited the conclusions that can be drawn. Based on the results of the last experiment however it is entirely conceivable that ShvO₂ could be used as a metric to assess treatment efficacy, however as mentioned this would require more work to characterise the correlations of oxygen saturation with tumour burden.

The treated cohort in this study were administered a single dose of 40 mg/kg of the drug. This is broadly in line with similar experiments ^[39, 42], though single doses range from 1 – 100 mg/kg, and comparisons have been made between single doses and continuous, daily and intermittent dosing ^[42] where it was shown that intermittent dosing produced the greatest reduction in tumour growth. As such, an improvement to the experimental approach described in this chapter could be to recommend that the treated subjects receive intermittent doses of the drug, or that imaging take place 24 hours after the administration of a single dose. Furthermore, increasing the numbers in each group would have allowed a more powerful statistical analysis, such that the results could be expressed with a greater degree of confidence.

A common metric used in similar studies has been to compare the mass of treated and untreated livers as a proxy for tumour burden, or to measure tumour necrosis via histology, however it has been suggested that a more accurate assessment of drug efficacy would measure the remaining viable tumour ^[41]. While it was not possible in this instance, it is conceivable that using QSM to measure the response of a single tumour to a gas challenge could yield information regarding the amount of viable vasculature present after treatment without the use of exogenous contrast agents.

The results of this experiment would benefit from the inclusion of more in-depth histopathological analysis. While the standard H & E stained images sufficiently showed the necrosis of the tumours that were affected by the VDA, more information could have been gleaned by the expansion of the imaging protocol. For example, intravenous injection of pimonidazole between the administration of the VDA and the second scanning session may

have confirmed hypoxia in tumours that were initially affected by the drug but then recovered. Equally, some of the mice could have been imaged using a dynamic contrast enhanced (DCE) protocol to discern changes in tumour blood flow caused by the VDA. It may then have been possible to compare DCE and QSM images of tumours, although, as already noted, drawing comparisons between individual tumours is extremely difficult in the liver due to the amorphous nature, and high degree of movement of the organ between scans. These limitations may be difficult to address however, as the mice under examination do not tolerate the administration of drugs, stains or anaesthetic well, and so the inclusion of additional imaging techniques may require redesigning the protocol of the entire experiment.

5.2.5 Conclusions

Though not statistically significant the difference in hepatic venous blood oxygen in between the pre- and post-treated groups reflects the results presented in section 5.1. It is conceivable the measurement of $ShvO_2$ with QSM could be used to assess the efficacy of the VDA, however further experimental work is required to confirm this.

References

1. Acosta-Cabronero, J., et al., *In vivo quantitative susceptibility mapping (QSM) in Alzheimer's disease*. PLoS One, 2013. **8**(11): p. e81093.
2. Barbosa, J.H., et al., *Quantifying brain iron deposition in patients with Parkinson's disease using quantitative susceptibility mapping, R2 and R2*. Magn Reson Imaging, 2015. **33**(5): p. 559-65.
3. Schweitzer, A.D., et al., *Quantitative susceptibility mapping of the motor cortex in amyotrophic lateral sclerosis and primary lateral sclerosis*. AJR Am J Roentgenol, 2015. **204**(5): p. 1086-92.
4. Du, G., et al., *Quantitative susceptibility mapping of the midbrain in Parkinson's disease*. Mov Disord, 2016. **31**(3): p. 317-24.
5. Wang, S., et al., *Hematoma volume measurement in gradient echo MRI using quantitative susceptibility mapping*. Stroke, 2013. **44**(8): p. 2315-7.
6. Xia, S., et al., *Decreased oxygen saturation in asymmetrically prominent cortical veins in patients with cerebral ischemic stroke*. Magn Reson Imaging, 2014. **32**(10): p. 1272-6.
7. Hsieh, M.C., et al., *Investigating hyperoxic effects in the rat brain using quantitative susceptibility mapping based on MRI phase*. Magn Reson Med, 2017. **77**(2): p. 592-602.
8. Zhang, J., et al., *Quantitative mapping of cerebral metabolic rate of oxygen (CMRO₂) using quantitative susceptibility mapping (QSM)*. Magn Reson Med, 2015. **74**(4): p. 945-52.
9. Ozbay, P.S., et al., *Effect of respiratory hyperoxic challenge on magnetic susceptibility in human brain assessed by quantitative susceptibility mapping (QSM)*. NMR Biomed, 2015. **28**(12): p. 1688-96.
10. Fan, A.P., et al., *Baseline oxygenation in the brain: Correlation between respiratory-calibration and susceptibility methods*. Neuroimage, 2016. **125**: p. 920-31.
11. Deistung, A., et al., *Quantitative susceptibility mapping differentiates between blood depositions and calcifications in patients with glioblastoma*. PLoS One, 2013. **8**(3): p. e57924.
12. Straub, S., et al., *Potential of quantitative susceptibility mapping for detection of prostatic calcifications*. Journal of Magnetic Resonance Imaging, 2017. **45**(3): p. 889-898.
13. Edrei, Y., et al., *Vascular Profile Characterization of Liver Tumors by Magnetic Resonance Imaging Using Hemodynamic Response Imaging in Mice*. Neoplasia, 2011. **13**(3): p. 244-IN5.
14. *Liver cancer statistics*. 2015.
15. Xu, L.H., et al., *Imaging diagnosis of colorectal liver metastases*. World J Gastroenterol, 2011. **17**(42): p. 4654-9.
16. Haddad, A.J., et al., *Colorectal liver metastases*. Int J Surg Oncol, 2011. **2011**: p. 285840.
17. Choti, M.A., et al., *Patient Variability in Intraoperative Ultrasonographic Characteristics of Colorectal Liver Metastases*. Arch Surg, 2008. **143**(1): p. 29 - 34.
18. Tzeng, C.W. and T.A. Aloia, *Colorectal liver metastases*. J Gastrointest Surg, 2013. **17**(1): p. 195-201; quiz p 201-2.
19. Bipat, S., et al., *Colorectal Liver Metastases: CT, MR imaging meta analysis*. Radiology, 2005. **237**: p. 123 - 131.

20. Bonanni, L., et al., *A comparison of diagnostic imaging modalities for colorectal liver metastases*. Eur J Surg Oncol, 2014. **40**(5): p. 545-50.
21. Niekel, M.C., S. Bipat, and J. Stoker, *Diagnostic Imaging of Colorectal liver metastases with CT, MR imaging, FDG PET, and/or FDG PET/CT: A meta-analysis of prospective studies including patients who have not previously undergone treatment*. Radiology, 2010. **257**(3): p. 674 - 684.
22. Robinson, S.P., et al., *Magnetic Resonance Imaging Techniques for monitoring changes in tumour oxygenation and blood flow*. Semin Radiat Oncol, 1998. **8**(3): p. 197 - 207.
23. Ramasawmy, R., et al., *Hepatic arterial spin labelling MRI: an initial evaluation in mice*. NMR in Biomedicine, 2015. **28**(2): p. 272-280.
24. Haugeberg, G., et al., *The vascularization of liver metastases*. J Cancer Res Clin Oncol, 1988. **114**(415 - 419).
25. Fidarova, E.F., et al., *Microdistribution of Targeted, Fluorescently Labeled Anti-Carcinoembryonic Antigen Antibody in Metastatic Colorectal Cancer: Implications for Radioimmunotherapy*. Clinical Cancer Research, 2008. **14**(9): p. 2639-2646.
26. Jordan, B.F. and P. Sonveaux, *Targeting tumor perfusion and oxygenation to improve the outcome of anticancer therapy*. Front Pharmacol, 2012. **3**: p. 94.
27. Padhani, A.R., *Diffusion magnetic resonance imaging in cancer patient management*. Semin Radiat Oncol, 2011. **21**(2): p. 119-40.
28. Robinson, S.P., et al., *Effects of different levels of hypercapnic hyperoxia on tumour R2s and areterial blood gases*. Magnetic Resonance Imaging, 2001. **19**: p. 161 - 166.
29. Karczmar, G.S., et al., *Effects of hyperoxia on T2* and resonance frequency weighted magnetic resonance images of rodent tumours* NMR Biomed, 1994. **7** (1-2): p. 3 -11.
30. Fan, Z., et al., *Blood Oxygen Level-Dependent Magnetic Resonance Imaging of the Human Liver: Preliminary Results*. Journal of Computer Assisted Tomography, 2010. **34**(4): p. 523-531.
31. Barash, H., et al., *Functional magnetic resonance imaging monitoring of pathological changes in rodent livers during hyperoxia and hypercapnia*. Hepatology, 2008. **48**(4): p. 1232-41.
32. Xu, F., et al., *Effect of Hypoxia and Hyperoxia on Cerebral Blood Flow, Blood Oxygenation, and Oxidative Metabolism*. Journal of Cerebral Blood Flow & Metabolism, 2012. **32**(10): p. 1909-1918.
33. Shmueli, K., et al., *Magnetic susceptibility mapping of brain tissue in vivo using MRI phase data*. Magn Reson Med, 2009. **62**(6): p. 1510-22.
34. Tao, R., et al., *An in vitro and in vivo analysis of the correlation between susceptibility-weighted imaging phase values and R2* in cirrhotic livers*. PLoS One, 2012. **7**(9): p. e45477.
35. Misiakos, E.P., N.P. Karidis, and G. Kouraklis, *Current treatment for colorectal liver metastases*. World J Gastroenterol, 2011. **17**(36): p. 4067-75.
36. Van Cutsem, E., et al., *Imaging in Colorectal Cancer: Progress and Challenges for the Clinicians*. Cancers (Basel), 2016. **8**(9).
37. Tirumani, S.H., et al., *Update on the Role of Imaging in Management of Metastatic Colorectal Cancer*. RadioGraphics, 2014. **34**(7): p. 1908-1928.
38. Salmon, H.W. and D.W. Siemann, *Effect of the second-generation vascular disrupting agent OXi4503 on tumor vascularity*. Clin Cancer Res, 2006. **12**(13): p. 4090-4.

39. Bothwell, K.D., M. Folaron, and M. Seshadri, *Preclinical Activity of the Vascular Disrupting Agent OXi4503 against Head and Neck Cancer*. *Cancers (Basel)*, 2016. **8**(1).
40. Sheng, Y., et al., *Combretastatin family member OXI4503 induces tumor vascular collapse through the induction of endothelial apoptosis*. *Int J Cancer*, 2004. **111**(4): p. 604-10.
41. Nguyen, L., T. Fifis, and C. Christophi, *Vascular disruptive agent OXi4503 and anti-angiogenic agent Sunitinib combination treatment prolong survival of mice with CRC liver metastasis*. *BMC Cancer*, 2016. **16**(1): p. 533.
42. Malcontenti-Wilson, C., et al., *Vascular targeting agent Oxi4503 inhibits tumor growth in a colorectal liver metastases model*. *J Gastroenterol Hepatol*, 2008. **23**.
43. Johnson, S.P., et al., *Photoacoustic assessment of OXi4503 pharmacodynamic effect and tumour vessel regrowth in colorectal carcinoma xenograft models of cancer*. *Conference Proc. Nat Cancer Research Inst*, 2013.

Chapter 6

Chapter 6 details the application of QSM to a model of liver cirrhosis. Data was acquired from a cohort of rats in which cirrhosis had been induced by bile duct ligation, as well as a cohort that had been subject to a sham operation. Susceptibility was measured in the liver tissue and major blood vessels of both sets of animals.

Liver Cirrhosis

6.1 Introduction

Liver fibrosis is characterised histologically by the presence of excess collagen caused by chronic inflammation ^[1]. Early stage fibrosis is potentially reversible, and causes only minor clinical symptoms or disturbance of liver function. Liver cirrhosis occurs in the final stage of liver fibrosis. It is an irreversible development, the transition to which involves inflammation, activation of hepatic stellate cells, and parenchymal extinction due to vascular occlusion ^[2]. Normal hepatic architecture is replaced with a spectrum of partially restorative nodules surrounded by fibrous bands, resulting in portal hypertension, hepatic perivascular shunting, and ultimately end-stage liver disease ^[3]. Normal liver function and perfusion are increasingly compromised as fibrosis progresses ^[4].

The severity of liver fibrosis is gauged using a series of histological gradations ranging from 0 - 4, with stage 4 liver fibrosis being equivalent to cirrhosis ^[5]. There are myriad factors that precipitate fibrosis, however all aetiologies of cirrhosis lead to the same pathology. Fibrosis and cirrhosis are often asymptomatic until patients present with ambiguous ailments, at which point blood testing may reveal abnormal liver function ^[3]. The extent of fibrosis will strongly influence the treatment pathway embarked upon, so accurate estimation of its progression is an important facet of the initial diagnosis.

Upon suspicion of cirrhosis there are numerous diagnostic procedures available to clinicians. Histological evaluation via liver biopsy remains the gold standard ^[3], but it is prone to sampling error, and the invasive nature of the procedure renders it unsuitable in many instances. Equally, there are a range of serum markers that are useful for differentiating between fibrosis and cirrhosis, but these often lack the accuracy required for differentiating between the early stages of fibrosis ^[6], particularly in cases of inflammation ^[7]. Conversely, there are a number of imaging modalities that can provide non-invasive assessment, but traditionally the primary role of radiography is the determination and assessment of the complications that accompany cirrhosis e.g. ascites or hepatocellular carcinoma ^[3].

In recent years, a number of novel imaging techniques have been developed that could allow accurate, non-invasive staging of fibrosis and cirrhosis. Magnetic Resonance Elastography (MRE) analyses the propagation of a mechanical wave generated by an external driver through the liver tissue. An overabundance of collagen will affect the stiffness of the

tissue, and subsequently the velocity and wavelength of the propagating wave. MRE has been shown to have a sensitivity of 98% and a specificity of 99% for diagnosing any grade of liver fibrosis ^[8], though it is noted in the literature that the MRE signal may be poor in patients with moderate to severe iron load, leading to failed examinations ^[6]. This may prove problematic, as siderosis is a known facet of advanced liver fibrosis.

Of particular interest in this instance are the phase based approaches to MRI imaging. One such technique is Susceptibility Weighted Imaging (SWI), the precursor to QSM. It too utilises the phase of a T_2^* -weighted signal, so is sensitive to compositional variations that affect magnetic susceptibility, however it uses this information to enhance its associated magnitude image. The accumulation of iron within reticuloendothelial cells is known to occur with the progression of fibrosis as ferritin is mobilised from damaged hepatocytes ^[9], and on this basis it has been shown that the detection and grading of liver fibrosis is feasible with SWI ^[7]. Furthermore, cirrhotic liver iron can also accumulate in the regenerative nodules associated with the disease, and it has been shown that SWI can more accurately identify siderotic nodules in the cirrhotic liver than conventional magnitude-based MRI techniques ^[9, 10]. Susceptibility weighted imaging, while more sensitive to iron deposition than conventional techniques, is not, however, quantitative in nature, and is beset by the blooming artefacts that can also be detrimental to T_2^* -weighted imaging. The latter in particular could prove problematic when performing liver imaging due to the relative size of the blood vessels.

The aim of this study was to apply QSM to a preclinical model of liver cirrhosis implemented in a cohort of Bile Duct Ligated (BDL) rats, and in doing so test three hypotheses. In the first instance, QSM overcomes the aforementioned quantification and non-locality problems that are inherent to SWI, and it is thought that the quantitative nature of the technique may allow a more accurate assessment of excess hepatic iron. To test this, the susceptibility of the liver tissue was measured under normoxic conditions, and compared to that of a sham cohort. Secondly, it has been shown that the livers of cirrhosis patients exhibit a significant enhancement of the T_2^* signal when administered pure O_2 that was not observed in healthy volunteers ^[11]. As such, the sensitivity of QSM to the changes in liver perfusion associated with advanced fibrosis was assessed by administering a hyperoxic gas challenge to the BDL rats, and comparing the change in susceptibility of the BDL and sham cohorts. Finally, it has been suggested in the literature that the progression of liver disease correlates inversely with tissue oxygen uptake ^[12]. As such, the final hypothesis explored here is that a

reduction in oxygen extraction from the blood by the liver tissue will be reflected in the hepatic venous oxygen saturation ($ShvO_2$) of the BDL cohort. To test this, $ShvO_2$ was calculated from the measured susceptibility of the blood in the hepatic vein and was compared to that of the sham cohort.

6.2 Theory

6.2.1 Cirrhosis Model

Cirrhosis in this instance was induced using via bile duct ligation (BDL) in order to implement obstructive cholestasis in the livers of the experimental subjects. Ligation of the duct is achieved via surgical means, and disrupts the secretion of bile causing it to accumulate in the liver tissue. The compounds of which bile is comprised e.g. bile salts, bilirubin, as well as the potentially toxic compounds that result from the clearance function of the liver result cause inflammation of the liver tissue, as well as the progressive development of fibrosis. The process ultimately results in liver failure, or progression to liver cancer^[13].

6.3 Methods

6.3.1 Animal preparation

Surgical preparations were performed as previously reported^[14]. Briefly, male Sprague-Dawley rats (body weight 350 – 400g) were obtained from Charles River Laboratories (Kent, UK). Under general anaesthesia (5% isoflurane in 100% O_2 for induction, 2% in air for maintenance) 30 rats underwent triple ligation of the bile duct (via laparotomy) to induce chronic liver injury. A number of rats ($n = 7$) were randomly selected for inclusion in the experiment presented here, and were imaged approx.. 4 weeks after surgery.

In addition to this, a number of rats that had undergone a sham operation ($n = 3$) were also selected for inclusion. However, one of these died while under anaesthetic in the scanner and was excluded from the study.

6.3.2 Data acquisition

Data were acquired on a 9.4T MRI scanner (Agilent Technologies, Santa Clara, CA, USA) using a 72-mm-diameter bird cage coil for signal transmission and reception (RAPID Biomed, Rimpfing, Germany). Subjects were anaesthetised using 5% isoflurane in 20% O₂, 80% medical air. During scanning, respiratory rate was monitored and maintained at ~60 - 70 breaths per minute by varying isoflurane concentration between 1.5 and 3%. Rectal temperature was maintained at $37.5 \pm 0.5^{\circ}\text{C}$ using a warm water circulation system.

Gases were administered through a nose cone at a rate of 1 ltr/min. Images were acquired under normoxic conditions as the subject was administered medical air (21% O₂/balance Nitrogen), and again under hyperoxic conditions as the subject was administered 100% O₂. 10 minutes were allowed between gases to allow the animal to acclimatise.

The acquisition parameters were as such: TR = 1000 ms, TE = 4 ms, FA = 70° , voxel size = 300 μm isotropic, acquisition bandwidth = 50 kHz, number of averages = 4. The FOV was adjusted such that the entire liver and water reference were imaged (see Chap. 4A sec. 4A.1.1), and the matrix size was adjusted to maintain isotropic voxel size.

Regions of interest were manually segmented on the magnitude images and transferred to QSM images after processing. ROIs included a large branch of the hepatic vein, which was segmented as discussed previously (see Chap. 4 sec. 4.1.2.5). In this instance, large regions of liver tissue were segmented because disruption to the liver architecture was not obvious from signal intensity changes in the magnitude image so as much tissue was included for examination as possible while avoiding large blood vessels (fig 6.1).

QSM processing (chap. 4 sec. 4.1.2.3) and venous oxygen saturation calculations (chap. 4 sec. 4.2.2.2) were performed as discussed in previous chapters.

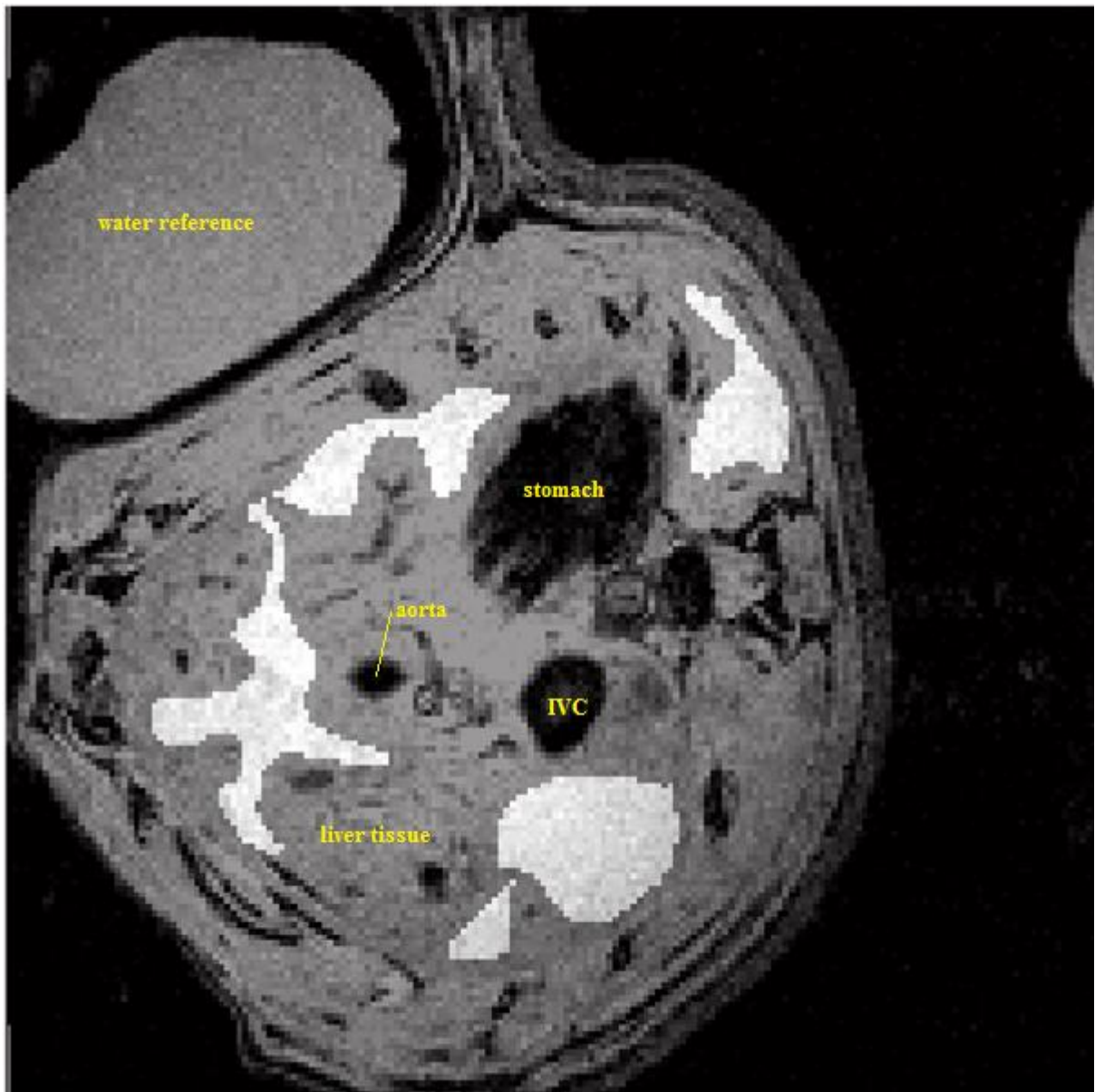


Figure 6.1: Slice showing liver tissue ROI on T_2^* - magnitude image (axial orientation). Due to the diffuse nature of the disease the ROI included as much liver tissue as possible, while avoiding any obvious blood vessels. As such, the tissue ROI included many slices in the liver volume.

6.3.3 Statistics

The diminutive size of the sham cohort precluded any meaningful statistical comparison between the groups, or within the sham cohort brought about by means of intervention (i.e. the gas challenge).

Where possible, parameter estimates were compared using a Wilcoxon matched-pairs signed rank test, in which a difference was considered statistically significant for $p < 0.05$.

6.4 Results

Figures 6.2 & 6.3 contain a T_2^* -weighted magnitude, raw phase, frequency map and susceptibility map of a subject each from the BDL (figure 6.2) and sham cohort (figure 6.3). Each image of every animal was subjected to the same visual inspections detailed elsewhere (chap. 5 sec 5.1.3), and all acquired data was deemed fit for inclusion in the study. As in the other experiments, frequency maps and subsequent susceptibility maps were calculated without issue.

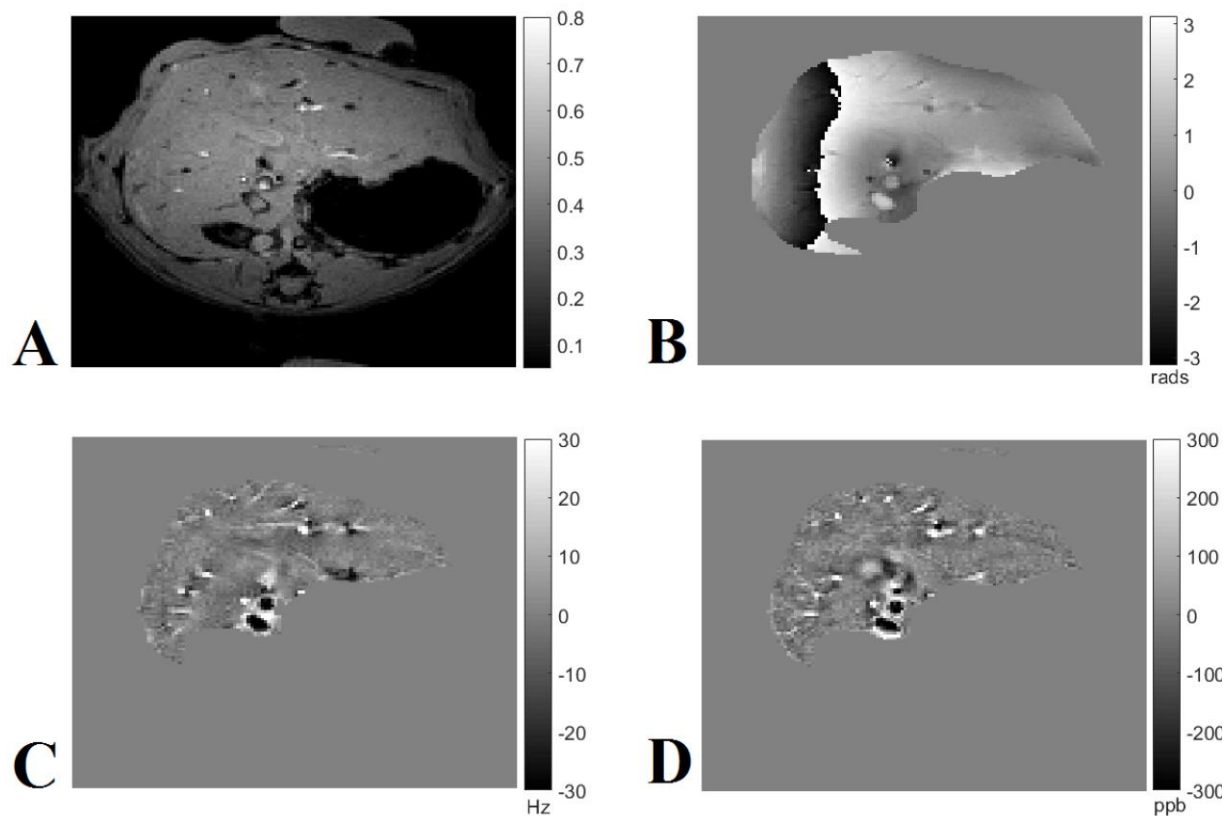


Figure 6.2 A- D: T_2^* -weighted magnitude (A), raw phase (B), frequency map (C) and susceptibility map (D) of a single animal from the **BDL** cohort.

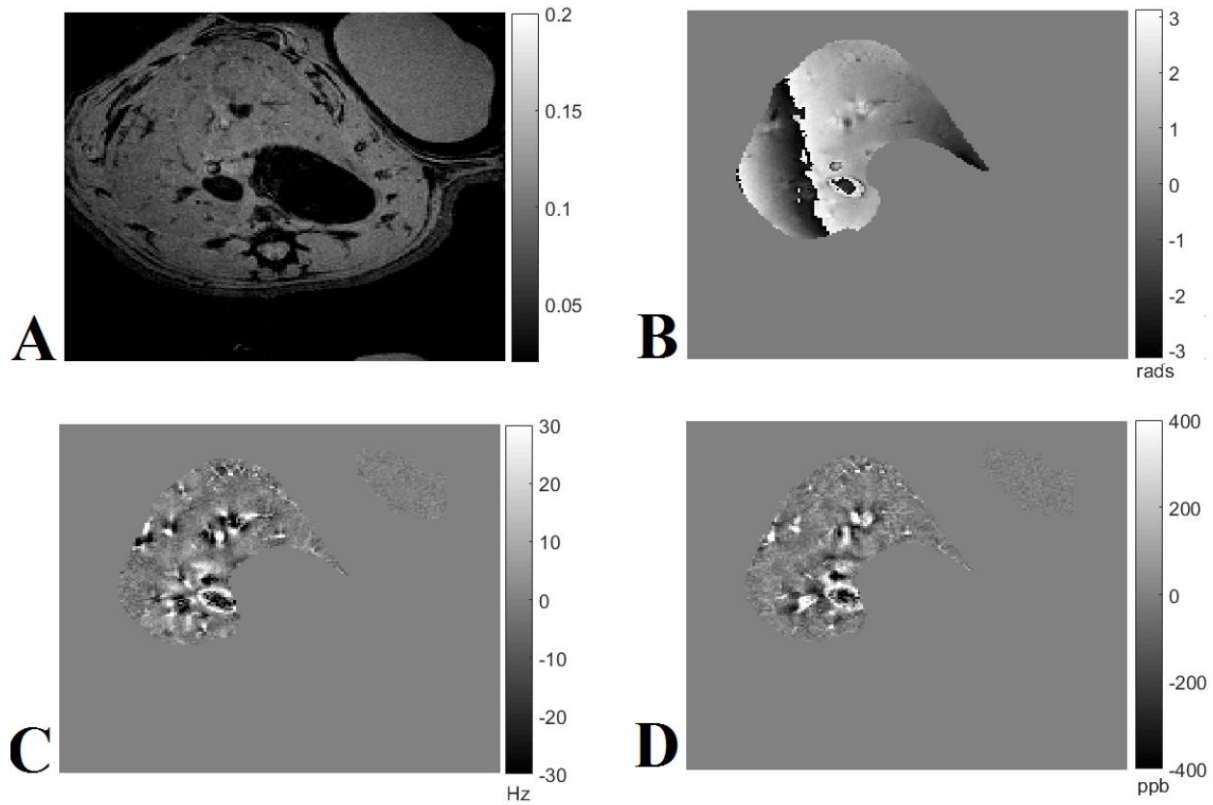


Figure 6.3 A - D: T_2^* -weighted magnitude (A), raw phase (B), frequency map (C) and susceptibility map (D) of a single animal from the **sham** cohort.

Figure 6.4 depicts the susceptibility (ppb) of the liver tissue in the BDL and sham animals under normoxic conditions. The mean values were -0.825 ± 5.97 ppb and -1.77 ± 0.366 ppb for the BDL and sham animals respectively. The difference between the cohorts was not significant.

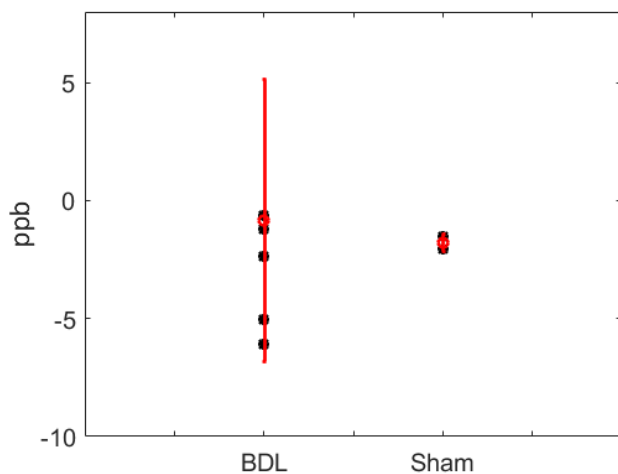


Figure 6.4: Magnetic susceptibility (ppb) of liver tissue of the BDL and sham animals. There was no significant difference between the cohorts.

Figure 6.5 is an image taken from the literature^[15] that shows segments taken from the livers of sham (a) and BDL model (b) rats, that have been histologically stained with Perl's iron stain. There is a small build-up of iron in the Kuppfer cells of the BDL model animals, however it would appear from the images that the change in liver iron content may not be enough to have a significant impact on the QSM measurements of the liver tissue of similar animals. This may explain the lack of significant difference between the QSM measurements taken from either cohort.

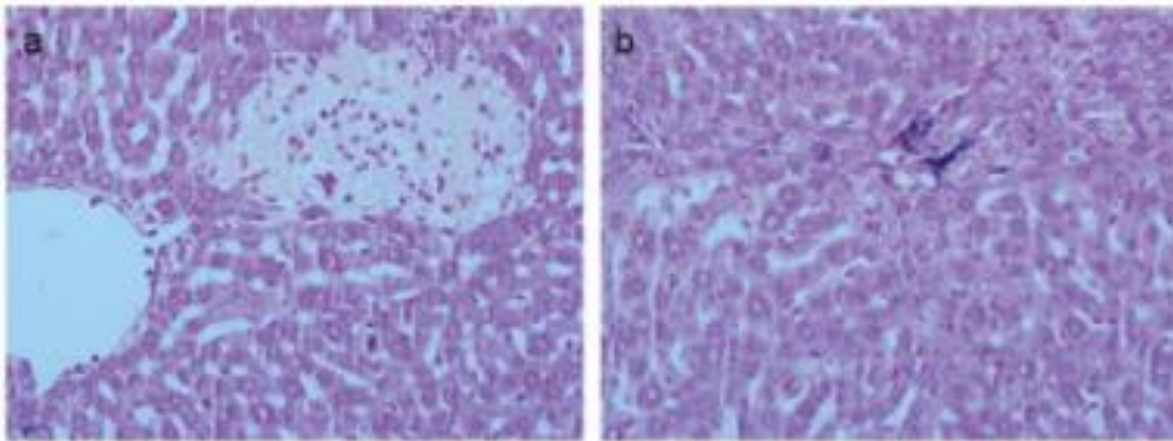


Figure 6.5 A & B: Perl stained histological images of liver segments from a sham (a) and BDL model rat (b). (Taken from the literature) This shows the iron accumulated in the liver of each animal. There is a slight build-up of iron in the kupffer cells of the BDL rats that is not present in the sham cohort.

Figure 6.6 contains graphs showing the susceptibility measured in the liver tissue of the BDL (A) and sham (B) cohorts. The results are summarised in table 1. There was no significant difference in susceptibility brought about by the gas challenge, and there were no significant differences between the groups. The data suggests that the liver tissue of the BDL rats is slightly more paramagnetic than that of the sham cohorts, but low numbers of sham animals makes it difficult to draw any conclusion.

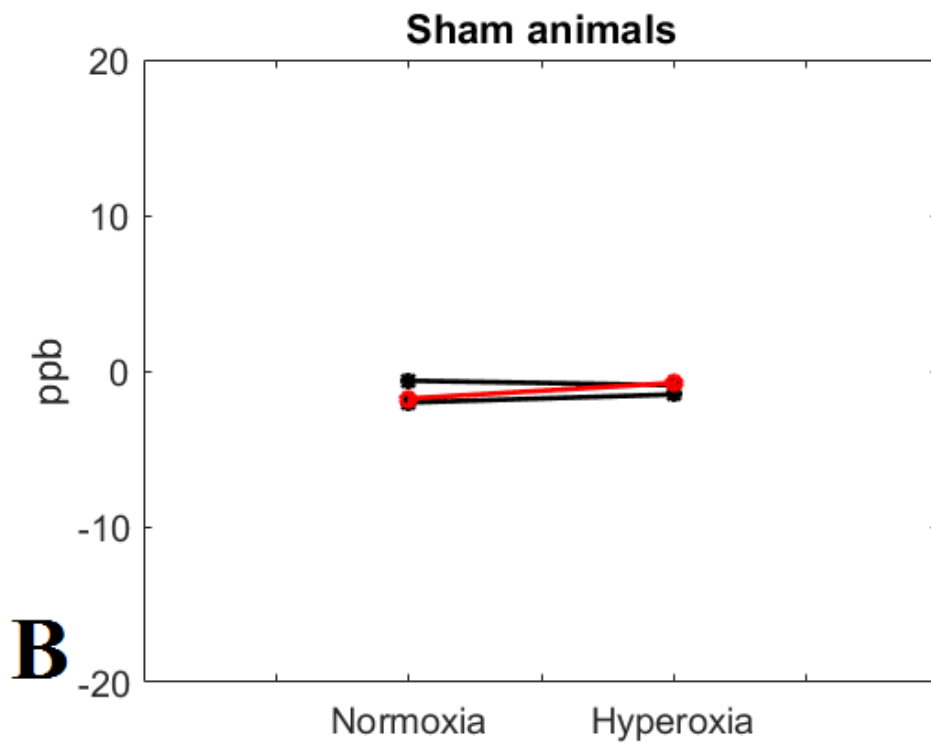
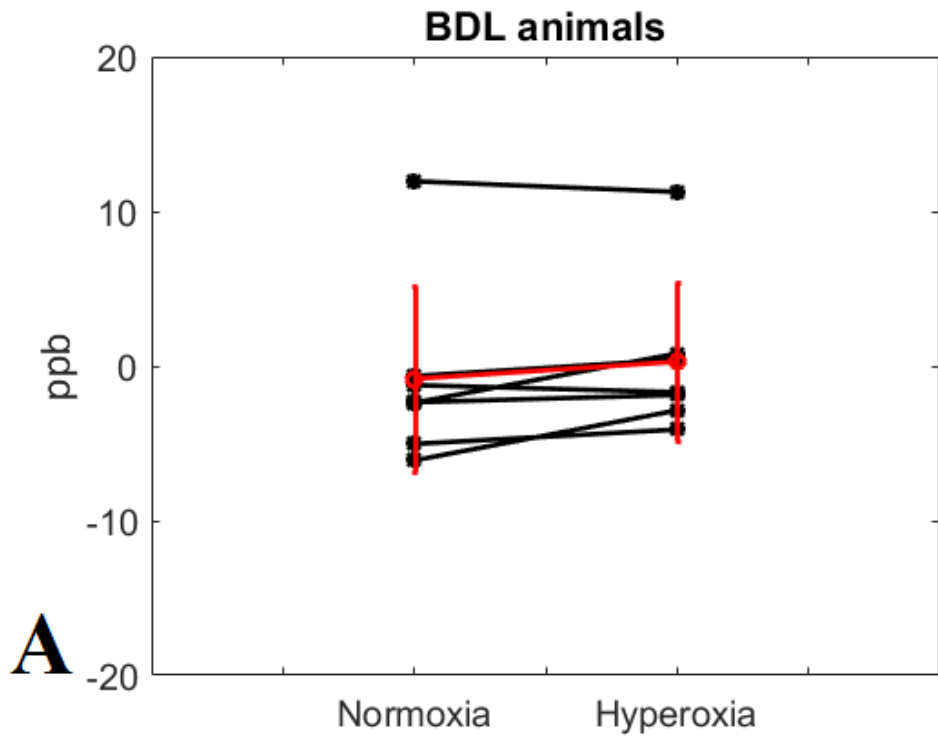


Figure 6.6 A & B: Susceptibility of liver tissue under norm- and hyperoxia measured in the BDL rats (A) and the sham rats (B)

	Normoxia (ppb)	Hyperoxia (ppb)
BDL (mean)	-0.825 ± 5.97	0.28 ± 5.14
Sham (mean)	-1.77 ± 0.36	-0.77 ± 0.202

Table 6.1: Summary data of the susceptibility of the liver tissue in either cohort under norm- and hyperoxia. Mean and SD displayed.

Figure 6.7 shows the venous oxygen concentration calculated from the measured susceptibility of the blood in the hepatic vein. The mean values were $48.87 \pm 13.8\%$ and $29.17 \pm 25.71\%$ for the BDL and sham rats respectively. The difference between the cohorts was not significant but the data suggests that the oxygen saturation of the blood from the BDL cohort is the higher of the two.

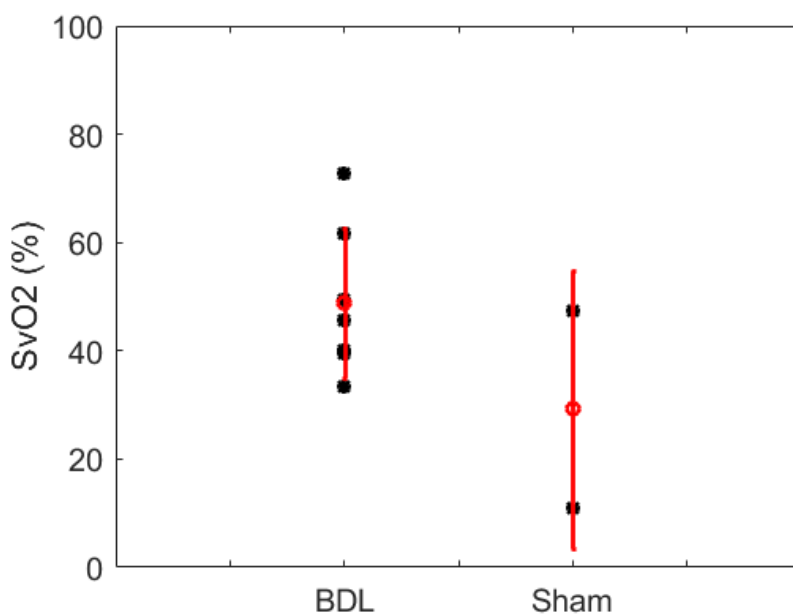


Figure 6.7: Venous Oxygen Saturation calculated from the susceptibility of the blood measured in the hepatic vein. There was no significant differences between the groups, but the data suggests that there $ShvO_2$ is higher in the BDL cohort.

6.5 Discussion

Liver disease is one of the largest causes of mortality in the UK, and is the only major cause of death still increasing year on year ^[16]. Diagnosis is notoriously difficult as most patients don't present until experiencing secondary symptoms such as ascites, sepsis, or encephalopathy, among others ^[2]. While it is not possible to reverse the sclerosis of the liver tissue, it is often possible to delay its progression or prevent further damage, as well as treat other complications that may arise.

It is increasingly accepted that cirrhosis is a dynamic process that is no longer a terminal condition ^[2]. The standard METAVIR system used to gauge the severity of fibrosis does not have a grade past cirrhosis, and a new sub-classification system has been proposed to gauge the severity of cirrhosis and the likelihood of mortality at each stage. For patients in the advanced stages of cirrhosis, these further prognostic scores are widely used to predict survival and the need for transplant. As such, the development of accurate, non-invasive diagnostic modalities is becoming increasingly important.

The susceptibility of the liver tissue measured in this experiment is consistent with the other experiments presented in this thesis, i.e. the susceptibility of the cirrhotic liver tissue as measured in QSM images is approximately the equal to that of the water reference, indicating no increase in hepatic iron in the BDL rats. In the previous mouse experiments it was shown histologically that the amount of iron present in the liver was minimal (chap. 4 fig. 4.10) , however it is known that the accumulation of excess liver iron is a facet of advanced liver diseases including cirrhosis. The findings in this experiment are in contrast with the expected results based on the findings of similar studies that have shown that shown that it is feasible to use changes in liver iron to accurately stage liver fibrosis such that susceptibility estimates correlate well with liver biopsies ^[17] and R_2^* measurements ^[18]. The reasons for this are unclear, however it may be the case that iron over load is not as prevalent in this model as was assumed (fig. 6.5).

Based on the results of a similar experiment ^[11], it was expected that a hyperoxic gas challenge would induce a meaningful shift in susceptibility from baseline (normoxic) conditions. This was not the case. In the experiment conducted by Patterson et. al., the significant increase in T_2^* observed in the livers of patients suffering from cirrhosis was hypothesised to be caused by a breakdown in the auto-regulatory mechanisms of the liver vasculature. The data suggests a paramagnetic shift in the susceptibility of almost all of the

animals in the BDL cohort (figure 6.6) in response to the gas challenge, but the difference was miniscule i.e. on the order of a few parts per billion.

The difference in oxygen extraction between cirrhotic and healthy livers is the subject of conflicting reports in the literature. It has been shown previously that oxygen uptake in patients with liver cirrhosis had an inverse relationship with the severity of the disease (as determined by Pugh score) ^[19]. One hypothesis to explain this was that this was due to an abnormal limitation of tissue extraction caused by the disease. Conversely, while it has been shown that $ShvO_2$ reflects the hepatic oxygen supply/demand ratio ^[20], it has also been shown in several studies that, despite the disruption to liver perfusion, there is no difference between the hepatic venous oxygen content of healthy and cirrhotic livers as measured in both preclinical and clinical studies ^[21, 22]. The data here would suggest that there is a reduction in the amount of O_2 extracted from the blood in the BDL animals, but due to the low numbers of the sham cohort, no conclusion could be reached.

This experiment encountered a number of limitations. Most importantly, the study is underpowered. More control animals are required to draw meaningful conclusions from the results. The reason the number of sham animals was so limited was that this experiment was outside of the initial scope of the project, which had originally intended to perform mouse experiments only. During the course of the PhD however, the opportunity presented itself to examine another disease model which had previously been unavailable. As the animals were intended for another study this resulted in a number of additional limitations. Firstly, obtaining the animals proved quite difficult due to clashes in the experimental calendars of this and the other study. Secondly, this precluded the possibility of further examination of the liver tissue (e.g. histological examination) which could have further informed the results of the QSM experiment, and thirdly, the animals had had a significant amount of time and effort invested by the group that owned them, and so obtaining the number of animals required for statistical validation was not possible. In the future, if access to greater numbers was possible, a longitudinal study of changes in susceptibility and $ShvO_2$ as cirrhosis progressed may yield interesting results.

Despite the apparent usefulness of the measurement ^[20, 23, 24], $ShvO_2$ has been the focus of very few studies, fewer still that focus on rats. Of the few studies that have examined rats, there are large variations in the measured $ShvO_2$ values ranging from ~30% ^[25] to ~65% ^[20] in healthy and sham hepatectomy rats respectively. Further work on this topic could

include an in-depth characterisation of changes in ShvO_2 , as well as a comparison of invasive and non-invasive measurements under a variety of experimental conditions.

In addition to the small cohort, the tuning rod of the transmit/receive coil used during scanning was broken at the time the data was acquired, so the signal intensity (and hence SNR) was reduced. As the animals that were the focus of this experiment were primarily being used in a separate study, the window of opportunity to acquire data was limited. This window coincided with a time during which the tuning rod on the transmit/receive coil was malfunctioning, thus undermining the quality of the acquired data. The data acquired from the BDL rats was more reliable as the cohort consisted of 7 animals, however the small size of the sham cohort disallowed meaningful statistical analysis of control data, as well as meaningful comparison between the two cohorts.

The BDL model of liver cirrhosis is the most common model used to induce obstructive cholestatic injury to mice and rats ^[1]. However, there are a number of methods available to inflict the same injury. Toxic models involve the administration of substances such as carbon tetrachloride or ethanol over roughly the same amount of time as the BDL rats examined here (~4 – 6 weeks), and it is noted in the literature that the administration of ethanol will decrease the response of the liver to hyper- and hypoxic challenges ^[26]. This is most likely due to the presence of ethanol, rather than the manifestation of the liver's response to the insult. This is somewhat representative of the clinical situation – the liver's reaction to a wide variety of insults from hepatitis to drug and alcohol abuse is reasonably similar, and results in the same pathological characteristics.

6.6 Conclusions

In this work, I have demonstrated that it is possible to measure the susceptibility, and to calculate the SvO_2 in the major blood vessels of a cirrhotic liver. The susceptibility of the liver tissue as measured with QSM did not reflect the expected increase in iron deposition in the disease cohort, and administration of pure oxygen did not seem to reflect the vascular disruption that is characteristic of liver fibrosis. These results were unexpected, and most likely reflect the limited number animals studied and hardware problems that were present at the time of data acquisition. Nevertheless, the data presented here provide a proof of principle for the application of QSM to animal models of liver cirrhosis, and also provide motivation for a follow-up study to investigate the usefulness of QSM for diagnosing and staging the disease.

References

1. Liedtke, C., et al., *Experimental liver fibrosis research update on animal models, legal issues and translational aspects*. *Fibrogenesis & Tissue Repair*, 2013. **6**(19): p. 2 - 24.
2. Tsochatzis, E.A., J. Bosch, and A.K. Burroughs, *Liver cirrhosis*. *The Lancet*, 2014. **383**(9930): p. 1749-1761.
3. Schuppan, D. and N.H. Afdhal, *Liver cirrhosis*. *The Lancet*, 2008. **371**(9615): p. 838-851.
4. van Beers, B.E., et al., *Hepatic Perfusion Parameters in chronic liver disease*. *AJR Am J Roentgenol*, 2001. **176**: p. 667 - 673.
5. Huber, A., et al., *State-of-the-art imaging of liver fibrosis and cirrhosis: A comprehensive review of current applications and future perspectives*. *Eur J Radiol Open*, 2015. **2**: p. 90-100.
6. Venkatesh, S.K., M. Yin, and R.L. Ehman, *Magnetic resonance elastography of liver: clinical applications*. *J Comput Assist Tomogr*, 2013. **37**(6): p. 887-96.
7. Tao, R., et al., *Detection of siderotic nodules in the liver with susceptibility*. *Chin Med J*, 2012. **125**(17): p. 3110 - 3114.
8. Yin, M., et al., *Preliminary Assessment of Hepatic Fibrosis With Magnetic Resonance Elastography*. *Clin Gastroenterol Hepatol*, 2007. **5**(10): p. 1207 - 1213.
9. Dai, Y., et al., *Improving detection of siderotic nodules in cirrhotic liver with a multi-breath-hold susceptibility-weighted imaging technique*. *J Magn Reson Imaging*, 2011. **34**(2): p. 318-25.
10. Chen, W., et al., *Improved siderotic nodule detection in cirrhosis with susceptibility-weighted magnetic resonance imaging: a prospective study*. *PLoS One*, 2012. **7**(5): p. e36454.
11. Patterson, A.J., et al., *Quantitative BOLD imaging at 3T: Temporal changes in hepatocellular carcinoma and fibrosis following oxygen challenge*. *J Magn Reson Imaging*, 2016. **44**(3): p. 739-44.
12. Schneeweiss, B., et al., *Energy metabolism in patients with acute and chronic liver disease*. *Hepatology*, 1990. **11**(3): p. 387-93.
13. Abshagen, K., et al., *Pathobiochemical signatures of cholestatic liver disease in bile duct ligated mice*. *BMC Systems Biology*, 2015. **9**(1): p. 83.
14. Hadjihambi, A., et al., *Ammonia mediates cortical hemichannel dysfunction in rodent models of chronic liver disease*. *Hepatology*, 2017. **65**(4): p. 1306-1318.
15. Wang, Q.M., et al., *Heme oxygenase/carbon monoxide pathway inhibition plays a role in ameliorating fibrosis following splenectomy*. *Int J Mol Med*, 2013. **31**(5): p. 1186-94.
16. *Facts About Liver Disease - British Liver Trust*. 2017; Available from: <https://www.britishlivertrust.org.uk/about-us/media-centre/facts-about-liver-disease/>.
17. Balassy, C., et al., *Susceptibility-weighted MR imaging in the grading of liver fibrosis- a feasibility study*. *Radiology*, 2013. **270**(1): p. 149 - 158.
18. Tao, R., et al., *An in vitro and in vivo analysis of the correlation between susceptibility-weighted imaging phase values and R2* in cirrhotic livers*. *PLoS One*, 2012. **7**(9): p. e45477.
19. Moreau, R., et al., *Abnormal tissue oxygenation in patients with cirrhosis and liver failure*. *Journal of Hepatology*, 1988. **7**(1): p. 98-105.
20. Yoshioka, S., et al., *Hepatic Venous Hemoglobin Oxygen Saturation Predicts Regenerative Status of Remnant Liver after Partial Hepatectomy in Rats*. *Hepatology*, 1998. **27**(5): p. 1349 - 1353.

21. Bendsten, F., et al., *Hepatic venous oxygen content in alcoholic cirrhosis and non-cirrhotic alcoholic liver disease*. *Liver*, 1897. **7**: p. 176 - 181.
22. Sezai, S., et al., *Hepatic arterial and portal venous oxygen content and extraction in liver cirrhosis*. *Liver*, 1993. **13**(1): p. 31 - 35.
23. Takano, H., et al., *Monitoring of hepatic venous oxygen saturation for predicting acute liver dysfunction after Fontan operations*. *The Journal of Thoracic and Cardiovascular Surgery*. **108**(4): p. 700-708.
24. Shimizu, H., et al., *Changes in hepatic venous oxygen saturation related to the extent of regeneration after partial hepatectomy in rats*. *Am J Surg*, 1999. **178**(5): p. 428 - 431.
25. Carmichael, F.J., et al., *Effect of propofol infusion on splanchnic hemodynamics and liver oxygen consumption in the rat. A dose-response study*. *Anesthesiology*, 1993. **79**: p. 1025 - 1060.
26. Foley, L.M., et al., *In vivo monitoring of hepatic oxygenation changes in chronically ethanol-treated rats by functional magnetic resonance imaging*. *Magn Reson Med*, 2003. **50**(5): p. 976-83.

Final Discussion

The primary aim of this thesis was to investigate novel applications of Quantitative Susceptibility Mapping (QSM). The work focussed specifically on the liver, as this is a niche area that has so far been almost entirely unexplored otherwise, but one which could provide a rich area for improving the diagnosis and understanding of disease. The experiments performed represent the development and implementation of QSM in the rodent (mouse and rat) liver for the first time, and, furthermore, demonstrate the first instances in which QSM has been applied to a diverse range of liver pathologies. While preliminary in nature, the undertaking has resulted in a viable paradigm within which future experiments can be carried out, and has laid the groundwork for further avenues of study.

QSM is an exciting field that has given researchers a novel way to explore tissue composition and microstructure. Initial applications focussed on quantifying the changes in tissue iron content that are indicative of neurological disorders, but the field has grown rapidly to give rise to a diverse range of clinically relevant applications, many of which have been discussed during the course of this thesis. A number of clinical trials are currently ongoing ^[1-3], including one that aims to evaluate regional gadolinium (Gd) retention in patients that have undergone Dynamic Contrast Enhanced (DCE) MRI ^[1]. This is of particular relevance, as at time of writing the issue of toxicity caused by residual Gd is a highly contentious one in the MR community ^[4], and the results may have significant implications for diagnostic MR in clinical practice.

Applications of QSM in organs outside the brain are still relatively few in number, and some of the reasons for this may be due to the relative simplicity of acquiring images of the brain. For example, the lack of organ motion is advantageous, as it allows the acquisition of repeatable images with relative ease, and the comparably small air/tissue interfaces in the head require the removal of less information during processing. Secondly, the consistent architecture of the brain allows more robust comparisons between subjects, or in the same subject longitudinally. Similarly, the wide availability of brain masks and atlases means that processing the images is far less cumbersome, allowing segmentation to be performed automatically in seconds, as opposed to the hours required to do so manually. This has the added advantage of reducing the error that could be caused by human intervention. Thirdly, while it has been shown that there is a negligible amount of fat in the animals examined here

(chap. 3A. sec. 3.4.1), this will be a challenge in clinical imaging, requiring a reasonably complex augmentation of the processing protocol ^[5].

A significant amount of experimental work was dedicated to addressing the obstacles encountered during the implementation phase of the project, and there is still scope for further improvement. For example, respiratory gating was used during the all of the acquisitions, necessitating a regular respiratory rate. While this was not an issue when imaging healthy subjects, controlling by means of anaesthetic the respiratory rate of animals that were at an advanced stage of disease required a considerable level of skill and patience. In some instances the animals would periodically hyperventilate, resulting in ghosting and increased image noise. Another solution to this problem could be to implement retrospective gating, meaning that data is acquired throughout the entire respiratory cycle. Slices acquired during motion could then be identified during processing and removed from the dataset ^[5]. The trade-off between prospective and retrospective gating is a complex one – the data may be acquired at a faster rate, as the sequence doesn't require a trigger from the respiratory cycle and instead acquires data constantly. Conversely, retrospective gating necessitates an increased number of signal averages to ensure the missing data is adequately compensated for, and so may increase acquisition time, and subsequently the risk of subject mortality.

Some of the difficulties encountered during implementation however gave rise to novel solutions that may benefit the field of QSM imaging as a whole. As discussed in chapter 4 sec. 4.1.2.4, the reference against which QSM values are measured can easily be a source of systematic error when taken from an internal region (e.g. CSF, white matter). The inclusion of a sample of distilled water to act as an external reference is an entirely novel solution to the problem, and elegantly addresses a number of known issues, such as standardisation, and ensuring easy identification in all images. Selection of a suitable reference has been a point of contention for some time in the QSM community ^[6], and it is hoped that this may go some way to settling the argument.

Similarly, the TKD algorithm selected to perform the QSM inversion is well-suited to the exploration of novel applications. As mentioned, the speed with which it can carry out the calculation is extremely advantageous, as empirically optimising an image processing protocol requires repeatedly performing the same calculation while incrementally adjusting a variety of parameters. The drawback of the algorithm is the trade-off between image quality and fidelity, and is most likely the reason it is underused in the literature. The solution (chap

3 Sec 3.2.4) presented here to the systematic underestimation of susceptibility values inherent in the algorithm is also entirely novel. As discussed, the correction curve presented in the literature was derived experimentally, specifically for images of the brain acquired at 3T. The solution proposed here allows a correction curve to be calculated from a single data set (negating the need for multi-orientation acquisitions and the requisite processing thereof), in any organ, at any field strength.

The main experimental chapters detailed the application of QSM to a diverse range of hepatic scenarios. A hyperoxic gas challenge was utilised in all experiments, as it was thought that controlled modulation of the deoxyhaemoglobin content of the blood would impart information regarding blood oxygenation (chapter 4) and vascular status (chapter 5 & 6).

Chapter 4 detailed the first attempt at using QSM measurements to calculate the venous oxygen saturation in large branches of liver vasculature. Data was acquired under normoxic and hyperoxic conditions, and susceptibility was measured in both the portal and hepatic veins. SvO₂ was then calculated in each under both conditions. This was validated by means of invasive measurement, and it was found that there was excellent agreement between the calculated and directly measured values under both norm- and hyperoxic conditions.

It was not possible to obtain susceptibility measurements from the hepatic artery with the imaging protocol used here. However, susceptibility measurements from all three hepatic blood vessels at once would be extremely useful. For instance, it has been shown previously that it is possible to measure the blood flow in each vessel in rats using phase contrast MRI ^[7]. If one could measure both blood flow and oxygen saturation in all three major hepatic vessels, it would be entirely possible to calculate the hepatic metabolic rate of oxygen consumption. The *cerebral* metabolic rate of oxygen consumption has proved to be an extremely useful marker when assessing a variety of brain insults, and is thought to be a direct index of energy homeostasis and brain health ^[8]. The ability to non-invasively measure oxygen metabolism in the liver could prove equally useful for a wide variety of applications.

Chapter 5 describes the first application of QSM to a pre-clinical model of colorectal liver metastases, or, indeed, any cancer outside of the brain. In sec. 5.1 susceptibility was measured in the tumours and healthy liver tissue, and it was found that the tumours were significantly more diamagnetic than the surrounding tissue. Hyperoxia was induced in order to assess the vascularity of the tumours, and it was found that the susceptibility of the

tumours was significantly more paramagnetic during the administration of pure O₂. This is in contrast to a number of similar experiments contained within the body of literature on the subject, and it is hypothesised that this is due to an increased influx of unbound paramagnetic O₂ molecules dissolved in the blood plasma. In addition, susceptibility was measured in the portal and hepatic veins, and the calculated oxygen saturation in each was compared to that of a healthy cohort under the same conditions. It was found that there was significantly less oxygen in the hepatic venous blood of the animals that had tumours when compared to the healthy cohort. This was ascribed to the increased metabolic demands of the cancer.

Chapter 5 sec 5.2 outlined the first attempt at using QSM in conjunction with a gas challenge to assess the efficacy of a Vascular Disrupting Agent (VDA). Currently, there is a critical need for noninvasive imaging biomarkers of the response of cancer to therapy, and the aim of this chapter was to evaluate hepatic QSM in this context. The study examined 10 mice that had been inoculated with cancer. Half were administered the drug, and half were not in order to act as a control. The mice were scanned immediately before and 72 hours after the VDA was given to the treated cohort, and hyperoxia was induced during both sessions. Susceptibility was measured in tumours under both hyper- and normoxic conditions at both time points. It was found that, as in sec. 5.1, the susceptibility of the tumours was more paramagnetic under hyperoxic conditions, however the response of the tumours to the gas challenge was reduced after the administration of the VDA, possibly indicating a reduction in tumour blood supply caused by the denigration of their vasculature. The effect of the drug was confirmed by histology.

The cancer studies discussed in chapter 5 were extremely technically challenging, and took roughly two years to complete. It proved extremely difficult to cultivate tumours in the animals, and attempts to implement the model in several strains of mice using a number of different cell lines repeatedly failed, or met with very limited success. When the model was implemented successfully, it was found that the animals did not tolerate anaesthetic very well, which somewhat precluded cross validation with other MRI techniques.

While in contradiction to the existing literature, the reaction of the tumours to hyperoxia as measured via susceptibility was consistent across a number of experiments. It could be argued that this study may have benefited from invasive measurement of tumour oxygenation, although the tumours were extremely small and diffuse, and the measurements taken from the susceptibility maps encompassed all the tumours en masse by necessity.

Invasive measurements would have had to have been made in several tumours in each animal in order accurately assess changes in the changes in oxygenation status. The difficulty of ensuring the sample was actually taken from a tumour notwithstanding, it is unlikely that the mice could have tolerated the severity of the protocol.

The reduced reaction of the tumours to the gas challenge after the administration of a VDA in sec. 5.2 is encouraging, though there is scope for improvement in the experimental design. For example, one obvious improvement is to increase the numbers in each cohort to 10 animals each. This would allow a more rigorous statistical analysis, allowing the results to be discussed with greater confidence. Conversely, administering the drug to half of the animals, but scanning once, at an earlier timepoint (i.e. 24 hours after the drug was administered) may have meant that the animals could have better tolerated the anaesthetic, and would have eliminated the need to ensure the animals survived the entirety of a longitudinal study. This may have allowed their time in the scanner to be extended, potentially allowing cross-validation with other MRI techniques (e.g. R_2^* or ASL).

The experiment described in chapter 6 was the first instance in which QSM had been applied to a model of liver cirrhosis. As mentioned, the experimental work was carried out as part of a broader experiment to study hepatic encephalopathy. As such, priority was placed on ensuring the survival of the animals by minimising their time in the scanner. Furthermore, there were some technical difficulties which have already been outlined (chapter 6). While the results of this experiment are limited, it is reasonably apparent that QSM cannot detect changes in liver iron deposition that are associated with liver cirrhosis. The precise reasons for this remain unclear, particularly as it has been shown in the literature that it is possible with SWI. It may be the case that the iron distributed through the liver tissue is too diffuse to have a noticeable effect on the bulk susceptibility of the liver that is measurable by QSM. This is unlikely however, as it has been shown in the experiments presented here that QSM is sensitive to changes in susceptibility of the order of part per billion. Conversely, it may be the case that, as is shown in fig 6.4, the accumulation of iron in this model may be so limited as to not have a significant effect on the QSM measurement.

In general, the mechanisms underpinning changes (or lack thereof) in susceptibility of rodent liver tissue, as measured with QSM in all of the above experiments, remain somewhat mysterious. Upon commencement of the project, it was thought that the variation of iron throughout the liver tissue would have been obvious, particularly so as iron delineation and

quantification was the initial focus of QSM experiments in the brain. Furthermore, it was also assumed that hyperoxia would have had a measureable effect on the susceptibility of the liver tissue, due to the fact it is a highly vascularised organ with a relatively high throughput of blood. This was not the case, although changes in blood oxygen status were apparent.

One challenge throughout the course of this project has been the lack of literature on the subject. While liver susceptometry has been carried out clinically to assess iron overload for a number of years, very little work has been performed in rodents. As such, it is very difficult to find any experiments that have examined venous blood oxygen saturation in either the rodent *or* human liver, or changes therein associated with gas challenges. Furthermore, the existing literature values vary wildly from one experiment to the next, so comparing experimental results to literature values was extremely difficult. As such, future work could involve cannulating the major hepatic blood vessels and characterising changes in blood oxygen saturation brought about by various gas challenges or disease states. This would most likely be carried out in rats due to the size of the blood vessels in mouse livers.

The novelty of the work also made validating the experimental results extremely difficult, as there is no “gold standard” to compare results to. This is partially due to the *semi*-quantitative nature of QSM (see chapter 4 sec. 4.1.2.4 – water reference), but also because performing susceptometry is a difficult endeavour. For example, validation of susceptibility values could be sought by comparing QSM results to those obtained from a Superconducting Quantum Interference Device (SQUID). Examining samples on a SQUID however is by no means a trivial process, requiring rigorous preparation of the sample. Equally, validating results with similar MRI techniques may not be suitable in all instances. R_2^* for example, while related to susceptibility, effectively gives proxy measurements of susceptibility via local field inhomogeneities. As such, validation of the results in the above experiments was done where possible by invasive, direct measurements (chapter 4), or by histology (chapter 4 & 5).

The combination of QSM and a hyperoxic gas challenge puts to good use its ability to exploit dHb as an endogenous contrast agent, and is potentially quite a useful technique. The assessment of tumour vasculature and oxygenation is an important component of oncologic diagnostic procedure, particularly when deciding a treatment pathway. It is thought that the administration of O_2 could be well tolerated by the vast majority of patients, and so could easily be integrated into clinical protocol. The added advantage of performing measurements

in the blood vessels is that fat does not need to be accounted for during processing. $ShvO_2$ is an underutilised measurement, and it would appear that it can tell a lot about the health of the liver. Its underuse may be because, currently, it can only be measured invasively. The ability to perform the measurement non-invasively may allow more in-depth diagnoses or post-operative monitoring at very little cost in terms of morbidity.

Susceptibility mapping has the potential to be a powerful diagnostic tool, however currently much of the work in the field is focussed on improving the processing techniques as opposed to investigating novel applications. It is hoped that the work put forward in this thesis will go some way to opening new avenues of research, and stimulating a discussion that will encourage the exploration of new clinical applications and diagnostic perspectives.

References

1. clinicaltrials.gov. *QSM and Regional DCE MRI Permeability Using GOCART Technique - Full Text View - ClinicalTrials.gov*. 2017; Available from: <https://clinicaltrials.gov/ct2/show/NCT03091803?term=Quantitative+Susceptibility+Mapping&rank=5>.
2. clinicaltrials.gov. *Atorvastatin Therapy in Cerebral Cavernous Malformation, Exploratory Proof of Concept Trial - Full Text View - ClinicalTrials.gov*. 2017; Available from: <https://clinicaltrials.gov/ct2/show/NCT02603328?term=Quantitative+Susceptibility+Mapping&rank=4>.
3. clinicaltrials.gov. *Longitudinal Quantitative Susceptibility Mapping (QSM) in Alzheimer 's Disease - Full Text View - ClinicalTrials.gov*. 2017; Available from: <https://clinicaltrials.gov/ct2/show/NCT02752750>.
4. Administration, U.S.F.D., *FDA identifies no harmful effects to date with brain retention of gadolinium-based contrast agents for MRIs*; . Drug Safety Comms, 2015: p. 1 - 4.
5. Ramasawmy, R., et al., *Hepatic arterial spin labelling MRI: an initial evaluation in mice*. NMR in Biomedicine, 2015. **28**(2): p. 272-280.
6. Straub, S., et al., *Suitable reference tissues for quantitative susceptibility mapping of the brain*. Magn Reson Med, 2017. **78**(1): p. 204-214.
7. Chouhan, M., et al., *Use of Caval Subtraction 2D Phase-Contrast Imaging to Measure Total Liver and Hepatic Arterial Blood Flow*. Radiology, 2016. **280**(3): p. 916 - 923.
8. Liu, C., et al., *Quantitative Susceptibility Mapping: Contrast Mechanisms and Clinical Applications*. Tomography, 2015. **1**(1): p. 3-17.

